Magnetohydrodynamics in Hot Jupiters

Alexander William Hindle

Thesis submitted for the degree of

Doctor of Philosophy

School of Mathematics & Statistics

Newcastle University

Newcastle upon Tyne

United Kingdom

May, 2021

To Mary Buchan Haigh (1921–2020) and Hazel Berry Hindle (1930-2020).

Acknowledgements

I would like to thank my supervisors Tami Rogers and Paul Bushby for their guidance, support, and kindness over the course of my PhD. Moreover, I would like to thank them for the opportunities they have given me and for introducing me to this fascinating research topic.

I thank Andrew Gilbert for sharing and allowing the use of his notes on diffusion in shallow-water MHD and thank Andrew Cumming for interesting discussions and insights early on in my PhD. During my PhD I have benefited from discussions and advice from various members of the Applied Mathematics section of Newcastle University's School of Mathematics, Statistics and Physics. I would like to thank my undergraduate supervisor Andrew Baggaley for encouraging me to pursue a PhD, and all past and current members of the Astrophysical and Geophysical Fluid Dynamics research group that have shown me interest and have given me useful suggestions throughout. For this, particular thanks go to Anvar Shukurov, Andrew Soward, Toby Wood, Celine Guervilly, Andrew Fletcher and Graeme Sarson. I would like to thank Philipp Edelmann, Rathish Ratnasingam, Natalia Gómez-Pérez, Amit Seta, and James Hollins for countless discussions, both technical and informal.

I would also like to thank Andrew Gilbert and Toby Wood for their time in examining this thesis and for their expertise and critique, which have improved it.

Many other people in the department have made my years as a PhD student more enjoyable. Aside from those already mentioned, I would like to thank Jack Walton and Laura Wadkin (who have not only endured my company as a PhD student but also throughout our undergraduate degrees), all those who regularly attended "group" lunches, and all my past and current office members for their humour and company.

Finally, but most importantly, I would like to thank my family and my partner Roisin for their constant care and support.

Abstract

Hot Jupiters are Jupiter-like exoplanets found in close-in orbits. This subjects them to high levels of stellar irradiance and is believed to tidally-lock them to their host stars, causing extreme day-night temperature differentials which in-turn drive atmospheric dynamics. A ubiquitous feature of hydrodynamic models of hot Jupiter atmospheres is equatorial superrotation, which advects their hotspots (equatorial temperature maxima) eastwards (prograde). Observational studies generally find eastward hotspot/brightspot offsets. However, recent observations of westward hotspot/brightspot offsets suggest that this is not ubiquitous. Prior to these observations, three-dimensional magnetohydrodynamic simulations predicted that westward hotspots could result from magnetohydrodynamic effects in the hottest hot Jupiters, yet the mechanism driving such reversals is not well understood.

We study the underlying physics of magnetically-driven hotspot reversals using a shallow-water magnetohydrodynamic model. This captures the leading order physics of hot Jupiter atmospheres, but with reduced mathematical complexity. The model's hydrodynamic counterpart is well-established and has successfully been used to explain equatorial superrotation in hydrodynamic models of hot Jupiter atmospheres in terms of planetary scale equatorial wave interactions. However, until now, shallow-water magnetohydrodynamic models have not been applied to hot Jupiters. Firstly, we find that the model can indeed capture the physics of magnetically-driven hotspot reversals. We use non-linear numerical simulations to understand the dominant force balances that drive the reversals and use a linear analysis of the system's planetary scale equatorial waves to understand the reversal mechanism in terms of wave interactions. We then use the developed theory to place physically motivated observational constraints on the magnetic field strengths of hot Jupiters exhibiting westward hotspot/brightspot offsets, finding that on the hottest of these the observations can be explained by moderate planetary magnetic field

strengths. Finally, we identify candidates that are likely to exhibit magnetically-driven hotspot reversals to help guide future observational missions.

Contents

List of Figures

List of Tables

Astronomical Units of Measure

AU Astronomical unit (mean Earth-Sun distance; $1.495\,978\,71 \times 10^{11}\,\mathrm{m}$).

bar Unit of pressure ($10^5\,\mathrm{Pa} = 10^5\,\mathrm{N\,m^{-2}} \approx 0.987\,\mathrm{atm}$).

$M_\oplus$ Earth mass ($5.972\,167\,87 \times 10^{24}\,\mathrm{kg}$).

M_J Jupiter mass ($1.898\,124\,6 \times 10^{27}\,\mathrm{kg}$).

$M_\odot$ Solar mass ($1.988\,409\,87 \times 10^{30}\,\mathrm{kg}$).

pc Parsec ($3.085\,677\,58 \times 10^{16}\,\mathrm{m}$).

R_J Nominal Jupiter equatorial radius ($7.1492 \times 10^{7}\,\mathrm{m}$).

$R_\odot$ Nominal solar radius ($6.957\,000\,00 \times 10^{8}\,\mathrm{m}$).

Chapter 1

An Introduction to Hot Jupiters

The first extrasolar planet found orbiting a Sun-like star was discovered in 1995 (Mayor & Queloz, 1995). This was 51 Pagasi b: a planet with approximately half the mass of Jupiter and a remarkably close-in nearly circular orbit, with an orbital radius of 0.05 AU[1]. This close-in gas giant astonished observers as its close proximity to its host challenged theories of planetary formation based on the Solar System paradigm (e.g., Dawson & Johnson, 2018). Nevertheless, throughout the late-1990s and 2000s more and more near-Jupiter-mass planets with close-in orbits were discovered and, by the end of the 2000s, the vast majority of known exoplanets were of this type. This lead to the construction of the *hot Jupiter* exoplanet class. The exact definition of the hot Jupiter classification criteria varies between sources, but in this work the term hot Jupiters will generally refer to extrasolar planets with masses comparable to Jupiter and with orbital semimajor axes of $a \lesssim 0.1\,\mathrm{AU}$ (e.g., Showman *et al.*, 2010; Laughlin *et al.*, 2011), where we use the mass range $0.1\,M_\mathrm{J} < M < 10\,M_\mathrm{J}$, with M and M_J denoting the planetary mass and Jupiter's mass respectively. This definition circumvents star/planet classification problems for the most massive planets by excluding planets with masses close to the limiting mass of thermonuclear fusion[2], and has a lower mass bound between the masses of Saturn and

[1]For comparison, Mercury's orbit has the semimajor axis $a = 0.39\,\mathrm{AU}$ (Carroll & Ostlie, 2006).

[2]Brown dwarfs, the least massive class of star, become hot enough to burn deuterium when $M \gtrsim 13\,M_\mathrm{J}$ (Carroll & Ostlie, 2006).

the smaller gas giants of the Solar System[3]. The name "hot Jupiter" derives from the fact that these gas giants share physical characteristics (i.e., mass and size) with Jupiter but, due to their close-in orbits, have much larger atmospheric temperatures. Typically, their orbit-averaged equilibrium temperature, T_{eq}, ranges between $T_{\mathrm{eq}} \sim 500$-$3000\,\mathrm{K}$, while for Jupiter $T_{\mathrm{eq}} = 124.4\,\mathrm{K}$ (Guillot, 2005).

While their origins remain enigmatic (for full review see Dawson & Johnson, 2018), compared to the number of detections of other exoplanet types, hot Jupiters are proportionally over-represented (see Figure 1.1). This finding stems from their properties being well-fitted to the natural biases of the most successful exoplanet detection techniques. Significantly, this finding has lead to a surge in observational interest and progress in characterising hot Jupiters, providing an outpouring of data. These observational advancements have made the testable study of hot Jupiter atmospheres possible, which has subsequently driven the development of explanatory dynamical theory. As a result of these advancements, from a fluid dynamics perspective, the atmospheres of hot Jupiters have been found to be both unique and are interesting in their own right. The field of explanatory atmospheric dynamics has now reached an exciting and auspicious phase, where theory and observations are simultaneously advancing the progress of one-another.

In this chapter, we aim to give an overview of the important observational and theoretical progress in understanding hot Jupiter atmospheres. We begin with a brief non-exhaustive overview of exoplanet detection and meteorological methods in Section 1.1. The benefits of this discussion are fourfold: first, it will illustrate the observational biases that make hot Jupiters so amenable for study; second, it will highlight which atmospheric features are measurable; third, it will enable us to discuss cited observational results freely throughout this work; forth, it is useful for framing the contributions of our work within the wider context of explanatory research. Once these observational foundations have been established, we shall discuss relevant observational findings to hot Jupiter atmospheres in Section 1.2. Following this, we provide a summary of some of the key aspects of dynamical

[3]For comparison, Saturn, Uranus, and Neptune have the respective masses $0.2994\,M_{\mathrm{J}}$, $0.0457\,M_{\mathrm{J}}$, and $0.0539\,M_{\mathrm{J}}$ (Carroll & Ostlie, 2006).

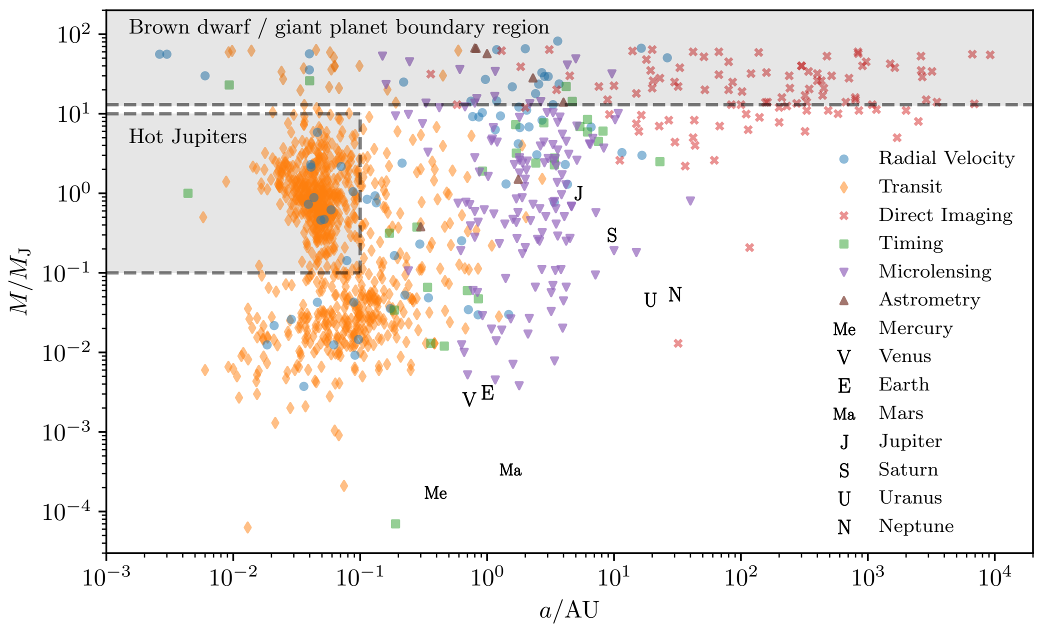

Figure 1.1: A parameter space diagram of exoplanet detections using data from the exoplanet.eu archive, accessed May 30, 2021. Detection methods for known planets are compared to the planets' orbital semimajor axes and mass. For reference, we also plot the parameter space locations of the Solar System planets and shade regions containing hot Jupiters ($a < 0.1\,\mathrm{AU}$ and $0.1\,M_\mathrm{J} < M < 10\,M_\mathrm{J}$) and Brown dwarfs ($M > 30\,M_\mathrm{J}$), where the theoretical deuterium burning mass threshold is used as the definition of the star-planet boundary. We comment that the data of the exoplanet.eu archive is cut off beyond $60\,M_\mathrm{J}$. The numbers of discoveries for each method can be found in Table 1.1.

theory of hot Jupiters in Sections 1.3 and 1.4. In Section 1.3 we shall discuss hydrodynamic theory including models, fundamental principles, and explanations of observed features; whereas in Section 1.4 we shall discuss previous applications of magnetohydrodynamic theory to hot Jupiters, highlighting some of the open questions and active research areas. These include whether magnetism can explain observed radius over-inflation on hot Jupiters, whether hot Jupiter atmospheres can support dynamo action, and understanding how magnetism can drive atmospheric wind variations in the photosphere of hot Jupiters. The last of these areas of study will be the main concern of this work and will feature throughout.

Table 1.1: Number of detected exoplanets for each of the methods discussed in the text, as well as astrometry (i.e., through the precise measurements of the positions of nearby astrophysical objects). We tabulate data for the two star-planet mass boundary cut-offs 60 M_{J} (used by www.exoplanet.eu and based on the object's mass-density-radius distribution) and 13 M_{J} (deuterium burning). This data is taken from www.exoplanet.eu, accessed May 30, 2021.

Detected exoplanets — May 2010						
Mass cut-off	Radial vel.	Transit	Imaging	Timing	Microlensing	Astrometry
60 M_{J}	940	3422	147	68	149	14
13 M_{J}	60	961	46	37	129	3

1.1 Observational methods for exoplanet detection and meteorology

1.1.1 Radial velocity method

In astronomy, the *radial velocity* of a star is the rate of change of the distance between the star and the observer on Earth. This can be measured using Doppler spectroscopy (i.e., comparing shifts in the known spectral lines of the star). If the star has an accompanying planet, the star-planet orbit will perturb the radial velocity from its usual star-Earth pattern in a periodic fashion. Using careful monitoring of distant stars, such signal deviations can be used to identify an orbiting exoplanet. Furthermore, if this method is successful in discovering a planet, the profiles and magnitudes of the radial velocity deviations can be used to place constraints on the orbital properties of the star-planet orbit (i.e., the orbital period, the star/planet mass ratio, the orbital semimajor axis, and the orbital eccentricity). The main limitation of the radial velocity method is that it only measures the star's movement along the line-of-sight. Therefore, if the orbital plane is not aligned with the line-of-sight, the true orbital motion of the star will be greater than the value measured from Doppler spectroscopy. To overcome this issue and obtain accurate planetary constraints, radial velocity measurements are usually combined with other measurements. Moreover, in order to apply Doppler spectroscopy accurately, the radial velocity method is most effective when applied to stars with stable emission spectra. The accuracy of radial velocity also depends on the sensitivity of the spectrograph used for measurements. The

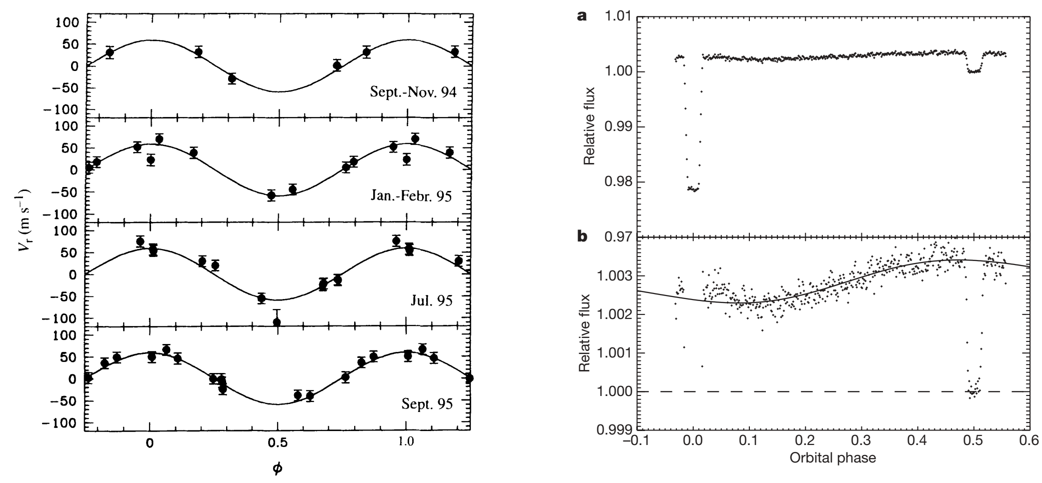

Figure 1.2: Radial velocity measurements and a photometric (infrared) phase curve. Lefthand panel (taken from Mayor & Queloz, 1995): The radial velocity of the star 51 Pagasi as a function of orbital phase, at four different epochs, where star-Earth motions have been removed and a fitting line has been overlaid to represent orbital motion. Righthand panel (taken from Knutson *et al.*, 2007): an infrared (8 µm) phase curve of one orbital cycle of the HD 209458 system, measured using the Spitzer Space Telescope. The phase curve is plotted on two scales: (*a*) 0.97-1.01 (top) and (*b*) 0.999-1.004 (bottom). The larger of these (top) clearly shows the primary and secondary eclipses; while the smaller of these (bottom) shows variations in the relative infrared flux between the eclipses.

most sensitive instruments for this tend to be on large ground-based telescopes,[4] however, sensitive spectrographs are also standard equipment on spaced-based telescopes (see Table 1.2).

The radial velocity method was the front-running exoplanet detection technique throughout the late 1990s and, to date, has identified 940 exoplanets, though a large number of these are beyond the deuterium burning mass threshold (see Table 1.1). The first of these discoveries was the aforementioned 51 Pagasi b. In the lefthand panel of Figure 1.2 we present the radial velocity of the star 51 Pagasi at four different epochs, taken from Mayor & Queloz (1995), where star-Earth motions have been removed. In this plot the orbital motion of the star 51 Pagasi, resulting from the planet 51 Pagasi b, can be identified from

[4]Examples of these include the Echelle SPectrograph for Rocky Exoplanets and Stable Spectroscopic Observations (ESPRESSO) on the Very Large Telescope (VTL) in Chile, the High Accuracy Radial Velocity Planet Searcher (HARPS) on the European Southern Observatory's (ESO) La Silla 3.6 m telescope in Chile, the EXtreme PREcision Spectrograph (EXPRES) on the Lowell Observatory's 4.3 m Lowell Discovery Telescope in the USA, and the CORALIE spectrograph on the 1.2 m Swiss-Euler telescope at La Silla Observatory, Switzerland.

Table 1.2: Spaced-based telescopes for transit photometry on exoplanets. All information was collated using official mission webpages. For wavelengths of the electromagnetic spectrum refer to Table 1.3.

Telescope	Launch date	Retired	Wavelengths
Hubble Space Telescope	April 1990	—	Ultraviolet, visible, and infrared (115-2500 nm)
Spitzer Space Telescope	August 2003	January 2020	Infrared (3-180 μm)
CoRoT[1]	December 2006	June 2014	Ultraviolet, visible, and infrared (250-1000 nm)
Kepler	March 2009	October 2018	Visible, infrared (430-890 nm)
TESS[2]	April 2018	—	Visible, infrared (600-1000 nm)
JWST[3]	Planned March 2021	—	Visible, infrared (0.6-28.5 μm)
PLATO[4]	Planned 2026	—	Visible, infrared (500-1000 nm)

[1] Convection, Rotation et Transits planétaires (in French).
[2] Transiting Exoplanet Survey Satellite.
[3] James Webb Space Telescope.
[4] PLAnetary Transits and Oscillations of stars.

the fitting lines. Clearly, the radial velocity method has a greatest signal when the star-planet gravitational interactions are greatest. Hence, due to Newton's law of universal gravitation, the radial velocity method is naturally adapted to seeking planets with large masses and/or close-in orbits. This can be seen by comparing the masses and semimajor axes of radial velocity exoplanet detections in Figure 1.1.

1.1.2 Transit photometry

A *transiting planet* is one that passes in front of its host star, as seen from Earth. The closer a planet is to its host star, the higher the probability that it passes in front of the Earth-bound observer's view of its host. Therefore, as the radial velocity method continued to detect close-in giant exoplanets throughout the late 1990s, astronomers anticipated the detection of a first transiting exoplanet. This expectation was realised at the end of 1999 when two groups simultaneously detected planetary transits around the star HD 209458 (Charbonneau *et al.*, 2000; Henry *et al.*, 2000). This discovery lead to the first implementation of *transit photometry:* characterising parameters and features of a tran-

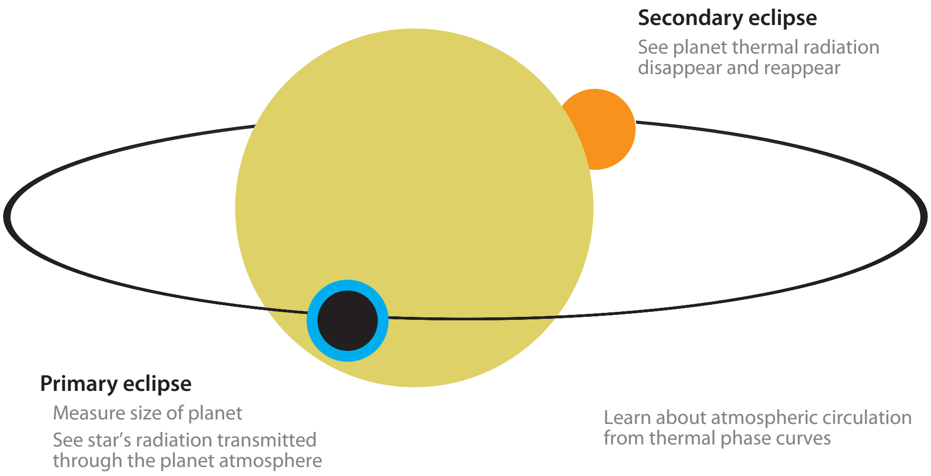

Figure 1.3: A schematic showing the possible measurements that can be taken when one observes a full orbital phase of a transiting exoplanet, taken from Seager & Deming (2010).

siting exoplanet through taking measurements of the irradiance (or the light intensity) of the combined star-planet system.

Observing a full orbital phase of a transiting exoplanet allows one to take a variety of useful measurements, as illustrated in the schematic diagram of Figure 1.3 (taken from Seager & Deming, 2010). We discuss this diagram alongside an example infrared phase curve (i.e., a time series of the relative light flux at 8 μm) of the star-planet system HD 189733 over one orbital cycle, which is taken from Knutson *et al.* (2007) and plotted in the righthand panel of Figure 1.2. This shows the relative flux of infrared light on two scales (a) 0.97-1.01 (top) and (b) 0.999-1.004 (bottom).

The first feature of the infrared phase curve in the righthand panel of Figure 1.2 is a large drop in relative flux, which can be seen in the upper zoomed-out phase curve at an orbital phase of zero. This is the *primary eclipse* or *transit*, where the planet passes between the star and the observer (compare to the schematic in Figure 1.3). During the transit the measured relative light flux drops by the amount of the planet-star area ratio so, if one knows the host star's radius, one can calculate the planetary radius.[5] Further, since the

[5]For example, the relative flux drop due to the primary eclipse of HD 189733 b in the infrared phase curve presented in Figure 1.2 is $\sim$ 0.02, Hence, one estimates the planet-star radius ratio in the HD 189733 system is $R/R_* \sim \sqrt{0.02} \approx 0.14$. Using data from exoplanet.eu to check this crude calculation, the actual planet-star radius ratio of the HD 189733 system is $R/R_* = 1.138\,R_\mathrm{J}/0.805\,R_\odot = 0.145$, where the

Table 1.3: The electromagnetic spectrum as defined in (Carroll & Ostlie, 2006)[1].

Type of radiation	Wavelength
Gamma ray	$\lambda < 1\,\mathrm{nm}$
X-ray	$1\,\mathrm{nm} < \lambda < 10\,\mathrm{nm}$
Ultraviolet	$10\,\mathrm{nm} < \lambda < 400\,\mathrm{nm}$
Visible	$400\,\mathrm{nm} < \lambda < 700\,\mathrm{nm}$
Infrared	$700\,\mathrm{nm} < \lambda < 1\,\mathrm{mm}$
Microwave	$1\,\mathrm{mm} < \lambda < 10\,\mathrm{cm}$
Radiowave	$\lambda > 10\,\mathrm{cm}$

[1] The boundaries of the wavelength regions are somewhat arbitrary and vary between sources.

magnitude of the primary eclipse's flux drop scales with the planet-star area ratio, exoplanet detections using transit photometry have selection biases favouring (close-in) giant planets. An additional benefit of observing a transit is that, during this primary eclipse, light from the host star grazes the exoplanet's atmosphere (see blue annulus in Figure 1.3). This means that during transit the chemical composition of the exoplanet's atmosphere can be investigated by taking an *absorption spectrum*, while filtering the spectral signals of the host star (which can be obtained at other orbital phases).

The second major feature of the infrared phase curve in the righthand panel of Figure 1.2 is a smaller drop in relative flux, which can be seen at an orbital phase of 0.5. This is the *secondary eclipse*, where the planet passes behind the star (from the observer's viewpoint). The reduction in the light flux is caused by the removal of the planet's signal. Therefore, the light flux of the planet is the drop in the system's total light flux during the secondary eclipse compared to just before/after the secondary eclipse. The most accurate measurements of these secondary eclipse flux differences can be taken when the light flux from the planet is comparable to the star (i.e., when the signal-noise ratio is large). In the lefthand panel of Figure 1.4 the blackbody flux of some Solar System bodies, as "seen" from 10 pc, are compared to the blackbody flux of a Sun-like star and a typical hot Jupiter, again, as "seen" from 10 pc. The light flux of each object is plotted across a spectrum of wavelengths between 0.1 μm (ultraviolet) and 40 μm (infrared) and, for reference, we

Jupiter-Sun radius ratio of $R_\mathrm{J}/R_\odot = 0.1028$ has been applied.

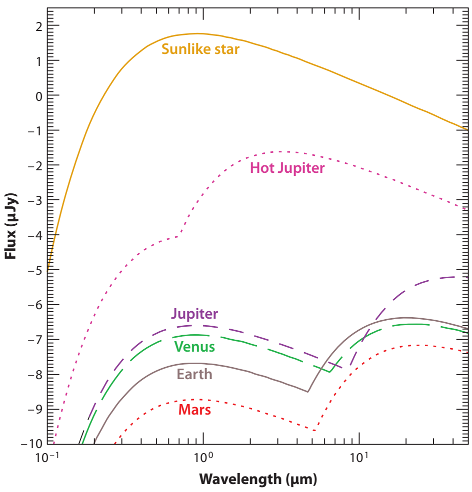

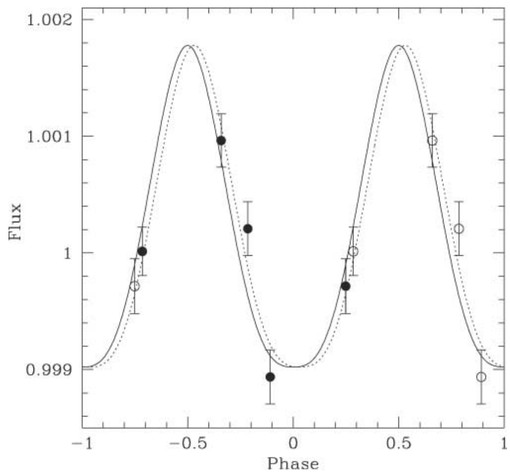

Figure 1.4: Lefthand panel: A comparison of light flux signals of different objects, from 10 pc, showing why Jupiters are amenable for study. Adapted from Seager & Deming (2010). The blackbody flux (i.e., the surface irradiance per unit frequency in units of $10^{-26}\,\mathrm{W\,m^{-2}\,Hz^{-1}}$, on a logarithmic scale) of some Solar System bodies as "seen" from 10 pc are compared to that of a typical hot Jupiter (with an equilibrium temperature of 1600 K and an albedo of 0.05). Righthand panel: a separated infrared (24 μm) phase curve of the planet υ Andromedae b, taken from Harrington *et al.* (2006). The phase curve is constructed using data from two orbital cycles, which are distinguished by solid (first) and empty (second) points, with associated error bars. The authors have included two fitting lines based on an analytic planetary emission model. The solid line denotes the phase curve with the hottest latitudinal point (the hotspot) located at the position of maximum stellar irradiance (the substellar point); the dashed line is the best-fit phase curve and has an eastward phase shift of 11° (i.e., with the hotspot positioned 11° east of the substellar point).

tabulate the wavelengths of the electromagnetic spectrum in Table 1.3. From Figure 1.4, one can see that a typical hot Jupiter has significant planet-star light flux ratio at near and mid infrared wavelengths and has a lesser (but still observable) planet-star light flux ratio in the visible spectrum. However, the light flux from exoplanets akin to the bodies in our Solar System would be orders of magnitude smaller. This makes their secondary eclipse photometric signals challenging to distinguish from noise. Measuring a hot Jupiter's secondary eclipse light flux drop at different wavelengths is useful for obtaining information about different atmospheric features. Infrared light flux measurements indicate the exoplanet's dayside temperature; whereas measurements in visible wavelengths can be used to determine the planetary albedo and estimate temperature by treating the planet as a blackbody (e.g., Cowan *et al.*, 2007).

Once the exoplanet's photometric signal has been separated from its host's signal, the system's phase curve measurements between the two eclipses can be used to elicit further information about the planet's atmosphere. If variations in the planet's phase curve contribution are distinguishable from noise (as seen in the lower phase curve in the righthand panel of Figure 1.2), it provides an observer information about how the temperature/brightness of the planet varies between its day and night sides. One can separate these variations and use planetary emission models to construct a planetary phase curve. An example of a planetary infrared phase curve of the planet υ Andromedae b, taken from Harrington *et al.* (2006), is plotted in the righthand panel of Figure 1.4 to illustrate this. Similarly, the separated planetary phase curve information can also be used to construct temperature/brightness maps of the exoplanet. In Figure 1.5, which is taken from Knutson *et al.* (2007), we present a temperature map of the hot Jupiter HD 189733b. This was constructed using the infrared phase curve of the HD 189733 system, which is presented in the righthand panel of Figure 1.2, and fitting treatment based on the expected relative light flux contribution of each longitudinal slice at a given orbital phase (for further discussion see Knutson *et al.*, 2007). Planetary phase curves and temperature maps like these provide useful testable comparisons for theories of atmospheric dynamics. In particular, they can be used to estimate a hot Jupiter's day-night temperature contrasts

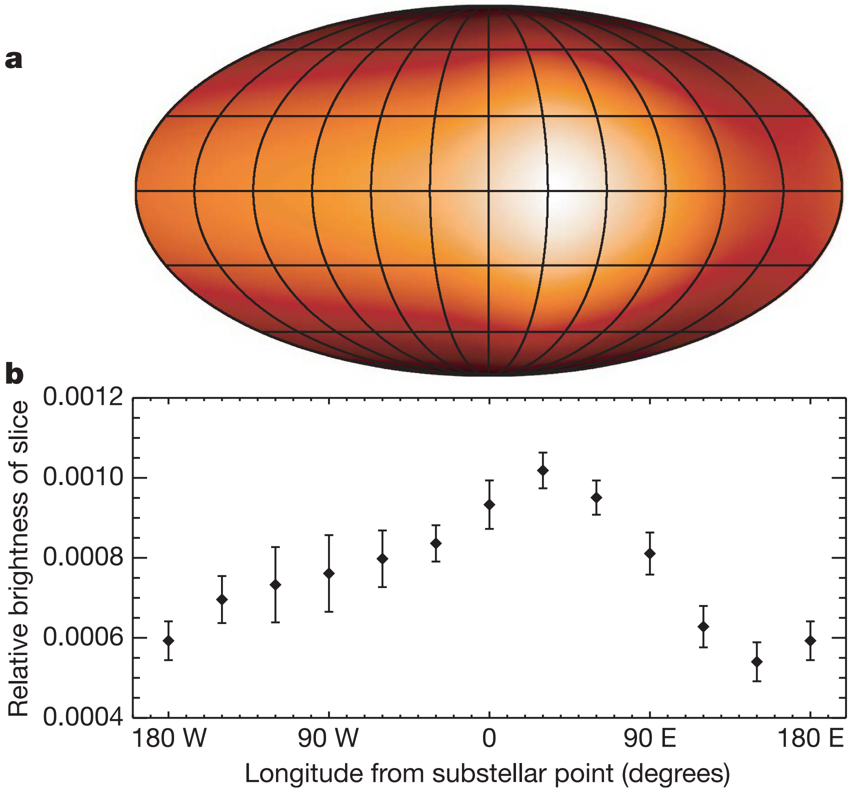

Figure 1.5: A temperature map of the hot Jupiter HD 189733b constructed using variations in the infrared phase curve presented in the righthand panel of Figure 1.2, taken from Knutson *et al.* (2007). The temperature map is calculated by assuming synchronous tidally-locked rotation, which is expected (see Section 1.2.2 for discussion). The planet is divided into longitudinal slices and the light flux from the phase curve at a given orbital phase is attributed to the longitudinal slice closest to the observer at that point (subject to a fitting treatment). In the upper half of this figure, the temperature is visualised as a colour map, with the brightest colours representing the hottest regions; in the lower half, the relative brightness of each longitudinal slice are displayed. Here the longitudinal axis is centred about the substellar point (i.e., the point at the noon on the dayside). In the temperature map, sinusoidal dependence on latitude is assumed.

and the location of its maximal temperature (i.e., its hotspot).

Transit photometry measurements can be taken by ground-based telescopes and ground-based transit photometry surveys have had a great deal of success in identifying exoplanets[6]. However, the Earth's atmosphere poses a significant challenge for photometric measurements with small signal-noise ratios (e.g., determining temperature/brightness maps). Cloud cover and turbulence in Earth's atmosphere hinder optical measurements; whereas water vapour in Earth's atmosphere absorbs much of the infrared signal. These problems can be circumvented by using space-based telescopes. In Table 1.2 we detail past, present, and future space-based telescopes with optical detectors in the visible and infrared wavelengths. These have amassed a huge amount of data since their launches and archival data from *Spitzer*, *CoRoT*, and *Kepler* are still producing interesting results years after their retirement. To date, transit photometry (from both ground-based and space-based telescopes) has yielded 3422 detections (see Table 1.1), making it the most successful detection method by far. This means that the pool of known exoplanets tend have features optimal for transit detections (i.e., large radii, close-in orbits, and short orbital periods).

1.1.3 Other detection and characterisation methods

By the end of the 2000s, radial velocity monitoring and transit photometry had become the leading exoplanet detection methods (see Figure 1.1). However, other planet-hunting methods have yielded discoveries and can be used to infer explanatory characteristics. Here we briefly discuss a few of them.

Direct imaging

The most intuitive way to observe an exoplanet is to take a direct image of it. This can be achieved by using a coronagraph, which is filter that blocks starlight. However, compared to their hosts, exoplanets are faint sources of light (for comparisons at 10 pc, see lefthand panel of Figure 1.4). This generally limits direct imaging to bright (massive and/or young)

[6] For example, the international Wide Angle Search for Planets (WASP) collaborative survey that uses transit photometry to perform an ultra-wide angle search with ground-base telescopes in Palma, Spain and Sutherland, South Africa. At the time of writing it has identified just under 200 planets.

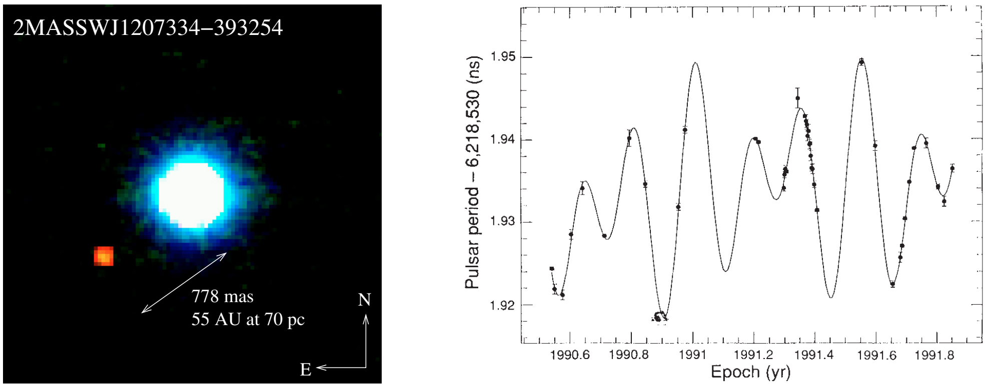

Figure 1.6: Direct imaging and pulsar timing. Lefthand panel (taken from Chauvin *et al.*, 2004): An image of the brown dwarf 2MASSWJ1207334–393254 (blue) and its giant planet companion 2MASSWJ1207334–393254 b (red). The colourings of the image denote different imaging wavelength bands (see original text for more details). Righthand panel (taken from Wolszczan & Frail, 1992): Variations in the orbital period of the pulsar PSR1257+12 (in nanoseconds), with the predicted variations of a two-planet model indicated by a solid line.

planets that are located far away enough from their host star that their signal is not lost in the stellar glare (see Figure 1.1). Imaging at infrared and optical wavelengths can yield information about the planet's atmospheric temperature and albedo (hence blackbody temperature), respectively. From such temperature measurements, planetary evolutionary models can be applied to estimate the planet's mass, albeit with a large relative uncertainty (Chauvin *et al.*, 2004). In the lefthand panel of Figure 1.6, we present an image of 2MASSWJ1207334–393254 b, which is taken from Chauvin *et al.* (2004). This was the first confirmed explanatory detection made by direct imaging. Since then, progress has been made with imaging techniques and successes have included observations from both ground-based and space-based telescopes (for further details see Traub & Oppenheimer, 2010). To date, 147 exoplanets have been detected using direct imaging, making it an increasingly viable characterisation method, though we comment that many of these are either the most massive exoplanets or have masses beyond the theoretic deuterium burning threshold (see Figure 1.1).

Timing methods

If the behaviour of an astrophysical object is well-known and consistent, deviations from their usual temporal cycles or signals can indicate a nearby companion object. For exoplanet detection, timing methods come in a few different guises.

Pulsar timing is a method that uses the regularity of a pulsar's rotation to search for orbiting exoplanets. A pulsar is a highly-magnetised, rapidly rotating neutron star that emits beams of electromagnetic radiation from its magnetic poles. As the pulsar rotates, its beam of radiation sweeps across the cosmos, only becoming visible to an Earth-bound observer when it is pointed at Earth (much like an observer on a boat viewing a sweeping lighthouse beam). Due to their very dense nature, pulsars have regular rotation periods and pulses arrive to Earth at regular intervals. The presence of an exoplanet can cause periodic variations of a pulsar's rotation period, which can be identified in their pulse signals. Pulsar timing was the method responsible for the first ever exoplanet discoveries: a planetary system around the pulsar PSR1257+12 (Wolszczan & Frail, 1992). In the righthand panel of Figure 1.6, we present the variations in the orbital period of PSR1257+12, taken from Wolszczan & Frail (1992). This plot has a solid line, which denotes the predicted period variations of a two-planet model, overlaid on the period measurements.

Similar timing methods can be applied to regularly pulsating or varying stars. The first exoplanet detection using *variable star timing* was made by Silvotti *et al.* (2007), who discovered the planet V 391 Pegasi b. This discovery was made by timing pulses from the post main-sequence star V 391 Pegasi (which are caused by core helium burning).

If a star has a known transiting exoplanet, *transit timing variations* (often abbreviated to TTV) can be used to search for additional bodies within its planetary system. The method of transit timing variations measures deviations in the transiting planet's orbital periodicity, from which orbital mechanics can be used to detect and constrain other planets within the system (Miralda-Escude, 2002). This method is highly sensitive for detecting additional non-transiting planets, even down to Earth-like masses (Agol *et al.*, 2005).

Further, the method of transit timing variations is useful for making detections in far-off systems, where radial velocity methods cannot detect them due to a low signal-noise ratio. The first exoplanet detected using transit timing variations was Kepler-19c (Ballard *et al.*, 2011). Kepler-19c is a planet with a mass similar to Neptune, which was found by studying the transit timing variations of Kepler-19b — a smaller transiting exoplanet, with approximately half the mass of Neptune.

The method of *eclipsing binary timings* is analogous to the method of transit timing variations but it considers systems with eclipsing binary stars, rather than those with a host star and a transiting planet. Exoplanets are sought by using orbital mechanics to explain the timing deviations of a system's binary eclipses (i.e., when one star passes in front of the other, as viewed from Earth). The first exoplanet prediction made using this method was for the planet PSR B1620-26 (AB) b, which was believed to be detected in 1993 (Thorsett *et al.*, 1993).[7] However, due to large uncertainties in its orbital parameters, it was not confirmed until 2003 (see the exoplanet.eu archive entry for more details).

As a whole, timing methods cover a range of settings so they have been successful in discovering exoplanets with a variety of planetary parameters (see Figure 1.1). However, they generally require measurements over a long time period in order to establish the long-term variations in measured periodicities. To date, timing methods account for 68 exoplanet detections (see Table 1.1).

Gravitational microlensing

One of the consequences of Einstein's theory of general relativity is that light can be bent and focused by the gravitational field of a star. Therefore, if two stars almost exactly line up, the light of the distant background star can be magnified by the gravitational field of the closer lensing star. This phenomenon is known as *gravitational microlensing*. The degree of gravitational microlensing can be used to infer information about the lensing star's gravitational field. Moreover, if a third object (i.e., an exoplanet) is gravitationally

[7] B1620-26 is a binary star system containing the pulsar B1620-26 A, the white dwarf B1620-26 B, and the exoplanet PSR B1620-26 (AB) b.

interacting with the lensing star, deviations to this lensing effect can cause variations in the light flux coming from the background star. Such variations can be used to determine the existence and orbital properties of the lensing star's companion (i.e., mass and orbital distance).

The main strength of gravitational microlensing is that it does not have a bias for massive exoplanets with close-in orbits. In fact, exoplanets have been found with separations ranging between 0.2 AU and 40 AU and gravitational microlensing struggles to detect planets with very close-in ($\lesssim 0.2$ AU) or far-off ($\gtrsim 100$ AU) orbits. Further, any sufficiently massive object can act as a gravitational lens, with masses of exoplanets discovered from gravitational microlensing ranging from $\sim 1.4\,M_{\oplus}$ upwards, where $M_{\oplus}$ is Earth's mass. This is remarkable in that it offers the possibility of finding Earth-like planets within the habitable zones of their host stars (see Figure 1.1). So far, all microlensing detections of exoplanets have been found at distances of several kiloparsec away from the Solar System, along the line-of-sight to the Galactic center (since there is a large line-of-sight stellar density at these distances). Hence, gravitational microlensing can provide an indication of the true population of planets with intermediately distant orbits lying towards the Galactic center (for review see Tsapras, 2018).

One of the main drawbacks of gravitational microlensing is that, since planetary microlensing events are one-offs with short observational time-windows, obtaining highly accurate orbital constraints is considerably challenging (Bond *et al.*, 2004). This is countered by coordinating different telescopes around the world to take independent microlensing measurements of the same events to build an ensemble picture. Another challenge is that, since this method requires the near alignment of two stars, the probability of detecting planetary microlensing deviations is low, $\sim 10^{-8}$ per star (Tsapras, 2018). However, wide-view surveys[8] monitor approximately a billion stars regularly, meaning that there enough monitored stars to tip the balance of probability. Consequently, to date, gravitational microlensing has lead to the discovery of 149 exoplanets (see Table 1.1). The first of these

[8]Examples of such surveys are the Optical Gravitational Lensing Experiment (OGLE), and the MAssive Compact Halo Objects (MACHO) project.

was OGLE-2003-BLG-235L b: a (Bond *et al.*, 2004). This is a $2.6 \pm 0.8\,M_{\mathrm{J}}$ planet orbiting about a $0.63 \pm 0.08\,M_{\odot}$ host star.

1.1.4 Concluding remarks on observational methods

In this section, we have given a brief overview of exoplanet detection and meteorological methods. Of these, transit photometry and the radial velocity method have proved the most prosperous (see Figure 1.1 and Table 1.1). When used in partnership, these methods can provide constraints on numerous planetary parameters. The radial velocity method can provide constraints on an exoplanet's mass, the orbital period, orbital semimajor axis, and orbital eccentricity; whereas transit photometry can provide constraints and measurements of an exoplanet's orbital period, radius (hence density when combined with mass), chemical composition, dayside temperature, planetary albedo, and longitudinal temperature/brightness dependences. When combined these measurements can yield significant information about an exoplanet's atmosphere, however, transit photometry and the radial velocity method have similar selection biases favouring exoplanets with short orbital periods, close-in orbits, large masses, large radii, and large optical/infrared light outputs — that is, hot Jupiters.

We also gave an overview of other detection and characterisation methods including direct imaging, timing methods, and gravitational microlensing. Of these, direct imaging alone can be used to constrain and measure atmospheric properties (i.e., temperature and albedo); while the others constrain orbital properties (i.e., mass, orbital period, orbital semimajor axis, and orbital eccentricity). These methods each come with their own selection biases so indicate characteristics of the true planetary population. In the future, these methods are likely to prove important in answering questions regarding habitability and the uniqueness of the Solar System. However, these methods do not currently output the sheer volume of detections and measurements of the radial velocity method and transit photometry, which have enabled astrophysicists to uncover interesting features, behaviours, and questions concerning hot Jupiters.

1.2 Characteristics of hot Jupiters

1.2.1 Typical planetary parameters

To get an idea of the typical planetary parameters of hot Jupiters ($a < 0.1\,\mathrm{AU}$ and $0.1\,M_\mathrm{J} < M < 10\,M_\mathrm{J}$), we plot a selection of their properties in Figure 1.7. We plot current estimates of planetary parameters against the equilibrium temperature, T_eq. It is useful to use T_eq as the independent variable as it gives an indication of both the planet's proximity to its host star and the size/luminosity of its host star. For this we calculate the orbit-averaged effective temperature from the exoplanet.eu dataset[9] assuming zero albedos, so $T_\mathrm{eq} = (R_*/2a)^{1/2}\,T_*/(1-e^2)^{1/8}$, where R_* and T_* are respectively the stellar radius and the stellar effective temperature (e.g., Laughlin *et al.*, 2011). In this instance, calculating T_eq like this proves more useful than using measured temperatures as it does not require our dataset to be reduced to planets with accurate secondary eclipse infrared photometric measurements.

First, as discussed at the start of this chapter, Figure 1.7 highlights that $T_\mathrm{eq} \sim 500$-$3000\,\mathrm{K}$. This means that the hottest hot Jupiters are hot enough to have partially-ionised atmospheres and that magnetism is expected to play an important role in their atmospheric dynamics (e.g., Perna *et al.*, 2010; Perna *et al.*, 2010; Menou, 2012*a*; Rogers & Showman, 2014; Rogers & Komacek, 2014; Rogers, 2017; Rogers & McElwaine, 2017). We will discuss current understanding of the role of magnetism in hot Jupiters in Section 1.4. Figure 1.7 also illustrates that the majority of observed hot Jupiters have planetary masses between $M \sim 0.1$-$4\,M_\mathrm{J}$, short orbital periods ($t_\mathrm{orbit} < 10$ Earth days) that are generally shortest for hottest/closest-in hot Jupiters, planetary radii between $R \sim 0.2$-$2\,R_\mathrm{J}$, where R_J denotes the (nominal equatorial) Jupiter radius, and small orbital eccentricities, particularly for the hottest/closest-in hot Jupiters.

[9] Accessed May 30, 2021. HJs with empty data entries for R, M, t_orbit, a, e, R_*, or T_* are removed, with the sole exception of extremely hot and close-in planet Kepler-76 b (for which we use $e = 0$), which we wish to keep in our dataset for future reference.

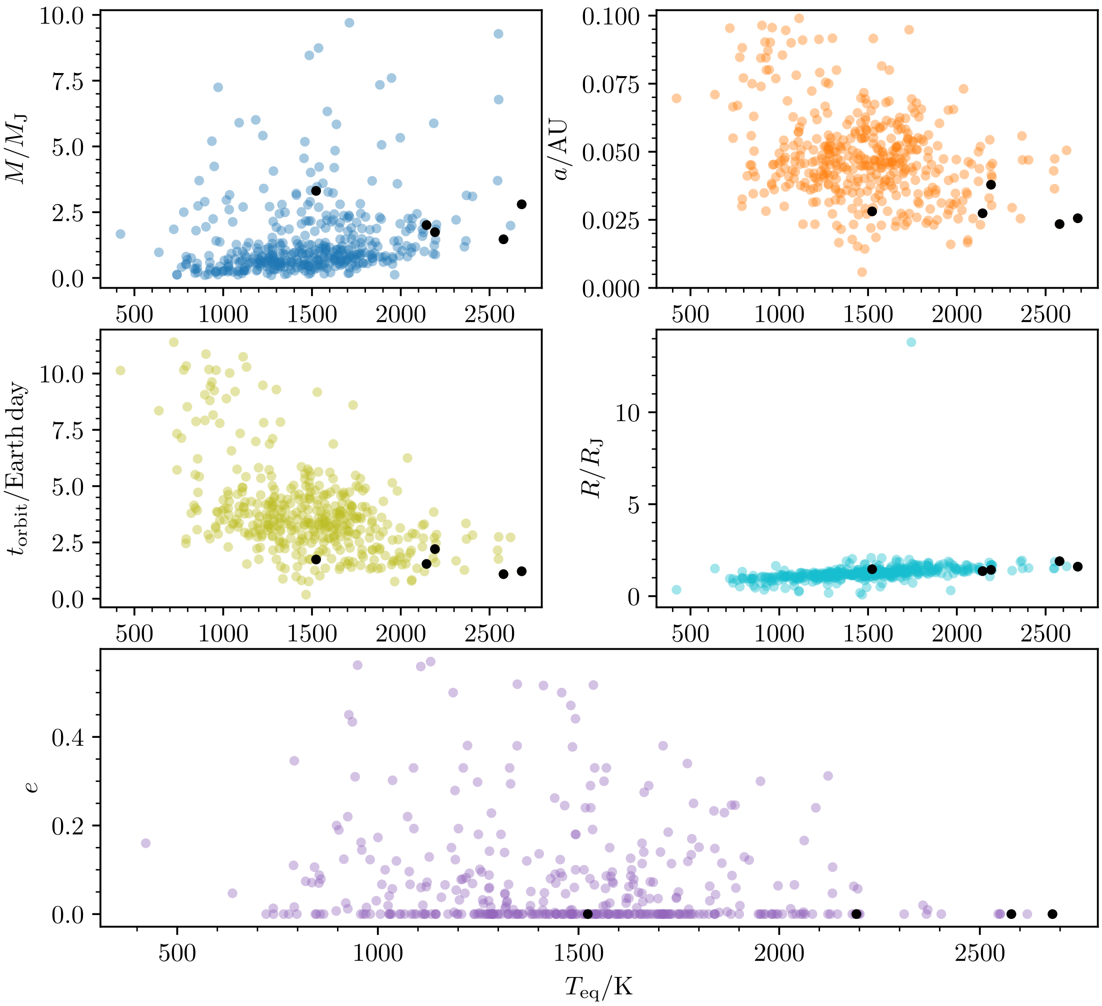

Figure 1.7: Properties of hot Jupiters in the exoplanet.eu catalogue with $a < 0.1\,\mathrm{AU}$, and $0.1\,M_J < M < 10\,M_J$. Using this dataset, we plot current estimates of the planetary mass (top left), orbital semimajor axis (top right), orbital period (middle left), planetary radius (middle right), and eccentricity (bottom) against the orbit-averaged effective temperature of hot Jupiters . The hot Jupiters CoRoT-2b ($T_{eq} \approx 1523\,\mathrm{K}$), Kepler-76b ($T_{eq} \approx 2145\,\mathrm{K}$), HAT-P-7b ($T_{eq} \approx 2192\,\mathrm{K}$), WASP-12b ($T_{eq} \approx 2578\,\mathrm{K}$), and WASP-33b ($T_{eq} 2681\,\mathrm{K}$), which are discussed specifically in this work, are marked with black opaque markers.

1.2.2 Synchronous rotation and large day-night temperature differentials

A feature of fundamental importance to their atmospheric dynamics is that, due to their close proximities, hot Jupiters are expected to be tidally-locked to their host stars, with the time required for tidally-locking expected to be $\sim 10^3$-10^4 times shorter than their expected age (Guillot *et al.*, 1996). Moreover, for hot Jupiters with small orbital eccentricity, orbital theory predicts synchronous rotation (Colombo & Shapiro, 1966; Guillot *et al.*, 1996; Showman *et al.*, 2015). That is, hot Jupiters are expected to have perpetual day and night sides. This, combined with the high levels of stellar irradiance that hot Jupiters are subjected to, causes extreme day-night temperature differentials.

As discussed in Section 1.1, these day-night temperature differentials can be estimated using transit photometry. In the hottest hot Jupiters, the day-night temperature differences are expected to be $\sim 1000\,\mathrm{K}$ (Harrington *et al.*, 2006; Komacek *et al.*, 2017) and could be as large as $2500\,\mathrm{K}$ (Helling *et al.*, 2019*a*). These temperature differentials between the (perpetual) daysides and nightsides of hot Jupiters drive interesting and dramatic atmospheric dynamics, which we will discuss in the hydrodynamic limit in Section 1.3.

1.2.3 Planetary structure and stratification

Structural models of hot Jupiters are based on our current understanding of the giant planets of the Solar System. In these examples, the vast amounts of energy from planetary formation are thought to cause long-term planetary cooling through either convective or radiative energy transport. In the deep interiors of giant planets, high opacities are thought to cause steep radial temperature gradients that drive convection; whereas towards the exterior, at sufficiently low pressures, gas becomes optically thin and so radial temperature gradients can be stably maintained by radiative cooling (e.g., Stevenson, 1991; Chabrier & Baraffe, 2000; Burrows *et al.*, 2001).

One of the early questions concerning hot Jupiters is how the intense stellar insolation they receive due to their close-in orbits affects this planetary cooling. Various authors have concluded that this external heating source does not halt the planetary cooling but it does affect the depth of the radiative-convective boundary. For Jupiter, Saturn, Uranus, and Neptune, the radiative-convective boundary lies at pressures somewhat less than ~ 0.01-1 bar. However, at these pressures on hot Jupiters, the absorbed stellar irradiance heats the uppermost layers and reduces the radial temperature gradients in the upper interior. This causes the radiative zone to become approximately radially isothermal and pushes the radiative-convective boundary downward to pressures as large as ~ 100-1000 bar, depending on age and the magnitude of insolation (e.g., Guillot *et al.*, 1996; Saumon *et al.*, 1996; Burrows *et al.*, 2000; Chabrier *et al.*, 2004; Guillot, 2005; Fortney *et al.*, 2010). Since for hot Jupiters this radiative-convective boundary is expected to extend far deeper than the infrared photosphere (i.e., where gas becomes optically thin to escaping infrared radiation), large observable horizontal photospheric temperature gradients can develop in the absence of convective mixing (Showman *et al.*, 2010). Moreover, Guillot & Showman (2002) showed that structural evolution is sensitive to atmospheric temperatures and horizontal temperatures inhomogeneities of this kind. Hence, to use planetary evolution for quantitive structural predictions, one needs to understand atmospheric dynamics.

Another question regarding planetary structure on hot Jupiters is whether or not a solid/liquid rock core is present. This is not known as constraints from observations still allow for a considerable range in core sizes and compositions (Bodenheimer *et al.*, 2003).

1.2.4 Over-inflated radii

With the advent of the first transit photometry measurements of HD 209458b (Charbonneau *et al.*, 2000; Henry *et al.*, 2000), planetary structure and evolution models became testable against observations. It soon emerged that, when compared to such models with realistic atmospheric temperatures, the radii of HD 209458b and a large number of the general hot Jupiter population are much larger than expected (Bodenheimer *et al.*, 2001, 2003; Showman & Guillot, 2002; Baraffe, I. *et al.*, 2003; Laughlin *et al.*, 2005, 2011). This problem has been dubbed the *radius anomaly* or the *radius over-inflation* problem. Radius over-inflation is illustrated in Figure 1.8, which is taken from Laughlin *et al.* (2011)

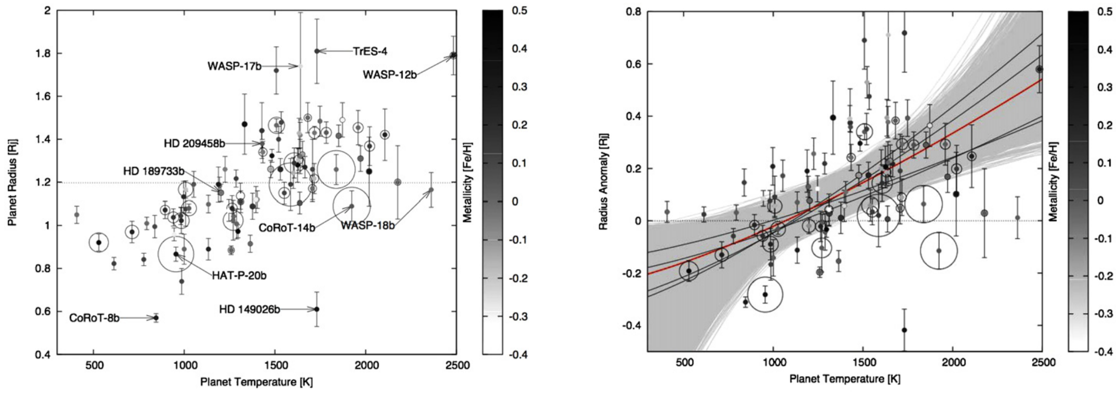

Figure 1.8: Radius over-inflation in hot Jupiters, taken from Laughlin *et al.* (2011). The radii (left) and radius anomalies (right) of hot Jupiters with $0.1\,M_{\rm J} < M < 10\,M_{\rm J}$ are plotted against their orbit-averaged effective temperature, $T_{\rm eq}$, with error bars. The planets are shaded with respect to their metallically and some are labelled. The radius anomaly is calculated by comparing the radii with those of structural models and its best-fit power-law dependence. Laughlin *et al.* (2011) found the radius anomaly is proportional to $T_{\rm eq}^{1.4\pm0.6}$, which is indicated by the red and interior black fitting lines in the righthand panel.

and shows the radii (lefthand panel) and the radius anomalies (righthand panel) of hot Jupiters compared to $T_{\rm eq}$, where the radius anomaly is defined as the difference between the observed and predicted radii.

The most likely explanation of this phenomena is that there is an additional, unaccounted for, heat source in the planetary interior that slows gravitational contraction and therefore decreases the planet's density. Proposed heat sources include tidal heating from the circularisation of orbits (Bodenheimer *et al.*, 2001, 2003), the downward transport then deposition of kinetic energy by atmospheric circulation (Showman & Guillot, 2002), the burial of heat by turbulence (Youdin & Mitchell, 2010), and heating via Ohmic dissipation of magnetic fields (Batygin & Stevenson, 2010; Perna *et al.*, 2010; Laughlin *et al.*, 2011). Understanding radius over-inflation in hot Jupiters is one of many open questions in exoplanetary physics and various works are currently attempting to gauge the relative importance of these different heating mechanisms (Thorngren & Fortney, 2018). Aside from tidal heating, which cannot fully explain the anomalous radii (Guillot, 2005; Thorngren & Fortney, 2018), all of these candidate inflation mechanisms require a strong understanding of hot Jupiters' dominant atmospheric processes, underlining the necessity in developing such theory.

1.2.5 Predominantly eastward hotspot offsets on cooler hot Jupiters

As discussed in Section 1.1, transit photometry has allowed observers to construct planetary phase curves (like the kind presented in Figure 1.4, righthand panel) and longitudinal temperature maps (like the kind presented in Figure 1.5). Using these methods it has generally been found that hotspots are located eastward of the substellar point (e.g., Harrington *et al.*, 2006; Cowan *et al.*, 2007; Knutson *et al.*, 2007, 2009; Charbonneau *et al.*, 2008; Swain *et al.*, 2009; Crossfield *et al.*, 2010; Wong *et al.*, 2016), where (following convention) eastward denotes the prograde direction, the term hotspot denotes the hottest longitudinal position, and the substellar point is the location of maximal insolation (noon on the dayside).

Indeed, eastward hotspots were found ubiquitously until recently when westward hotspots or brightspots were measured on a handful of exceptional hot Jupiters. Continuous optical measurements from *Kepler* found east-west brightspot oscillations on the ultra-hot Jupiters[10] HAT-P-7b (Armstrong *et al.*, 2016) and Kepler-76b (Jackson *et al.*, 2019); optical phase curve measurements from *TESS* found westward brightspot offsets on the ultra-hot Jupiter WASP-33b (von Essen *et al.*, 2020)[11]; while thermal phase curve measurements from *Spitzer* found westward hotspots on the ultra-hot Jupiter WASP-12b (Bell *et al.*, 2019) and the cooler hot Jupiter CoRoT-2b (Dang *et al.*, 2018).

These westward hotspots/brightspots measurements are highly significant as they turn out to be at odds with general understanding of hydrodynamic theory of synchronously rotating hot Jupiters, which always predicts eastward hotspots (Showman & Polvani, 2011) and shall be discussed in more detail in Section 1.3. Three main explanations for these observations have been proposed: reflections from cloud asymmetries confounding optical measurements (Demory *et al.*, 2013; Lee *et al.*, 2016; Parmentier *et al.*, 2016; Roman & Rauscher, 2017), asynchronous rotation (Rauscher & Kempton, 2014), and magnetism (Rogers & Komacek, 2014; Rogers, 2017; Hindle *et al.*, 2019).

[10]Ultra-hot Jupiters are an emerging sub-class of hot Jupiters, with atmospheric temperatures that can greatly exceed 2000 K.

[11]Although von Essen *et al.* (2020) acknowledge that systematic effects in the data, due to host star variability, cannot be ruled out as a potential cause of their westward brightspot measurements.

The first of these explanations, cloud asymmetries, only offers explanations for westward brightspot measurements taken at optical wavelengths. It is believed to explain westward brightspot measurements (from *Kepler*) that were found on another (warm) hot Jupiter, Kepler-7b. This is the case because the westward brightspot measurements of Kepler-7b were found alongside eastward hotspot measurements, which were taken at infrared wavelengths by *Spitzer* (Demory *et al.*, 2013). This could potentially explain the westward brightspot observations on HAT-P-7b, Kepler-76b, and WASP-33b (but not WASP-12b or CoRoT-2b). However, ultra-hot Jupiters like these are expected to be too hot for condensates to form so are thought to have cloud-free daysides (Helling *et al.*, 2019*a*). In particular, Helling *et al.* (2019*b*) recently ruled out cloud asymmetries as the explanation for westward brightspots on HAT-P-7b.

Asynchronous rotation can explain the findings from a fluid dynamics perspective (Rauscher & Kempton, 2014). However, this would suggests shortcomings in current understand of tidal evolution theory. As discussed in Section 1.2.2, tidal evolution theory predicts that hot Jupiters should be tidally-locked. Moreover, other spin-orbit resonances are only expected on planets with non-circular orbits (Colombo & Shapiro, 1966; Guillot *et al.*, 1996; Showman *et al.*, 2015).[12] Such non-synchronous tidal locking does not appear to be consistent with the planets with observed westward hotspots/brightspots, which, where measured, have near-zero orbital eccentricities (see black opaque marked planets on Figure 1.7, bottom left panel). The exception to this could be Kepler-76b, for which the orbital eccentricity is not currently constrained. However, planets as close-in as Kepler-76b ($a = 0.028$) are expected to have undergone active circulation throughout their lifetime (Bodenheimer *et al.*, 2001, 2003).

Using three-dimensional magnetohydrodynamic (MHD) simulations, Rogers & Komacek (2014) predicted that in the hottest hot Jupiters, where the atmosphere is partially-ionised, magnetism can cause variable winds that drive east-west hotspot oscillations. When the observation of east-west brightspot oscillations on HAT-P-7b emerged, Rogers

[12] A classic example of non-synchronous tidal locking is Mercury, which has a 3-to-2 relationship between rotation and orbital periods and a somewhat eccentric orbit with $e = 0.205$ (Colombo & Shapiro, 1966; Carroll & Ostlie, 2006).

(2017) applied the MHD simulations to the expected parameter regime of HAT-P-7b and placed a lower-bound on HAT-P-7b's planetary magnetic field. This work approach highlights that, if the magnetic mechanism that drives atmospheric wind variations can be understood and the conditions leading to its onset identified, it can be used to provide indirect constraints on the typical magnetic field strengths of hot Jupiters. This is powerful as typical magnetic field strengths on hot Jupiters are not well understood and currently rely on our knowledge of the Solar System. Understanding the wind reversal mechanism will predominantly be the topic of this thesis. To introduce the problem more completely, we delve into the current understanding of atmospheric hydrodynamics and MHD in Sections 1.3 and 1.4 respectively.

1.3 Hydrodynamic atmospheric circulation on hot Jupiters

The study of atmospheric circulation (i.e., near-planetary-scale fluid dynamics) on Earth is well-established and has a rich history founded in the need to understand Earth's atmospheric and oceanic phenomena (e.g., equatorial trade winds, the Gulf stream, the polar jet stream, and El Niño) for practical purposes (e.g., nautical navigation, aviation, and forecasting). By the end of twentieth century, space missions (e.g., the Venera missions, the Mariner missions, the Voyager missions, Galileo, and Cassini-Huygens) had collected enough data to allow the study of atmospheric dynamics to be applied to our nearest Solar System neighbours.

Understanding the diverse dynamics of the other planets in our Solar System has so far proved difficult, though not without successes (e.g., see Dowling, 1995; Guillot, 2005; Showman *et al.*, 2010; Read & Lebonnois, 2018). Such difficulties arise because atmospheric fluid dynamics is highly non-linear and involves complex interactions between turbulence, convective and/or radiative heat transfer, waves, vortices, and jet streams. Disentangling the roles that each of these phenomena is often difficult so one could be forgiven for asking whether attempting to model and characterise planetary circulation on hot Jupiters is a reasonable goal when the atmosphere of Jupiter is still not fully understood. However, as discussed in the first two sections of this chapter, hot Jupiters differ from Jupiter in some significant ways. First and foremost, hot Jupiters are believed to rotate synchronously with their orbits. The resulting permanent day and night sides creates an interesting and somewhat unique problem. From a fluid dynamics perspective, the time-independent forcing of hot Jupiter atmospheres makes for a "clean" system, which generally outputs less temporally complex behaviours than asynchronously rotating planets. This makes Jupiters an excellent testbed for the extension and development of existing theory into different parameter regimes outside of our local experience. Secondly, the theoretical push towards understanding hot Jupiters has largely been driven by a desire to understand incoming observational data. While the observational data that has so far been accrued for hot Jupiters is relatively unrefined, there is an abundance of it and it has highlighted shared characteristics between hot Jupiters (see Section 1.2). From this, an ensemble approach to identifying important atmospheric characteristics is possible. Such an approach offers a different lens for viewing and testing atmospheric circulation theory, which previously, due to a lack of comparable examples, has generally been probed with an individualistic approach. Explicitly, rather than looking to explain highly specific characteristics of an individual planet, which can often lead to a highly tuned understanding of planetary dynamics, one attempts to update theory by seeking an understanding of the fundamental mechanisms behind shared characteristics of a collection of similar planetary bodies. Since the same physical laws determine the behaviour of all atmospheres, the study of extrasolar planets and Solar System are not mutually exclusive and progress with one can inform the other. In this section we shall discuss the hydrodynamic models and underlying theory that have proved important in understanding hot Jupiter atmospheres, before discussing some results relevant to our study. The hydrodynamic models we discuss are standard and can be found in various texts (e.g., Batchelor, 1967; Vallis, 2006; Showman *et al.*, 2010).

1.3.1 Hydrodynamic models

Three-dimensional atmospheric models are often called global circulation models (GCMs) and are invaluable tools for understanding the large-scale atmospheric dynamics occurring in hot Jupiters. GCMs can include a wide array of physics including (but not limited to) rotation, thermal stratification, turbulence, magnetism, and/or cloud formation. However, aside from each piece of physics increasing a model's computational complexity, highly sophisticated GCMs can often be difficult to interpret without simplification or well directed diagnostics. Hence, while GCMs are excellent for building a qualitative picture, it can be difficult to glean mathematical results and/or physical understanding from them. Moreover, when observational comparisons are limited, idealised models can often be sufficient in describing the available information. Such reduced models have the added benefit that, if they can reproduce similar fundamental dynamics to GCMs, they can be more specific about the physical processes that drive them. The caveat to this, of course, is that the model has to be well-understood and based on valid approximations. Looking holistically, GCMs and reduced models tend to complement each other's shortfalls, so the most prosperous approach when developing theory is often to use both in harmony. This is a so-called *hierarchical approach.*

In a hierarchical approach one uses a sophisticated GCM to identify the main characteristics of a prevalent dynamical process, which ideally has an observable signal. Then, if the predominant conditions in which the process emerges are known, one can make informed approximations that reduce the phenomenon to its rudiments. Once the system has been reduced, it is often more amenable to mathematical manipulation. Hence, if the phenomenon in question can be isolated and reproduced, its physics can be probed. With this concept in mind we should consider four different models that cover the spectrum of dynamical complexity that has proved useful for the study of hot Jupiters.

Compressible three-dimensional hydrodynamic equations

Consider a non-magnetic three-dimensional fluid with the velocity field, $\mathbf{u}_3(\mathbf{x}_3, t)$, the density, $\rho(\mathbf{x}_3, t)$, the temperature, $T(\mathbf{x}_3, t)$, and the pressure, $p(\mathbf{x}_3, t)$, where $\mathbf{x}_3, \mathbf{u}_3 \in \mathbb{R}^3$. The momentum of the fluid can change due to the action of surface and body forces (per unit volume). The surface forces can be written as the sum of pressure and viscous forces: $\boldsymbol{\sigma}_3 = -pI_3 + \mu\boldsymbol{\tau}_3$, where I_3 is the 3×3 identity matrix, μ is the constant viscosity, and

$\boldsymbol{\tau}_3 = \nabla_3 \mathbf{u}_3 + (\nabla_3 \mathbf{u}_3)^T - (2/3) I_3 (\nabla_3 \cdot \mathbf{u}_3)$ is the viscous stress tensor. The body force is gravity (and the Lorentz force in magnetic systems), which can be written as the gradient of a potential. Moreover, if the fluid is viewed in a rotating reference frame (where $\mathbf{u}_3$ donates the velocity relative to the frame), the fluid experiences further accelerations due to the Coriolis force and the centrifugal force that respectively result from angular momentum conservation and inertia. The Coriolis force per unit mass is $-2(\boldsymbol{\Omega} \times \mathbf{u}_3)$, where $\boldsymbol{\Omega}$ is the angular velocity of the reference frame, and the centrifugal force can be written as the gradient of a potential. Hence, applying Newton's second law, the motion of a fluid subject to these forces and accelerations can be written as

$$\rho \frac{\mathrm{D}_3 \mathbf{u}_3}{\mathrm{D}_3 t} \equiv \rho \frac{\partial \mathbf{u}_3}{\partial t} + \rho (\mathbf{u}_3 \cdot \nabla_3) \mathbf{u}_3 = -2\rho (\boldsymbol{\Omega} \times \mathbf{u}_3) - \nabla_3 p - \rho \nabla_3 \mathit{\Phi} + \mu \nabla_3 \cdot \boldsymbol{\tau}_3, \tag{1.1a}$$

where $\mathrm{D}_3/\mathrm{D}_3 t \equiv \partial/\partial t + (\mathbf{u}_3 \cdot \nabla_3)$ is the three-dimensional Lagrangian derivative and $\mathit{\Phi} = \mathit{\Phi}_g + \mathit{\Phi}_c$ is the geopotential, which contains components due to both gravitational acceleration ($\mathit{\Phi}_g$) and the centrifugal force ($\mathit{\Phi}_c$). Generally, for planetary flows $|\mathit{\Phi}_c / \mathit{\Phi}_g| \ll 1$, so the centrifugal force is often neglected and one sets $\mathit{\Phi} = \mathit{\Phi}_g = gz$, where the constant g is either the gravitational acceleration or the effective gravitational acceleration that contains a centrifugal contribution, and z is the system's vertical coordinate.[13] Alongside Equation (1.1a), the fluid's density evolves subject to mass (per unit volume) conservation

$$\frac{\partial \rho}{\partial t} + \nabla_3 \cdot (\rho \mathbf{u}_3) = 0 \quad \Longleftrightarrow \quad \frac{\mathrm{D}_3 \rho}{\mathrm{D}_3 t} + \rho \nabla_3 \cdot \mathbf{u}_3 = 0. \tag{1.1b}$$

This fluid system is closed with an equation of state, which describes the evolution of pressure in system. Understanding how the equation of state varies throughout the interior of hot Jupiters is a topic unto itself (e.g., for discussion, see Fortney *et al.*, 2010). However, the ideal gas law,

$$p = \mathcal{R} \rho T, \tag{1.1c}$$

[13] In non-relativistic systems Newton's law of universal gravitation gives $\mathbf{g} = -\nabla_3 \mathit{\Phi}_g = -g\widehat{\mathbf{z}} = -GM/r^2 \widehat{\mathbf{z}}$, where r is the radial coordinate. If $|r - R| = H$ is the vertical scale of an atmospheric model, the binomial theorem gives $g = GM/R^2(1 + O(H/R))$ for $H/R \ll 1$. Generally, for hot Jupiter atmospheres $H/R \ll 1$ (see Figure 1.10) so, to leading order, we are free to neglect vertical variations in g.

is often adequate to first order in the upper atmosphere (Fortney *et al.*, 2010; Showman *et al.*, 2010), where $\mathcal{R}$ is the atmospheric gas constant (i.e., the universal gas constant divided by the mean molecular weight of the atmosphere) and T is the temperature. In a *simple* ideal gas, the ideal gas law gives $p(\rho, T)$, the heat capacity at constant volume, c_V, is constant, the internal energy per unit volume is $\rho c_V T$, and internal energy (per unit volume) transport is described by

$$\frac{\partial(\rho c_V T)}{\partial t} + \nabla_3 \cdot (\rho c_V T \mathbf{u}_3) = -p(\nabla_3 \cdot \mathbf{u}_3) + \nabla_3 \cdot (K \nabla_3 T) + \frac{\mu}{2}\tau_3^2 + \mathcal{Q}, \tag{1.1d}$$

where the second term on the righthand side describes heat transport phenomena using the so-called diffusive approximation for a thermal conductivity, K, $(\mu/2)\tau_3^2 = (\mu/2)\boldsymbol{\tau}_3 : \boldsymbol{\tau}_3 = (\mu/2)\sum_i \sum_j (\tau_3)_{i,j}(\tau_3)_{i,j}$ describes viscous heating, and $\mathcal{Q}$ is the rate of thermodynamic heating (per unit volume) from external sources, which in terms of hot Jupiters corresponds to radiative heat/cooling from stellar insolation. Equation (1.1b) is often used to rewrite the lefthand side of Equation (1.1d) as the density multiplied by the material derivative of the specific internal energy (i.e., $\partial(\rho c_V T)/\partial t + \nabla_3 \cdot (\rho c_V T \mathbf{u}_3) = \rho \mathrm{D}_3(c_V T)/\mathrm{D}_3 t$).

Equations (1.1a) to (1.1d) fully describe the hydrodynamic system with six equations for six unknowns (i.e., $\mathbf{u}_3, \rho, p, T$). Different types of external heating can be incorporated into the system via $\mathcal{Q}$ and chemistry can be included via complex treatments of the equation of state. Since viscous terms are generally expected to be small for large scale flows with typical μ values, the viscous terms in Equations (1.1a) to (1.1d) are often simplified, modified, or neglected for convenience. Strictly speaking, one should be careful when doing this as modified diffusion treatments can violate desirable conservational properties or cause numerical instabilities in simulations. An example of a hot Jupiter GCM that solves the compressible three-dimensional hydrodynamic equations is the equatorial-to-mid latitude model of Dobbs-Dixon & Lin (2008).

Primitive equations

We have already alluded to the fact that some physical processes described by Equations (1.1a) to (1.1d) play a more important role in describing the dynamical processes that drive large scale flows than others. Hence, with judicious assumptions, one can formulate dynamically similar models but with less complexity.

Many global circulation models (GCMs) take advantage of such simplifications. The so-called *primitive equations* are a useful illustration of this and have played an important role in the development of atmospheric circulation theory on hot Jupiters (e.g., Showman & Guillot, 2002; Cooper & Showman, 2005, 2006). Their name derives from the fact that they represent a beginning for studies in atmospheric fluid dynamics and they come in various forms. These are underpinned by three fundamental assumptions. Firstly, the *hydrostatic approximation* assumes that in the vertical momentum equation vertical accelerations are small and the geopotential term is exactly balanced by the pressure gradient term. This is so-called *hydrostatic balance*:

$$\frac{\partial p}{\partial z} = -\rho \frac{\partial \Phi}{\partial z} = -\rho g, \tag{1.2}$$

Secondly, in spherical coordinates the *shallow-fluid approximation* uses the radial coordinate decomposition $r = R + z$, for $|z/R| \ll 1$, where the constant R is the planetary radius and z is the system's radial or local normal coordinate, which is antiparallel to gravitational acceleration. In this approximation, the coordinate r is replaced by R, except wherever it used as the differentiating argument, in which case r is replaced by z. Thirdly, the *traditional approximation* involves neglecting all Coriolis terms in the horizontal momentum equation involving the vertical velocity (i.e., one takes $\mathbf{\Omega} = \Omega \sin\theta \widehat{\mathbf{z}}$, where θ denotes latitude) and, in spherical coordinates, the metric terms uw/r and vw/r are also neglected. The shallow-fluid approximation and the traditional approximation both arise from an asymptotic expansion assuming a small vertical/horizontal length scale ratio. Hence, if one of the shallow-fluid approximation and the traditional approximation is taken, so should the other (e.g., Vallis, 2006). These two assumptions are formally valid in the limit of strongly stable stratification, when $N^2/\Omega^2 \gg 1$ (e.g., Salby, 1996; Showman *et al.*, 2010), where N is the Brunt-Väisälä frequency and

$$N^2 = g\left(\frac{1}{\gamma}\frac{\mathrm{d}\ln P}{\mathrm{d}z} - \frac{\mathrm{d}\ln\rho}{\mathrm{d}z}\right), \tag{1.3}$$

for the adiabatic index, $\gamma = c_p/c_v$ ($\gamma = 5/3$ and $\mathcal{R} = c_p - c_V$ for a monoatomic ideal gas), with the constant pressure specific heat capacity, c_p. The Brunt-Väisälä frequency is the oscillation frequency of a fluid parcel if it is perturbed vertically in a stably stratified fluid. If N is large and real, the thermal stratification is strongly stable and radiative heating/cooling is the predominant mechanism of internal energy transfer; whereas, if N is imaginary, the thermal stratification is unstable and convection emerges.

We choose to present a version of the primitive equations that represent an incompressible system (i.e., a system in which density is materially conserved and sound waves are removed) in isobaric coordinates (as in Salby, 1996; Showman *et al.*, 2010). To transform the system into isobaric coordinates (i.e., coordinates with vertical levels of constant pressure), one writes the vertical coordinate, $z = z(\mathbf{x}, p, t)$, as a variable that depends on the system's independent variables, which are now the horizontal displacement, $\mathbf{x} \in \mathbb{R}^2$, pressure, and time. The system is described by horizontal velocity field, $\mathbf{u}(\mathbf{x}, p, t) \in \mathbb{R}^2$, the vertical velocity in pressure coordinates, $\varpi(\mathbf{x}, p, t)$, the fluid density, $\rho(\mathbf{x}, p, t)$, and the thermodynamic properties of the system are expressed in terms of the potential temperature, $\Theta(\mathbf{x}, p, t) = T(p_{\mathrm{ref}}/p)^{\kappa}$, where p_{ref} is a reference pressure and $\kappa = \mathcal{R}/c_p$. The isobaric primitive equations are (e.g., Salby, 1996; Showman *et al.*, 2010)

$$\frac{\mathrm{D}_p\mathbf{u}}{\mathrm{D}_p t} = \nabla_p\Phi - f\widehat{\mathbf{z}} \times \mathbf{u} - \mathcal{D}, \tag{1.4a}$$

$$\frac{\partial\Phi}{\partial p} = -\frac{1}{\rho}, \tag{1.4b}$$

$$\frac{\partial\varpi}{\partial p} = -\nabla_p \cdot \mathbf{u}, \tag{1.4c}$$

$$\frac{\mathrm{D}_p\Theta}{\mathrm{D}_p t} = \frac{\Theta}{c_p T}\dot{q}_{\mathrm{net}}, \tag{1.4d}$$

where $\nabla_p \equiv ((\partial/\partial x)_p, (\partial/\partial y)_p)$ is the horizontal gradient evaluated along an isobaric (constant pressure) surface, with x denoting the eastward coordinate and y denoting the northward coordinate, $\mathrm{D}_p/\mathrm{D}_p t \equiv \partial/\partial t + (\mathbf{u}\cdot\nabla_p) + \varpi\partial/\partial p$ is the Lagrangian derivative in isobaric coordinates with $\varpi(\mathbf{x}, p, t) \equiv \mathrm{D}_p p/\mathrm{D}_p t$. In this set of equations the Coriolis parameter, $f = 2\Omega \sin\theta$, depends on latitude, θ, and describes the locally vertical component of the planetary vorticity vector (more discussion below and in Chapter 2). Additionally, $\mathcal{D}$ denotes a parameterisation of large scale horizontal drags and $\dot{q}_{\mathrm{net}}$ is the net diabatic heating rate, which includes radiative heating/cooling and thermal conductivity. The primitive equations have five unknown dependent variables (i.e., $\mathbf{u}, \varpi, \rho, \Theta$) so the applied assumptions reduced the system's degrees of freedom by one. The potential temperature quantifies the thermal energy available to be converted into mechanical work and is related to entropy, s, via $\mathrm{d}s = c_p\,\mathrm{d}\ln\Theta$ (e.g., Salby, 1996; Showman *et al.*, 2010). Equation (1.4d) highlights that when there is no diabatic heating Θ is materially conserved along isobaric surfaces so there is no thermal energy exchange between different pressure levels.

Shallow-water model

To study shallow phenomena, where vertical motion is of lower order interest, the fluid equations can be reduced a set of *shallow-water* equations. This often proves useful as it reduces the system's complexity to an extent where features such as waves, vortices, and jets can be isolated and analytic mathematical approaches become possible. Here we present the simplest shallow-water model: the single-layer homogenous (i.e., constant density) model, though both multi-layer models (e.g., Vallis, 2006) and inhomogeneous models (e.g., Dellar, 2003) can also be used to include different physics while remaining mathematically simple. Since we shall use shallow models throughout this work, we provide a full derivation in Chapter 2. However, for now, we note that when the hydrostatic and traditional approximations are applied to a thin constant density layer that is bounded below by an impermeable wall and above by free surface, horizontal motions become approximately vertically independent and their magnitudes become large compared to those of vertical motions, which become approximately linearly dependent on depth. In this limit, the inviscid equations of motion can be integrated over the vertical coordinate to yield an explicit expression for horizontal pressure gradients, $\rho^{-1}\nabla p = g\nabla h$, where $h(\mathbf{x}, t)$ is the thickness of the layer. Moreover, the incompressibility condition can also be integrated over the vertical coordinate and, as a result, the governing fluid equations become

$$\frac{\mathrm{D}\mathbf{u}}{\mathrm{D}t} + f\widehat{\mathbf{z}} \times \mathbf{u} = -g\nabla h, \tag{1.5a}$$

$$\frac{\partial h}{\partial t} + \nabla \cdot (h\mathbf{u}) = 0 \quad \Longleftrightarrow \quad \frac{\mathrm{D}h}{\mathrm{D}t} + h\nabla \cdot \mathbf{u} = 0, \tag{1.5b}$$

where $\nabla \equiv (\partial/\partial x, \partial/\partial y)$ denotes the horizontal gradient operator (for a constant vertical coordinate, z), with x denoting the eastward coordinate and y denoting the northward coordinate, and $\mathrm{D}/\mathrm{D}t \equiv \partial/\partial t + \mathbf{u} \cdot \nabla$ denotes the horizontal Lagrangian derivative. The single-layer homogenous shallow-water model has three unknowns that fully describe its motion (i.e., $\mathbf{u}, h$), so is greatly reduced from the three-dimensional thermodynamic fluid equations. However, due to its lack of vertical dependence, thermodynamics cannot be included in it explicitly. This is usually remedied with a source term in Equation (1.5b) (e.g., Shell & Held, 2004; Langton & Laughlin, 2007; Showman & Polvani, 2010, 2011; Perez-Becker & Showman, 2013). Doing so has technical requirements, such as the need for a second layer for mass conservation, which we shall discuss more comprehensively in Chapter 2.

Two-dimensional incompressible Navier-Stokes

The system can be reduced further still. The simplest useful model for atmospheric circulation is the two-dimensional incompressible Navier-Stokes equations. If one takes the fluid density to be constant and entirely excludes vertical motions and gravitational effects from the system, Equations (1.1a) and (1.1b) yield

$$\frac{\mathrm{D}\mathbf{u}}{\mathrm{D}t} + f\widehat{\mathbf{z}} \times \mathbf{u} = -\frac{1}{\rho}\nabla p, \tag{1.6a}$$

$$\nabla \cdot \mathbf{u} = 0. \tag{1.6b}$$

Since the horizontal velocity is solenoidal, it can be fully described in terms of a streamfunction that is defined by $\mathbf{u} = -\nabla \times \psi\widehat{\mathbf{z}} = (-\partial\psi/\partial y, \partial\psi/\partial x)$. Using this, and taking the curl of Equation (1.6a), gives the *two-dimensional vorticity equation*:

$$\frac{\mathrm{D}(\zeta + f)}{\mathrm{D}t} = 0 \quad \text{with} \quad \zeta = \nabla^2\psi, \tag{1.7}$$

where $\zeta \equiv (\nabla \times \mathbf{u}) \cdot \widehat{\mathbf{z}}$ is the vertical component of the fluid vorticity (i.e., local circulation) and, as before, f is the Coriolis parameter. Equation (1.7) highlights that the Coriolis parameter is the vertical component of the planetary vorticity. This model only has one degree of freedom (i.e., ψ). This makes it limited in scope but easy to manipulate mathematically. Its description in terms of a streamfunction is also illustrative. Note that the normal to a line of constant streamfunction is $\nabla\psi$, and that the flow through this normal is $\mathbf{u} \cdot \nabla\psi = -(\partial\psi/\partial y)(\partial\psi/\partial x) + (\partial\psi/\partial x)(\partial\psi/\partial y) = 0$. Hence, in this model flows travel down lines of constant streamfunction. These are known as streamlines.

While the two-dimensional incompressible model is comparatively simple, it is often useful for modelling large scale atmospheric processes. Further, its simplicity makes it fairly intuitive. In the remainder of this section we shall discuss some fundamental principles of hydrodynamic theory in hot Jupiter atmospheres. We shall attempt to present important theory and flow features in terms of the simplest models that can discribe them and, where possible, we shall highlight the shared characteristics between the different models we have discussed.

1.3.2 Fundamental principles of hydrodynamical theory

In principle, assuming sub-grid scale processes can be parameterised within the large-scale framework, the models discussed in Section 1.3.1 provide a mathematical description of the large scale atmospheric flows on hot Jupiters. In this subsection we discuss some of the dominant balances, processes, and flow features to outline a conceptual understanding of the atmospheric dynamics.

Energy cycle

In the stably stratified regions of hot Jupiter atmospheres (i.e., $N > 0$), the thermodynamic system simultaneously attempts to drive itself towards radiative equilibrium and mechanical equilibrium. The competition between the mechanisms driving the system towards these equilibria is the fundamental cause of all atmospheric dynamics.

In planetary atmospheres heating and cooling drive the system towards radiative equilibrium. However, heating and cooling are generally inhomogeneous processes and result in temperature gradients. Radiative heating from a planet's host is generally strongest towards the equator and weakest at the poles. Moreover, in the case of hot Jupiters, we have already seen that their perpetual dayside nightside configuration also leads to large longitudinal temperature differentials. Such temperature differentials cause horizontal pressure gradients, which drive winds by converting excess internal energy from the temperature gradients (i.e., accessible/excess thermal energy) into kinetic energy. The winds caused by these pressure gradients drive the system towards mechanical equilibrium. However, such motions recirculate internal energy so perturb the system further from radiative equilibrium. Heating/cooling processes attempt to correct this, completing a cycle of energy exchange/redistribution. The overall result is some kind of balance between the two equilibrium states.

The interplay between these two processes is often complex and subtle. However, for hot Jupiters, various studies have shown that the time-independent day-night heating caused by stellar insolation dominates thermodynamic processes to first order (e.g., Showman & Guillot, 2002; Shell & Held, 2004; Cooper & Showman, 2005, 2006; Langton & Laughlin, 2007; Dobbs-Dixon & Lin, 2008; Menou & Rauscher, 2009; Rauscher & Menou, 2010; Dobbs-Dixon *et al.*, 2010; Perna *et al.*, 2010; Heng *et al.*, 2011; Perez-Becker & Showman, 2013). This reduces the problem considerably and allows us to draw much of our focus towards atmospheric driving mechanisms with approximately fixed pressure gradients.

Shallow-water gravity-wave speed

In the rotation free limit ($f = 0$), Equations (1.5a) and (1.5b) can be linearised about the background state $\{\mathbf{u}_0, h_0\} = \{\mathbf{0}, H\}$, where H is a constant reference layer thickness, to yield

$$\frac{\partial^2 h_1}{\partial t^2} = gH\nabla^2 h_1 = c_g^2 \nabla^2 h_1, \tag{1.8}$$

where $c_g \equiv \sqrt{gH}$ is the *shallow-water gravity-wave speed* and h_1 denotes the layer-thickness perturbation to H, with $|h_1/H| \ll 1$. This is the wave equation in the two dimensions of the horizontal plane and describes the motion of shallow-water gravity waves. Since in the absence of rotation the horizontal directions are dimensionally invariant, one is free to reduce the problem to one horizontal direction (i.e., x here) and apply a symmetry argument in the other (i.e., y here). The one-dimensional version of Equation (1.8) is $\partial^2 h_1/\partial t^2 = c_g^2 \partial^2 h_1/\partial x^2$, which satisfies d'Alembert's solution (e.g., Vallis, 2006):

$$h_1(x,t) = \frac{1}{2}(h_{1,i}(x - c_g t) + h_{1,i}(x + c_g t)), \tag{1.9}$$

for the initial conditions $h_1(x, 0) = h_{1,i}(x)$ and $\partial h_1/\partial t|_{t=0} = 0$. Equation (1.9) describes two wave packets, which have the same profile but half the magnitude of the initial layer thickness perturbation, moving in opposite directions along the x axis with the velocity c_g. The dispersion relation of shallow-water gravity waves can be examined by applying the planar wave ansatz, $h_1 = \hat{h}e^{i(kx-\omega t)}$, to the one-dimensional wave equation, where k denotes the wavenumber in the x direction and ω denotes the oscillation frequency. This yields the one-dimensional shallow-water gravity wave dispersion relation:

$$\omega = \pm c_g k, \tag{1.10}$$

for arbitrary $\hat{h}$. Shallow-water gravity waves are non-dispersive (i.e., the phase speed, $c_p \equiv \omega/k$, and the group velocity, $c_g \equiv \partial\omega/\partial k$, are equal, and are both independent of the wavenumber) and describes two waves moving in opposite directions along the x axis with the velocity c_g. Together Equations (1.9) and (1.10) highlight that, since non-dispersive waves propagate at a speed that is independent of scale, they maintain their shape as they travel (e.g., Pedlosky, 2013).

Shallow-water gravity waves are driven to restore pressure gradients that arise due to layer thickness variations in the shallow-water system (in the absence of rotation and drag). Similarly, if one excludes rotation and drag from the incompressible three-dimension fluid equations, pressure gradients caused by thermal stratification deviations are restored by internal gravity waves, which (for one horizontal dimension) have the dispersion relation $\omega = \pm Nk/(k^2 + m^2)^{1/2}$, where m is the vertical wavenumber (e.g., Vallis, 2006). Hence, shallow-water gravity waves provide a shallow-water analogue of internal gravity waves[14]. Moreover, from Equation (1.9) and using this analogy, one sees that when in the absence of rotation and drag the shallow-water gravity wave speed is a fundamental velocity scale for pressure driven atmospheric flows. This characteristic scale is particularly relevant in the longitudinal direction along the equator, where the Coriolis parameter vanishes and winds travel freely without experiencing Coriolis deflection.

Geostrophic balance

Pressure gradients drive atmospheric winds but the Coriolis force acts perpendicularly and proportionally to the flow velocity. If a flow's typical horizontal velocity is $\mathcal{U}$ and its typical horizontal length scale is $\mathcal{L}$, the magnitude ratio between advection and the Coriolis force is

$$Ro \sim \frac{|\mathbf{u} \cdot \nabla \mathbf{u}|}{|f\widehat{\mathbf{z}} \times \mathbf{u}|} \sim \frac{\mathcal{U}}{f\mathcal{L}}, \tag{1.11}$$

where Ro is a dimensionless number called the Rossby number. If $Ro \gg 1$, rotation only plays a small lower-order role in atmospheric dynamics. However, if $Ro \ll 1$, flows are significantly deflected by the Coriolis force as they advect. In this limit, and when horizontal drags are neglected, the horizontal components of Equation (1.1a) reduce to

[14] In the shallow-water limit, $|k/m| \ll 1$, so $(k^2 + m^2)^{-1/2} \approx m^{-1} \sim H$. Moreover, if the layer is isothermal and hydrostatic, $p = p_0 \mathrm{e}^{-z/H_p}$ and $\rho = \rho_0 \mathrm{e}^{-z/H_p}$ for some scale height H_p (see the atmospheric scale height discussion below), so $N = [g(1 - \gamma^{-1})/H_p]^{1/2} \sim (g/H_p)^{1/2}$. Hence, a shallow layer with $H \sim H_p$ has $\omega = Nk(k^2 + m^2)^{-1/2} \sim c_g k$.

geostrophic balance:

$$fv = \frac{1}{\rho}\frac{\partial p}{\partial x} \qquad fu = -\frac{1}{\rho}\frac{\partial p}{\partial y}, \tag{1.12}$$

where cardinal Cartesian coordinates (i.e., x east, y north, and z vertical) have been used. This describes an exact balance between horizontal pressure gradients and the Coriolis force. Geostrophic balance is fundamental to planetary dynamics of rapidly or moderately rotating planets, for which planetary-scale flows have $Ro \ll 1$. Geostrophic balance emerges in all four of the models of Section 1.3.1 (in the $Ro \ll 1$ limit). In the primitive equations it appears as

$$fv = \left(\frac{\partial \Phi}{\partial x}\right)_p \qquad fu = -\left(\frac{\partial \Phi}{\partial y}\right)_p, \tag{1.13}$$

which is identical to Equation (1.12), as can be seen by noting that $0 = \nabla\Phi \equiv \nabla_p\Phi + (\partial\Phi/\partial p)\nabla p = \nabla_p\Phi - \rho^{-1}\nabla p$, so $\rho^{-1}\nabla p = \nabla_p\Phi$. Similarly, in the shallow-water model the horizontal pressure gradient is known explicitly and geostrophic balance appears as

$$fv = g\frac{\partial h}{\partial x} \qquad fu = -g\frac{\partial h}{\partial y}. \tag{1.14}$$

The two-dimensional incompressible Navier-Stokes model has the same geostrophic form as Equation (1.12) but writing it in terms of the streamfunction yields

$$f\nabla\psi = \frac{1}{\rho}\nabla p, \tag{1.15}$$

which highlights that, for an approximately constant Coriolis parameter, geostrophic balance is described by horizontal winds that move approximately along or parallel to isobars. In geostrophic balance, flow patterns are oriented with winds circulating clockwise about pressure highs in the northern hemisphere (where $f > 0$) and pressure lows in the southern hemisphere (where $f < 0$); conversely, geostrophic winds circulate anticlockwise about pressure lows in the northern hemisphere and pressure highs in the southern hemisphere. This behaviour is illustrated schematically in Figure 1.9.

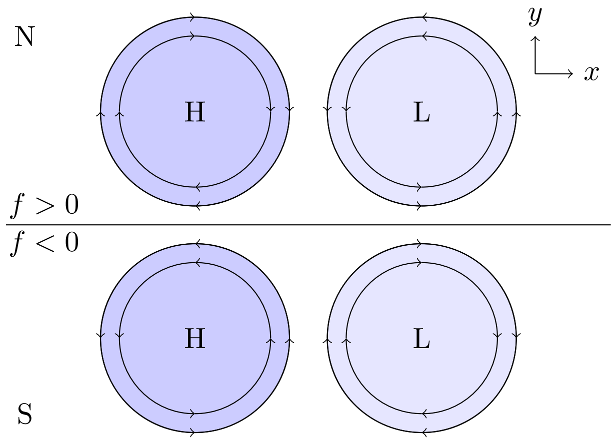

Figure 1.9: A schematic of geostrophic balance in a system (in cardinal Cartesian coordinates) with constant density and a piecewise constant Coriolis parameter, f. High and low pressure structures are indicated by labeled circles and the streamlines associated with the geostrophic balance are indicated with arrows. For $f > 0$, as in the northern hemisphere of planets, flows rotate clockwise along the isobars of high pressure structures and anticlockwise along the isobars of low pressure structures; whereas for $f < 0$, as in the southern hemisphere of planets, flows rotate anticlockwise along the isobars of high pressure structures and clockwise along the isobars of low pressure structures.

Looking locally, geostrophic balance is important at mid-to-high latitudes on Earth, where the Coriolis parameter is large enough to cause low Rossby number flows. In particular, Europe is located at fairly high latitudes, and interactions between the atmosphere and Europe's coastline mean that geostrophic vortices tend to sit over the UK or Continental Europe as they pass the UK. This explains much of the UK's weather. Clockwise high pressure circulations in the UK bring air from the south/west. If a high pressure circulation sits over the UK, it brings temperate weather from the Atlantic; whereas, if it sits over the Europe, in the summer it can cause "heatwaves" by drawing hot air northwards from North Africa and/or Continental Europe. Conversely, low pressure circulations in the UK bring air from the northeast, so tend to bring colder weather from the northern regions of the Atlantic, the poles, or Scandinavia depending in the position of the circulation pattern.

Rossby deformation radius

By considering Ro, one can see that geostrophic balance plays an important role in horizontal dynamics at a sufficiently large horizontal length scale. If one takes $\mathcal{U} = c_g$, $Ro = 1$

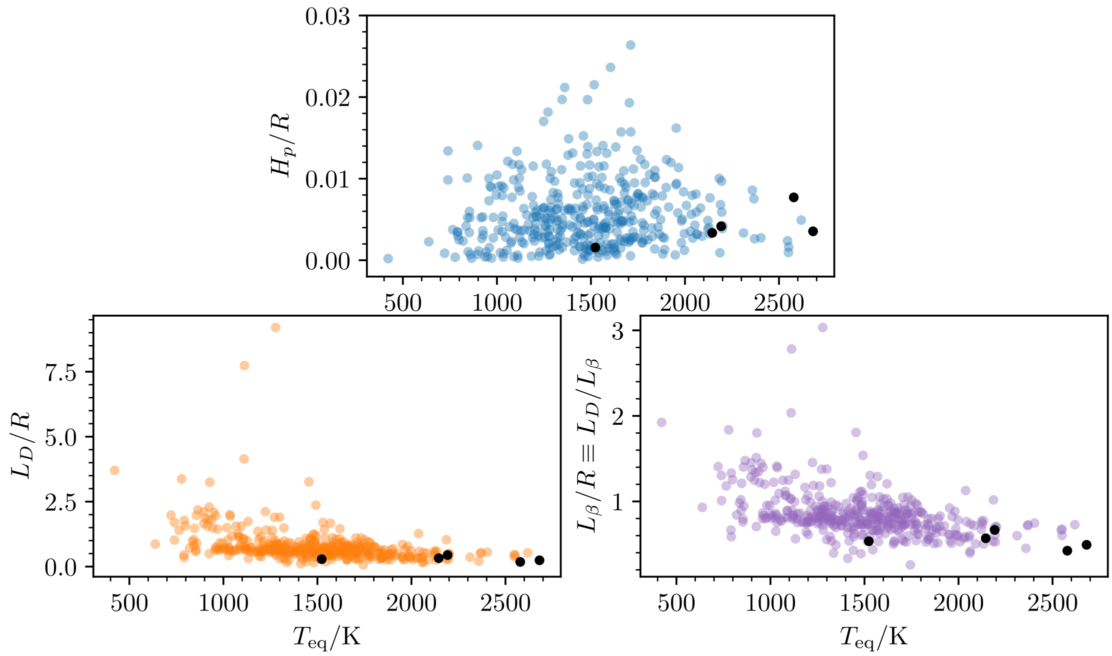

Figure 1.10: Atmospheric length scale ratios are plotted for hot Jupiters in the exoplanet.eu catalogue with $a < 0.1\,\mathrm{AU}$, and $0.1\,M_\mathrm{J} < M < 10\,M_\mathrm{J}$. $H_p/R \equiv \mathcal{R}T/gR$ is plotted in the upper panel; $L_D/R \sim c_g/2\Omega$ is plotted in the lower left panel; $L_\beta/R \equiv L_D/L_\beta \sim (c_g/2\Omega R)^{1/2}$ is plotted in the lower right panel. All these ratios are plotted against the orbit-averaged effective temperature of hot Jupiters. Note that in the righthand panel L_β (the Rhines scale) is evaluated with $\mathcal{U} = c_g$, so is equivalent to $L_{\rm eq}$ (the equatorial Rossby deformation radius). As in Figure 1.7, the hot Jupiters CoRoT-2b ($T_{\rm eq} \approx 1523\,\mathrm{K}$), Kepler-76b ($T_{\rm eq} \approx 2145\,\mathrm{K}$), HAT-P-7b ($T_{\rm eq} \approx 2192\,\mathrm{K}$), WASP-12b ($T_{\rm eq} \approx 2578\,\mathrm{K}$), and WASP-33b ($T_{\rm eq}2681\,\mathrm{K}$) are identified with opaque black markers.

for

$$\mathcal{L} = L_D \equiv \frac{c_g}{f}, \tag{1.16}$$

where $L_D \equiv c_g/f$ is the so-called *Rossby deformation radius*. It is the horizontal length scale over which stratification and rotation balance. More generally, the Rossby deformation radius has the definition $L_D = HN/f$ in three-dimensional systems, where H is the vertical scale of the flow (e.g., Vallis, 2006). The incompressible two-dimensional model has no stratification, so in this limit $L_D \to \infty$. This makes the incompressible two-dimensional model limited in scope when stratification and rotation are simultaneously important, as is often the case in planetary atmospheres. Typically, for hot Jupiters $L_D \sim R$, as shown in Figure 1.10, in which length scale ratios of hot Jupiter atmospheres are plotted.

Atmospheric scale height

If vertical forces are in hydrostatic balance, the vertical pressure gradient is related to the gravitational body force via Equation (1.2). If the atmosphere behaves like an ideal gas, Equations (1.1c) and (1.2) can be combined to yield:

$$\frac{\partial p}{\partial z} = -g\frac{p}{\mathcal{R}T} \equiv -\frac{p}{H_p}, \tag{1.17}$$

hence, if $H_p \equiv \mathcal{R}T/g$ is locally constant over a region of the atmosphere (i.e., the region is isothermal), then

$$p = p_0 \exp(-z/H_p), \qquad \rho = \rho_0 \exp(-z/H_p). \tag{1.18}$$

In this context, the vertical length scale H_p is known as the pressure scale height, the density scale height, or the atmospheric scale height. The name pressure scale height arises from the fact it denotes the height over which pressure changes by a factor e and similarly for the density scale height, which is the same here. The atmospheric scale height is important as it sets the typical vertical length scale over which incompressibility remains valid in the hydrostatic approximation. Beyond this scale height, density variations are no longer negligible and the incompressible approximation should be dropped. GCMs have typically found large-scale flows to vary vertically over a length comparable to H_p and that compressible and incompressible models of hot Jupiteres generally produce the same atmospheric behaviours (e.g., Showman & Guillot, 2002; Cooper & Showman, 2005, 2006; Dobbs-Dixon & Lin, 2008; Showman *et al.*, 2010). In the upper panel of Figure 1.10, we present values of H_p in units of planetary radii for known hot Jupiters, showing that typically $H_p/R \lesssim 0.03$. Since, $L_D \sim R$ (see lower left panel), this indicates that atmospheric flows on hot Jupiters typically have a *large aspect ratio* (i.e., a large horizontal-vertical length scale ratio).

Consequences of a large aspect ratio

The first consequence of a large atmospheric aspect ratio is that it implies that typical vertical velocity scales, $\mathcal{W}$, are small compared to typical horizontal velocity scales, $\mathcal{U}$, which can be shown with a simple scale analysis of the incompressibility condition. If $H \sim H_p$, $\nabla_3 \cdot \mathbf{u}_3 \equiv \nabla \cdot \mathbf{u} + \partial w/\partial z \approx 0$, where w is the vertical velocity. Hence, a scale analysis yields

$$\mathcal{W} \sim \frac{H}{L}\mathcal{U} \ll \mathcal{U}. \tag{1.19}$$

Secondly, a large aspect ratio implies the validity of the hydrostatic approximation (e.g., Vallis, 2006). Applying the traditional approximation to the horizontal components of the inviscid version of Equation (1.1a) yields

$$\underbrace{\frac{\mathrm{D}_3\mathbf{u}}{\mathrm{D}_3 t}}_{\mathcal{U}^2/L} + \underbrace{f\widehat{\mathbf{z}} \times \mathbf{u}}_{f\mathcal{U}} = \underbrace{-\frac{1}{\rho}\nabla p}_{\mathcal{P}/L}, \tag{1.20}$$

where underbrackets denote the typical magnitude associated with each term and $\mathcal{P}$ is the typical magnitude of p/ρ. From this, $\mathcal{P}/L \sim \max\{\mathcal{U}^2/L, f\mathcal{U}\}$. Similarly, the vertical component of the inviscid version of Equation (1.1a) is

$$\underbrace{\frac{\mathrm{D}_3 w}{\mathrm{D}_3 t}}_{(H/L)(\mathcal{U}^2/L)} = \underbrace{-\frac{1}{\rho}\frac{\partial p}{\partial z}}_{(L/H)\max\{\mathcal{U}^2/L, f\mathcal{U}\}} - g. \tag{1.21}$$

Hence, vertical advections are at least $O(L^2/H^2)$ smaller than vertical pressure gradients. For hot Jupiters, $H^2/L^2 \lesssim 10^{-3}$ (see above discussion), so hydrostatic balance is expected to be a good first-order approximation of planetary flows.

The Taylor-Proudman theorem

The Taylor-Proudman theorem implies that, for approximately constant $f\widehat{\mathbf{z}}$, velocities are approximately vertically-independent. To show this, one takes the curl of Equation (1.1a) in the traditional approximation, to yield the following vorticity equation:

$$\frac{\mathrm{D}_3\omega}{\mathrm{D}_3 t} = (\omega + f\widehat{\mathbf{z}}) \cdot \nabla_3 \mathbf{u}_3 - (\omega + f\widehat{\mathbf{z}})(\nabla_3 \cdot \mathbf{u}_3) + \frac{1}{\rho^2}\nabla_3\rho \times \nabla_3 p + \nabla_3 \times (\nu\nabla_3 \cdot \boldsymbol{\tau}_3), \quad (1.22)$$

where $\nu = \mu/\rho$ is the kinematic viscosity and f has been taken as a constant. If geostrophic balance dominates motion (i.e., $Ro \ll 1$ and $Re \gg 1$)[15], this reduces to

$$f\widehat{\mathbf{z}}(\nabla_3 \cdot \mathbf{u}_3) - f\widehat{\mathbf{z}} \cdot \nabla_3 \mathbf{u}_3 \sim \frac{1}{\rho^2}\nabla_3\rho \times \nabla_3 p. \quad (1.23)$$

Hence, if the baroclinic term, $\rho^{-2}\nabla_3\rho \times \nabla_3 p$, vanishes (i.e., density only varies along isobars)[16] and the atmosphere is incompressible, Equation (1.23) reduces further to

$$\frac{\partial \mathbf{u}_3}{\partial z} \sim \mathbf{0}. \quad (1.24)$$

This is known as the *Taylor-Proudman theorem* and implies that, under these conditions, velocities are approximately vertically-independent (e.g., Vallis, 2006). Moreover, if the baroclinic term in Equation (1.23) vanishes but incompressibility is not assumed, the vertical component on the lefthand side of Equation (1.23) yields $\nabla \cdot \mathbf{u} \sim 0$; while the horizontal components of Equation (1.23) yield $\partial\mathbf{u}/\partial z \sim \mathbf{0}$, as before. This variation of the Taylor-Proudman theorem implies that horizontal velocities are approximately horizontally divergence-free and vertically-independent (e.g., Showman *et al.*, 2010). In atmospheres, the Taylor-Proudman theorem implies that flows align themselves into vertically-independent columns known as Taylor columns. Consequently, in the context of of rapidly rotating planets, it is often useful to consider horizontal and vertical motions independently.

[15]Here $Re \equiv \mathcal{U}L/\nu$ is the Reynolds number, which describes the relative importance of inertial and viscous accelerations.

[16]For an ideal gas atmosphere ($\rho = p/\mathcal{R}T$), the baroclinic term vanishes if the atmosphere is isothermal as, for $\rho(p)$, $\nabla_3\rho \times \nabla_3 p = \mathrm{d}\rho/\mathrm{d}p(\nabla_3 p \times \nabla_3 p) = 0$.

Potential vorticity

Potential vorticity is a fundamentally important property of hydrodynamic atmospheric flows. In the isobaric primitive equations it is defined as

$$q_{\mathrm{PE}} = \left[\frac{(\zeta + f)}{\rho}\right] \cdot \nabla_p \Theta, \tag{1.25}$$

which is the dot product (i.e., the projectional intersection) of the vertical component of the planetary vorticity (per unit density) and the normal of the potential temperature (which is the variable that determines deviations in temperature stratification), with respect to an isobaric fluid surface.

In the single-layer homogeneous shallow-water model, where there is no explicit temperature treatment and stratification of the constant density layer is exactly described by hydrostatic equilibrium, this simplifies to

$$q_{\mathrm{SW}} = \frac{(\zeta + f)}{h}. \tag{1.26}$$

Furthermore, in the two-dimensional incompressible model, which has no vertical dependence, the potential vorticity is defined by

$$q_{\mathrm{2D}} = \zeta + f, \tag{1.27}$$

which is simply the locally normal planetary vorticity.

From Equation (1.7), it is clear that q_{2D} is materially conserved property. In fact, all of these potential vorticity formulations are materially conserved in their respective models. This encodes a hidden statement regarding angular momentum conservation in hydrodynamic systems and has important dynamical consequences, such as the emergence of Rossby waves.

Rossby waves

In geostrophic or quasi-geostrophic systems, the conservation of potential vorticity and the latitudinal variation of the Coriolis parameter combine to drive the propagation of so-called Rossby waves. Their significance to planetary circulation is so important that they are often simply called planetary waves.

First, we explain them physically, using the schematic in Figure 1.11, which is taken from Vallis (2006). The schematic illustrates the behaviour of two fluid parcels that are initially at rest and sit on a line of zero potential vorticity, η. These parcels are then instantaneously perturbed latitudinally: one northward and the other southward. Since the Coriolis parameter increases at it moves northward, just after the perturbation the northward parcel has $\zeta < 0$ (clockwise) and the southward parcel has $\zeta > 0$ (anticlockwise). Hence, both have westward velocities towards the points they originated from and shift westward as time progresses. Likewise, if the line η is perturbed in a wave-like fashion, the same potential vorticity mechanism will cause its phase to propagate westward. This westward propagating wave is the Rossby wave.

The simplest way to describe Rossby waves mathematically is with a latitudinally dependent Coriolis parameter in the two-dimensional incompressible model. The simplest form for this latitudinal dependence in f is the so-called equatorial beta-plane approximation, with $f = \beta y$, where $\beta = 2\Omega/R$ is a constant that denotes the local variations in the Coriolis parameter at the equator[17]. With this choice, Equation (1.7) can be linearised about a background rest state to yield

$$\frac{\partial \zeta_1}{\partial t} + \beta v_1 = 0 \iff \frac{\partial \nabla^2 \psi_1}{\partial t} + \beta \frac{\partial \psi_1}{\partial x} = 0. \tag{1.28}$$

Hence, if the streamfunction perturbation satisfies the planar wave ansatz, $\psi_1 = \hat{\psi} e^{i(kx+ly-\omega t)}$, where k and l respectively denote the wavenumbers of the x and y coordinates, Equa-

[17]The equatorial beta-plane approximation is discussed more fully in Section 2.2.3.

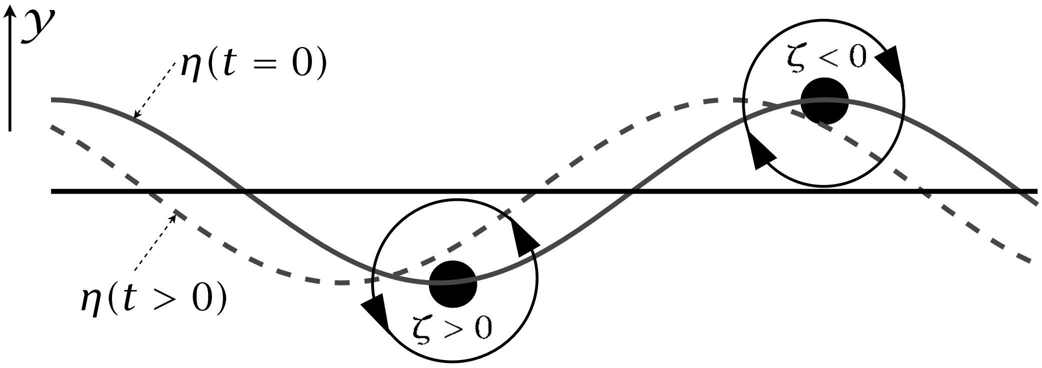

Figure 1.11: Rossby wave propagation schematic, taken from Vallis (2006). The schematic lies in the x-y plane, with positive y denoting north and positive x (i.e., right) denoting east and t denoting time. The schematic depicts two fluid parcels along the line, η, which conserves potential vorticity, $q_{2D} \equiv f + \zeta$, where f is the (northward increasing) Coriolis parameter and $\zeta \equiv \partial v/\partial x - \partial u/\partial y$ is the vertical component of the relative vorticity. The two fluid parcels start at rest (i.e., $\zeta = 0$) and one is perturbed northward and the other is perturbed southward. Since q_{2D} is materially conserved, the northward parcel has $\zeta < 0$ so rotates clockwise; whereas the southward parcel has $\zeta > 0$ so rotates anticlockwise. Consequently, since both parcels are oriented with westward velocities towards the centre, the parcels propagate westwards for $t > 0$. If this schematic is translated into a wave-like perturbation at $t = 0$ (solid black line), the wave's phase propagates westwards $t > 0$ (see dashed black line).

tion (1.28) gives the dispersion relation:

$$\omega = -\frac{k\beta}{k^2 + l^2}, \tag{1.29}$$

for arbitrary $\hat{\psi}$. The east-west phase velocity of this, $c_p \equiv \omega/k = -\beta/(k^2 + l^2)$ is westward, recovering the same result as the physical potential vorticity argument discussed above, which this is just a mathematical representation of.

We highlight here that Rossby waves propagate differently to gravity waves. the pressure perturbation that drives the Rossby wave satisfies geostrophic balance so the vorticity perturbation corresponding to it causes westward velocities along regions of minimal $|f|$, which drives westward phase propagation. In contrast, gravity waves travel in either direction in order to equalise pressure perturbations directly. Moreover, while gravity waves are non-dispersive (i.e., the group and phase velocities are equivalent and they travel as solitons), Rossby waves are dispersive (i.e., their phase and group velocities differ and are scale dependent) so they can transfer/exchange energy and angular momentum as they propagate (e.g., Pedlosky, 2013). Rossby waves prove to be fundamental to atmospheric dynamics in hot Jupiters and will be discussed much in other parts of this work.

The inverse energy cascade of quasi-two-dimensional turbulence

Turbulence is both chaotic and highly ordered. The advection of a fluid parcel is highly non-linear and chaotic, so the flow is highly sensitive to initial conditions and small perturbations. This makes it impossible to exactly model flow trajectories in isolation. However, since the flow is highly ordered, average properties of the flow do adhere to behaviours that can be modelled, repeated, and understood with theory.

In three-dimensional turbulence, large scale eddies break up into smaller scale eddies, which break up into smaller eddies still, until they are small enough to that viscous dissipation can effectively convert their kinetic energy into heat at some small dissipation scale that is determined by the microphysical properties of the flow. This leads to a process that is known as the *forward cascade* or the Richardson cascade (Richardson, 1926), which transfers energy through an inertial range of scales and the statistics of small scales are universally and uniquely determined by the kinematic viscosity, $\nu \equiv \mu/\rho$, and the rate of energy dissipation (Kolmogorov, 1941*a*,*b*). This is known as the universality hypothesis.

However, the Taylor-Proudman theorem shows that planetary flows are quasi-two-dimensional. This has important planetary consequences as the arguments that imply that three-dimensional turbulence has a forward cascade become modified in two-dimensional geometry. The important physical property to explain this is enstrophy, which in three-dimensions is $Z_3 \equiv (\nabla_3 \times \mathbf{u}_3) \cdot (\nabla_3 \times \mathbf{u}_3)$ and in two-dimensions is simply $Z_3 = \zeta^2$. In three-dimensions, enstrophy may be amplified by vortex stretching, $(\nabla_3 \times \mathbf{u}_3) \cdot \nabla_3 \mathbf{u}_3$. However, two-dimensional systems contain no vortex stretching and enstrophy, $Z \equiv \zeta^2$, and is materially conserved in the inviscid limit (e.g., Tabeling, 2002; Boffetta & Ecke, 2012). For non-zero viscosity, this ultimately results in a dual cascade in which energy has an *inverse cascade* from small scales to large scales and enstrophy has a forward cascade from large scales to small scales (Fjørtoft, 1953; Kraichnan, 1971). Charney (1971) showed that in quasi-geostrophic three-dimensional turbulence enstrophy is conserved and that it consequently behaves similarly to two-dimensional turbulence, with its inverse energy cascade possessing the same wavenumber dependence as two-dimensional isotropic turbulence.

Rhines scale

In isotropic two-dimensional turbulence, the inverse energy cascade can cause the emergence of system-scale vortices (Kraichnan, 1971; Laurie *et al.*, 2014). On the moderate-to-large scales of planetary atmospheres, where f is approximately constant, circular vortices can emerge as a result of the inverse energy cascade. This is believed to explain the formation of the large-scale vortices that are found inside the banded jets on Jupiter and Saturn such as Jupiter's Great Red Spot (Showman, 2007), which can be identified in the north east of the photograph of Jupiter in Figure 1.12. However, Rhines (1975) showed that, for rapidly rotating planets like Jupiter and Saturn, latitudinal variations in f cause anisotropy over planetary sized scales. As a consequence, turbulent flows on such planets become elongated in the azimuthal direction, causing zonal (east-west) planetary jets with the characteristic latitudinal width (Rhines, 1975; Vallis & Maltrud, 1993):

$$L_\beta \sim \left(\frac{\mathcal{U}}{\beta}\right)^{1/2}. \tag{1.30}$$

This is known as the Rhines scale. The Rhines scale represents a transition scale between quasi-two-dimensional isotropic geostrophic turbulence and dynamics associated with large-scale Rossby waves. Specifically, the inverse energy cascade of quasi-two-dimensional isotropic geostrophic turbulence causes the upscale cascading of kinetic energy, from relatively small energy injection scales up to moderate scales and so on until vortices approach the Rhines scale in diameter. At this point the latitudinal variations of f become dynamically significant. We have already discussed how (in potential vorticity conserving systems) such variations lead the propagation of Rossby waves, but we now discuss how Rossby waves caused this zonal banding to occur. For this, we refer to a simple scaling argument made by Rhines (1975). This notes that the Rossby wave dispersion relation of

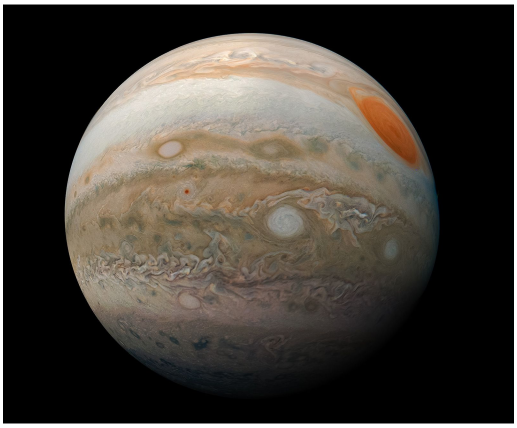

Figure 1.12: Jupiter viewed by the Juno space probe, taken from the Juno nasa.gov mission page. Circular vortices, with a diameter $\lesssim L_D$, are found within the atmosphere's banded structures. These banded structures correspond to zonal jets that have latitudinal widths $\sim L_\beta$, where on Jupiter $L_\beta > L_D$. Jupiter's famous Great Red Spot, which can be identified in the north east of the photograph, has a length scale between these characteristic scales and exhibits zonal elongation (for further discussion, see main text and Showman, 2007).

Equation (1.29) can be rewritten as

$$\omega = -\frac{\beta \cos\vartheta}{K}, \tag{1.31}$$

where $K = (k^2 + l^2)^{1/2}$ is a total wavenumber magnitude and ϑ is the angle between Rossby wave propagation and the positive x coordinate (east). The argument assumes that the magnitude of ω is similar to the turbulent frequency, $\omega_{\mathrm{turb}} \sim \mathcal{U}K$, and yields the anisotropic Rhines wavenumber:

$$K_\beta^2 \sim \frac{\beta}{\mathcal{U}}|\cos\vartheta|. \tag{1.32}$$

For $\vartheta = 0, \pi$, $L_\beta \sim 1/K_\beta \sim (\mathcal{U}/\beta)^{1/2}$; whereas for $\vartheta = \pm\pi/2$, $L_\beta \to \infty$. From the definitions above $k = K\cos\vartheta$ and $l = K\sin\vartheta$. Therefore, $\vartheta = 0, \pi$ correspond to $L_x/L_y = l/k = 0$ (i.e., latitudinal flows); whereas, $\vartheta = \pm\pi$ correspond to $L_y/L_x = k/l = 0$ (i.e., zonal flows). Hence, potential vorticity conservation and latitudinal variation in the Coriolis parameter place the bound $\mathcal{L}_y \lesssim L_\beta$, where $\mathcal{L}_y$ is the latitudinal length scale, but do not place a bound on the longitudinal length scale. This simple argument explains the famous banding structures in the atmospheres of Jupiter and Saturn (Showman, 2007), and is relevant to all planets (discussion in Showman *et al.*, 2010).

The above arguments were made using the two-dimensional incompressible model. This model does not include any dependence on stratification so has no shallow-water gravity waves and has an infinite Rossby deformation radius. However, for models with gravity waves and a finite Rossby deformation radius, it has been found that the relative sizes of L_β and L_D determine the nature of planetary-scale flows. If $L_\beta/L_D \ll 1$, the above arguments are more or less unchanged and banded zonal jets with a latitudinal width L_β emerge; whereas, if $L_\beta/L_D \gg 1$, Coriolis deflection causes flows to exhibit geostrophic behaviour on smaller scales than L_β, so circular vortices with a diameter L_D emerge (Okuno & Masuda, 2003; Smith, 2004; Showman, 2007). Figure 1.10 shows that hot Jupiters typically have, $L_D \sim R$, $L_\beta \sim R$ and, for the hottest hot Jupiters $L_D/L_\beta \lesssim 1$, so, from a length scale analysis alone, one would expect to find that hot Jupiters have planetary-scale geostrophic vortices that interact with zonal jets over a similar scale.

1.3.3 Equatorial superrotation on synchronously rotating exoplanets

As discussed in Section 1.2, hot Jupiters are believed to be tidally locked and observational measurements (e.g., Harrington *et al.*, 2006; Cowan *et al.*, 2007; Knutson *et al.*, 2007, 2009; Charbonneau *et al.*, 2008; Swain *et al.*, 2009; Crossfield *et al.*, 2010; Wong *et al.*, 2016) generally find them to have equatorial temperature maxima (hotspots) located eastward of their substellar points. This suggests that eastward equatorial flows are recirculating thermal energy eastwards via advection.

The emergence of prograde equatorial circulation like this is often referred to as equatorial superrotation. Generally, hydrodynamic GCMs of synchronously rotating hot Jupiters are consistent with these observational findings and produce two archetypal flow patterns: planetary scale quasi-geostrophic structures at mid-to-high latitudes and a superrotating jet at low-to-equatorial latitudes (e.g., Showman & Guillot, 2002; Shell & Held, 2004; Cooper & Showman, 2005, 2006; Langton & Laughlin, 2007; Dobbs-Dixon & Lin, 2008; Menou & Rauscher, 2009; Rauscher & Menou, 2010; Dobbs-Dixon *et al.*, 2010; Perna *et al.*, 2010; Heng *et al.*, 2011; Perez-Becker & Showman, 2013), with the fundamental mechanism responsible for driving the equatorial superrotating jet first explained by Showman

& Polvani (2011).

The fact that equatorial superrotation emerges in hot Jupiters is, in itself, an interesting finding and suggests the presence of a subtle dynamical mechanism that can redistribute energy and angular momentum. This is a consequence of a theorem from Hide (due to Hide, 1969*a*), which was presented in the hot Jupiter context by Showman & Polvani (2011). It states that equatorial superrotation cannot result from atmospheric circulations that are longitudinally symmetric or that conserve specific angular momentum about the planetary rotation axis, and can only be a result of an angular momentum pumping mechanism that is driven by waves or eddies. The theorem arises from the fact that, since equatorial flows are located furthest from the planet's axis of rotation, a superrotating equatorial jet corresponds to an angular momentum maxima so may only be maintained by an *up-gradient* transport mechanism, which transfers eastward angular momentum from higher latitudes into the equatorial region. This suggests that there are some interesting wave/eddy interactions in equatorial regions of synchronously rotating hot Jupiters. The actual mechanism that is responsible for this angular momentum pumping is of high interest to this study and we shall discuss it in more detail in subsequent chapters (particularly in Chapters 3 to 5). However, in this subsection, we shall give an illustrative overview of the general findings of Showman & Polvani (2011).

Planetary scale equatorial shallow-water waves

The dynamical mechanism that Showman & Polvani (2011) showed drives equatorial superrotation relies on a dynamical properties of linear planetary-scale *equatorial shallow-water* waves. In this context shallow-water denotes that a shallow-water treatment of stratification is included and equatorial denotes that the waves are contained within specific latitudinal regions, in which the Coriolis force transitions from being of negligible dynamical importance (i.e., along the equator) to of leading order importance (i.e., at mid-to-high latitudes). These waves were first studied by Matsuno (1966) and shall be discussed more extensively in Chapter 3. However, Showman & Polvani (2011) showed that in the parameter regime that contains hot Jupiters, the $n = 1$ equatorial Rossby wave

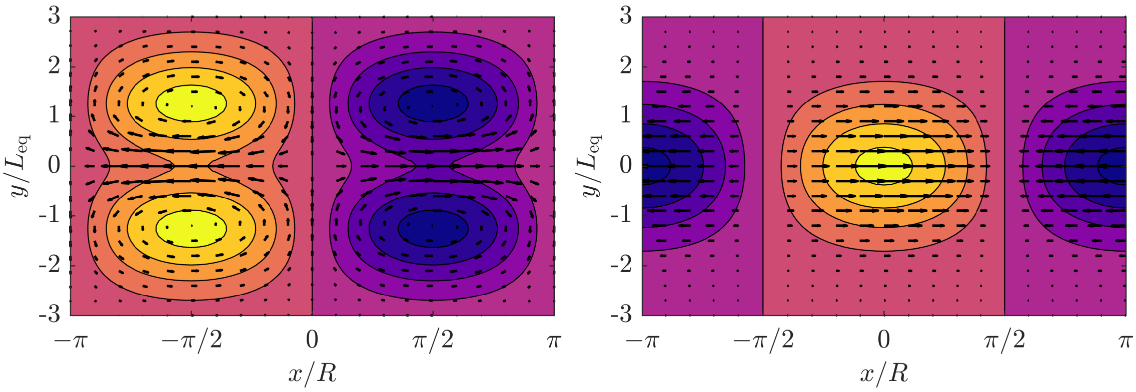

Figure 1.13: The structural form of the $n = 1$ equatorial Rossby wave (left panel) and the equatorial Kelvin wave (right panel), with the azimuthal wavenumber $k = 1/R$, are plotted in cardinal Cartesian coordinates, with x denoting the eastward coordinate and y denoting the northward coordinate. The northward coordinate is given in units of $L_{\rm eq}$, the equatorial Rossby deformation radius, which determines the latitudinal length scales of the waves. The structures of the waves are visualised with pressure contours (i.e., contours of h in the shallow-water model), with yellow/blue contours denoting pressure highs/lows respectively, and horizontal velocity vectors are overplotted. The $n = 1$ equatorial Rossby wave behaves geostrophically at mid-to-high latitudes and travels westward; while the equatorial Kelvin wave travels eastward with no meridional component, and velocity maxima at its pressure maxima. The plots are made using the solutions of Matsuno (1966) for $L_{\rm eq}/R = 0.67$, which is the approximate value of this ratio on the hot Jupiter HAT-P-7b. The azimuthal phase of the plotted free waves is arbitrary and time-dependent.

and the equatorial Kelvin wave are the most significant equatorial waves.

The $n = 1$ equatorial Rossby wave is an analogous to the standard Rossby wave discussed earlier in this section but propagates only in the zonal direction. The $n = 1$ label denotes that its meridional (latitudinal) velocity is zero at one point (i.e., the equator). For equatorial shallow-water waves all odd n labels denote equatorially-symmetric pressure structures and zonal velocities (h, u), and equatorially-antisymmetric meridional velocities (v); whereas these symmetries flip for even n (i.e., v antisymmetric; h and u symmetric). The $n = 1$ equatorial Rossby wave behaves in a geostrophic manner so is described by westward propagating vortices that circulate about pressure highs and lows (see Figure 1.13, lefthand panel). Its latitudinal profile is determined by the length scale, $L_{\rm eq} \equiv (c_g/\beta)^{1/2}$, which is known as the *equatorial Rossby deformation radius* and is the equatorial analogue of L_D. Note that, for $\mathcal{U} \sim c_g$, $L_{\rm eq}$ is simply the Rhines scale, which describes the latitudinal width of planetary zonal jets. This similarity is not a coincidence as the equatorial waves provide a latitudinal reference guide for the turbulent dynamics (see discussion on the Rhines scale). The similarity between these two scales means that linear or weakly non-linear equatorial shallow-water wave treatments of planetary scale flows generally have good first order agreement with fully nonlinear GCMs (e.g., Showman & Guillot, 2002; Shell & Held, 2004; Cooper & Showman, 2005, 2006; Langton & Laughlin, 2007; Dobbs-Dixon & Lin, 2008; Menou & Rauscher, 2009; Rauscher & Menou, 2010; Dobbs-Dixon *et al.*, 2010; Perna *et al.*, 2010; Showman & Polvani, 2011; Heng *et al.*, 2011; Perez-Becker & Showman, 2013). This is because quasi-two-dimensional turbulence will always pump energy and momentum up to these scales. Moreover, hot Jupiters typically have the property that $L_{\mathrm{eq}} \sim R$ so radiative heating from their host star typically varies on L_{eq}, meaning that energy is directly injected at this wave scale without needing an energy cascade, explaining why this description has been so powerful in explaining the dynamics of hot Jupiters.

The equatorial Kelvin wave propagates along the equator where the Coriolis parameter vanishes. It is akin to the shallow-water gravity wave in that it has the azimuthal phase velocity c_g and is non-dispersive in the zonal direction. However, while the shallow-water gravity wave comes in two oppositely travelling varieties, there is only one equatorial Kelvin wave, which propagates eastward. The equatorial Kelvin wave also has a length scale determined by L_{eq}, but has the additional interesting characteristics that its meridional velocity is suppressed by rotation and its velocity maxima are located at its pressure maxima (see Figure 1.13, righthand panel).

Matsuno (1966) showed that, when a linearised, time-independent, equatorial beta-plane shallow-water system is exposed to a forcing source on h with the latitudinal scale L_{eq}, the resulting stationary response, $\{h(\mathbf{x}), \mathbf{u}(\mathbf{x})\}$, dominated by the standing wave superposition of the $n = 1$ equatorial Rossby wave and the equatorial Kelvin wave (see Figure 1.14, which is taken from Matsuno (1966)). The $n = 1$ equatorial Rossby wave's response causes mid-to-high latitude flows to behave in a geostrophic manner, with the pressure highs and lows shifted westward; whereas the equatorial Kelvin wave's response causes flows along the equator to be is zonally dominated, with eastward shifted pressure highs and lows. Showman & Polvani (2011) showed that, since gh is equivalent of

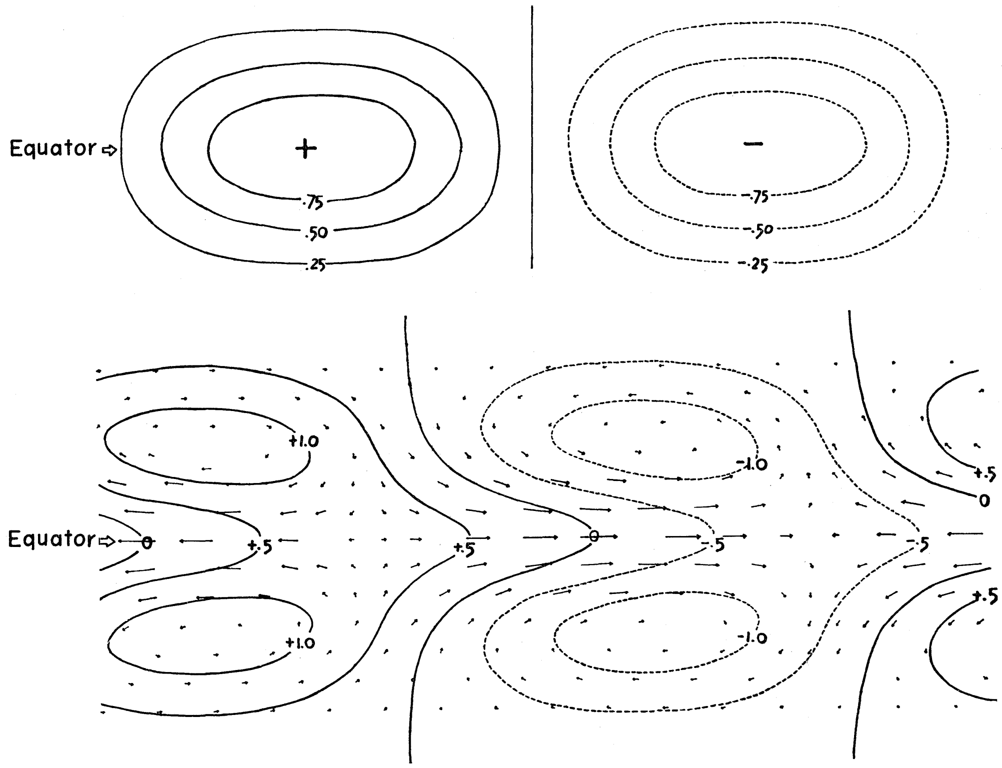

Figure 1.14: The time-independent response (bottom panel) of a linearised shallow-water system in the beta-plane approximation when it is subjected to a stationary forcing profile on h (top panel) that varies on system sized spatial scales, taken from Matsuno (1966). Highs/lows in geopotential energy, gh, which are also pressure highs/lows in shallow-water models, are marked by solid/dashed contours and velocity vectors are overplotted. These solutions are dominated by standing wave superposition of the $n = 1$ equatorial Rossby wave and the equatorial Kelvin wave.

$p/\rho \equiv \mathcal{R}T$ in the shallow-water momentum equation (Equation (1.5a)) and $L_{\mathrm{eq}} \sim R$ on hot Jupiters, these kinds of forcing responses arise in the context of time-independent planetary-scale thermal forcing on hot Jupiters and are closely tied to the emergence equatorial superrotation.

Equatorial superrotation due to eddy momentum pumping

Showman & Polvani (2011) showed that linear steady state recirculation patterns, related to the stationary forcing responses of these planetary-scale equatorial waves, induce equatorial superrotation through an angular momentum pumping mechanism involving eddy interactions. The key subfigures for outlining the angular momentum pumping mechanism of Showman & Polvani (2011) are combined in Figure 1.15. The two top left panels of Figure 1.15 show steady solutions of a linearised, equatorial beta-plane, shallow-water model, (b), when exposed to a time-independent layer thickness forcing profile, (a), which is designed to mimic heating on a synchronously rotating hot Jupiter. These solutions are presented alongside the resulting zonally-averaged zonal accelerations that such linearised solutions generate (see Figure 1.15, bottom panel; see caption for details) and the mechanism schematic that Showman & Polvani (2011) provided (see Figure 1.15, top right panel).

Equatorial superrotation is driven by the zonally-averaged-zonal-wind/eddy interactions that planetary-scale quasi-geostrophic redistribution patterns cause. These redistribution patterns, which behave quasi-geostrophically at mid-to-high latitudes, can be associated with the planetary-scale equatorial shallow-water waves (as discussed above). They cause planetary-scale eddies to tilt so that winds predominantly circulate westward-poleward and eastward-equatorward about regions of high geopotential, gh. This tilting can be identified by the eastward-pointing chevron-shaped geopotential/flow patterns in the linear solution in Figure 1.15 (top left panel, (b)). Due to the geostrophic characteristics of the mid-to-high latitude flows, the regions of large geopotential gradients (i.e., the flanks of the geopotential high) are the regions in which flows have the largest momentum. Therefore, as these tilted eddies redistribute geopotential energy from the western

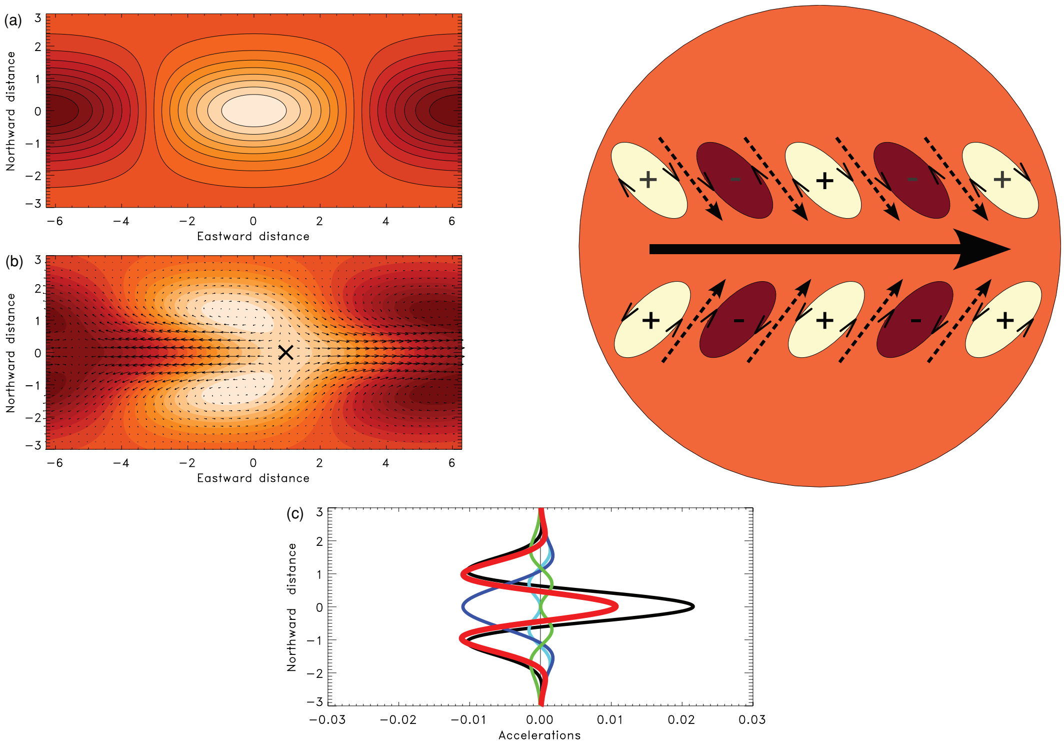

Figure 1.15: Eddy momentum pumping due to equatorial waves, taken from Showman & Polvani (2011). The upper left panels show, (a), an applied forcing profile on h and, (b), a corresponding linearised time-independent solution, $\{h_0(\mathbf{x}), \mathbf{u}_0(\mathbf{x})\}$, of the resulting forced shallow-water equations, in the equatorial beta-plane approximation, with a marked hotspot (black cross). This forcing profile and linearised solution are similar to those displayed in Figure 1.14. The bottom panel, (c), shows zonally-averaged eastward accelerations resulting from the non-linear interactions that these linear solutions cause. In this plot, total mean zonal accelerations, which are found to be eastward, are plotted in red. Alongside this, the plot also shows the relative importance of the contributing mean zonal accelerations. The equatorward transport of eastward eddy momentum (black) provides the dominant contribution and the other components are mean zonal accelerations due to vertical eddy momentum transport (blue), Rayleigh drag in the model (cyan), and mean meridional circulation (green). The upper right panel contains a schematic of how the linear solutions induce this equatorward transport of eastward eddy momentum (though Showman & Polvani (2011) changed the azimuthal wavenumber in the schematic for illustrative purposes). The fundamental feature is the eastward pointing chevron-shaped flow patterns/pressure contours, which cause eddies to tilt so that they carry eastward angular momentum from the westward high latitude regions into equatorial region.

dayside up towards the poles and then back to the eastern dayside, they also transport eastward angular momentum in a net equatorward fashion. This equatorward transport of eastward angular momentum by eddies is closely related to the negative of the horizontal Reynolds stress (i.e., $-\overline{u'v'}$, where the overbar denotes a zonal average and the primes denote deviations thereof). It is positive at equatorial latitudes, where flows are either poleward-westward or equatorward-eastward, but negative at mid-to-high latitudes, where Coriolis deflection turns poleward flows back towards the equator. This can been seen from Figure 1.15 by comparing the black line (the average eastward accelerations due to meridional eddy circulations) in the bottom panel of Figure 1.15 to the directions of $u'v'$ on the flanks of the geopotential highs in the linear solution. This net eastward-equatorward eddy momentum pumping in equatorial regions provides a means of transporting angular momentum up-gradient.

Ultimately, this up-gradient angular momentum transport allows equatorial superrotation to be maintained. The mechanism of Showman & Polvani (2011) predicts that the latitudinal width of the equatorial superrotating jet is comparable to the equatorial Rossby deformation radius and highlights that, in hydrodynamic models, planetary-scale redistribution patterns can be approximately described by wave dynamics. The mechanism is based on weakly non-linear interactions and Showman & Polvani (2011) assessed its robustness by comparing predictions of the linear analytic shallow-water model to non-linear shallow-water simulations, and sophisticated three-dimensional GCMs. They found hierarchical consistency between the models in describing the interactions. This is due to the linear nature of the dominant geostrophic balances that cause them.

1.4 Magnetism in hot Jupiter atmospheres

1.4.1 Magnetic field generation in hot Jupiters

One of the reasons that hot Jupiters are so interesting from a fluid dynamics perspective is that, as a collection of bodies, their atmospheric temperatures bridge over the region of parameter space between which magnetism transitions from being of subdominant to leading order dynamical importance (e.g., Perna *et al.*, 2010; Menou, 2012*a*; Rogers & Komacek, 2014). The extension of planetary dynamo theory into the hot Jupiter regime is not well understood. That said, from current dynamo theory one would expect hot Jupiters to have planetary dynamos that are sustained within the convective deep interior and generate deep-seated poloidal magnetic fields. The hottest hot Jupiters also have weakly-ionised atmospheres. If their atmospheres are sufficiently ionised, the zonally-dominated atmospheric flows become sufficiently connected to the planet's deep-seated poloidal magnetic field to induce atmospheric toroidal fields (e.g., Menou, 2012*a*; Rogers & Komacek, 2014). Assuming this picture, and the planet's deep-seated magnetic field to be dipole dominated, the induction of the azimuthal component of the magnetic field, $\mathbf{B}_\phi \equiv B_\phi \widehat{\phi}$, is approximated by (e.g., Menou, 2012*a*)

$$\begin{aligned} \frac{\partial \mathbf{B}_\phi}{\partial t} &\approx \nabla_{(3)} \times [\mathbf{V}_\phi \times \mathbf{B}_{\rm dip}] - \nabla_{(3)} \times (\eta \nabla_{(3)} \times \mathbf{B}_\phi) \\ &\approx -(\mathbf{V}_\phi \cdot \nabla_{(3)})\mathbf{B}_{\rm dip} + (\mathbf{B}_{\rm dip} \cdot \nabla_{(3)})\mathbf{V}_\phi - \nabla_{(3)} \times (\eta \nabla_{(3)} \times \mathbf{B}_\phi), \end{aligned} \tag{1.33}$$

where $\mathbf{B}_{\rm dip}$ is the planetary dipolar field, $\mathbf{V}_\phi \equiv V_\phi \widehat{\phi}$ is the zonal component of the atmospheric flow, η is the magnetic diffusivity. Moreover, if the planetary dipole is axially-aligned, Equation (1.33) reduces to

$$\frac{\partial \mathbf{B}_\phi}{\partial t} \approx (\mathbf{B}_{\rm dip} \cdot \nabla_{(3)})\mathbf{V}_\phi - \nabla_{(3)} \times (\eta \nabla_{(3)} \times \mathbf{B}_\phi). \tag{1.34}$$

The ratio of toroidal field induction and diffusion is estimated via the magnetic Reynolds number:

$$R_m \sim \frac{|\nabla_{(3)} \times [\mathbf{V}_\phi \times \mathbf{B}_{\rm dip}]|}{|\nabla_{(3)} \times (\eta \nabla_{(3)} \times \mathbf{B}_\phi)|}. \tag{1.35}$$

Using the assumption that the electric currents generating the dipolar planetary field are located far below the upper atmosphere, Menou (2012*a*) showed that the magnitudes of B_ϕ and $B_{\rm dip}$ can be approximately related by the scaling law

$$|B_\phi| \sim R_m |\mathbf{B}_{\rm dip}|, \tag{1.36}$$

with

$$R_m = \frac{U_\phi H_p}{\eta}, \tag{1.37}$$

where U_ϕ is the typical scale of the zonal wind speed, and H_p is the pressure scale height. Hence, if toroidal field induction dominates toroidal field diffusion in the atmosphere ($R_m \gtrsim 1$), the large scale zonal winds on hot Jupiters are expected to induce strong toroidal fields that dominate the atmospheric magnetic field geometry. Further, from Equation (1.34), it can be seen that one should expect these toroidal fields to be antisymmetric about the equator, with a maximum/minimum at mid-latitudes in the northern/southern hemisphere and toroidal field magnitude decreasing towards each pole, depending on the latitudinal profiles of $\mathbf{V}_\phi$ and $\mathbf{B}_{\rm dip}$.

This is exactly the type of dominant magnetic field profile found by Rogers & Komacek (2014), as visualised in Figure 1.16, which is taken from their paper. This shows the magnetic field profiles generated in simulations of a three-dimensional hot Jupiter model, which calculates a radially and time dependent η based on their model's radial reference temperature. For cooler planets (top row), toroidal field dissipation dominates toroidal field induction and magnetic field profiles largely resemble the imposed dipolar field. For hotter planets, toroidal field induction is significant and equatorially-antisymmetric toroidal fields dominate the magnetic field geometry (middle row). If hotter planets have large enough magnetic field strength, the magnetic field couples with the flow, resulting in magnetically-driven wind variations, which we shall discuss in great depth within this work.

Aside from being hot enough to support magnetism, the perpetual day/night sides on hot Jupiters has the potential to drive complex and fascinating magnetohydrodynamics. This is because the extreme day-night temperature differentials cause longitudinal variations in the degree of atmospheric ionisation, which in-turn causes longitudinal variations in the magnetic diffusivity. These inhomogeneities are expected to be substantial with $R_m \ll 1$ on the nightsides and $R_m \sim$ 100-1000 on daysides of the hottest hot Jupiters (Rogers & Komacek, 2014). Hence, the daysides of the hottest hot Jupiters are expected

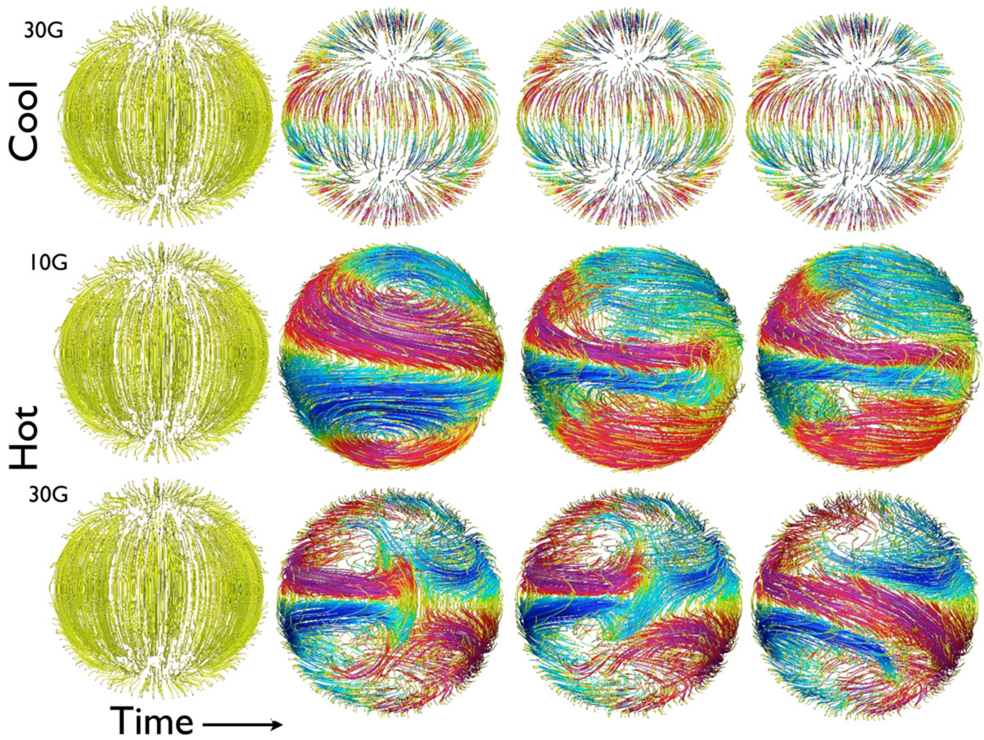

Figure 1.16: The evolution of magnetic field profiles in three-dimensional MHD simulations, taken from Rogers & Komacek (2014). The magnetic field in simulated hot Jupiter atmospheres, as viewed from the nightside, with colours representing the toroidal field magnitude (red/magenta positive; blue/green negative; and yellow moderate, relative to extremes, positive/negative). Times are different for each model with the purpose of providing a qualitative picture of magnetic field evolution. The quoted magnetic field strength is that of the radial field at the pole, at the base of the simulated atmosphere. In cool 3D MHD simulations atmospheres are weakly ionised, meaning that winds do not couple to the planet's deep-seated magnetic field significantly (top row). In hot 3D MHD simulations, when ionised winds couple with the planet's deep-seated magnetic field, they induce atmospheric toroidal fields that are dominated by a planetary scale equatorially-antisymmetric component (middle row). When this atmospheric toroidal field overcomes a critical threshold in its magnitude, it causes complex MHD behaviours including wind/hotspot reversals to develop (bottom row). These behaviours arise from the how the toroidal field couples with the ionised winds, which we model in this work.

to be dominated by dynamics related to toroidal field induction; whereas on the nightsides magnetic fields are expected be predominantly diffusive in behaviour. This atmospheric property, which may be unique to hot Jupiters, is likely to have interesting global consequences. For instance, using three-dimensional global simulations with a horizontally (as well as radially) varying magnetic diffusivity, Rogers & McElwaine (2017) found that the hottest hot Jupiters may be able to sustain variable-η-driven dynamo action (like the kind proposed by Pétrélis *et al.*, 2016) in their thin stably stratified atmospheres.

1.4.2 Is radius over-inflation caused by Ohmic heating?

As discussed in Section 1.2.4, hot Jupiters generally have radii larger than expected based on the predictions of planetary evolution/structure theory, suggesting that an internal heating mechanism is actively slowing gravitational contraction. One such heating source that has been proposed as an explanation to this over-inflation problem is Ohmic heating. That is, heating via conversion of magnetic energy into internal energy, through the generation of electric currents.

This explanation was first proposed by Batygin & Stevenson (2010), who used a kinematic approach (i.e., one without consistent magnetic induction) to present a possible heating mechanism. Their model is illustrated in Figure 1.17, which is their cross-sectional diagram of the current induced on a planet with purely zonal flows in the thin atmosphere and a deep-seated planetary dipole magnetic field that is aligned with the rotation axis. Batygin & Stevenson (2010) highlighted that ionised purely zonal winds passing through an axially-aligned dipole will induce a toroidal field and current that flows perpendicular to the magnetic field lines of both the toroidal and dipolar fields. More precisely, at high latitudes the induced currents flow meridionally from the poles to the equator; while in equatorial regions the induced currents penetrate into the planet's convective interior, causing Ohmic heating. In their kinematic approach, Batygin & Stevenson (2010) imposed a motionless deep interior and took the atmospheric winds to be purely zonal, setting $\mathbf{u}_3 = V_\phi \widehat{\phi}$, where V_ϕ was prescribed based on findings of hydrodynamic simulations. Then, neglecting magnetic induction (i.e., $\partial \mathbf{B}_3/\partial t = -\nabla_3 \times \mathbf{E}_3 = 0$), they calculated the expected Ohmic heating, $|\mathbf{J}_3|^2/\sigma$, using Ohm's law, $\mathbf{J}_3 = \sigma(\mathbf{E}_3 + \mathbf{V}_\phi \times \mathbf{B}_{\text{dip}})$, and Ampére's law, $\mathbf{J}_3 = \nabla_3 \times \mathbf{B}_{\text{dip}}$, where $\mathbf{J}_3$ is the current density, σ a prescribed radially dependent conductivity, and the electric field is defined in terms of an electrostatic potential, $\mathbf{E}_3 \equiv -\nabla_3 \Psi_e$. Using this method and comparing to past planetary evolution theory, Batygin & Stevenson (2010) calculated that there would be enough Ohmic heating in the planetary interior to explain the inflated radii of the hot Jupiter HD 209458b and, if it has enhanced metallicity, the hot Jupiter Tres-4b.

After this initial attempt to quantify the amount of Ohmic heating in the interiors of hot Jupiters, various authors applied similar kinematic theory to planetary structure/evolution models more widely across the sample of known hot Jupiters (Laughlin *et al.*, 2011; Huang & Cumming, 2012; Wu & Lithwick, 2013). These included an Ohmic heating term in their evolution equations, which was calculated with a method similar to Batygin & Stevenson (2010). Perna *et al.* (2010) calculated the Ohmic heating that would be generated in the presence of an imposed magnetic field within their three-dimensional hydrodynamic GCM, using a prescription for drag due to the Lorentz force that they derived in (Perna *et al.*, 2010). The findings of such kinematic studies tended to have between one and two orders of magnitude disagreement so could not comprehensively determine whether or not Ohmic heating could inject enough internal energy into the interiors of hot Jupiters to explain their sizes. Attempting to elucidate this problem, Rogers & Showman (2014) measured the volume integrated Ohmic heating present in a self-consistent three-dimensional MHD model with radially-dependent magnetic diffusivity, finding it to be between one and two orders of magnitude too small to explain radius inflation on HD 209458b. However, in spite of this finding, Rogers & McElwaine (2017) highlight that a temperature dependent magnetic diffusivity could possibly could result in enhanced Ohmic heating by providing the conditions necessary for a thermo-resistive instability (proposed by Menou, 2012*b*) to emerge. Research in this area is onging.

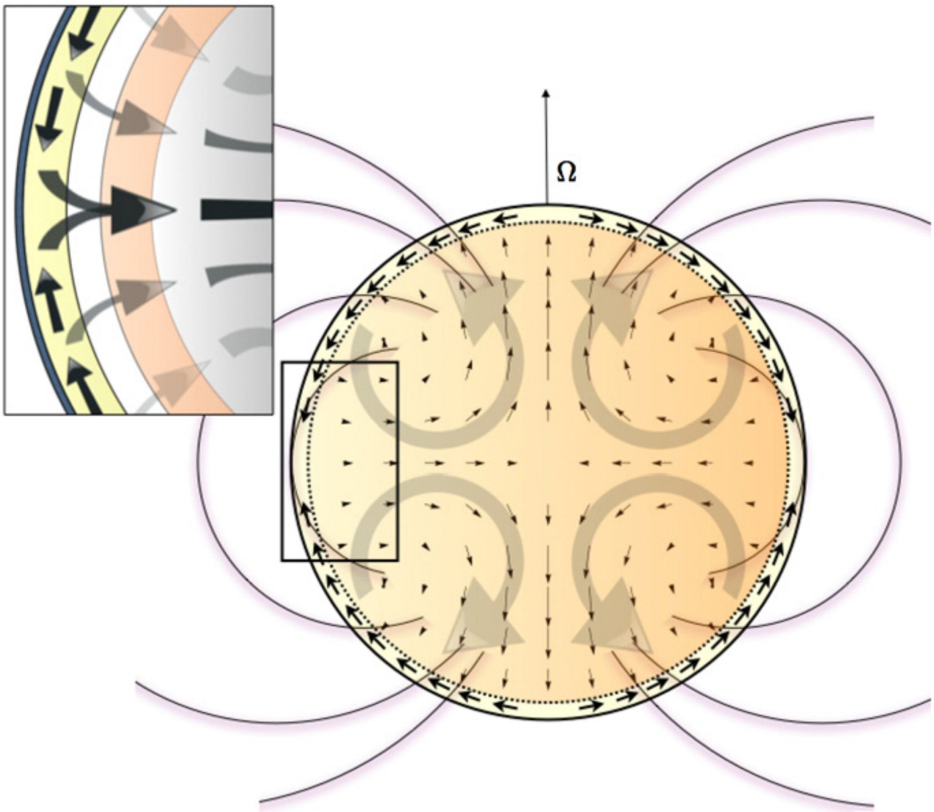

Figure 1.17: Induced current due to zonal wind flow in the presence of an axially-aligned deep-seated planetary dipolar magnetic field, taken from Batygin & Stevenson (2010). This side view cross-section shows the thin radiative atmosphere and a convective deep interior, separated by the radiative-convective boundary (dotted line). The plot shows the field lines of the planet's deep-seated dipolar magnetic field extending out of the convective interior. The quiver arrows denote the direction and magnitude of the induced current for a model containing purely zonal winds in the thin atmosphere and no flows in the convective interior. The large translucent arrows are illustrations of the general loop in the flow of current in the model. The inset window shows a zoomed-in cross section of currents at the equator, which become radially directed and penetrate into the deep interior, causing Ohmic heating.

1.4.3 Magnetism can drive hotspots westwards

As discussed in Section 1.2.5, Rogers & Komacek (2014) used three-dimensional MHD simulations to predict that magnetic fields could cause wind variations that drive east-west hotspot oscillations in the hottest hot Jupiters; a prediction that was followed by measurements of westward hotspots/brightspots on the ultra-hot Jupiters HAT-P-7b (Armstrong *et al.*, 2016), Kepler-76b (Jackson *et al.*, 2019), WASP-12b (Bell *et al.*, 2019), and WASP-33b (von Essen *et al.*, 2020), as well as the cooler CoRoT-2b (Dang *et al.*, 2018). Temporarily ignoring magnetism, these observations have been elsewhere explained by cloud asymmetries confounding optical measurements (Demory *et al.*, 2013; Lee *et al.*, 2016; Parmentier *et al.*, 2016; Roman & Rauscher, 2017) and retrograde flows in planets with asynchronous rotation (Rauscher & Kempton, 2014). The hotspot observations of WASP-12b and CoRoT-2b were measured using thermal phase curves so reflections from cloud asymmetries cannot confound these measurements. Moreover, ultra-hot Jupiters are expected to be too hot for condensates to form and are believed to have cloud-free daysides (Helling *et al.*, 2019*a*), suggesting that optical observations on ultra-hot Jupiters are free from such interferences and that a dynamical explanation is more likely. Furthermore, all of these hot Jupiters have near-circular orbits so are expected to be tidally locked with synchronous rotation (Colombo & Shapiro, 1966; Guillot *et al.*, 1996; Showman *et al.*, 2015). In light of these factors, it seems likely that magnetism plays an important role in explaining at least some of these observations.

After Armstrong *et al.* (2016) found east-west brightspot oscillations on HAT-P-7b, Rogers (2017) showed that, if these oscillations result from magnetism, such observations can inform on HAT-P-7b's magnetic field strengths, which are otherwise unmeasurable. Moreover, Rogers (2017) used three-dimensional simulations to identify that a relationship between the timescales associated with shallow-water wave propagation and a magnetic drag timescale over which the Lorentz force from the dipolar magnetic field can significantly reduce flows. However, while three-dimensional MHD simulations have demonstrated that westward flows can develop in the presence of strong magnetic fields (Rogers

& Komacek, 2014) and this timescale relationship appears to match the findings of the simulations Rogers (2017), the actual mechanism for wind reversals is hitherto unknown. Naively, one would expect that the restorative Lorentz force generated by zonal flows in the presence of a dipolar magnetic field could slow and halt but not actually reverse flows. This suggests that the atmospheric toroidal field plays an important dynamical role in the wind reversal phenomenon.

Identifying the physical mechanism that drives wind/hotspot reversal may also help refine and/or explain constraints on the magnetic fields of ultra-hot Jupiters that exhibit westward hotspot offsets. In their three-dimensional MHD simulations, Rogers & Komacek (2014) identified that reversals occurred when

$$\tau_{\mathrm{mag}} \lesssim \tau_{\mathrm{wave}}, \tag{1.38}$$

where $\tau_{\mathrm{wave}} \equiv L_{\mathrm{eq}}/c_g$ is the characteristic timescale of equatorial shallow-water waves in the system (e.g., Matsuno, 1966; Showman & Polvani, 2011; Perez-Becker & Showman, 2013) and $\tau_{\mathrm{mag}} \equiv \eta/V_{\mathrm{A,dip}}^2 \equiv \eta\mu_0\rho/|\mathbf{B}_{\mathrm{dip}}|^2$ is the timescale over which the Lorentz force associated with the deep-seated dipolar magnetic field will bring zonal flows to rest, in the absence of other forces, with $V_{\mathrm{A,dip}}$ denoting the Alfvén speed of the assumed deep-seated dipolar magnetic field (which has magnitude $|\mathbf{B}_{\mathrm{dip}}|$). The timescale τ_{mag} is elsewhere know as the Joule timescale and has previously been used in the hot Jupiter context as the timescale of simplified linear Rayleigh drag prescriptions of the Lorentz force (e.g., Perna *et al.*, 2010; Showman & Polvani, 2011; Rauscher & Menou, 2013; Perez-Becker & Showman, 2013). While Rogers & Komacek (2014) and Rogers (2017) found that Equation (1.38) qualitatively agrees with their simulations, this criterion is difficult to interpret. Not least because the reversals are expected to be caused by the atmospheric toroidal field, yet this criterion applies to the deep-seated dipolar field. The explanation of this disconnect is plausibly linked to the aforementioned Menou (2012*a*) scaling law that connects the magnitudes of the two field components via $|B_\phi| \sim R_m|\mathbf{B}_{\mathrm{dip}}|$, but requires a greater level of understanding. Another gap in understanding comes from the fact that

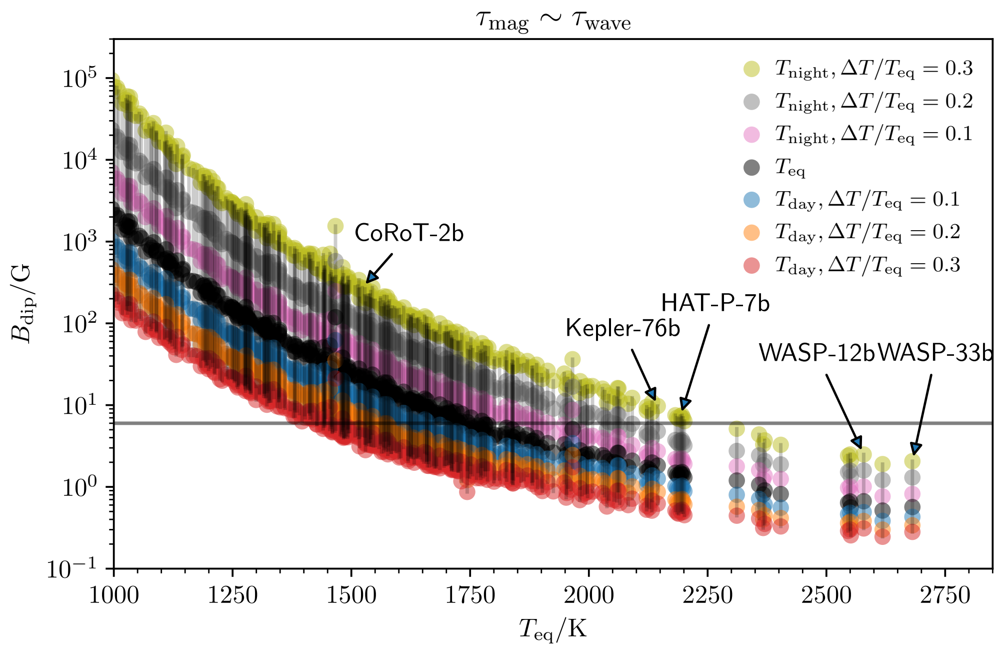

Figure 1.18: $B_{\rm dip}$ for which $\tau_{\rm mag} \sim \tau_{\rm wave}$ (as in Rogers, 2017) for the exoplanet.eu dataset. In this comparison $c_g = (\mathcal{R}T_{\rm eq})$ is taken (see Chapter 2 or Chapter 7 for explaination), ρ is calculated using the ideal gas law, and η is calculated using the method used by Rauscher & Menou (2013) and Rogers & Komacek (2014) (see Chapter 7 for details) for a depth of $P = 10\,\rm mbar$. For $T_{\rm day}$ and $T_{\rm night}$ we use dayside and nightside root mean squared values, assuming a sinusoidal longitudinal temperature distribution (i.e., $T_{\rm day} = T_{\rm eq} + \Delta T/\sqrt{2}$ and $T_{\rm night} = T_{\rm eq} - \Delta T/\sqrt{2}$). The reference line marks 6 G, the prediction of HAT-P-7b's critical reversal dipole field strength in Rogers & Komacek (2014) and Rogers (2017).

the η choice that Rogers (2017) found was appropriate for agreement between this scaling and HAT-P-7b simulations corresponds to the nightside temperatures (see Figure 1.18). This is in contrast to the naive expectation that, since hotspot variations are a dayside phenomenon, the magnetohydrodynamics responsible for hotspot variations should be tied to dayside quantities. These questions point to the need for detailed study of the reversal phenomenon.

1.4.4 Our aims and approach

The aim of this study is to clarify the role the atmospheric toroidal field has on the equatorial dynamics of the hottest hot Jupiters, with a particular focus on understanding the magnetically-driven wind/hotspot reversal process. Many of the main characteristics of this process, and the MHD of hot Jupiter atmospheres in general, have already been identified by the sophisticated three-dimensional MHD simulations of Rogers & Komacek (2014) and Rogers (2017). However, in order to complete a hierarchical understanding of the role of magnetism in hot Jupiter atmospheres, investigations with reduced-physics process models are also needed. To date, no such simplified atmospheric model, with consistent MHD treatments, have been applied to hot Jupiter atmospheres. This, combined with the recent development of exoplanetary meteorological techniques that make such reversals observable, make this study novel, timely, and necessary for theoretical development.

Our reduced-physics approach will consist of applying a two-layer shallow-water MHD (SWMHD) model that is adapted from the single layer SWMHD model of Gilman (2000). The model we construct has a pseudo-thermal forcing treatment like the hydrodynamic shallow-water models that have proved most successful for modelling the atmospheres of cooler hot Jupiters (e.g., Shell & Held, 2004; Langton & Laughlin, 2007; Showman & Polvani, 2010, 2011; Perez-Becker & Showman, 2013). Since the wind/hotspot reversal phenomenon is expected to be driven by the dynamics local to the equatorial region, we use an equatorial-beta plane approximation, which allows the equatorial dynamics to be described in Cartesian geometry. This two-layer Cartesian SWMHD model is expected to be the simplest possible model that contains the necessary physics to capture the reversal process, as it is thought to depend on the interactions between rotation, magnetism, and thermally-driven shallow-water waves.

In Chapter 2, we outline this SWMHD model and the fundamental assumptions, features, and conservational properties that underpin it. In this chapter we also discuss relevant parameters (both dimensional and non-dimensional) to highlight the regions of magnetohydrodynamic parameter space that relevant hot Jupiter atmospheres occupy. In Chapter 3, we apply linear theory of SWMHD to the parameter space of a typical ultra-hot Jupiter (HAT-P-7b) to provide an indication of the expected atmospheric wave dynamics that is likely to be important. In Chapter 4, we use non-linear simulations of the SWMHD model to study if and how the hotspot/wind reversal phenomenon can be described in the shallow-layer limit. Following this, in Chapter 5 we use the findings of these simulations to develop the linear theory of the reversals. In Chapter 7 we discuss the consequences that our study's results have on past and future observations of westward hotspots on hot Jupiters, before summarising our conclusions and directions of future work and potential progress in Chapter 8.

1.4.5 Statement on publications

At the time of writing, the work in this thesis has been the topic of three papers: one published (Hindle *et al.*, 2019) and two recently submitted (to the Astrophysical Journal and Astrophysical Journal Letters). Hindle *et al.* (2019) is predominantly a proof of concept paper. It presents the numerical SWMHD model outlined in Chapter 2, a brief numerical comparison between shallow-water hydrodynamic and SWMHD solutions, and a conjecture about wave modifications based on qualitative similarities between numerical solutions and equatorial wave modifications in the weakly-magnetic limit (as discussed in Chapter 3). In the work submitted to the Astrophysical Journal (ApJ; resubmitted May 2021), we present detailed non-linear numerical and linear semi-analytic analyses of the SWMHD model, identifying the physical mechanism that drives hotspot reversals, how it relates to wave dynamics, magnetic hotspot reversal thresholds, and how the findings relate to three-dimensional MHD models (contents in Chapters 4 to 6). The contents of the letter submitted to Astrophysical Journal Letters (to be resubmitted in the near future) is predominantly contained within Chapter 7, which discusses the consequences of our findings on observations of westward hotspots.

Chapter 2

A Cartesian SWMHD Model for Hot Jupiter Atmospheres

In this chapter we construct a *reduced gravity* shallow-water magnetohydrodynamic (SWMHD) model from first principles, with the purpose of modelling the dominant large scale atmospheric dynamics present in hot Jupiter atmospheres. The model is based on the single-layer SWMHD model of Gilman (2000), but in the so-called reduced gravity geometry (e.g., Vallis, 2006). The reduced gravity SWMHD model is the MHD analogue of its hydrodynamic namesake, which is a stacked two-layer shallow-water model with a dynamic layer sitting above an inactive abyssal layer.

The purpose of this SWMHD model is not to exactly capture the detailed dynamics of hot Jupiter atmospheres. This could be done to far higher degrees of accuracy by using simulations of the full three-dimensional MHD equations (as in Rogers & Komacek, 2014; Rogers, 2017; Rogers & McElwaine, 2017). Rather, we are interested in developing scientific understanding of the fundamental dynamical processes present in hot Jupiter atmospheres (specifically, hotspot reversals). In Chapter 1 we introduced shallow-water (hydrodynamic) models, highlighting that they are amongst the simplest useful models for studying atmospheric flows. Their simplicity is useful for intuition as various processes can be isolated and/or related to the system's conservational properties. However, they can also capture the leading order atmospheric physics: gravity, rotation, simple stratification, and (for thermally-ionised atmospheres) magnetism, so are sophisticated enough to be useful. In the past, hydrodynamic versions of the model we develop have proved important for developing theoretical understanding of hot Jupiter atmospheres and are consistent with observations up to the point where magnetic fields become significant (e.g., Langton & Laughlin, 2007; Showman & Polvani, 2010; Showman *et al.*, 2013; Perez-Becker & Showman, 2013).

For completeness and future comparison, we outline the derivations of single-layer shallow-water models in Section 2.1. The hydrodynamic version of this (Section 2.1.1) is well-studied and often features in atmospheric fluid dynamics textbooks (e.g., Vallis, 2006); whereas Gilman (2000) presented the single-layer SWMHD model (Section 2.1.2) comparatively recently. In Section 2.2 we develop the reduced gravity SWMHD model from first principles. First, in Section 2.2.1, we outline the derivation of the hydrodynamic reduced gravity shallow-water equations. Then, in Section 2.2.2, we show how it can be extended to include MHD. In the remainder of Section 2.2 we highlight how rotation, diffusion, and pseudo-thermal forcing treatments relevant to the hot Jupiter system can be included. Once the full system of governing equations has been established, we provide a discussion on conservation laws, appropriate boundary treatments, and parameter choices.

2.1 Single layer shallow-water models

2.1.1 Derivation of the hydrodynamic single-layer shallow-water model

Standard homogeneous single-layer shallow-water models are described by a thin fluid layer of constant density, ρ. Generally, the layer is bounded above by a free surface at $z = S_t(x, y, t)$ and below by a rigid surface at $z = S_b(x, y)$. However, for convenience, we consider the case with no bottom topography, where $S_b = 0$ and the layer thickness is given by $h(x, y, t) = S_t(x, y, t)$. The fluid above the shallow-layer is assumed to have negligible density[1] and so has negligible inertia (see Figure 2.1).

We seek a reduced set of governing shallow-water equations from the three-dimensional fluid equations that describe the evolution of this system. We illustrate this using Cartesian coordinates, taking the active layer to have the horizontal coordinates $-L_x \leq x \leq L_x$ and $-L_y \leq y \leq L_y$, and the vertical coordinate $0 \leq z \leq h(x, y, t)$. The axes are orientated so that they rotate with a vertically-aligned angular velocity, which is taken to be time independent and antiparallel to the constant gravitational acceleration, $-g\widehat{\mathbf{z}}$. Recall from Chapter 1 that taking the angular velocity vector to be $\mathbf{\Omega} = \mathit{\Omega} \sin\theta \widehat{\mathbf{z}}$, where $\mathit{\Omega}$ is the planetary rotation rate and θ denotes latitude, is known as the traditional approximation and is valid in the limit of strongly stable stratification, $N^2/\mathit{\Omega}^2 \gg 1$, which we show to be valid for our parameter choices in Section 2.2.10. In the hydrodynamic limit, inviscid constant density flows satisfy

$$\frac{\partial \mathbf{u}_3}{\partial t} + (\mathbf{u}_3 \cdot \nabla_3)\mathbf{u}_3 + \mathbf{f} \times \mathbf{u}_3 = -\frac{1}{\rho}\nabla_3 p - g\widehat{\mathbf{z}}, \tag{2.1}$$

$$\nabla_3 \cdot \mathbf{u}_3 = 0, \tag{2.2}$$

where $\mathbf{u}_3 \equiv (u, v, w)$ is the three-dimensional velocity, $\nabla_3 \equiv (\partial_x, \partial_y, \partial_z)$ is the three-dimensional gradient operator, and $\mathbf{f} \equiv f\widehat{\mathbf{z}} \equiv 2\mathit{\Omega} \sin\theta \widehat{\mathbf{z}}$. The time independent Coriolis parameter, f, is allowed to vary in the horizontal direction only (see Section 2.2.3 for discussion on form). Equation (2.1), the three-dimensional *momentum equation*, evolves the system in a manner that conserves (specific) momentum; whereas Equation (2.2), the three-dimensional *incompressibility condition*, ensures the conservation of mass in the constant density layer.

Single layer shallow-water momentum equation

In the so-called *shallow-water limit* $(H/L \ll 1)$[2], the typical horizontal length scale, L, is much larger than the vertical length scale of the layer, H. Therefore, if the ratios

[1] If the density of the fluid layer above cannot be considered negligible, multi-layered models should be considered.

[2] Recall from Chapter 1 that typically $H/L \sim 10^{-2}$ in hot Jupiter atmospheres (see Figure 1.10).

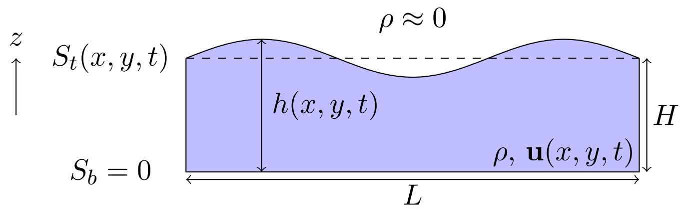

Figure 2.1: A schematic of a hydrodynamic single-layer shallow-water model, which has a constant density active layer and is bounded by a free material surface from above and a rigid surface (with no bottom topography) below.

of the vertical and horizontal velocity field magnitudes are assumed to scale with their spatial scales (i.e., $|w|/|u| \sim H/L$ and $|w|/|v| \sim H/L$), then, to leading order, vertical advections and can be neglected for all time and the hydrostatic approximation is valid (see Chapter 1). Consequently, the vertical component of the three-dimensional momentum equation simplifies and the pressure, p, can be described by hydrostatic balance:

$$\frac{\partial p}{\partial z} = -\rho g, \tag{2.3}$$

for all time. This balance allows vertical dependence to be integrated out of the governing equations. Integrating Equation (2.3) with respect z yields

$$p(x, y, z, t) = -\rho g z + P_0(x, y, t). \tag{2.4}$$

Since the weight of the fluid above the upper interface is negligible, $p = 0$ at $z = S_t = h$. Therefore, $P_0 = \rho g h$, giving

$$p(x, y, z) = \rho g(h - z). \tag{2.5}$$

Using this explicit form for the pressure and the horizontal components of Equation (2.1), one can write the *shallow-water momentum equation* in a rotating reference frame as

$$\frac{\mathrm{D}\mathbf{u}}{\mathrm{D}t} + f\widehat{\mathbf{z}} \times \mathbf{u} = -g\nabla h, \tag{2.6}$$

where $\mathbf{u} \equiv (u, v)$ is the horizontal velocity, $\nabla \equiv (\partial_x, \partial_y)$ is the horizontal gradient operator, and $\mathrm{D}/\mathrm{D}t \equiv \partial/\partial t + \mathbf{u} \cdot \nabla$ is the horizontal Lagrangian time derivative operator (or material derivative). Note that $\mathrm{D}\mathbf{u}/\mathrm{D}t$ does not include horizontal advections due to vertical dependences in the horizontal velocity (i.e., $\mathrm{D}\mathbf{u}/\mathrm{D}t$ contains no $w\partial\mathbf{u}/\partial z$ component). This is because the non-advective terms are independent of z, so an initially vertically-independent flow will remain vertically-independent for all time. Consequently, all spatial differential operators will henceforth be two-dimensional unless stated otherwise with a subscript (e.g., ∇_3, $\mathbf{u}_3$, $\mathbf{B}_3$).

Shallow-water continuity equation

The time evolution of h can be recovered from the three-dimensional incompressibility condition, which can be written as

$$\frac{\partial w}{\partial z} = -\nabla \cdot \mathbf{u}. \tag{2.7}$$

Since the righthand side of Equation (2.7) is independent of z, it can be integrated from the bottom of the fluid layer to the free surface, yielding

$$[w]_{z=S_b}^{z=S_t} = -h\nabla \cdot \mathbf{u}. \tag{2.8}$$

The horizontal flow is independent of z so a test particle on the free surface will remain there so $\mathrm{D}S_t/\mathrm{D}t = w|_{z=S_t}$ (i.e., the free surface is a material surface). In this model we choose the bottom surface to be rigid so $w|_{z=S_b} = \mathrm{D}S_b/\mathrm{D}t = 0$. Therefore,

$$[w]_{z=S_b}^{z=S_t} = \frac{\mathrm{D}(S_t - S_b)}{\mathrm{D}t} = \frac{\mathrm{D}S_t}{\mathrm{D}t} \equiv \frac{\mathrm{D}h}{\mathrm{D}t}. \tag{2.9}$$

Together Equations (2.8) and (2.9) give the *shallow-water continuity equation*:

$$\frac{\mathrm{D}h}{\mathrm{D}t} + h\nabla \cdot \mathbf{u} = 0 \qquad \Longleftrightarrow \qquad \frac{\partial h}{\partial t} + \nabla \cdot (h\mathbf{u}) = 0. \tag{2.10}$$

The shallow-water momentum and continuity equations govern the time evolution of $\mathbf{u}$ and h. These are both vertically independent and w does not influence their evolution.

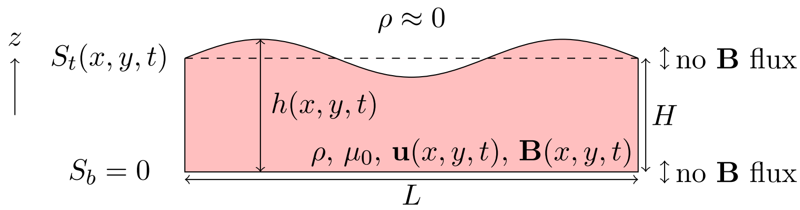

Figure 2.2: A schematic of a single-layer SWMHD model, which has constant density and magnetic permeability in the active layer. The active layer is bounded by a free surface from above and by a rigid surface (with no bottom topography) below.

However, w is generally non-zero and evolves in order to satisfy three-dimensional incompressibility (i.e., mass conservation of the fluid column). It can be found by integrating Equation (2.7) with respect to the vertical coordinate. In this system, which has a rigid bottom surface at $z = 0$ with no topography, $w(x, y, z, t) = -(\nabla \cdot \mathbf{u})z$. Hence, in the shallow-water limit the initial assumption, $|w|/|\mathbf{u}| \sim H/L \ll 1$, is justified and horizontal velocities are vertically independent (if they are initially, see above). In this context, taking these self-consistent assumptions in unison, alongside the free surface boundary conditions, is often known as the *shallow-water approximation*.

2.1.2 Derivation of the single-layer SWMHD model

Gilman (2000) showed that a similar single-layer SWMHD model can be derived in the shallow-water limit. Here we outline the derivation for reference in Section 2.2.2.

If the same setup that we used in Section 2.1.1 is taken for an electrically-conducting, rotating, constant density fluid (see Figure 2.2), with constant magnetic permeability, μ_0, in the active layer and no diffusion (i.e., the flow is inviscid and perfectly conducting), the three-dimensional governing fluid equations become

$$\frac{\partial \mathbf{u}_3}{\partial t} + (\mathbf{u}_3 \cdot \nabla_3)\mathbf{u}_3 + \mathbf{f} \times \mathbf{u}_3 = -\frac{1}{\rho}\nabla_3 p - g\widehat{\mathbf{z}} + \frac{1}{\rho}\mathbf{J}_3 \times \mathbf{B}_3, \tag{2.11}$$

$$\nabla_3 \cdot \mathbf{u}_3 = 0, \tag{2.12}$$

$$\frac{\partial \mathbf{B}_3}{\partial t} = \nabla_3 \times (\mathbf{u}_3 \times \mathbf{B}_3) \equiv (\mathbf{B}_3 \cdot \nabla_3)\mathbf{u}_3 - (\mathbf{u}_3 \cdot \nabla_3)\mathbf{B}_3, \tag{2.13}$$

$$\nabla_3 \cdot \mathbf{B}_3 = 0. \tag{2.14}$$

where $\mathbf{B}_3 \equiv (b_x, b_y, b_z)$ is the three-dimensional magnetic field and $\mathbf{J}_3 \equiv (\nabla_3 \times \mathbf{B}_3)/\mu_0$ is the current density. Equation (2.13), the *induction equation*, is derived from the Maxwell equations in the non-relativistic limit and governs the evolution of the magnetic field. Equation (2.14) is *Gauss' law* of magnetism, which excludes magnetic monopoles by maintaining a divergence-free three-dimensional magnetic field. By taking the divergence of the induction equation, one can easily show that

$$\frac{\partial(\nabla_3 \cdot \mathbf{B}_3)}{\partial t} = 0, \tag{2.15}$$

so if Equation (2.14) holds initially, it holds for all time.

Shallow-water induction equation

From the righthand form of Equation (2.13) one can see that, if horizontal velocity fields are vertically independent (as in the hydrodynamic shallow-water setting) and horizontal magnetic fields are initially vertically independent, the horizontal magnetic fields remain vertically independent for all time. Therefore, the horizontal components of Equation (2.13) give the *shallow-water induction equation*:

$$\frac{\partial \mathbf{B}}{\partial t} = (\mathbf{B} \cdot \nabla)\mathbf{u} - (\mathbf{u} \cdot \nabla)\mathbf{B}, \tag{2.16}$$

where $\mathbf{B} \equiv (B_x, B_y) = (b_x/\sqrt{\mu_0 \rho}, b_y/\sqrt{\mu_0 \rho})$ is the vertically-independent horizontal magnetic field, which, since μ_0 and ρ are both constant, we write in units of velocity for convenience. Writing the horizontal magnetic field in velocity units, highlights the equivalence between magnetic fields and Alfvén velocities in SWMHD systems (up to a constant factor). We also comment that in the planetary setting $\mathbf{B}$ can be interpreted as the vertically-averaged (rescaled) horizontal magnetic field.

Shallow-water continuity equation

In SWMHD, while the three dimensional forms of the incompressibility condition and Gauss' law of magnetism remain satisfied, the horizontal divergences of $\mathbf{u}$ and $\mathbf{B}$ are generally non-zero and arise due to horizontal interface variations. In Section 2.1.1 we showed that in the hydrodynamic shallow-water model the three-dimensional incompressibility condition reduces to the shallow-water continuity equation (Equation (2.10)), which represents mass conservation in the fluid column. This remains unchanged in the single-layer SWMHD model as the assumptions used to derive it (i.e., $\mathbf{u}$ is vertically independent and the interfaces are material surfaces) remain valid.

Shallow-water divergence-free condition

To recover the shallow-water version of Gauss' law, we note that it can be rewritten as

$$\frac{\partial B_z}{\partial z} = -\nabla \cdot \mathbf{B}, \tag{2.17}$$

where $B_z = b_z/\sqrt{\mu_0 \rho}$ is the vertical magnetic field in velocity units (so is the vertical Alfvén velocity). Since the righthand side is independent of z, this can be integrated vertically (from the lower rigid surface at $z = S_b = 0$ to the upper free surface at $z = S_t = h$), giving

$$[B_z]_{z=S_b}^{z=S_t} = -h\nabla \cdot \mathbf{B}, \tag{2.18}$$

Alongside the hydrodynamic requirement that S_t and S_b are material surfaces, SWMHD allows no magnetic flux across the interfaces at $z = S_t(x, y, t) = h(x, y, t)$ and $z = S_b = 0$ (i.e., surface magnetic fields are fixed and parallel to the surfaces). Therefore, on the upper surface, $\mathbf{B}_3 \cdot \widehat{\mathbf{n}}_3 = \mathbf{B}_3 \cdot (\widehat{\mathbf{z}} - \nabla S_t) = 0$, where $\widehat{\mathbf{n}}_3 \equiv (\widehat{\mathbf{z}} - \nabla S_t)$ is the unit normal vector on the upper surface, so $B_z|_{z=S_t} = \mathbf{B} \cdot \nabla S_t = \mathbf{B} \cdot \nabla h$. Similarly, at the lower surface, $B_z|_{z=S_t} = \mathbf{B} \cdot \nabla S_b = 0$. Hence,

$$[B_z]_{z=S_b}^{z=S_t} = \mathbf{B} \cdot \nabla S_t - \mathbf{B} \cdot \nabla S_b = \mathbf{B} \cdot \nabla h. \tag{2.19}$$

This can be combined with Equation (2.18) to give the *SWMHD divergence-free condition*:

$$\nabla \cdot (h\mathbf{B}) = 0, \tag{2.20}$$

which is the shallow-water version of Gauss' law of magnetism and ensures that the horizontal magnetic flux through a vertically-independent fluid column is conserved. Before proceeding to derive the momentum equation for SWMHD we comment that

$$\begin{aligned}\nabla \times (\mathbf{u} \times h\mathbf{B}) &= -\nabla \cdot [h\mathbf{u}\mathbf{B} - h\mathbf{B}\mathbf{u}] \\ &= -[\mathbf{B}\nabla \cdot (h\mathbf{u}) + h(\mathbf{u} \cdot \nabla)\mathbf{B}] + [\mathbf{u}\nabla \cdot (h\mathbf{B}) + h(\mathbf{B} \cdot \nabla)\mathbf{u}] \\ &= h(\mathbf{B} \cdot \nabla)\mathbf{u} - h(\mathbf{u} \cdot \nabla)\mathbf{B} - \mathbf{B}\nabla \cdot (h\mathbf{u}) + \cancelto{0}{\mathbf{u}\nabla \cdot (h\mathbf{B})} \\ &= h(\mathbf{B} \cdot \nabla)\mathbf{u} - h(\mathbf{u} \cdot \nabla)\mathbf{B} - \mathbf{B}\nabla \cdot (h\mathbf{u}),\end{aligned} \tag{2.21}$$

where Equation (2.20) has been used in the last step and the divergence of the tensor product of two vectors is written in tensor notation as $[\nabla \cdot (\mathbf{ab})]_i = \partial(a_j b_i)/\partial x_j$ for $i, j = 1, 2$. From this, Equations (2.10) and (2.16) can be combined to yield (Mak, 2013)

$$\begin{aligned}\frac{\partial(h\mathbf{B})}{\partial t} &= h\frac{\partial \mathbf{B}}{\partial t} + \mathbf{B}\frac{\partial h}{\partial t} \\ &= h(\mathbf{B} \cdot \nabla)\mathbf{u} - h(\mathbf{u} \cdot \nabla)\mathbf{B} - \mathbf{B}\nabla \cdot (h\mathbf{u}) \\ &= \nabla \times (\mathbf{u} \times h\mathbf{B}),\end{aligned} \tag{2.22}$$

which highlights that

$$\frac{\partial}{\partial t}(\nabla \cdot (h\mathbf{B})) = 0, \tag{2.23}$$

so, if the divergence-free condition is initially satisfied, it is remains satisfied for all time.

Single layer SWMHD momentum equation

Finally, we seek the single-layer SWMHD version of the momentum equation. For this we note that the Lorentz force, $\mathbf{J}_3 \times \mathbf{B}_3$, can be re-expressed using

$$\mathbf{J}_3 \times \mathbf{B}_3 = \frac{1}{\mu_0}(\mathbf{B}_3 \cdot \nabla_3)\mathbf{B}_3 - \frac{1}{2\mu_0}\nabla_3(\mathbf{B}_3 \cdot \mathbf{B}_3), \tag{2.24}$$

which can be used to rewrite Equation (2.11) as

$$\frac{\partial \mathbf{u}_3}{\partial t} + (\mathbf{u}_3 \cdot \nabla_3)\mathbf{u}_3 + \mathbf{f} \times \mathbf{u}_3 = -\frac{1}{\rho}\nabla_3 P_T + g\widehat{\mathbf{z}} + \frac{1}{\mu_0 \rho}(\mathbf{B}_3 \cdot \nabla_3)\mathbf{B}_3, \tag{2.25}$$

where $P_T = p + (\mathbf{B}_3 \cdot \mathbf{B}_3)/2\mu_0$ is the total pressure (the sum of gas and magnetic pressure).

The MHD version of the shallow-water approximation is that both the ratios of the vertical and horizontal velocity field magnitudes and the ratios of the vertical and horizontal magnetic field magnitudes are assumed to scale with their spatial scales[3] (i.e., $|w|/|u| \sim H/L$, $|w|/|v| \sim H/L$, $|B_z|/|B_x| \sim H/L$, and $|B_z|/|B_y| \sim H/L$). Hence, in the shallow-water limit ($H/L \ll 1$), the leading order balance in the vertical component of Equation (2.25) is magneto-hydrostatic balance:

$$\frac{\partial P_T}{\partial z} = -\rho g. \tag{2.26}$$

This can be integrated with respect z to give

$$P_T = -\rho g z + P_0, \tag{2.27}$$

where P_0 is fixed by the requirement that the total pressure must be continuous. If we take the total pressure at the interface $z = S_t = h$ to be the arbitrary constant $P_{T,\mathrm{atm}}$, then

$$P_T = \rho g(h - z) + P_{T,\,\mathrm{atm}}. \tag{2.28}$$

We comment that, as P_T now includes the magnetic pressure, the arbitrary constant $P_{T,\,\mathrm{atm}}$ is not necessarily zero, though its actual value does not affect the system's evolution. Equation (2.28) can be used in the horizontal components of Equation (2.25) to form the momentum equation of single-layer SWMHD:

$$\frac{\mathrm{D}\mathbf{u}}{\mathrm{D}t} + \mathbf{f} \times \mathbf{u} = -g\nabla h + (\mathbf{B} \cdot \nabla)\mathbf{B}. \tag{2.29}$$

[3]No assumption is made about the magnitudes of the velocity fields relative to the magnetic fields or the gas pressure relative to the magnetic pressure.

The single-layer SWMHD momentum, continuity, and induction equations (i.e., Equations (2.10), (2.16) and (2.29)) govern the time evolution of $\mathbf{u}$, h, and $\mathbf{B}$, while maintaining the shallow-water divergence-free condition $\nabla\cdot(h\mathbf{B}) = 0$ for all time. All these variables are vertically independent, with neither w nor B_z influencing their evolution. In this system, which has a rigid bottom surface at $z = 0$ with no topography or magnetic fluxes, these can hypothetically be evaluated as $w(x, y, z, t) = -(\nabla \cdot \mathbf{u})z$ and $B_z(x, y, z, t) = -(\nabla \cdot \mathbf{B})z$ (by integrating Equations (2.7) and (2.17)).

2.2 The reduced gravity shallow-water model

Given their simplicity, the single-layer shallow water models of Section 2.1 can prove remarkably powerful in understanding the dynamics of atmospheres, particularly for the study of unforced wave dynamics (see Chapter 3). However — alongside the already included gravity, rotation, and magnetism — simple stratification is necessary for the inclusion of treatments that mimic the extreme thermal forcing present in the atmospheres of hot Jupiters (see Section 2.2.6). The two-layer model we use is the so-called reduced gravity model, which has proved a useful aid for understanding the atmospheric dynamics of hot Jupiters in the hydrodynamic setting (e.g., Langton & Laughlin, 2007; Showman & Polvani, 2010; Showman *et al.*, 2013; Perez-Becker & Showman, 2013). First, for completion and comparison, we outline the derivation of the reduced gravity shallow-water equations as found elsewhere (e.g., Vallis, 2006). Then, we proceed to extend the model by including relevant treatments of magnetism, rotation, pseudo-thermal forcing, and diffusion. Finally, we discuss conservation laws, appropriate horizontal boundary treatments, and parameter choices.

2.2.1 Derivation of the basic hydrodynamic reduced gravity model

The reduced gravity model (see Figure 2.3 for schematic) describes the motion of an active fluid layer, of thickness $h(x, y, t)$ and constant density ρ, which sits between two inactive fluid layers: the active fluid layer is bounded above by an inactive layer with

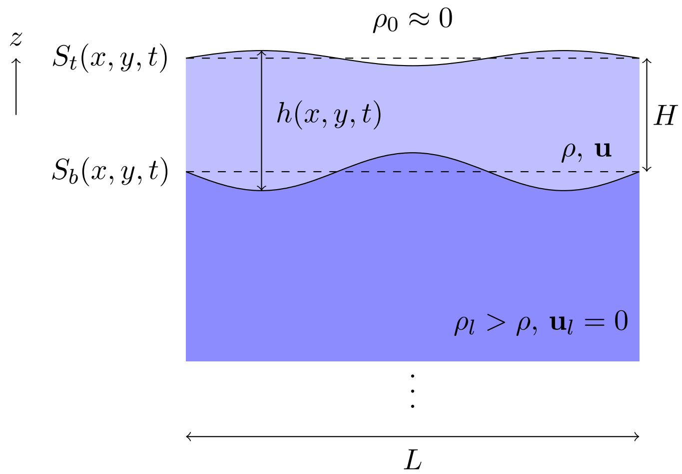

Figure 2.3: A schematic of a reduced gravity hydrodynamic shallow-water model, which has a constant density active layer and is bounded by above by a free surface and below by an infinitely-deep quiescent fluid layer.

negligible density[4] and below by an infinitely deep inactive lower layer with constant density, ρ_l, with $\rho_l > \rho$ for stable density stratification. The upper and lower interfaces, which are respectively found at $z = S_t(x, y, t)$ and $z = S_b(x, y, t)$, are material surfaces that are allowed to evolve freely with respect to the system's governing equations and interface conditions. The active layer thickness is defined as their difference, $h(x, y, t) = S_t(x, y, t) - S_b(x, y, t)$ and has the rest-state thickness, H.

Reduced gravity shallow-water momentum equation

As in the single-layer models of Section 2.1, in the shallow-water limit ($H/L \ll 1$) the shallow-water approximation can be employed to reduce the vertical component of the three-dimensional momentum equation to the hydrostatic equation:

$$\frac{\partial p}{\partial z} = -\rho g, \tag{2.30}$$

where p is the pressure, which is continuous across the model's interfaces. Since the weight of the fluid above the upper surface is negligible, $p = 0$ at $z = S_t(x, y, t)$. Integrating the

[4]This is the same as the upper boundary in the single-layer model. The layer above the upper boundary has negligible density so pressure gradients cannot form and the layer is inactive.

hydrostatic equation down from the upper surface, with this condition, yields

$$p(x, y, z, t) = g\rho(S_t - z). \tag{2.31}$$

Therefore, in the active layer, the horizontal pressure gradient is given by $\nabla p/\rho = g\nabla S_t$ and the shallow water momentum equation becomes

$$\frac{\mathrm{D}\mathbf{u}}{\mathrm{D}t} + \mathbf{f} \times \mathbf{u} = -g\nabla S_t, \tag{2.32}$$

where $\mathbf{u}$ is the horizontal velocity in the active layer. In the lower layer, the pressure is given by the weight of the fluid above it, so integrating the hydrostatic equation down from the upper surface yields

$$p(x, y, z, t) = g\rho(S_t - S_b) + g\rho_l(S_b - z). \tag{2.33}$$

Since the lower layer is taken to be motionless, the horizontal pressure gradient in this layer is zero (see Equation (2.1)). Hence

$$g\rho\nabla(S_t - S_b) + g\rho_l\nabla S_b = 0. \tag{2.34}$$

This can be re-expressed as

$$g\rho\nabla S_t = -g'\rho\nabla S_b, \tag{2.35}$$

where $g' \equiv g(\rho_l - \rho)/\rho$ is the *reduced gravity* as defined in Vallis (2006). Using Equation (2.35), the shallow-water momentum equation becomes

$$\frac{\mathrm{D}\mathbf{u}}{\mathrm{D}t} + \mathbf{f} \times \mathbf{u} = g'\nabla S_b. \tag{2.36}$$

Furthermore, one can rewrite the shallow-water momentum equation in terms of the active layer thickness, $h = S_t - S_b$, by noting that Equation (2.34) also gives $\nabla S_b = -(\rho/\rho_l)\nabla h$.

Hence,

$$\frac{\mathrm{D}\mathbf{u}}{\mathrm{D}t} + \mathbf{f} \times \mathbf{u} = -g^* \nabla h, \tag{2.37}$$

where $g^* \equiv g'\rho/\rho_l = g(\rho_l - \rho)/\rho_l$ is the reduced gravity as defined in Perez-Becker & Showman (2013). Writing the shallow-water momentum equation in this way provides a straightforward coupling to the mass conservation equation.

Before continuing with the derivation, we note that dividing Equation (2.35) by ρg gives the relation

$$\nabla S_t = -\frac{\rho_l - \rho}{\rho} \nabla S_b, \tag{2.38}$$

which, for $\rho_l > \rho$, implies that the upper and lower boundaries of the active layer bow in opposite directions. Further, it is generally assumed that the layers have comparable densities, in which case $|\nabla S_t| \ll |\nabla S_b|$ (i.e., displacements in the upper surface are smaller than those of the lower layer). These two properties ensure that, in the lower layer, the total mass of a fluid column above a given depth is constant (see Figure 2.3).

Shallow-water continuity equation

As in the single-layer model of Section 2.1.1, this can be derived from integrating the three-dimensional incompressibility condition with respect to z, which gives

$$[w]_{z=S_b}^{z=S_t} = -h \nabla \cdot \mathbf{u}. \tag{2.39}$$

As in Section 2.1.1, S_t is a free material surface so $\mathrm{D}S_t/\mathrm{D}t = w|_{z=S_t}$. However, in the reduced gravity model S_b is also a free material surface so $\mathrm{D}S_b/\mathrm{D}t = w|_{z=S_b}$ is generally non-zero, giving

$$[w]_{z=S_b}^{z=S_t} = \frac{\mathrm{D}S_t}{\mathrm{D}t} - \frac{\mathrm{D}S_b}{\mathrm{D}t} = \frac{\mathrm{D}(S_t - S_b)}{\mathrm{D}t} \equiv \frac{\mathrm{D}h}{\mathrm{D}t}, \tag{2.40}$$

which can be combined with Equation (2.39) to yield the shallow-water continuity equation:

$$\frac{\partial h}{\partial t} + \nabla \cdot (h\mathbf{u}) = 0, \tag{2.41}$$

though in the reduced gravity model $h = S_t - S_b$ (rather than $h = S_t$).

The system's evolution is fully described by Equations (2.37) and (2.41). As in the single-layer model, w is generally non-zero in the active layer and evolves in order to satisfy three-dimensional incompressibility, $\partial w/\partial z = -\nabla \cdot \mathbf{u}$. However, in the reduced gravity geometry w is not specified explicitly (and, generally, nor is the z-origin). To get a gauge of its magnitude, we are free to fix $z = 0$ as the average position of S_t at a given point in time. With this choice, three-dimensional incompressibility gives $w = w|_{z=S_t} - (\nabla \cdot \mathbf{u})z$. As before, $w|_{z=S_t} = \mathrm{D}S_t/\mathrm{D}t$ and $w|_{z=S_b} = \mathrm{D}S_b/\mathrm{D}t$, so

$$w|_{z=S_b} = \frac{\mathrm{D}S_b}{\mathrm{D}t} = \frac{\mathrm{D}S_t}{\mathrm{D}t} - (\nabla \cdot \mathbf{u})z. \tag{2.42}$$

We showed above that $|\nabla S_t| \ll |\nabla S_b|$ for layers of comparable density, so vertical velocities at $z = S_b$ are expected to be dominated by the last term in the far righthand side of Equation (2.42), giving $|w|/|\mathbf{u}| \sim H/L \ll 1$, as required.

2.2.2 Derivation of the basic reduced gravity SWMHD model

The reduced gravity model can be extended to SWMHD by considering the magnetohydrodynamics of a perfectly-conducting, inviscid, active fluid layer, with constant density and magnetic permeability, that sits upon a denser infinitely-deep inactive fluid layer and is bounded above by a free surface of negligible density. We permit no magnetic flux across the material surfaces at $z = S_t(x, y, t)$ and $z = S_b(x, y, t)$, and enforce continuous total pressure to derive the system's governing equations. As in the hydrodynamic version of this system, the active layer thickness is defined as their difference, $h(x, y, t) = S_t(x, y, t) - S_b(x, y, t)$, and has the rest-state thickness, H (see Figure 2.4).

Reduced gravity SWMHD momentum equation

Like the hydrodynamic model, the inactive lower layer in the MHD model has no flow ($\mathbf{u}_l = 0$). Hence, the lower layer is purely magneto-hydrostatic for all time. In the shallow-water limit ($H/L \ll 1$), the SWMHD approximation (see Section 2.1.2) applies

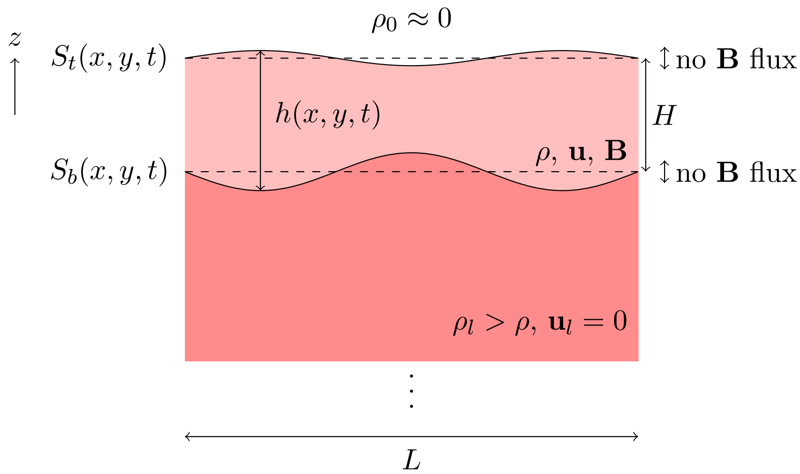

Figure 2.4: A schematic of a reduced gravity layer SWMHD model, which has a constant density active layer and is bounded above by a free surface and below by an infinitely-deep quiescent fluid layer.

to the active layer, yielding a leading order magneto-hydrostatic balance:

$$\frac{\partial P_T}{\partial z} = -\rho g, \tag{2.43}$$

where P_T is the total pressure as defined in Section 2.1.2. Integrating down from $z = S_t$ and taking the total pressure to be continuous, with $P_T = P_{T,\,\mathrm{atm}}$ at $z = S_t$, for the arbitrary constant $P_{T,\,\mathrm{atm}}$, gives

$$P_T = \rho g(S_t - z) + P_{T,\,\mathrm{atm}}, \tag{2.44}$$

in the active layer. Therefore, in the active layer, horizontal gradients in the total pressure can be expressed as

$$\frac{1}{\rho}\nabla P_T = g\nabla S_t. \tag{2.45}$$

As discussed above, the inactive lower layer also satisfies the magneto-hydrostatic equation. Integrating down from $z = S_t$ and enforcing continuous total pressure yields

$$P_T = \rho g(S_t - S_b) + \rho_l g(S_b - z) + P_{T,\,\mathrm{atm}}, \tag{2.46}$$

in the inactive lower layer. Noting that, since the lower layer is inactive it has no horizontal pressure gradients, gives

$$\rho g \nabla (S_t - S_b) + \rho_l g \nabla S_b = 0, \tag{2.47}$$

which can be rearranged identically to the hydrodynamic surface gradient relation in Section 2.1.2 to produce $\nabla S_t = (\rho_l - \rho)/\rho_l \nabla h$. Hence, Equation (2.45) can be used in the horizontal components of Equation (2.25) to give the reduced gravity SWMHD momentum equation:

$$\frac{\mathrm{D}\mathbf{u}}{\mathrm{D}t} + \mathbf{f} \times \mathbf{u} = -g^* \nabla h + (\mathbf{B} \cdot \nabla)\mathbf{B}, \tag{2.48}$$

where $g^* \equiv g(\rho_l - \rho)/\rho_l$ is the same reduced gravity defined in Section 2.1.2.

Continuity equation

Since $\mathbf{u}$ is vertically independent and the layer interfaces are material surfaces, the derivation of the shallow-water continuity equation used in Section 2.2.1 can be repeated to give

$$\frac{\partial h}{\partial t} + \nabla \cdot (h\mathbf{u}) = 0. \tag{2.49}$$

Induction equation

As in Section 2.1.2, vertically independent horizontal velocity fields and initially vertically independent horizontal magnetic fields result in horizontal magnetic fields that remain vertically independent for all time. Therefore, in the active layer of the reduced gravity SWMHD model, the shallow-water induction equation is mathematically identical to the single-layer shallow-water induction equation:

$$\frac{\partial \mathbf{B}}{\partial t} = (\mathbf{B} \cdot \nabla)\mathbf{u} - (\mathbf{u} \cdot \nabla)\mathbf{B}. \tag{2.50}$$

Divergence-free condition

As in the single-layer SWMHD model, integrating Gauss' law with from $z = S_b$ to $z = S_t$ yields

$$[B_z]_{z=S_b}^{z=S_t} = -h\nabla \cdot \mathbf{B}. \tag{2.51}$$

Prohibiting magnetic flux across the (now free) interfaces gives

$$[B_z]_{z=S_b}^{z=S_t} = \mathbf{B} \cdot \nabla S_t - \mathbf{B} \cdot \nabla S_b = \mathbf{B} \cdot \nabla (S_t - S_b) \equiv \mathbf{B} \cdot \nabla h. \tag{2.52}$$

Together Equations (2.51) and (2.52) give the SWMHD divergence-free condition:

$$\nabla \cdot (h\mathbf{B}) = 0. \tag{2.53}$$

As shown in Section 2.1.1, Equations (2.50) and (2.53) can be combined to yield the following two useful forms for horizontal columnar magnetic flux evolution:

$$\begin{aligned} \frac{\partial (h\mathbf{B})}{\partial t} &= -\nabla \cdot [h\mathbf{u}\mathbf{B} - h\mathbf{B}\mathbf{u}] \\ &= \nabla \times (\mathbf{u} \times h\mathbf{B}). \end{aligned} \tag{2.54}$$

The conservative form of Equation (2.54) highlights that the total horizontal magnetic flux, $h\mathbf{B}$, is conserved within the active layer; while, writing Equation (2.54) as the curl of the vertically-aligned vector $\mathbf{u} \times h\mathbf{B}$, highlights that

$$\frac{\partial}{\partial t}(\nabla \cdot (h\mathbf{B})) = 0. \tag{2.55}$$

This states that if the divergence-free condition is initially satisfied, it remains satisfied for all time.

Magnetic flux function

As a requirement of SWMHD is that the horizontal columnar magnetic flux, $h\mathbf{B}$, is solenoidal, it is useful to define it as the curl of a vector potential (e.g., Dellar, 2002, for a single-layer model):

$$h\mathbf{B} \equiv \nabla \times A\widehat{\mathbf{z}}, \tag{2.56}$$

where A is the magnetic flux function and $\nabla \times \cdot \widehat{\mathbf{z}} \equiv (\partial_y, -\partial_x)$ represents the curl of a scalar field about the vertical coordinate. We comment that the magnetic flux function definition differs from the two-dimensional magnetic vector potential through the inclusion of h in Equation (2.56).[5] This arises as the magnetic flux function describes the vertically-integrated horizontal magnetic field over the whole fluid column ($h\mathbf{B}$), rather than simply the horizontal magnetic field at a specific vertical level ($\mathbf{B}$). Using this definition, one finds $(\mathbf{u} \times h\mathbf{B}) = -(\mathbf{u} \cdot \nabla)A\widehat{\mathbf{z}}$. Therefore, "uncurling" Equation (2.54) yields

$$\frac{\mathrm{D}A}{\mathrm{D}t} \equiv \frac{\partial A}{\partial t} + (\mathbf{u} \cdot \nabla)A = 0. \tag{2.57}$$

That is, A is a materially conserved quantity. This property of SWMHD is also inherent to the single-layer system of Section 2.1.1 (Dellar, 2002). The material conservation of A useful for intuition as it highlights that lines of constant A ($h\mathbf{B}$ field lines) are simply advected through the system.

Columnar horizontal momentum

Another consequence of the divergence-free condition is that it can be used to write the momentum equation in terms of specific columnar horizontal momentum, $h\mathbf{u}$. For this Equations (2.48), (2.49) and (2.53) can be combined to yield

$$\frac{\partial (h\mathbf{u})}{\partial t} + \nabla \cdot \left[h\mathbf{u}\mathbf{u} - h\mathbf{B}\mathbf{B} + \tfrac{1}{2}g^* h^2 \mathbf{I}\right] = fh\mathbf{u} \times \widehat{\mathbf{z}}. \tag{2.58}$$

where $\mathbf{I}$ is the 2×2 identity matrix and the divergence of the tensor product of two vectors is written in tensor notation as $[\nabla \cdot (\mathbf{ab})]_i = \partial(a_j b_i)/\partial x_j$ for $i, j = 1, 2$. Equation (2.58) highlights that, in the absence of rotation ($f = 0$), $h\mathbf{u}$ is conserved within the active layer.

[5] In the two-dimensional limit, where h is taken to be a constant, the definitions become equivalent.

Summary

In summary, in the inviscid, perfectly-conducting, unforced reduced gravity SWMHD model, the time evolution of the active layer variables: $\mathbf{u}(x, y, t)$, the active layer horizontal velocity; $h(x, y, t)$, the active layer thickness; and $\mathbf{B}(x, y, t)$, the active layer horizontal magnetic field (in velocity units) is governed by the following set of equations:

$$\frac{\mathrm{D}\mathbf{u}}{\mathrm{D}t} + f\widehat{\mathbf{z}} \times \mathbf{u} = -g^*\nabla h + (\mathbf{B}\cdot\nabla)\mathbf{B}, \tag{2.59a}$$

$$\frac{\partial h}{\partial t} + \nabla\cdot(h\mathbf{u}) = 0, \tag{2.59b}$$

$$\frac{\mathrm{D}\mathbf{B}}{\mathrm{D}t} \equiv \frac{\partial \mathbf{B}}{\partial t} + (\mathbf{u}\cdot\nabla)\mathbf{B} = (\mathbf{B}\cdot\nabla)\mathbf{u}, \tag{2.59c}$$

which maintains the shallow-water divergence-free condition, $\nabla\cdot(h\mathbf{B}) = 0$, for all time. The conserved quantities of the system are h, $h\mathbf{B}$, and, in the absence of rotation, $h\mathbf{u}$. It can therefore be useful to replace Equations (2.59a) and (2.59c) with

$$\frac{\partial(h\mathbf{u})}{\partial t} + \nabla\cdot\left[h\mathbf{u}\mathbf{u} - h\mathbf{B}\mathbf{B} + \tfrac{1}{2}g^*h^2\mathbf{I}\right] = fh\mathbf{u}\times\widehat{\mathbf{z}}, \tag{2.60a}$$

$$\frac{\partial(h\mathbf{B})}{\partial t} + \nabla\cdot\left[h\mathbf{u}\mathbf{B} - h\mathbf{B}\mathbf{u}\right] = 0, \tag{2.60b}$$

where $\mathbf{I}$ is the 2×2 identity matrix and the divergence of the tensor product of two vectors is written in tensor notation as $[\nabla\cdot(\mathbf{ab})]_i = \partial(a_j b_i)/\partial x_j$ for $i, j = 1, 2$. Moreover, the horizontal magnetic field evolution of the shallow-water system can also be fully described by the magnetic flux function, A, which is materially conserved ($\mathrm{D}A/\mathrm{D}t = 0$) and is defined by

$$h\mathbf{B} \equiv \nabla\times A\widehat{\mathbf{z}}. \tag{2.61}$$

The parameters in this system are the reduced gravity, $g^* \equiv g(\rho_l - \rho)/\rho_l$, and the Coriolis parameter, $f = 2\Omega\sin\theta$. The variables h, $\mathbf{u}$, and $\mathbf{B}$ are vertically independent and their evolution does not explicitly depend on either the vertical velocity, w, or the vertical magnetic field, B_z, which are assumed $O(H/L)$ smaller than their horizontal counterparts. Explicit forms of w and B_z are not generally known/calculated in the reduced gravity model, but one can follow a similar argument to the one we presented in Section 2.2.1 to show that $|w|/|\mathbf{u}| \sim H/L \ll 1$ and $|B_z|/|\mathbf{B}| \sim H/L \ll 1$, as required.

2.2.3 Rotation in the Cartesian geometry

So far we have considered shallow-water models in a simple Cartesian framework. While this is useful for discussing the shallow-water equations, we cannot ignore spherical effects when modelling large scale planetary flows. The spherical effects of rotation are included using the so-called *equatorial beta-plane* approximation of Rossby (1939), who showed that the most significant dynamical effect of a planet's sphericity derives from the locally normal component of the planetary angular velocity vector (i.e., $\mathbf{\Omega}\cdot\widehat{\mathbf{z}}$) and its variation with respect to latitude, θ. This means that the dynamical effects of sphericity can be approximated within the Cartesian framework by choosing the system's geometry so that the Coriolis force in the (rotating) Cartesian coordinate system, $f\widehat{\mathbf{z}}\times\mathbf{u}$, replicates latitudinal variations in $2(\mathbf{\Omega}\cdot\widehat{\mathbf{z}})\widehat{\mathbf{z}}\times\mathbf{u}$, the Coriolis force caused by the angular velocity vector's locally normal component. In the equatorial beta-plane approximation, one uses the Taylor expansion of $f = 2\mathbf{\Omega}\cdot\widehat{\mathbf{z}} = 2\Omega\sin\theta$ about the equator ($\theta_0 = 0$), using $\theta = y/R$ for $|\theta| = |y/R| \ll 1$, to give

$$
\begin{aligned}
f &= 2\Omega\sin(\theta) \\
&= \left(\frac{2\Omega}{R}\right)y + O\left((y/R)^3\right) \\
&= \beta y + O\left((y/R)^3\right),
\end{aligned}
\tag{2.62}
$$

where Ω is the planetary rotation rate and R is the planetary radius. The approximation is named after the constant parameter, β, which is the local latitudinal variation of the Coriolis parameter at the equator ($\beta \equiv \mathrm{d}f/\mathrm{d}y|_{y=0} = 2\Omega/R$). Apart from this choice of Coriolis parameter, the system's governing equations remain identical to those derived using the Cartesian coordinate system, but now y/R approximately corresponds to the latitudinal coordinate, with $y = 0$ corresponding to the equator. Using this geometry, x/R approximately corresponds to the azimuthal coordinate, which we are free to centre as convenient.

Clearly the beta-plane approximation is not valid for the whole latitudinal extent of a spherical system (i.e.,$-\pi/2 \leq \theta \leq \pi/2$). In the polar regions geometric curvature effects become significant and solutions in the beta-plane approximation should be treated with caution. However, in the hydrodynamic version of the model we develop in this chapter, beta-plane shallow-water models have proved useful in capturing the fundamental flow patterns found in more sophisticated three-dimensional GCMs of hot Jupiters (Showman & Polvani, 2011).

2.2.4 Magnetic field geometry

In our reduced gravity SWMHD model, the horizontal magnetic field has one degree of freedom, so we can only model dynamics relating to the atmospheric toroidal field *or* the deep-seated poloidal field.[6] Upon encountering this apparently significant limitation, we should assess the restrictions it places on our approach and the influence it has on us achieving our model aims. Our aim is the develop understanding of the role the atmospheric magnetic field has on the equatorial dynamics of the hottest hot Jupiters, where we particularly focus on attempting to glean physical understanding of hotspot reversals using a simplified reduced-physics model. In the hottest hot Jupiters, three-dimensional MHD simulations have already identified that an equatorially-antisymmetric toroidal field geometry is expected to dominate magnetic field geometries in the hottest hot Jupiters (Rogers & Komacek, 2014, see Figure 1.16, middle row, and discussion of Section 1.4). Moreover, Rogers & Komacek (2014) and Rogers (2017) identified that in the limit where the toroidal field remains weak and decoupled to flows (i.e., $R_m \ll 1$), simulations behave similarly to their hydrodynamic counterparts. In such cases, Rayleigh drag treatments of the kind discussed in Section 2.2.6 have provided a reasonable leading order means of estimating the influence of the deep-seated magnetic field in hydrodynamic simulations (e.g., Perna *et al.*, 2010; Rauscher & Menou, 2013). Therefore, like these hydrodynamic

[6] We make the additional remark that the requirement that $\partial\mathbf{B}/\partial z = \mathbf{0}$ places significant difficulties on modelling poloidal fields.

studies, we shall use a Rayleigh drag treatment of the deep-seated magnetic field (see Section 2.2.6), but we will include the additional complexity of modelling the dominant atmospheric toroidal field explicitly. Provided hotspot reversals are driven by dynamics caused by the atmospheric toroidal field, this should not restrict our ability to determine the driving mechanics. However, we note that the main limitation with this approach is that it does not include toroidal field induction arising from the deep-seated poloidal field. Consequently, we must carefully choose initial magnetic field profiles based on the field geometries of three-dimensional MHD simulations. Further, since the relative orientation of zonal winds and the deep-seated poloidal field determine the sign of toroidal field induction, if zonal winds reverse we must take care when interpreting the physical significance of SWMHD solutions in post-reversal phases.

Based on three-dimensional MHD simulations, we use purely azimuthal initial magnetic field profiles, which are generally equatorially-antisymmetric. That is, the initial background magnetic field profiles take the form:

$$\mathbf{B}_0 = B_0(y)\widehat{\mathbf{x}}. \tag{2.63}$$

This can be written in terms of a latitudinally dependent initial magnetic flux function, $A_0(y) = \int hB_0(y)\mathrm{d}y$, which is specified up to a constant of integration that can be chosen as convenient without loss of generality. Moreover, $\nabla \cdot A\widehat{\mathbf{z}} = 0$ is guaranteed irrespective of this choice.

2.2.5 Diffusion treatments

For simulations of the SWMHD model, diffusion treatments are primarily included for numerical stability. However, shallow-water models have horizontal variables that are vertically independent over the active layer's vertical length scale, H, which, in the hot Jupiter setting, can be hundreds of kilometres deep (see Section 2.2.10). Therefore, since viscous and magnetic diffusion arise from microphysical fluid properties, this naturally leads to the question: what do viscous and magnetic diffusion mean in this context? The answer is drawn from our modelling motivations. We are interested in diagnosing specific physical causes of large scale planetary phenomena. Therefore, to do so, our diffusion treatments should capture the leading order large scale effects of diffusion, while not introducing any unphysical violations of the system's conservational properties.

Viscous diffusion

Here we seek a viscous dissipation treatment that replicates the macrophysical effects that viscosity has on large scale flow phenomena such as turbulence, waves, jets and vortices. We take the treatment discussed in Gilbert *et al.* (2014), but first, for context, we shall consider viscosity in three-dimensional fluid equations. In the unforced version of the three-dimensional MHD system, with viscous effects included, motion in a constant density active layer can be described by the following momentum equation:

$$\begin{aligned}\frac{\partial \mathbf{u}_3}{\partial t} + (\mathbf{u}_3 \cdot \nabla_3)\mathbf{u}_3 + \mathbf{f} \times \mathbf{u}_3 &= -\frac{1}{\rho}\nabla_3 P_T + g\widehat{\mathbf{z}} + \frac{1}{\mu_0 \rho}(\mathbf{B}_3 \cdot \nabla_3)\mathbf{B}_3 + \nu \nabla_3 \cdot \boldsymbol{\tau}_3, \\ &= -\frac{1}{\rho}\nabla_3 P_T + g\widehat{\mathbf{z}} + \frac{1}{\mu_0 \rho}(\mathbf{B}_3 \cdot \nabla_3)\mathbf{B}_3 + \nu \nabla_3^2 \mathbf{u}_3,\end{aligned} \tag{2.64}$$

where $\boldsymbol{\tau}_3 = \nabla_3 \mathbf{u}_3 + (\nabla_3 \mathbf{u}_3)^T$ (or $[\nabla_3 \cdot \boldsymbol{\tau}_3]_i = \partial(\partial u_i/\partial x_j + \partial u_j/\partial x_i)/\partial x_j$ for $i, j = 1, 2, 3$ in tensor notation) is the three-dimensional viscous stress tensor of the incompressible flow (i.e., with $\nabla_3 \cdot \mathbf{u}_3 = 0$) and the kinematic viscosity, ν, is taken as constant.

Viscous diffusion can be implemented into shallow-water systems in a variety of ways. Naively, one could use Equation (2.64) to repeat the derivation of Section 2.2.2, without further consideration of effects at the surfaces $z = S_b$ and $z = S_t$, and arrive on a shallow-water momentum equation with a Laplacian viscous term, $\nu\nabla^2\mathbf{u}$, in the righthand side. However, Gilbert *et al.* (2014) showed that a Laplacian treatment of this kind can produce energy sources arising from unphysical surfaces stresses[7]. Hyperviscosity (i.e., viscosity implementations with higher order derivatives) is also regularly implemented in numerical

[7]Gilbert *et al.* (2014) noted that incompressibility gives $\partial w/\partial z = -\nabla \cdot \mathbf{u}$, which leads to a three-dimensional viscous stress tensor, $\boldsymbol{\tau}_3$, for which tangential interface stresses are generally non-zero on the material surfaces (i.e., $[\boldsymbol{\tau}]_{1,3}, [\boldsymbol{\tau}]_{2,3}, [\boldsymbol{\tau}]_{3,1}, [\boldsymbol{\tau}]_{3,2}$ are non-zero on material surfaces). In a three-dimensional model there would be a transition between a bulk solution, with properties similar to the shallow-water model, and a boundary layer, which ensures that there are no surface stresses. Planetary flows have large Reynolds numbers so this boundary layer, which we neglect, would be expected to be thin.

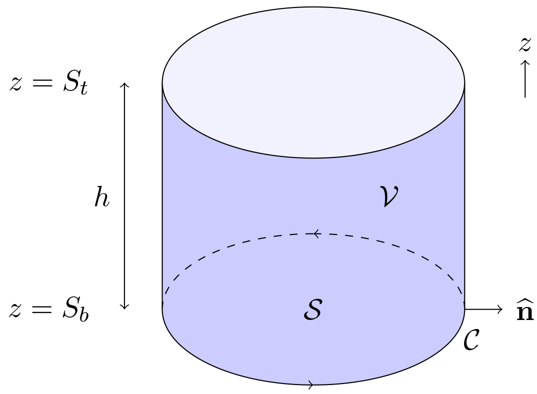

Figure 2.5: A schematic of illustrating the geometry used in the derivation of shallow-water viscous diffusion term presented by Gilbert *et al.* (2014). In this derivation, the horizontal component of the stress force is integrated over the sides of volume, $\mathcal{V}$ contained by the vertical fluid column with height, h, and base, $\mathcal{S}$. The horizontal surface, $\mathcal{S}$, forming the base of this column is bordered by the closed curve, $\mathcal{C}$, which lies in the (x, y) plane and has the horizontal outward-pointing unit normal vector $\widehat{\mathbf{n}}$.

shallow-water models to allow numerical solvers to capture a larger range of inertial length scales for a given grid resolution (e.g., Showman & Polvani, 2010, 2011; Perez-Becker & Showman, 2013). However, one should be careful to ensure that a given treatment satisfies relevant conservational properties. For instance, high order Laplacian treatments on the momentum equation do not generally conserve either or both of energy and angular momentum (Ochoa *et al.*, 2011; Gilbert *et al.*, 2014).

Gilbert *et al.* (2014) outlined a derivation for a viscous diffusion expression, $\mathbf{D}_\nu$, to be added the righthand side of the shallow-water momentum equation. Gilbert *et al.* (2014) presented this derivation for a single-layer model but, with only superficial changes, the derivation can be applied to our reduced gravity model. For completion, we replicate the derivation for the reduced gravity geometry here. One calculates the horizontal stress force through any point of a closed curve, $\mathcal{C}$, which lies in the (x, y) plane, has the horizontal outward-pointing unit normal vector, $\widehat{\mathbf{n}}$, and bounds a horizontal surface $\mathcal{S}$. Additionally, $\mathcal{V}$ is defined as the volume contained within the fluid column that has $\mathcal{S}$ as its base (see Figure 2.5). Briefly, since the shallow-water model is concerned with capturing bulk effects, one neglects surface viscous stresses at the interfaces and equates the total columnar horizontal viscous diffusion with the total horizontal stress force per unit mass passing through the sides of fluid column containing $\mathcal{V}$ (see Figure 2.5, with the integration through the darkly shaded side-walls of the column):

$$\begin{aligned}\int_{\mathcal{S}}\int_{S_b}^{S_t}\mathbf{D}_\nu\,\mathrm{d}z\,\mathrm{d}S &= \nu\oint_{\mathcal{C}}\int_{S_b}^{S_t}\widehat{\mathbf{n}}\cdot\boldsymbol{\tau}_3\,\mathrm{d}z\,\mathrm{d}s\\ &= \nu\oint_{\mathcal{C}}\int_{S_b}^{S_t}\widehat{\mathbf{n}}\cdot\boldsymbol{\tau}\,\mathrm{d}z\,\mathrm{d}s\\ &= \nu\oint_{\mathcal{C}} h\widehat{\mathbf{n}}\cdot\boldsymbol{\tau}\,\mathrm{d}s\\ &= \nu\int_{\mathcal{S}}\nabla\cdot[h\boldsymbol{\tau}]\,\mathrm{d}S\\ &= \int_{\mathcal{S}}\nabla\cdot\left[\nu h\left(\nabla\mathbf{u}+(\nabla\mathbf{u})^T\right)\right]\,\mathrm{d}S,\end{aligned} \tag{2.65}$$

using the two-dimensional version of Gauss' divergence theorem and the vertical independence of $\boldsymbol{\tau}=\nabla\mathbf{u}+(\nabla\mathbf{u})^T$, the two-dimensional viscous stress tensor, which is the upper 2×2 block of $\boldsymbol{\tau}_3$. Since $\mathcal{S}$ is arbitrary and $\mathbf{D}_\nu$ is vertically independent by construction, this yields (Gilbert *et al.*, 2014):

$$\mathbf{D}_\nu = \nu h^{-1}\nabla\cdot\left[h\left(\nabla\mathbf{u}+(\nabla\mathbf{u})^T\right)\right], \tag{2.66}$$

where we have taken ν to be constant. Gilbert *et al.* (2014) recommend the more general expression, $\mathbf{D}_\nu=\nu h^{-1}\nabla\cdot\left[h\left(\nabla\mathbf{u}+(\nabla\mathbf{u})^T\right)+\varsigma h(\nabla\cdot\mathbf{u})\right]$, with either $\varsigma=0$, which we take, or $\varsigma=-2$, which is derived by including a viscous contribution to the system's magneto-hydrostatic balance (Gilbert *et al.*, 2014). Further, they show that neither version of this formulation has energy sources and that both treatments behave in a physically-realistic manner when administered to solid body rotation.

Magnetic diffusion

In the non-relativistic limit, the diffusive three-dimensional induction equation for electrically-conducting fluid of constant density is

$$\begin{aligned}\frac{\partial\mathbf{B}_3}{\partial t} &= \nabla_3\times(\mathbf{u}_3\times\mathbf{B}_3)-\nabla_3\times(\eta\nabla_3\times\mathbf{B}_3),\\ &= (\mathbf{B}_3\cdot\nabla_3)\mathbf{u}_3-(\mathbf{u}_3\cdot\nabla_3)\mathbf{B}_3+\mathbf{D}_{\eta,3},\end{aligned} \tag{2.67}$$

where $\mathbf{D}_{\eta,3} = -\nabla_3 \times (\eta \nabla_3 \times \mathbf{B}_3)$ is the three-dimensional magnetic diffusion term and $\eta = 1/\mu_0 \sigma$ is the magnetic diffusivity, with σ denoting the conductivity. This can be derived directly from the Maxwell equations (alongside Ohm's law for a moving medium) but in SWMHD the correct diffusion treatment is less clear. We seek a horizontal magnetic diffusion term, $\mathbf{D}_\eta$, in the righthand side of the shallow-water induction equation (Equation (2.59c)) so that

$$\frac{\mathrm{D}\mathbf{B}}{\mathrm{D}t} = (\mathbf{B} \cdot \nabla)\mathbf{u} + \mathbf{D}_\eta. \tag{2.68}$$

A *naive* approach might be to state that since the horizontal magnetic field is independent of z, $\mathbf{D}_{\eta,\mathrm{naive}} = -\nabla \times (\eta \nabla \times \mathbf{B})$. However, we note that this approach is inconsistent with SWMHD as combining the resulting shallow-water induction and continuity equations yields

$$\left\{\frac{\partial(h\mathbf{B})}{\partial t}\right\}_{\mathrm{naive}} = \nabla \times (\mathbf{u} \times h\mathbf{B}) - h\nabla \times (\eta \nabla \times \mathbf{B}), \tag{2.69}$$

which is not generally divergence-free. Hence, the shallow-water version of Gauss' law, $\nabla \cdot (h\mathbf{B}) = 0 \; \forall \; t$, is violated.

The problem with this naive approach is that $\mathbf{D}_{\eta,3,H}$, the leading order approximation of the horizontal component of $\mathbf{D}_{\eta,3}$ in the shallow-water limit, is not generally independent of z. Instead, Andrew Gilbert (personal correspondence) identified that $\mathbf{D}_\eta$ can be obtained by integrating the leading order horizontal components of Equation (2.67) vertically over the extent of the fluid column. If $\partial \mathbf{u}/\partial z = \mathbf{0}$ and $\partial \mathbf{B}/\partial z = \mathbf{0}$ for all time, this gives

$$h\left(\frac{\mathrm{D}\mathbf{B}}{\mathrm{D}t} - (\mathbf{B} \cdot \nabla)\mathbf{u}\right) = \int_{S_b}^{S_t} \mathbf{D}_{\eta,3,H} \mathrm{d}z, \tag{2.70}$$

where the integral on the righthand side can evaluated using the following boundary conditions:

$$\widehat{\mathbf{n}}_3 \cdot \mathbf{B}_3 = 0 \quad \text{and} \quad \widehat{\mathbf{n}}_3 \times (\nabla_3 \times \mathbf{B}_3) = \mathbf{0}, \tag{2.71}$$

on the $z = S_t(x, y, t)$ and $z = S_b(x, y, t)$ interfaces, where $\widehat{\mathbf{n}}_3 = \widehat{\mathbf{n}}_t \equiv \widehat{\mathbf{z}} - \nabla S_t$ and $\widehat{\mathbf{n}}_3 = \widehat{\mathbf{n}}_b \equiv \widehat{\mathbf{z}} - \nabla S_b$ are the upward-pointing unit normal vectors on the upper and lower surfaces respectively. The first of these boundary conditions ($\widehat{\mathbf{n}}_3 \cdot \mathbf{B}_3 = 0$) is the usual no

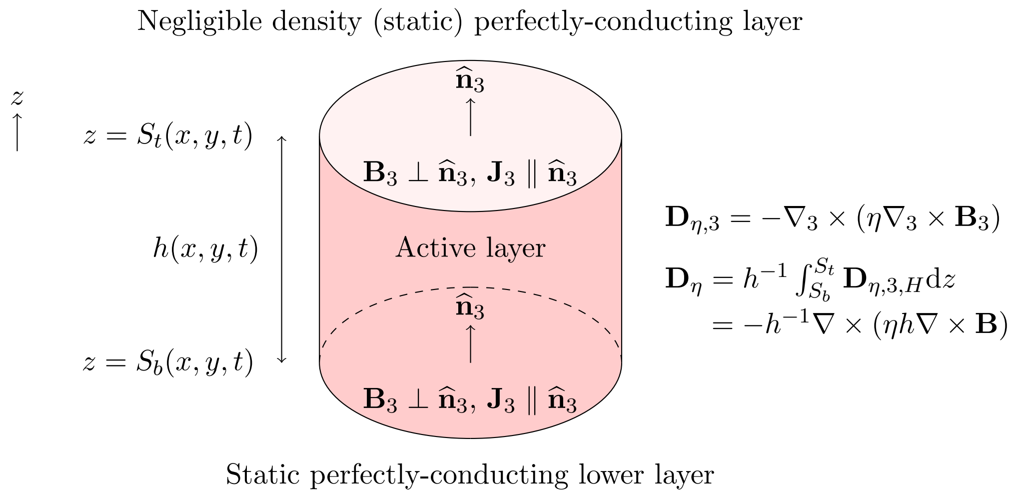

Figure 2.6: A schematic of illustrating the geometry used in the derivation of shallow-water magnetic diffusion term, $\mathbf{D}_\eta$, as adapted from the derivation of Andrew Gilbert (personal correspondence). This derivation uses an asymptotic expansion to calculate the leading order contributions to the three-dimensional magnetic diffusion term, $\mathbf{D}_{\eta,3}$, in the shallow-water limit. The derivation finds that $\mathbf{D}_\eta$ is given by the thickness-weighted average of $\mathbf{D}_{\eta,3,H}$, the leading order approximation of the horizontal component of $\mathbf{D}_{\eta,3}$, when the magnetic field and current density are respectively held as perpendicular and parallel/antiparallel to the upward-pointing unit normal of the interfaces, $\widehat{\mathbf{n}}_3$.

magnetic flux condition of SWMHD; whereas the second ($\widehat{\mathbf{n}}_3 \times (\nabla_3 \times \mathbf{B}_3) = \mathbf{0}$) requires that the current density at interfaces is parallel/antiparallel to $\widehat{\mathbf{n}}_3$. Combining Ampère's law and Ohm's law for a moving medium gives

$$\begin{aligned} \eta[\widehat{\mathbf{n}}_3 \times (\nabla_3 \times \mathbf{B}_3)] &= \eta\mu_0[\widehat{\mathbf{n}}_3 \times \mathbf{J}_3], \\ &= \eta\mu_0\sigma[\widehat{\mathbf{n}}_3 \times \mathbf{E}_3 + \widehat{\mathbf{n}}_3 \times (\mathbf{u}_3 \times \mathbf{B}_3)] \\ &= [\widehat{\mathbf{n}}_3 \times \mathbf{E}_3 - (\widehat{\mathbf{n}}_3 \cdot \mathbf{u}_3)\mathbf{B}_3], \end{aligned} \tag{2.72}$$

where $\mathbf{J}_3$ denotes the three-dimensional current density, $\mathbf{E}_3$ denotes the three-dimensional electric field, and $\widehat{\mathbf{n}}_3 \cdot \mathbf{B}_3 = 0$ has been applied alongside the vector identity $\mathbf{a} \times (\mathbf{b} \times \mathbf{c}) = \mathbf{b}(\mathbf{a} \cdot \mathbf{c}) - \mathbf{c}(\mathbf{a} \cdot \mathbf{b})$. If the regions outside the active layer are considered static perfect conductors, $\eta = 0$ and $\mathbf{u}_3 = \mathbf{E}_3 = 0$, so both sides of Equation (2.72) are equally zero. Therefore, imposing $\widehat{\mathbf{n}}_3 \times (\nabla_3 \times \mathbf{B}_3) = \mathbf{0}$ ensures that both sides of Equation (2.72) are continuous (and zero) at interfaces of the active region, where η steps in value.

By careful consideration of the asymptotic expansion of Equation (2.67), and application of the boundary conditions in Equation (2.71), one can show that

$$\int_{S_b}^{S_t} \mathbf{D}_{\eta,3,H} \mathrm{d}z = -\nabla \times (\eta h \nabla \times \mathbf{B}), \tag{2.73}$$

yielding

$$\mathbf{D}_\eta = -h^{-1} \nabla \times (\eta h \nabla \times \mathbf{B}), \tag{2.74}$$

which is a thickness-weighted version of its three-dimensional counterpart and is vertically-independent, so the $\partial \mathbf{u}/\partial z = \partial \mathbf{B}/\partial z = \mathbf{0}$ assumption used to obtain Equation (2.70) remains satisfied. Since our reduced gravity model assumptions vary slightly (in interface conditions) from those of single-layer SWMHD (as considered by Andrew Gilbert, personal correspondence), in Appendix A we have made the necessary adaptations to present the derivation of Equation (2.74) for the reduced gravity model. We have summarised the key aspects of the derivation in Figure 2.6.

Using this treatment of magnetic diffusion, the horizontal magnetic field evolution is described by the following three consistent formulations:

$$\frac{\mathrm{D}\mathbf{B}}{\mathrm{D}t} = (\mathbf{B} \cdot \nabla)\mathbf{u} - h^{-1} \nabla \times (\eta h \nabla \times \mathbf{B}), \tag{2.75}$$

$$\frac{\partial (h\mathbf{B})}{\partial t} = \nabla \times [\mathbf{u} \times h\mathbf{B} - \eta h \nabla \times \mathbf{B}], \tag{2.76}$$

$$\frac{\mathrm{D}A}{\mathrm{D}t} = \eta(\nabla^2 A - h^{-1} \nabla h \cdot \nabla A), \tag{2.77}$$

where Equation (2.77) is obtained by "uncurling" Equation (2.76) with $h\mathbf{B} \equiv \nabla \times A\widehat{\mathbf{z}}$ and $\nabla \times \mathbf{B} \equiv \nabla \times (h^{-1} \nabla \times A\widehat{\mathbf{z}}) = -\nabla \cdot (h^{-1} \nabla A\widehat{\mathbf{z}})$, which uses $\nabla \cdot A\widehat{\mathbf{z}} = 0$. Further, taking the horizontal divergence of Equation (2.76) highlights that this treatment is consistent with the shallow-water divergence free condition ($\nabla \cdot (h\mathbf{B}) = 0 \; \forall \; t$).

2.2.6 Forcing and drag treatments

Forcing treatment

Homogeneous shallow-water models (i.e., those with constant density layers) are vertically independent so cannot contain consistent thermodynamic treatments (Dellar, 2003). Current understanding of the hottest hot Jupiters points towards a fairly unique scenario, in which the dominant thermodynamic feature of their atmospheres is strong tidally-locked thermal forcing (see Chapter 1). In hydrodynamic models of hot Jupiters, thermal forcing of this kind is found to drive atmospheric dynamics that can be well described by simple shallow-water models (Showman & Polvani, 2011). Mathematically, the simplest way to parameterise this forcing in a shallow-water model is to include a Newtonian cooling treatment, Q, in the righthand side of the shallow-water continuity equation (e.g., Shell & Held, 2004; Langton & Laughlin, 2007; Showman & Polvani, 2010, 2011; Showman *et al.*, 2012; Perez-Becker & Showman, 2013):

$$\frac{\partial h}{\partial t} + \nabla \cdot (h\mathbf{u}) = \frac{h_{\rm eq} - h}{\tau_{\rm rad}} \equiv Q. \tag{2.78}$$

Physically, the Newtonian cooling relaxes the system towards a prescribed radiative equilibrium thickness profile, $h_{\rm eq}(x, y)$, over a radiative timescale, $\tau_{\rm rad}$, by transferring mass vertically from the quiescent lower layer to the active layer of the reduced gravity model (see Figure 2.7). The transfer of mass caused by Q generates horizontal pressure gradients, which drive recirculation via the generation of planetary scale shallow-water gravity waves. Analogously, in three dimensional models, pressure gradients caused by heating drive recirculation via internal gravity waves. Using this analogy, mass sources and sinks represent heating and cooling respectively. This connection has been used extensively in hydrodynamic models of hot Jupiters, with the active layer geopotential, g^*h, used as a proxy for specific thermal energy (Langton & Laughlin, 2007; Showman & Polvani, 2010; Showman *et al.*, 2013; Perez-Becker & Showman, 2013). Using this physical link, we equate the model's active layer reference geopotential, $g^*H \equiv c_g^2$, to the reference thermal energy,

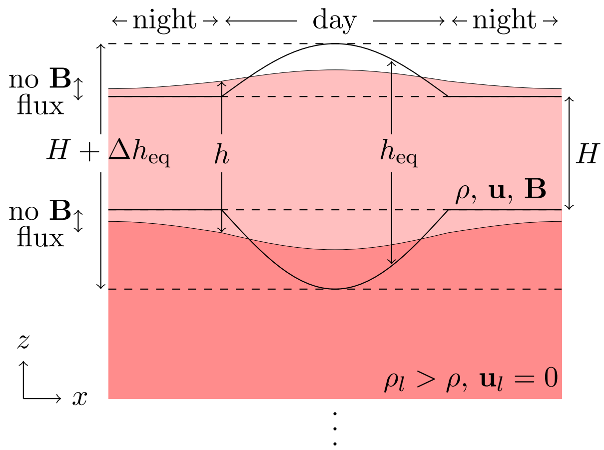

Figure 2.7: The forced reduced-gravity SWMHD model schematic. An active layer sits upon an infinity-deep quiescent fluid layer, where both layers have constant densities (ρ and ρ_l). No magnetic flux is permitted across the active layer's upper and lower boundaries, which are material surfaces that evolve in time. Newtonian forcing is used to generate horizontal pressure gradients in the active layer: the active layer thickness (h) is relaxed towards an imposed radiative equilibrium thickness profile ($h_{\rm eq}$) over a radiative timescale ($\tau_{\rm rad}$). The resulting horizontal pressure gradients drive horizontal motion.

$\mathcal{R}T_{\rm eq}$, of the modelled planet's atmosphere, where c_g, $\mathcal{R}$ and $T_{\rm eq}$ respectively denote the shallow-water gravity wave speed, the specific gas constant and the equilibrium reference temperature. Since this analogy adjusts the physical interpretation of the quantity g^*H, we hereafter drop the star superscript notation on g^*.

This mass exchange treatment proves useful for including thermal forcing in our reduced gravity SWMHD model. However, we must be careful that the mass exchange is physically meaningful and does not violate physical conservation laws or the model assumptions we discussed in Section 2.2.2.

We ensure that the mass exchanges conserve specific horizontal momentum, $h\mathbf{u}$, by using a vertical mass transport term, $\mathbf{R}$, which is added to the righthand side of Equation (2.59a). In "cooling" regions ($Q < 0$) mass sinks from the active layer to the quiescent layer and without causing any net accelerations to either the active layer or the quiescent layer[8]. However, in "heating" regions ($Q > 0$) the upward transport of motionless fluid causes deceleration of horizontal active layer velocities. This deceleration due to heating

[8]The momentum that is removed from the active layer is transferred to the quiescent layer. However, since the quiescent layer is infinitely-deep, the momentum of the transferred mass plus the quiescent layer is conserved with no change to the quiescent layer's velocity.

is calculated by requiring that mass exchanges between layers conserve specific horizontal momentum[9], yielding

$$\mathbf{R} = \begin{cases} 0 & \text{for } Q \leq 0 \\ -\frac{\mathbf{u}Q}{h} & \text{for } Q > 0, \end{cases} \tag{2.79}$$

which has also been used in the hydrodynamic version of this model (e.g., Shell & Held, 2004; Showman & Polvani, 2010, 2011; Showman *et al.*, 2012; Perez-Becker & Showman, 2013).

Furthermore, we do not allow the vertical mass transfer to violate the divergence-free condition of SWMHD:

$$\nabla \cdot (h\mathbf{B}) = 0. \tag{2.80}$$

This derives from Gauss' law of magnetism and the condition that no magnetic fluxes can cross the interfaces. Therefore, for consistency, we impose the requirement that mass exchanges do not directly effect the evolution of the horizontal magnetic flux contained within a fluid column in the active layer, $h\mathbf{B}$, which is solenoidal and determined by

$$\frac{\partial(h\mathbf{B})}{\partial t} = \nabla \times (\mathbf{u} \times h\mathbf{B}) - \nabla \times (\eta h \nabla \times \mathbf{B}), \tag{2.81a}$$

which can also be written in the conservative form

$$\frac{\partial(h\mathbf{B})}{\partial t} + \nabla \cdot \left[h\mathbf{u}\mathbf{B} - h\mathbf{B}\mathbf{u} - \eta h \left(\nabla\mathbf{B} - (\nabla\mathbf{B})^T\right)\right] = 0, \tag{2.81b}$$

where in tensor notation $[\nabla \cdot (\mathbf{ab})]_i = \partial(a_j b_i)/\partial x_j$ for $i, j = 1, 2$. Since the evolution of hB is unchanged with the inclusion of forcing, so is the evolution of A and, as before,

$$\frac{\mathrm{D}A}{\mathrm{D}t} = \eta(\nabla^2 A - h^{-1}\nabla h \cdot \nabla A), \tag{2.82}$$

can be obtained by "uncurling" Equation (2.81). However, using the chain rule to note

[9]That is, $\mathbf{R}$ is chosen so that $\partial(h\mathbf{u})/\partial t$ is unaffected by the inclusion of vertical mass exchanges when $Q > 0$.

that $\partial \mathbf{B}/\partial t = h^{-1}(\partial(h\mathbf{B})/\partial t - \mathbf{B}\partial h/\partial t)$, Equations (2.78), (2.80) and (2.81) now yield

$$\frac{\partial \mathbf{B}}{\partial t} = -(\mathbf{u}\cdot\nabla)\mathbf{B} + (\mathbf{B}\cdot\nabla)\mathbf{u} - \frac{\mathbf{B}Q}{h} + \mathbf{D}_\eta, \tag{2.83}$$

where $\mathbf{D}_\eta$ is the diffusion treatment given in Equation (2.74). This includes the forcing dependent term, $-\mathbf{B}Q/h$, which ensures that the horizontal columnar magnetic flux, $h\mathbf{B}$, is unaffected by mass exchanges and remains divergence-free. This term is purely a result of the system's geometry as we allow for instantaneous and vertically-independent vertical mass transport from the quiescent layer but do not allow magnetic flux to cross the active-quiescent interface. Having one without the other may be considered somewhat unphysical, but it is the the sacrifice we make to include pseudo-thermal forcing within the simplified shallow-water geometry. One can view this as a "dilation" of the pointwise (or vertically-averaged) horizontal magnetic field, $\mathbf{B}$, because it acts to reduce its magnitude in regions of increasing volume ($Q > 0$) and increases $\mathbf{B}$ in regions of decreasing volume ($Q < 0$). The consequence of this pointwise magnetic dilation is that in regions of extreme forcing accelerations due the Lorentz force can be reduced, a phenomenon that one should be wary of when analysing highly forced solutions. In the numerical solutions of Chapter 4, we find that this dilation phenomenon has little qualitative influence solutions, which are dominated by the same physical processes in both the weakly-forced and strongly-forced cases. Moreover, for their useful conservational properties, we will tend to work with $h\mathbf{B}$ and A, rather than $\mathbf{B}$, hereafter.

Rayleigh drag treatment

We parameterise atmospheric drag with a linear Rayleigh drag treatment, $-\mathbf{u}/\tau_{\text{drag}}$, which is added to the righthand side of the momentum equation (Equation (2.59a)) and acts to reduce the magnitude of planetary flows. Here τ_{drag} is the timescale of the dominant horizontal drag process in the thin active layer. Previous hydrodynamic studies use this Rayleigh drag to parameterise Lorentz forces (e.g., Perna *et al.*, 2010; Rauscher & Menou, 2013) or basal drag at the bottom of the radiative zone (e.g., Held & Suarez, 1994; Liu

& Showman, 2013; Komacek & Showman, 2016). In our study, we include Lorentz forces explicitly. However, due to the geometry of the SWMHD model, we only explicitly include the Lorentz forces caused by the atmospheric toroidal magnetic field (see Section 2.2.4 for a discussion of the magnetic field geometry in the atmosphere). We hence use the Rayleigh drag treatment to parameterise the Lorentz forces caused by planet's deep-seated poloidal magnetic field, which are not included explicitly. This is consistent with the treatment proposed by Perna *et al.* (2010), who set

$$\tau_{\text{drag}} = \tau_{\text{mag}} \equiv \frac{\eta}{V_{\text{A,dip}}^2}, \tag{2.84}$$

where $V_{\text{A,dip}}$ is the Alfvén speed of the assumed deep-seated dipolar magnetic field and τ_{mag}, the Joule timescale, is the timescale over which the Lorentz force from the deep-seated dipolar magnetic field will bring zonal flows to rest in the absence of other forces. Though (on geometric grounds) one could argue that in this setting the Rayleigh drag should have no meridional component, for comparison with past hydrodynamic results, we follow the commonly applied treatment of using Rayleigh drag in both horizontal directions (e.g., Perna *et al.*, 2010; Showman & Polvani, 2011; Rauscher & Menou, 2013; Perez-Becker & Showman, 2013).[10] We also comment that Rogers & Komacek (2014) found that magnetically driven wind variations emerge in the upper radiative atmosphere (where basal drags are negligible), so we do not consider basal drag in this work.

2.2.7 Dimensional equations

Governing equations

In summary, when linear drag and mass exchanges between the upper active and lower quiescent layers are included in the inviscid, perfectly-conducting, reduced gravity SWMHD model, the dynamical behaviour of the active layer can be described by the following set

[10]We find that the meridional component of the Rayleigh drag never has a leading order influence, being 1-2 orders of magnitude smaller than the system's dominant meridional accelerations, so does not qualitatively influence any of our results. An example of this can be seen in Figure 4.2 (Chapter 4).

of governing equations:

$$\frac{\mathrm{D}\mathbf{u}}{\mathrm{D}t} + f(\widehat{\mathbf{z}} \times \mathbf{u}) = -g\nabla h + (\mathbf{B}\cdot\nabla)\mathbf{B} + \mathbf{R} - \frac{\mathbf{u}}{\tau_{\mathrm{drag}}} + \nu h^{-1}\nabla\cdot\left[h\left(\nabla\mathbf{u} + (\nabla\mathbf{u})^{T}\right)\right], \tag{2.85a}$$

$$\frac{\partial h}{\partial t} + \nabla\cdot(h\mathbf{u}) = \frac{h_{\mathrm{eq}} - h}{\tau_{\mathrm{rad}}} \equiv Q, \tag{2.85b}$$

$$\frac{\mathrm{D}A}{\mathrm{D}t} = \eta(\nabla^2 A - h^{-1}\nabla h\cdot\nabla A). \tag{2.85c}$$

$$h\mathbf{B} \equiv \nabla\times A\widehat{\mathbf{z}}, \tag{2.85d}$$

where $\mathbf{u}(x, y, t)$, is the horizontal active layer fluid velocity, $h(x, y, t)$ is the active layer thickness which is used as the model's temperature proxy, $\mathbf{B}(x, y, t)$ is the active layer's pointwise (or vertically-averaged) horizontal magnetic field (in velocity units), $A(x, y, t)$ is the magnetic flux function of the active layer, and the equatorial beta-plane approximation is taken using $f = \beta y$. Thermal forcing is mimicked using vertical mass exchanges between the layers, which are included through the Newtonian cooling treatment, Q. In these mass exchanges, no magnetic fluxes are permitted to cross the interfaces and specific momentum is conserved through the vertical mass transport term:

$$\mathbf{R} = \begin{cases} 0 & \text{for } Q \leq 0 \\ -\frac{\mathbf{u}Q}{h} & \text{for } Q > 0. \end{cases} \tag{2.86}$$

The Newtonian cooling treatment drives the system towards the prescribed radiative equilibrium thickness profile, $h_{\mathrm{eq}}(x, y)$, over a radiative timescale, τ_{rad}. Using this analogy, inline with the parameter choice $gH \equiv c_g^2 \sim \mathcal{R}T_{\mathrm{eq}}$, corresponds to a shallow-water model in which mass sources/sinks represent heating/cooling. Forcing the system in this way drives horizontal pressure gradients in the system, which drive magnetohydrodynamic flows. These flows are slowed by the linear atmospheric drag treatment, $-\mathbf{u}/\tau_{\mathrm{drag}}$.

Conservative form

To discuss conservation laws more freely, it can be useful to write the system in the equivalent conservative form:

$$\frac{\partial(h\mathbf{u})}{\partial t} + \nabla\cdot\left[h\mathbf{u}\mathbf{u} - h\mathbf{B}\mathbf{B} + \tfrac{1}{2}gh^2\mathbf{I} + \nu h\boldsymbol{\tau}\right] = fh(\mathbf{u}\times\widehat{\mathbf{z}}) + Q\mathbf{u} + h\mathbf{R} - \frac{h\mathbf{u}}{\tau_{\mathrm{drag}}}, \tag{2.87a}$$

$$\frac{\partial h}{\partial t} + \nabla\cdot(h\mathbf{u}) = Q, \tag{2.87b}$$

$$\frac{\partial(h\mathbf{B})}{\partial t} + \nabla\cdot\left[h\mathbf{u}\mathbf{B} - h\mathbf{B}\mathbf{u} - \eta h\left(\nabla\mathbf{B} - (\nabla\mathbf{B})^T\right)\right] = 0, \tag{2.87c}$$

$$\nabla\cdot(h\mathbf{B}) = 0, \tag{2.87d}$$

where $\boldsymbol{\tau} = \nabla\mathbf{u} + (\nabla\mathbf{u})^T$, Equation (2.87c) is equivalent to Equation (2.81), $\mathbf{I}$ is the 2×2 identity matrix, and in tensor notation $[\nabla\cdot(\mathbf{ab})]_i = \partial(a_j b_i)/\partial x_j$ for $i, j = 1, 2$. For this formulation, we have noted that the magnetic diffusion treatment of Equation (2.74) can be equivalently written as

$$\begin{aligned}\mathbf{D}_\eta &= -h^{-1}\nabla\times(\eta h\nabla\times\mathbf{B}) \\ &= -h^{-1}\nabla\times(\eta h\mathbf{J}) \\ &= h^{-1}\nabla\cdot\left[\eta h\left(\nabla\mathbf{B} - (\nabla\mathbf{B})^T\right)\right],\end{aligned} \tag{2.88}$$

where $\mathbf{J} = J\widehat{\mathbf{z}} \equiv \nabla\times\mathbf{B}$ is the (vertical) current density associated with the pointwise horizontal magnetic field (in units of frequency), with $J = \partial B_y/\partial x - \partial B_x/\partial y$.

The Lorentz force and magnetic tension

In SWMHD models the explicit Lorentz force contribution of the shallow-water momentum equation (Equation (2.85a)) is $\mathbf{B}\cdot\nabla\mathbf{B}$. This represents the vertically-averaged Lorentz force within the active layer's fluid column (Dellar, 2003). It may also be expressed as $\mathbf{B}\cdot\nabla\mathbf{B} = \nabla(\mathbf{B}\cdot\mathbf{B}/2) + \mathbf{J}\times\mathbf{B}$. In this decomposition $\nabla(\mathbf{B}\cdot\mathbf{B}/2)$ originates from the vertical magneto-hydrostatic balance of the model, while $\mathbf{J}\times\mathbf{B}$ is the Lorentz force generated by the (vertically-independent) horizontal component of the magnetic field (Gilman, 2000). Expressing the vertically-averaged Lorentz force as $\mathbf{B}\cdot\nabla\mathbf{B}$ highlights its equivalence to the magnetic tension of the horizontal magnetic field components (i.e., it acts to straighten bent horizontal magnetic field lines).

Potential vorticity

Dellar (2002) showed that potential vorticity of hydrodynamic shallow-water models is no longer materially conserved in SWMHD and, further, has no materially invariant counterpart (though A is materially conserved in non-diffusive SWMHD). Recall the shallow-water hydrodynamic definition of potential vorticity (dropping the "SW" labelling of Chapter 1) is

$$q = \frac{\zeta + f}{h}, \tag{2.89}$$

where, as before, $\zeta \equiv (\nabla \times \mathbf{u}) \cdot \widehat{\mathbf{z}} \equiv \partial v/\partial x - \partial u/\partial y$ is the relative vorticity of flows in the horizontal plane. Using Equations (2.85a) and (2.85b), it can be shown that, in our SWMHD model, the potential vorticity evolution satisfies (see Appendix B)

$$\frac{\mathrm{D}q}{\mathrm{D}t} = \frac{1}{h}[\nabla \times (\mathbf{J} \times \mathbf{B})] \cdot \widehat{\mathbf{z}} - q\frac{Q}{h} + \frac{1}{h}(\nabla \times \mathbf{R}) \cdot \widehat{\mathbf{z}} - \frac{\zeta}{h\tau_{\mathrm{drag}}} + (\nabla \times \mathbf{D}_\nu) \cdot \widehat{\mathbf{z}}, \tag{2.90}$$

where $\mathbf{D}_\nu = \nu h^{-1} \nabla \cdot \left[h\left(\nabla \mathbf{u} + (\nabla \mathbf{u})^T\right)\right]$, as defined in Equation (2.66) and is expected to be small compared to other terms for planetary scale flows (Vallis, 2006; Showman *et al.*, 2010). Equation (5.14) shows that q is only materially conserved in the hydrodynamic, unforced, drag-free, inviscid limit. Note that the mass sources/sinks contribution of Equation (5.14) can be written as

$$-q\frac{Q}{h} + \frac{1}{h}(\nabla \times \mathbf{R}) \cdot \widehat{\mathbf{z}} = \begin{cases} -q\frac{Q}{h} & \text{for } Q \leq 0 \\ -q\frac{Q}{h} - \frac{1}{h}\left[\nabla \times \left(\frac{\mathbf{u}Q}{h}\right)\right] \cdot \widehat{\mathbf{z}} & \text{for } Q > 0. \end{cases} \tag{2.91}$$

This shows that at mass sources (i.e., heating regions with $Q > 0$), where fluid with zero relative vorticity is transported upwards and h increases, forcing acts to diminish the magnitude of potential vorticity; whereas at mass sinks (i.e., cooling regions with $Q \leq 0$), where h decreases with no change to the relative vorticity, forcing acts to enhance the magnitude of potential vorticity. Equation (5.14) also shows that Rayleigh drag acts to dampen potential vorticity transport. These two facts highlight that strong forcing (i.e., short $\tau_{\rm rad}$) and/or strong drag (i.e., short $\tau_{\rm drag}$) diminish the efficiency of processes that arise due to potential vorticity conservation (i.e., the propagation of Rossby waves, see Chapter 1 for discussion).

Equation (5.14) also shows that the curl of the Lorentz force generated by the horizontal magnetic field component, $[\nabla \times (\mathbf{J} \times \mathbf{B})] \cdot \widehat{\mathbf{z}}$, generally prevents potential vorticity conservation in the magnetic limit, regardless to whether forcing, drags, or viscous diffusion are present. This suggests that in regions of large Lorentz force, processes that arise due to potential vorticity conservation, such as Rossby wave propagation, are expected to be magnetically altered. We discuss planetary-scale SWMHD waves in the presence of rotation and magnetism in Chapters 3 and 5.

Pointwise induction equation

For considering energy evolution, it is useful to use the second of these forms of $\mathbf{D}_\eta$ in the pointwise induction equation:

$$\frac{\partial \mathbf{B}}{\partial t} = (\mathbf{B} \cdot \nabla)\mathbf{u} - (\mathbf{u} \cdot \nabla)\mathbf{B} - \frac{\mathbf{B}Q}{h} - h^{-1}\nabla \times (\eta h \mathbf{J}). \tag{2.92}$$

The energy equation

The total specific *pointwise energy* in the model's active layer is

$$\varepsilon = \tfrac{1}{2}|\mathbf{u}|^2 + \tfrac{1}{2}|\mathbf{B}|^2 + gh, \tag{2.93}$$

This is the sum of the specific pointwise kinetic, magnetic and geopotential (or gravitational potential) energy contributions. However, a more useful property is the total specific *columnar energy* (Gilman, 2000):

$$E = \tfrac{1}{2}h|\mathbf{u}|^2 + \tfrac{1}{2}h|\mathbf{B}|^2 + \tfrac{1}{2}gh^2, \tag{2.94}$$

which is obtained by integrating ε over the thickness of the active layer's fluid column. Recall that the SWMHD model doesn't include consistent thermodynamic treatments so neither of these expressions include a thermal energy contribution. However, in the shallow-water model the active layer thickness, h, is used as a temperature proxy and the gravitational potential energy is used to trace the thermal energy.

Before describing the evolution of specific columnar kinetic energy, $\frac{1}{2}h|\mathbf{u}|^2$, we note that

$$\begin{aligned}|\boldsymbol{\tau}|^2 = \boldsymbol{\tau} : \boldsymbol{\tau} &= (\nabla\mathbf{u} + (\nabla\mathbf{u})^T) : (\nabla\mathbf{u} + (\nabla\mathbf{u})^T) \\ &= \nabla\mathbf{u} : \nabla\mathbf{u} + 2\nabla\mathbf{u} : (\nabla\mathbf{u})^T + (\nabla\mathbf{u})^T : (\nabla\mathbf{u})^T \\ &= 2\nabla\mathbf{u} : \nabla\mathbf{u} + 2\nabla\mathbf{u} : (\nabla\mathbf{u})^T \\ &= 2\nabla\mathbf{u} : \boldsymbol{\tau},\end{aligned} \tag{2.95}$$

where the "double" dot product is defined so that $\boldsymbol{\varsigma} : \boldsymbol{\sigma} = \sum_i \sum_j \varsigma_{ij}\sigma_{ij}$, for $i, j = 1, 2$. That is, $\nabla\mathbf{u} : \boldsymbol{\tau} = \sum_i \sum_j (\partial u_i/\partial x_j)(\partial u_i/\partial x_j + \partial u_j/\partial x_i)$

The evolution of specific columnar kinetic energy can be determined by combining Equations (2.85a), (2.85b) and (2.95) with the divergence-free condition as follows:

$$\begin{aligned}\frac{\partial(\frac{1}{2}h|\mathbf{u}|^2)}{\partial t} &= \tfrac{1}{2}|\mathbf{u}|^2\frac{\partial h}{\partial t} + h\mathbf{u}\cdot\frac{\partial \mathbf{u}}{\partial t} \\ &= \tfrac{1}{2}|\mathbf{u}|^2(-\nabla\cdot(h\mathbf{u}) + Q) \\ &\quad + h\mathbf{u}\cdot\left(-(\mathbf{u}\cdot\nabla)\mathbf{u} - g\nabla h + (\mathbf{B}\cdot\nabla)\mathbf{B} + \mathbf{R} - \frac{\mathbf{u}}{\tau_{\text{drag}}} + \nu h^{-1}\nabla\cdot(h\boldsymbol{\tau})\right) \\ &= -\nabla\cdot(\tfrac{1}{2}h|\mathbf{u}|^2\mathbf{u}) + \cancel{h\mathbf{u}\cdot\nabla(\tfrac{1}{2}|\mathbf{u}|^2)} + \tfrac{1}{2}|\mathbf{u}|^2 Q \\ &\quad \cancel{-h\mathbf{u}\cdot[(\mathbf{u}\cdot\nabla)\mathbf{u}]} - \mathbf{u}\cdot\nabla(\tfrac{1}{2}gh^2) + \nabla\cdot[h(\mathbf{u}\cdot\mathbf{B})\mathbf{B}] - \cancelto{0}{(\mathbf{u}\cdot\mathbf{B})\nabla\cdot(h\mathbf{B})} \\ &\quad - h\mathbf{B}\cdot[(\mathbf{B}\cdot\nabla)\mathbf{u}] + h\mathbf{u}\cdot\mathbf{R} - \frac{h|\mathbf{u}|^2}{\tau_{\text{drag}}} + \nabla\cdot[\nu h\mathbf{u}\cdot\boldsymbol{\tau}^T] - \nu h\nabla\mathbf{u}:\boldsymbol{\tau} \\ &= -\nabla\cdot\left[\tfrac{1}{2}h|\mathbf{u}|^2\mathbf{u} - h(\mathbf{u}\cdot\mathbf{B})\mathbf{B} - \nu h\mathbf{u}\cdot\boldsymbol{\tau}\right] - \mathbf{u}\cdot\nabla(\tfrac{1}{2}gh^2) \\ &\quad - h\mathbf{B}\cdot[(\mathbf{B}\cdot\nabla)\mathbf{u}] - \tfrac{1}{2}\nu h|\boldsymbol{\tau}|^2 + \left[\tfrac{1}{2}|\mathbf{u}|^2 Q + h\mathbf{u}\cdot\mathbf{R}\right] - \frac{h|\mathbf{u}|^2}{\tau_{\text{drag}}}.\end{aligned} \tag{2.96}$$

where constant ν and symmetry in $\boldsymbol{\tau}$ (i.e., $\boldsymbol{\tau}^T = \boldsymbol{\tau}$) have been applied. From left to right, the terms in the final line of Equation (2.96) are the convergence of columnar kinetic energy flux, the columnar kinetic energy transport due to the Lorentz force, the columnar kinetic energy transport due to viscosity, the columnar rate of work from the advection of geopotential energy, the columnar rate of work from the Lorentz force, the columnar kinetic energy loss from viscous heating, the active layer's columnar kinetic energy loss from the Newtonian cooling, and the columnar kinetic energy loss from Rayleigh drag.

Similarly, the evolution of specific columnar magnetic energy can be determined by combining Equations (2.85b) and (2.92) with the divergence-free condition:

$$\begin{aligned}
\frac{\partial(\frac{1}{2}h|\mathbf{B}|^2)}{\partial t} &= \tfrac{1}{2}|\mathbf{B}|^2\frac{\partial h}{\partial t} + h\mathbf{B}\cdot\frac{\partial \mathbf{B}}{\partial t} \\
&= \tfrac{1}{2}|\mathbf{B}|^2(-\nabla\cdot(h\mathbf{u}) + Q) \\
&\quad + h\mathbf{B}\cdot\left((\mathbf{B}\cdot\nabla)\mathbf{u} - (\mathbf{u}\cdot\nabla)\mathbf{B} - \frac{\mathbf{B}Q}{h} - h^{-1}\nabla\times(\eta h\mathbf{J})\right) \\
&= -\nabla\cdot(\tfrac{1}{2}h|\mathbf{B}|^2\mathbf{u}) + \cancel{h\mathbf{u}\cdot\nabla(\tfrac{1}{2}|\mathbf{B}|^2)} + \tfrac{1}{2}|\mathbf{B}|^2 Q \\
&\quad + h\mathbf{B}\cdot[(\mathbf{B}\cdot\nabla)\mathbf{u}] - \cancel{h\mathbf{B}\cdot[(\mathbf{u}\cdot\nabla)\mathbf{B}]} - |\mathbf{B}|^2 Q \\
&\quad - \nabla\cdot[\eta h(\mathbf{J}\times\mathbf{B})] - \eta h\mathbf{J}\cdot(\nabla\times\mathbf{B}) \\
&= -\nabla\cdot\left[\tfrac{1}{2}h|\mathbf{B}|^2\mathbf{u} + \eta h(\mathbf{J}\times\mathbf{B})\right] \\
&\quad + h\mathbf{B}\cdot[(\mathbf{B}\cdot\nabla)\mathbf{u}] - \eta h|\mathbf{J}|^2 - \tfrac{1}{2}|\mathbf{B}|^2 Q.
\end{aligned} \tag{2.97}$$

From left to right, the terms in the final line of Equation (2.97) are the convergence of columnar magnetic energy flux, the columnar magnetic energy transport due to magnetic diffusion, the columnar rate of work from the Lorentz force, the columnar magnetic energy loss from Ohmic heating, and the change in columnar magnetic energy due to Newtonian cooling.

Finally, the evolution of specific columnar geopotential energy can be determined from

Equation (2.85b) as follows:

$$
\begin{aligned}
\frac{\partial(\frac{1}{2}gh^2)}{\partial t} &= gh\frac{\partial h}{\partial t} \\
&= gh(-\nabla\cdot(h\mathbf{u}) + Q) \\
&= -\nabla\cdot(gh^2\mathbf{u}) + (\mathbf{u}\cdot\nabla)(\tfrac{1}{2}gh^2) + ghQ.
\end{aligned}
\tag{2.98}
$$

From left to right, the terms in the final line of Equation (2.98) are the columnar geopotential energy transport due to the convergence of mass fluxes, the advection of columnar geopotential energy, and columnar geopotential "heating" from the Newtonian cooling.

Together, Equations (2.96) to (2.98) describe the evolution of the active layer's total specific columnar energy:

$$\frac{\partial E}{\partial t} + \nabla\cdot\mathbf{F} = \mathcal{Q}_\nu + \mathcal{Q}_\eta + \mathcal{Q}_f, \tag{2.99a}$$

$$\mathbf{F} = \left(\tfrac{1}{2}h|\mathbf{u}|^2 + gh^2\right)\mathbf{u} + \mathbf{S} - \nu h\mathbf{u}\cdot\boldsymbol{\tau}, \tag{2.99b}$$

$$\mathbf{S} = \tfrac{1}{2}h|\mathbf{B}|^2\mathbf{u} - h(\mathbf{u}\cdot\mathbf{B})\mathbf{B} + \eta h(\mathbf{J}\times\mathbf{B}), \tag{2.99c}$$

$$\mathcal{Q}_\nu = -\tfrac{1}{2}\nu h|\boldsymbol{\tau}|^2, \tag{2.99d}$$

$$\mathcal{Q}_\eta = -\eta h|\mathbf{J}|^2, \tag{2.99e}$$

$$\mathcal{Q}_f = \left(\tfrac{1}{2}|\mathbf{u}|^2 - \tfrac{1}{2}|\mathbf{B}|^2 + gh\right)Q + h\mathbf{u}\cdot\mathbf{R} - \frac{h|\mathbf{u}|^2}{\tau_{\text{drag}}}, \tag{2.99f}$$

where $\mathbf{F}$ describes the processes that conserve total specific columnar energy in the active layer, $\mathbf{S}$ is the diffusive shallow-water version of the Poynting vector, $\mathcal{Q}_\nu$ is the columnar kinetic energy loss from viscous heating, $\mathcal{Q}_\eta$ is the columnar magnetic energy loss from Ohmic heating, and $\mathcal{Q}_f$ is the rate of work due to the forcing and Rayleigh drag treatments.

The divergence of the shallow-water Poynting vector, $\nabla\cdot\mathbf{S}$, describes the transport of E out of a point, resulting from electromagnetism. In three-dimensional systems, the Poynting vector is defined as $\mathbf{S}_3 = \mathbf{E}_3\times\mathbf{B}_3$, where $\mathbf{E}_3$ is the electric field. Therefore, combining the non-relativistic version of Ampére's law ($\nabla_3\times\mathbf{B}_3 = \mu_0\mathbf{J}_3$) with Ohm's law in a moving medium ($\mathbf{J}_3 = \sigma(\mathbf{E}_3 + \mathbf{u}_3 \times \mathbf{B}_3)$) yields

$$\begin{aligned}\mathbf{S}_3 &= \mathbf{E}_3 \times \mathbf{B}_3 \\ &= (-\mathbf{u}_3 \times \mathbf{B}_3 + \frac{1}{\sigma}\mathbf{J}_3) \times \mathbf{B}_3 \\ &= \mathbf{B}_3 \times (\mathbf{u}_3 \times \mathbf{B}_3) + \eta\mu_0 \mathbf{J}_3 \times \mathbf{B}_3 \\ &= |\mathbf{B}_3|^2 \mathbf{u}_3 - (\mathbf{u}_3 \cdot \mathbf{B}_3)\mathbf{B}_3 + \eta\mu_0 \mathbf{J}_3 \times \mathbf{B}_3,\end{aligned} \tag{2.100}$$

where $\eta = 1/\mu_0\sigma$. The forms of Equations (2.99c) and (2.100) are similar but the shallow-water version of the Poynting vector is vertically integrated (with vertically independent horizontal components of $\mathbf{u}$ and $\mathbf{B}$) so each term of $\mathbf{S}$ has a prefactor h. Further, since magnetic pressure is absorbed into the total pressure in the magneto-hydrostatic approximation of SWHMD (see Section 2.2.2), the magnetic energy flux contribution of $\mathbf{S}$ is half its three-dimensional counterpart (as discussed in Hunter, 2015, for non-diffusive models). The diffusive term also differs from the three-dimensional version by a factor $1/\mu_0$ as the system's vertical independence allows us to work in the mathematically convenient units where $\mathbf{B}$ is in units of speed and $\mathbf{J}$ is in units of frequency.

From Equation (2.99), it is apparent that, in the unforced ($Q = 0$), drag-free ($\tau_{\text{drag}}^{-1} \to 0$), diffusion-free ($\nu = \eta = 0$) limit of a fully-periodic system (where boundary effects are neglected), total specific columnar energy is conserved. However, when forcing, drag, and/or diffusion are included within the SWMHD framework, energy sources and sinks are added. We now discuss the physical relevance of these sources/sinks.

The kinetic energy contribution that arises from Rayleigh drag (i.e., $-h|\mathbf{u}|^2/\tau_{\text{drag}}$) is negative semi-definite so only removes kinetic energy from the system, acting to dampen flows. The active layer motions are driven by the inclusion of the forcing Newtonian cooling forcing prescription, which generates pressure gradients by exchanging mass between the active and quiescent layers of our model. This enters the active layer's energy equation through the columnar geopotential "heating" contribution (i.e., ghQ). The kinetic energy contribution from the mass exchanges (i.e., $|\mathbf{u}|^2 Q/2+h\mathbf{u}\cdot\mathbf{R}$) is negative semi-definite so the exchanges only remove kinetic energy from the active layer, with damping of the specific columnar kinetic energy in equal to $-|\mathbf{u}|^2Q/2$ for $Q > 0$ and $|\mathbf{u}|^2Q/2$ for $Q < 0$. Due to the SWMHD requirement that no magnetic flux may cross the active-quiescent interface, the mass exchanges cause magnetic energy sinks/sources (i.e., $-|\mathbf{B}|^2Q/2$). This results from changes in the fluid column's volume, though we enforce the condition that the horizontal columnar magnetic field ($h\mathbf{B}$) remains unaffected by such exchanges (see Section 2.2.6). In the weakly forced regime, these magnetic energy sinks/sources are suppressed.

In Equations (2.99d) and (2.99e) $\mathcal{Q}_\nu = -\nu h|\boldsymbol{\tau}|^2/2$ and $\mathcal{Q}_\eta = -\eta h|\mathbf{J}|^2$, where $\boldsymbol{\tau} = \nabla\mathbf{u}+(\nabla\mathbf{u})^T$ and $\mathbf{J} = (\partial B_y/\partial x - \partial B_x/\partial y)\widehat{\mathbf{z}}$. Writing $\mathcal{Q}_\nu$ and $\mathcal{Q}_\eta$ in this way illustrates that $\mathcal{Q}_\nu$ and $\mathcal{Q}_\eta$ are both negative semi-definite (as h, ν, and η are strictly positive). In three-dimensional systems, the energy losses from $\mathcal{Q}_\nu$ and $\mathcal{Q}_\eta$ would normally be transferred into thermal energy but, since our shallow-water model does not include thermodynamics, the kinetic and magnetic energy removed by $\mathcal{Q}_\nu$ and $\mathcal{Q}_\eta$ is lost from the system.

Aside: Energy equation for Laplacian viscous diffusion

In Section 2.2.5 we noted that a naive Laplacian treatment of viscous diffusion, $\nu\nabla^2\mathbf{u}$, can produce energy sources arising from unphysical surfaces stresses (Gilbert *et al.*, 2014). To illustrate this we note that

$$\begin{aligned} h\mathbf{u}\cdot(\nu\nabla^2\mathbf{u}) &= \nabla\cdot[\nu h\mathbf{u}\cdot(\nabla\mathbf{u})^T] - \nu\nabla\mathbf{u} : \nabla(h\mathbf{u}) \\ &= \nabla\cdot[\nu h\mathbf{u}\cdot(\nabla\mathbf{u})^T] - \nu h|\nabla\mathbf{u}|^2 - \nu\nabla(\tfrac{1}{2}|\mathbf{u}|^2)\cdot\nabla h, \end{aligned} \tag{2.101}$$

where constant ν has been applied. Hence,

$$\frac{\partial E}{\partial t} + \nabla\cdot\mathbf{F}_{\nabla^2} = \mathcal{Q}_{\nu,\nabla^2} + \mathcal{Q}_\eta + \mathcal{Q}_f, \tag{2.102a}$$

$$\mathbf{F}_{\nabla^2} = \left(\tfrac{1}{2}h|\mathbf{u}|^2 + gh^2\right)\mathbf{u} + \mathbf{S} - \nu h\mathbf{u}\cdot(\nabla\mathbf{u})^T, \tag{2.102b}$$

$$\mathcal{Q}_{\nu,\nabla^2} = -\nu h|\nabla\mathbf{u}|^2 - \nu\nabla(\tfrac{1}{2}|\mathbf{u}|^2)\cdot\nabla h, \tag{2.102c}$$

with $\mathbf{S}$, $\mathcal{Q}_\eta$, and $\mathcal{Q}_f$ unchanged. This highlights that $\mathcal{Q}_{\nu,\nabla^2}$ is only guaranteed to be negative semi-definite if $\nabla h = 0$ everywhere for all time (i.e., in the two-dimensional limit).[11] However, generally, a Laplacian viscous diffusion treatment can provide spurious energy sources if layer thickness gradients are large in the direction antiparallel to pointwise kinetic energy gradients. This can be illustrated with a v constant and $\partial u/\partial y = 0$ flow, in which case pointwise kinetic energy gradients lie in the $\widehat{\mathbf{x}}$ or $-\widehat{\mathbf{x}}$ direction and

$$\mathcal{Q}_{\nu,\nabla^2} = -\nu h \left(\frac{\partial u}{\partial x}\right)^2 - \nu \frac{\partial(\frac{1}{2}u^2)}{\partial x}\frac{\partial h}{\partial x} = -\nu h \left(\frac{\partial u}{\partial x}\right)^2 - \nu u \frac{\partial u}{\partial x}\frac{\partial h}{\partial x}. \tag{2.103}$$

Therefore, since only the layer thickness gradient contribution to $\mathcal{Q}_{\nu,\nabla^2}$ can be positive, $\mathcal{Q}_{\nu,\nabla^2} > 0$ if

$$\left(\frac{\partial h}{\partial x}\right)\left(\frac{\partial(u^2/2)}{\partial x}\right) < 0 \quad \text{and} \quad \left|\frac{\partial(\ln|h|)}{\partial x}\right| > \left|\frac{\partial(\ln|u|)}{\partial x}\right|. \tag{2.104}$$

2.2.8 Horizontal boundary conditions and integral conservation laws

We now discuss horizontal boundary conditions for our system that are relevant to planetary geometries and, where possible, satisfy integral conservation laws. Recall that the horizontal Cartesian coordinates are defined on $-L_x \leq x \leq L_x$ and $-L_y \leq y \leq L_y$. Furthermore, as discussed in Section 2.2.3, in the equatorial beta-plane approximation y/R approximately corresponds to the latitudinal coordinate, with $y = 0$ corresponding to the equator. Similarly, x/R approximately corresponds to the azimuthal coordinate, which we are free to centre so that the substellar point, which in our model is the point of maximal h_{eq}, lies at $(x, y) = (0, 0)$.

We impose periodic boundary conditions on all variables in the x direction, choosing $L_x = R\pi$. In the y direction we impose impermeable walls at $y = \pm L_y$, which are stress-free. As in the vertical direction, at these y boundaries no normal magnetic flux (i.e., $\widehat{\mathbf{n}} \cdot \mathbf{B} = 0$) nor tangential currents (i.e., $\widehat{\mathbf{n}} \times (\nabla \times \mathbf{B}) = \mathbf{0}$) are permitted, where $\widehat{\mathbf{n}} = \pm\widehat{\mathbf{y}}$ is the horizontal outward-pointing unit normal vector and the second condition is consistent

[11] Note that, on the basis of matching $\mathbf{F}$ and $\mathbf{F}_{\nabla^2}$ in the two-dimensional limit, an argument could be made for taking $\boldsymbol{\tau} = \nabla\mathbf{u}$ in shallow-water models (as generally, $\mathbf{F} = (\frac{1}{2}h|\mathbf{u}|^2 + gh^2)\mathbf{u} + \mathbf{S} - \nu h\mathbf{u}\cdot\boldsymbol{\tau}^T$, if $\boldsymbol{\tau}$ is not necessarily symmetric). However, Gilbert *et al.* (2014) showed that this treatment behaves unphysically when exposed to solid body rotation and noted that symmetry in the stress tensor is important for angular momentum conservation.

with the impermeable walls constituting perfect conductors (see Section 2.2.5). Therefore, since $\mathbf{J} \equiv \nabla \times \mathbf{B} \equiv J\widehat{\mathbf{z}}$ is perpendicular to $\widehat{\mathbf{y}}$, we apply

$$v|_{y=\pm L_y} = 0, \quad \left.\frac{\partial u}{\partial y}\right|_{y=\pm L_y} = 0, \quad B_y|_{y=\pm L_y} = 0, \quad J|_{y=\pm L_y} = 0, \tag{2.105}$$

for all time. As noted above, we solve the system in terms of a magnetic flux function A. Using the definitions, $h\mathbf{B} \equiv \nabla \times A\widehat{\mathbf{z}}$ and $J \equiv (\nabla \times \mathbf{B}) \cdot \widehat{\mathbf{z}}$, we note that the evolution equation for A can be re-expressed as

$$\begin{aligned} \frac{\partial A}{\partial t} &= -(\mathbf{u} \cdot \nabla)A + \eta(\nabla^2 A - h^{-1}\nabla h \cdot \nabla A), \\ &= huB_y - hvB_x - \eta hJ, \end{aligned} \tag{2.106}$$

where $B_y = -h^{-1}\partial A/\partial x$. Hence, since $h > 0$, fixing $B_y|_{y=\pm L_y} = 0$ is equivalent to fixing $\partial A/\partial x|_{y=\pm L_y} = 0$ and, from Equation (2.106), fixing $v|_{y=\pm L_y} = B_y|_{y=\pm L_y} = J|_{y=\pm L_y} = 0$ maintains $\partial A/\partial t|_{y=\pm L_y} = 0$. Consequently, when we solve the system in terms of A, we fix $A|_{y=\pm L_y} = a_0$ for all time, where a_0 is some arbitrary constant (along $y = \pm L_y$). Finally, we note that for consistency in the governing equations and to conserve mass in boundary regions, we evaluate y-boundary values of h using the shallow-water continuity equation (Equation (2.85b)).

In summary, in our system we apply periodic boundary conditions at $x = \pm L_x = \pm R\pi$ and in the y direction we apply

$$v|_{y=\pm L_y} = 0, \quad \left.\frac{\partial u}{\partial y}\right|_{y=\pm L_y} = 0, \quad A|_{y=\pm L_y} = a_0, \tag{2.107}$$

for all time, where a_0 is some arbitrary constant and y-boundary values of h are updated using the shallow-water continuity equation (Equation (2.85b)). Since we are interested in equatorial dynamics, L_y is chosen so that these walls lie at high enough latitudes that the boundaries do not significantly influence equatorial regions.

In Appendix C, we derive some integral conservation laws that our system satisfies. The boundary conditions satisfy the integral form of shallow-water divergence-free condition,

$\iiint_{\mathcal{V}} \nabla_3 \cdot \mathbf{B}_3 \mathrm{d}x\mathrm{d}y\mathrm{d}z = \iint \nabla \cdot h\mathbf{B}\mathrm{d}x\mathrm{d}y = 0$, so magnetic monopoles are forbidden. The conditions also hold total horizontal magnetic flux, $\iint h\mathbf{B}\mathrm{d}x\mathrm{d}y$, constant for all time; conserve total active layer mass, $\iint h\mathrm{d}x\mathrm{d}y$, in the absence of prescribed mass exchanges; and preclude energy entering the system by any means other than the imposed forcing.

2.2.9 Non-dimensional governing equations

Thus far we have considered our model in dimensional units but it is often useful to work in non-dimensional units. Doing so makes sure we limit the number of parameters we input into our system and can be useful for gauging the relative importance of particular mathematical terms and physical processes a priori, particularly when working in the linear case with small amplitude forcing.

As discussed in Section 2.2.7, the dimensional governing equations of the forced reduced gravity SWMHD model are given by

$$\frac{\mathrm{D}\mathbf{u}}{\mathrm{D}t} + \beta y(\widehat{\mathbf{z}} \times \mathbf{u}) = -g\nabla h + (\mathbf{B} \cdot \nabla)\mathbf{B} + \mathbf{R} - \frac{\mathbf{u}}{\tau_{\mathrm{drag}}} + \nu h^{-1}\nabla \cdot (h\boldsymbol{\tau}), \tag{2.108a}$$

$$\frac{\partial h}{\partial t} + \nabla \cdot (h\mathbf{u}) = \frac{h_{\mathrm{eq}} - h}{\tau_{\mathrm{rad}}} \equiv Q, \tag{2.108b}$$

$$\frac{\mathrm{D}A}{\mathrm{D}t} = \eta(\nabla^2 A - h^{-1}\nabla h \cdot \nabla A). \tag{2.108c}$$

$$h\mathbf{B} \equiv \nabla \times A\widehat{\mathbf{z}}. \tag{2.108d}$$

We rescale the system so that

$$\mathbf{x} = L\tilde{\mathbf{x}}, \quad \mathbf{u} = \mathcal{U}\tilde{\mathbf{u}}, \quad h = H\tilde{\mathbf{h}}, \quad \mathbf{B} = \mathcal{B}\tilde{\mathbf{B}}, \quad A = HL\mathcal{B}\tilde{A}, \quad t = (L/\mathcal{U})\tilde{t}, \tag{2.109}$$

where tildes denote non-dimensional quantities and the typical horizontal length scale is L, the typical vertical length scale is H, the typical velocity scale is $\mathcal{U}$, the typical magnetic field strength (in velocity units) is $\mathcal{B}$, the typical scale of the magnetic flux function is $HL\mathcal{B}$, and the typical advective timescale is $L/\mathcal{U}$. Using this rescaling, multiplying Equation (2.108a) by $(L/\mathcal{U}^2)$, Equation (2.108b) by $(L/H\mathcal{U})$, Equation (2.108c) by $(1/H\mathcal{U}\mathcal{B})$, and Equation (2.108d) by $(1/H\mathcal{B})$ yields

$$\begin{aligned}\frac{\mathrm{D}\tilde{\mathbf{u}}}{\mathrm{D}\tilde{t}} + \frac{1}{Ro}\tilde{y}(\widehat{\mathbf{z}} \times \tilde{\mathbf{u}}) &= -\frac{1}{F^2}\tilde{\nabla}\tilde{h} + M^2(\tilde{\mathbf{B}} \cdot \tilde{\nabla})\tilde{\mathbf{B}} + Nc\tilde{\mathbf{R}} \\ &\quad - Dr\tilde{\mathbf{u}} + \frac{1}{Re}\tilde{h}^{-1}\tilde{\nabla} \cdot \left(\tilde{h}\tilde{\boldsymbol{\tau}}\right),\end{aligned} \tag{2.110a}$$

$$\frac{\partial \tilde{h}}{\partial \tilde{t}} + \tilde{\nabla} \cdot (\tilde{h}\tilde{\mathbf{u}}) = Nc(\tilde{h}_{\mathrm{eq}} - \tilde{h}) \equiv Nc\tilde{Q}, \tag{2.110b}$$

$$\frac{\mathrm{D}A}{\mathrm{D}\tilde{t}} = \frac{1}{Rm}(\tilde{\nabla}^2\tilde{A} - \tilde{h}^{-1}\nabla\tilde{h} \cdot \tilde{\nabla}\tilde{A}). \tag{2.110c}$$

$$\tilde{h}\tilde{\mathbf{B}} \equiv \tilde{\nabla} \times \tilde{A}\widehat{\mathbf{z}}. \tag{2.110d}$$

where $\tilde{h}_{\mathrm{eq}} = h_{\mathrm{eq}}/H$ and all variables are now non-dimensional and the non-dimensional vertical transport term is

$$\tilde{\mathbf{R}} = \begin{cases} 0 & \text{for } \tilde{Q} \leq 0, \\ -\frac{\tilde{\mathbf{u}}\tilde{Q}}{\tilde{h}} & \text{for } \tilde{Q} > 0. \end{cases} \tag{2.110e}$$

Additionally, we have defined seven dimensionless parameters (i.e., Ro, F, M, Nc, Dr, Re, and Rm), which we shall now discuss. The relevant *Rossby* number for the equatorial-beta plane approximation (see Section 2.2.3) is given by

$$Ro = \frac{\mathcal{U}}{\beta L^2}, \tag{2.111a}$$

and represents the ratio between the inertial and Coriolis forces. We comment that for $\mathcal{U} = c_g \equiv \sqrt{gH}$ and $L = L_{\mathrm{eq}} \equiv (c_g/\beta)^{1/2}$, $Ro = 1$. Hence, these scales represent a boundary between flows that are inertially ($Ro \gg 1$) and geostrophically ($Ro \ll 1$) dominated. The *Froude* number is given by

$$F = \frac{\mathcal{U}}{c_g}, \tag{2.111b}$$

and represents the balance between a characteristic horizontal velocity scale and the shallow-water gravity wave speed for the reduced gravity system. In the SWMHD system, the magnitude of F is determined by the magnitude of the prescribed forcing profile

$h_{\mathrm{eq}}(x, y)$. Since planetary flows are generally pressure driven, F is generally moderate. The *inverse Alfvén-Mach* number is given by

$$M = \frac{\mathcal{B}}{\mathcal{U}}, \tag{2.111c}$$

and represents the ratio of the characteristic horizontal Alfvén speed and the characteristic horizontal flow velocity. This depends on the magnetic field's magnitude, which is a free-parameter in our study. When $M \sim 1/F$ the Lorentz force becomes significant to the pressure driven flows. The *cooling* number is given by

$$Nc = \frac{L}{\mathcal{U}\tau_{\mathrm{rad}}}, \tag{2.111d}$$

and represents the ratio between the advective and radiative timescales. If $Nc \gtrsim 1$, layer thickness profiles are expected to be dominated by the system's forcing profile. The *drag* number is given by

$$Dr = \frac{L}{\mathcal{U}\tau_{\mathrm{drag}}}, \tag{2.111e}$$

and represents the ratio between the advective and drag timescales. If $Dr \gtrsim 1$, Rayleigh drag is expected to significantly dampen pressure driven flows. The *Reynolds* number is given by

$$Re = \frac{\mathcal{U}L}{\nu}, \tag{2.111f}$$

and represents the ratio between the inertial and viscous forces. Finally, the *magnetic Reynolds* number is given by

$$Rm = \frac{\mathcal{U}L}{\eta}, \tag{2.111g}$$

and represents the ratio between the horizontal advection and diffusion of the magnetic flux function that we impose to mimic the effects of the toroidal magnetic field in the Cartesian shallow-water geometry.

Table 2.1: Planetary parameters for HAT-P-7b. $T_{\rm eq}$ denotes the planet's orbit-averaged effective temperature, $t_{\rm orbit}$ denotes the orbital period, M denotes the planet's mass, and R denotes the planetary radius, which we give in both nominal Jupiter equatorial radii and metres.

$T_{\rm eq}\,(\mathrm{K})^a$	$t_{\rm orbit}\,(\mathrm{days})^a$	$M\,(M_J)^a$	$R\,(R_J)^a$	$R\,(\mathrm{m})$
2200	2.20	1.74	1.43	1.0×10^8

Data taken from www.exoplanet.eu, accessed May 30, 2021. $T_{\rm eq}$ is calculated as in Laughlin *et al.* (2011) and is given to 2 significant figures.

We comment that in Chapter 7 we consider a different *magnetic Reynolds number*:

$$R_m = \frac{U_\phi H}{\eta}, \tag{2.112}$$

which represents the ratio between the induction and diffusion of the toroidal field in three-dimensional geometry. This differs as in three-dimensional geometry the atmospheric toroidal field is induced by its interactions with zonal winds (with velocity U_ϕ) and the planet's assumed deep-seated poloidal magnetic field. In a three-dimensional system there are two degrees of freedom in the induction equation so these interactions can be modelled; whereas in the shallow-water system there is only one degree of freedom in the induction equation so poloidal-toroidal coupling cannot occur.

2.2.10 Parameter choices for hot Jupiter atmospheres

From Equations (2.108a) to (2.108d) it can be seen that the dimensional simulation parameters of the SWMHD model are c_g, β, H, $\tau_{\rm rad}$, $\tau_{\rm drag}$, ν, and η. Alongside these parameters, we prescribe a radiative equilibrium forcing profile, $h_{\rm eq}(x,y)$ and a purely-azimuthal initial horizontal magnetic field, $\mathbf{B}_0 \equiv B_0(y)\widehat{\mathbf{x}}$, which each have a parameter that defines their relative scale (discussed specifically in Chapter 4). In the solutions we present in this work we shall vary $\tau_{\rm rad}$ and $\tau_{\rm drag}$ (which vary Nc and Dr respectively), as well as the forms/scales of $h_{\rm eq}$ and B_0 (which vary F and M respectively).

Our choices for the remaining fixed simulation parameters (i.e., c_g, β, H, ν, and η) are based on the planetary parameters of HAT-P-7b, an ultra-hot Jupiter with observed east-west brightspot variations (Armstrong *et al.*, 2016) that can be well explained by

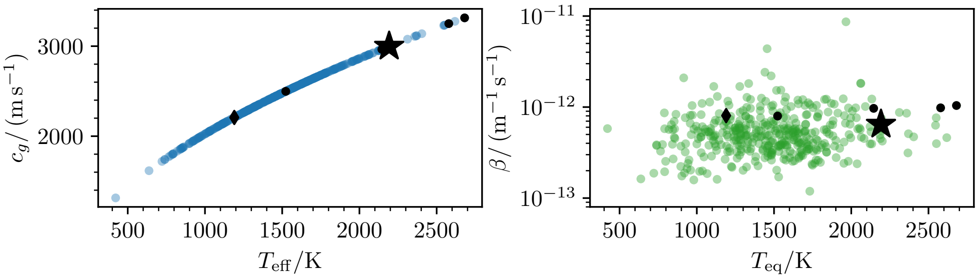

Figure 2.8: The shallow-water gravity wave speed, $c_g \sim (\mathcal{R}T_{\mathrm{eq}})^{1/2}$ (lefthand panel), and the equatorial beta-plane parameter, $\beta \equiv 2\Omega/R$ (righthand panel), are plotted (against T_{eq}) for known hot Jupiters. HAT-P-7b ($T_{\mathrm{eq}} \approx 2192\,\mathrm{K}$) is marked with a black opaque star, the cool hot Jupiter HD 189733b (whose parameters are briefly applied in Chapter 3) is marked with a black opaque diamond, and the hot Jupiters with observed westward hotspot/brightspots (other than HAT-P-7b) are marked with opaque black circles. These are CoRoT-2b ($T_{\mathrm{eq}} \approx 1523\,\mathrm{K}$), Kepler-76b ($T_{\mathrm{eq}} \approx 2145\,\mathrm{K}$), HAT-P-7b ($T_{\mathrm{eq}} \approx 2192\,\mathrm{K}$), WASP-12b ($T_{\mathrm{eq}} \approx 2578\,\mathrm{K}$), and WASP-33b ($T_{\mathrm{eq}}2681\,\mathrm{K}$). Due to its large atmospheric temperatures, HAT-P-7b has a fairly large c_g value. Typically, on hot Jupiters, $1.8\,\mathrm{km\,s^{-1}} \lesssim c_g \lesssim 3.2\,\mathrm{km\,s^{-1}}$; while $2 \times 10^{-13}\,\mathrm{m^{-1}\,s^{-1}} \lesssim \beta \lesssim 2 \times 10^{-12}\,\mathrm{m^{-1}\,s^{-1}}$.

three-dimensional MHD simulations (Rogers, 2017). Relevant planetary parameters of HAT-P-7b are presented in Table 2.1 and the corresponding simulation parameters are given in Table 2.2. As discussed above, we equate the active layer's reference geopotential with a radiative equilibrium thermal energy reference level. Therefore the gravity wave speed is set using $c_g \equiv \sqrt{gH} = \mathcal{R}T_{\mathrm{eq}}$, where we use the planet's orbit-averaged effective temperature for the equilibrium reference temperature and the specific gas constant is calculated using the solar system abundances in Lodders (2010). We assume synchronous orbits so $\Omega = 2\pi/t_{\mathrm{orbit}}$, with t_{orbit} denoting the planet's orbital period. Using these definitions, and the parameters in Table 2.1 we calculate $c_g \approx 3\,\mathrm{km\,s^{-1}}$ and $\beta \equiv 2\Omega/R = 6.6 \times 10^{-13}\,\mathrm{m^{-1}\,s^{-1}}$ for HAT-P-7b, which are typical of hot Jupiters (see Figure 2.8) and give the equatorial Rossby deformation radius as

$$L_{\mathrm{eq}} \equiv \left(\frac{c_g}{\beta}\right)^{1/2} \approx 6.7 \times 10^7\,\mathrm{m}. \tag{2.113}$$

This is a fundamental length scale over which gravitational and rotational effects balance and the interaction length scale of planetary scale flows. These also provide the

Table 2.2: Fixed simulation parameters for the shallow-water model of HAT-P-7b. c_g is the gravity wave speed, Ω is the planetary rotation frequency, H is the active layer thickness, η is the magnetic diffusivity, and ν is is the kinematic viscosity.

$c_g\,(\mathrm{m\,s^{-1}})$	$\beta\,(\mathrm{m^{-1}\,s^{-1}})$	$H\,(\mathrm{m})$	$\eta\,(\mathrm{m^2\,s^{-1}})$	$\nu\,(\mathrm{m^2\,s^{-1}})$
3.0×10^{3}	6.6×10^{-13}	4.3×10^{5}	4×10^{8}	4×10^{8}

The data for the calculated parameters (c_g, β, and H) is taken from www.exoplanet.eu, accessed June 12, 2019. The calculated parameters are given to 2 significant figures. The chosen values of η (realistic) and ν (large) are chosen to be small enough to make the dynamical timescales of our system much smaller than the diffusion timescales.

characteristic wave travel timescale:

$$\tau_{\mathrm{wave}} \equiv \frac{L_{\mathrm{eq}}}{c_g} \approx 2.2\times10^{4}\,\mathrm{s} \approx 0.26\ \text{Earth days}, \tag{2.114}$$

which is the time a shallow-water gravity wave takes to travel over the distance L_{eq}. We set the reference thickness of the model's active layer to the atmospheric pressure scale height, that is $H = H_p \equiv \mathcal{R}T_{\mathrm{eq}}R^2/GM = 4.3\times10^{5}\,\mathrm{m}$, where M is the planetary mass and G is Newton's gravitational constant. We comment that $H/L_{\mathrm{eq}} \simeq 6\times10^{-3} \ll 1$, so our parameter choices lie well within the range of validity of the shallow-water approximation. Recall that the typical vertical/horizontal length scale ratios on hot Jupiters are comparable, with $H/R \ll 1$ and $L_{\mathrm{eq}} \sim R$ (see Figure 1.10). Also, we comment that the traditional approximation (i.e., taking $\mathbf{\Omega} = \Omega\hat{\mathbf{z}}$), which we used to construct of model, is valid in the limit of strongly stable stratification, $N^2/\Omega^2 \gg 1$ (e.g., Vallis, 2006). An isothermal (magneto-)hydrostatic atmosphere has $N \sim c_g/H_p$ (see Chapter 1), so $N^2/\Omega^2 \sim (c_g/H_p)^2/(\beta R/2)^2 = 4(L_{\mathrm{eq}}/H_p)^2(L_{\mathrm{eq}}/R)^2 \sim 4\times10^{4} \gg 1$ (for length scale ratios, see Figure 1.10), so the traditional approximation is well-founded.

Generally, planetary flows are expected to have very large Reynolds numbers (i.e., planetary flows are highly turbulent), so realistic values cause numerical difficulties (e.g., Vallis, 2006; Showman *et al.*, 2010). The simulations presented in this work have a viscous diffusion of $\nu = 4\times10^{8}\,\mathrm{m^2\,s^{-1}}$ ($Re \sim 5\times10^{2}$ for $L \sim L_{\mathrm{eq}}$ and $\mathcal{U} \sim c_g$). In terms of "true" physical values, this diffusion coefficient is comparatively large; yet, upon checking, we find that viscous components of Equation (2.108a) remain negligibly small. This is to be expected as we are predominantly modelling bulk large-scale planetary flows, upon which viscous dissipation generally has little direct influence. We set the magnetic diffusivity to $\eta = 4 \times 10^8\,\mathrm{m}^2\,\mathrm{s}^{-1}$ ($Rm \sim 5 \times 10^2$ for $L \sim L_{\mathrm{eq}}$ and $\mathcal{U} \sim c_g$), which is within the expected η range in HAT-P-7b's atmosphere (Rogers, 2017). These values of η and ν are both small enough to make the dynamical timescales of our system much smaller than the diffusion timescales (typically $\tau_{\mathrm{dyn}}/\tau_\eta \sim$ 0.01-0.1, where τ_{dyn} is the longest dynamical timescale over which simulated solutions evolve.). In three-dimensional geometries, longitudinal variations in η are likely to play an important role in the evolution of the magnetic field, but we defer considerations of this more complicated problem to future work.

Chapter 3

Linear Waves of the SWMHD Model

In a hydrodynamic study, Showman & Polvani (2011) showed that the eastward equatorial winds on hot Jupiters are linked to energy and momentum redistribution arising from the planets' largest scale equatorially-confined shallow-water waves. Therefore, if we wish to understand the conditions under which magnetism can cause equatorial winds to reverse direction, it follows that we need to consider the role that magnetism plays in determining the characteristics of such planetary scale waves. In the past various authors have studied the linear waves present in rotating MHD systems. Early studies, which used quite general (usually uniform) flow/field geometries, focussed on the influence that these waves have on the geodynamo (Hide, 1966, 1969*b*; Acheson & Hide, 1973). However, since the development of SWMHD (Gilman, 2000), authors have been able to utilise its reduced geometry to study more specific flow/field geometries in thin-layered systems.

A series of investigations have studied the influence that rotating SWMHD waves have in the solar tachocline (Schecter *et al.*, 2001; Zaqarashvili *et al.*, 2007, 2009; Zaqarashvili, 2018), which like the atmosphere of hot Jupiters is expected to have an equatorially-antisymmetric toroidal dominant magnetic field geometry. Schecter *et al.* (2001) studied waves in the local regions of the solar tachocline; whereas Zaqarashvili *et al.* (2007, 2009) studied their global influence for the two extreme cases ($\epsilon \gg 1$ and/or $\epsilon \ll 1$) of the parameter $\epsilon = 4\Omega^2 R^2/c_g^2$, which compares the relative importance of stratification and rotation. These two extremes are applicable for the innermost and outermost regions of the solar tachocline however the HAT-P-7b parameter space used in this work gives $\epsilon \approx 4.8$. Zaqarashvili (2018) studied the equatorial SWMHD waves in the presence of a uniform and an equatorially-antisymmetric (latitudinally-linear) azimuthal background magnetic field using an equatorial beta-plane model. We shall apply some of these results to the hot Jupiter parameter regime in this chapter in order to obtain some intuition of the waves in the system. However, we must be aware that the study of Zaqarashvili (2018) used weakly-magnetic assumptions that the hot Jupiter regime is likely to violate. Further, London (2017) and London (2018) studied some asymptotic solutions of the beta-plane and spherical version of the system, with an equatorially-antisymmetric azimuthal field, in certain weak and strong field limits, but we wish to study the transition where magnetism becomes dynamically important.

The rotating SWMHD system has also been studied for other magnetic field geometries. Heng & Spitkovsky (2009) used the rotating SWMHD system to study Type I X-ray bursts from neutron stars with an initially radial magnetic field geometry. Márquez-Artavia *et al.* (2017) carried out a comprehensive study of rotating SWMHD waves with an azimuthal magnetic field in spherical geometry, across a large region of parameter space. However, as the toroidal magnetic field in their system was symmetric about the equator (with an equatorial maximum), it is unclear how their findings relate to the hot Jupiter system, which is expected to have an equatorially-antisymmetric dominant field geometry.

3.1 Linearised SWMHD equations

To study the linear equatorial waves of the system, we linearise the non-diffusive, unforced, drag-free versions of the dimensional governing equations of the reduced gravity SWMHD model of Chapter 2 (i.e., Equations (2.108a) to (2.108d)). In this limit, the governing equations of the reduced gravity SWMHD system reduce to

$$\frac{\mathrm{D}\mathbf{u}}{\mathrm{D}t} + f(\widehat{\mathbf{z}} \times \mathbf{u}) = -g\nabla h + (\mathbf{B}\cdot\nabla)\mathbf{B}, \tag{3.1a}$$

$$\frac{\partial h}{\partial t} + \nabla\cdot(h\mathbf{u}) = 0, \tag{3.1b}$$

$$\frac{\mathrm{D}A}{\mathrm{D}t} = 0, \tag{3.1c}$$

$$h\mathbf{B} \equiv \nabla \times A\widehat{\mathbf{z}}, \tag{3.1d}$$

which are mathematically identical to the governing equations of the single layer SWMHD model of Gilman (2000) (i.e., Equations (2.10), (2.16), (2.23) and (2.29) in Chapter 2). Consequently, we can use results of single layer SWMHD models to inform on the behaviours of freely propagating waves in the reduced gravity SWMHD system. These freely propagating waves should prove insightful provided that their travel timescales are shorter than the timescales of diffusion, drags, and radiative heating/cooling in the full model (i.e., $Re \gg 1, Rm \gg 1, Nc \ll 1, Dr \ll 1$).

We linearise Equations (3.1a) to (3.1d) about the background state, $\{u_0, v_0, h_0, A_0\} = \{0, 0, H, A_0(y)\}$, where H is the (constant) background layer thickness and A_0 is defined such that $\mathrm{d}A_0/\mathrm{d}y = HB_0$ for some generally latitudinally-dependent azimuthal background magnetic field, $\mathbf{B}_0 = B_0(y)\widehat{\mathbf{x}}$, which is in velocity units. The evolution of the perturbations to this background state is determined by the following linearised SWMHD system:

$$\frac{\partial u_1}{\partial t} = fv_1 - g\frac{\partial h_1}{\partial x} + B_0\frac{\partial B_{x,1}}{\partial x} + \frac{\mathrm{d}B_0}{\mathrm{d}y}B_{y,1}, \tag{3.2a}$$

$$\frac{\partial v_1}{\partial t} = -fu_1 - g\frac{\partial h_1}{\partial y} + B_0\frac{\partial B_{y,1}}{\partial x}, \tag{3.2b}$$

$$\frac{\partial h_1}{\partial t} = -H\left(\frac{\partial u_1}{\partial x} + \frac{\partial v_1}{\partial y}\right), \tag{3.2c}$$

$$\frac{\partial A_1}{\partial t} = -HB_0v_1, \tag{3.2d}$$

$$B_{x,1} = \frac{1}{H}\left(\frac{\partial A_1}{\partial y} - B_0h_1\right), \tag{3.2e}$$

$$B_{y,1} = -\frac{1}{H}\frac{\partial A_1}{\partial x}, \tag{3.2f}$$

where subscripts of unity denote perturbations from the background state, we use the Cartesian coordinates that we introduced in Chapter 2, in which x, y, and z respectively denote the eastward, northward, and vertical coordinates.

3.2 Plane wave solutions for a uniform background field

The simplest results can be obtained using a uniform background magnetic field,

$$\mathbf{B}_0 = V_\mathrm{A}\widehat{\mathbf{x}}, \tag{3.3}$$

where V_A is a constant background Alfvén speed. Likewise, simplest way to study waves in the presence of a latitudinally varying planetary vorticity is with a beta-plane treatment of the Coriolis parameter (e.g., Vallis, 2006):

$$f = f_0 + \beta y, \tag{3.4}$$

where $f_0 \equiv f(y_0) = 2\mathit{\Omega}\sin\theta_0$ is the value of the Coriolis parameter at some reference latitude, $\theta_0 \equiv y_0/R$, and $\beta \equiv \mathrm{d}f/\mathrm{d}y|_{y=0} = (2\mathit{\Omega}/R)\cos\theta_0$ is the Coriolis parameter's first order local latitudinal variation. Note that this treatment only differs from the equatorial beta-plane approximation discussed in Chapter 2 (Section 2.2.3), in the respect that θ_0 is kept general for convenience. As before, Equation (3.4) is obtained via a Taylor expansion about y_0, where f_0 and βy are respectively the $O(1)$ and $O(y/R)$ terms. The key difference between this general beta-plane treatment and the equatorial beta-plane treatment that we use elsewhere in this work is that y is centred about the reference latitude, θ_0, rather than the equator.

Using the simple treatments of Equations (3.3) and (3.4), Equations (3.2a) to (3.2f) can be simplified to

$$\frac{\partial u_1}{\partial t} = (f_0 + \beta y)v_1 - g\frac{\partial h_1}{\partial x} + V_{\mathrm{A}}\frac{\partial B_{x,1}}{\partial x}, \tag{3.5a}$$

$$\frac{\partial v_1}{\partial t} = -(f_0 + \beta y)u_1 - g\frac{\partial h_1}{\partial y} + V_{\mathrm{A}}\frac{\partial B_{y,1}}{\partial x}, \tag{3.5b}$$

$$\frac{\partial h_1}{\partial t} = -H\left(\frac{\partial u_1}{\partial x} + \frac{\partial v_1}{\partial y}\right), \tag{3.5c}$$

$$\frac{\partial B_{x,1}}{\partial t} = V_{\mathrm{A}}\frac{\partial u_1}{\partial x}, \tag{3.5d}$$

$$\frac{\partial B_{y,1}}{\partial t} = V_{\mathrm{A}}\frac{\partial v_1}{\partial x}. \tag{3.5e}$$

If $|y/R| \ll 1$, $|\beta y| \ll |f_0|$ and the coefficients of all the terms in this linear set of equations are approximately constant. Therefore, Equations (3.5a) to (3.5e) may be approximately solved with the plane wave ansatz:

$$(u_1, v_1, h_1, B_{x,1}, B_{y,1}) = (\hat{u}, \hat{v}, \hat{h}, \hat{B}_x, \hat{B}_y)\mathrm{e}^{i(kx+ly-\omega t)}, \tag{3.6}$$

where hatted variables are amplitudes of the plane wave solutions, k is the azimuthal wavenumber, l is the latitudinal wavenumber, and ω is the oscillation frequency. Combining Equation (3.6) with Equations (3.5a) to (3.5e), and seeking solutions that are first order in the Coriolis parameter only, yields the following dispersion relation (Zaqarashvili *et al.*, 2007; Heng & Spitkovsky, 2009):

$$\omega^4 - \omega^2(K^2c_g^2 + 2k^2V_{\mathrm{A}}^2 + f_0^2) - \omega\beta kc_g^2 + k^2V_{\mathrm{A}}^2(K^2c_g^2 + k^2V_{\mathrm{A}}^2) = 0, \tag{3.7}$$

for arbitrary wave amplitudes, where $K \equiv (k^2 + l^2)^{1/2}$ is the magnitude of the horizontal wavevector, $\mathbf{k} \equiv (k, l)$, and $c_g \equiv (gH)^{1/2}$ is the (rotationless) shallow-water gravity wave speed.

3.2.1 Waves in a non-rotating system

First, it is illustrative to consider wave-like solutions in the rotation-free limit ($f_0 = \beta = 0$), whereby Equation (3.7) reduces to give

$$(\omega^2 - (K^2 c_g^2 + k^2 V_\mathrm{A}^2))(\omega^2 - k^2 V_\mathrm{A}^2) = 0. \tag{3.8}$$

Hence, we have four solutions (Schecter *et al.*, 2001):

$$\omega^2 = \begin{cases} c_m^2 k^2 + c_g^2 l^2, & (3.9\mathrm{a}) \\ V_\mathrm{A}^2 k^2, & (3.9\mathrm{b}) \end{cases}$$

where $c_m \equiv (c_g^2 + V_\mathrm{A}^2)^{1/2}$ is the magneto-gravity wave speed in the direction of the background field (i.e., the azimuthal direction). The two solutions given by Equation (3.9a) represent horizontally propagating *magneto-gravity* waves, which are waves driven by a combination of gravitational restoration and magnetic tension; whereas the two solutions given by Equation (3.9b) are *Alfvén waves*, which are driven by magnetic tension and travel parallel to the background magnetic field. In the hydrodynamic limit ($V_\mathrm{A} = 0$), the solutions given by Equation (3.9b) are lost and Equation (3.9a) reduces to the shallow-water gravity wave dispersion relation, which we discussed for the one-dimensional case in Chapter 1. We comment that, since the Alfvén waves in a uniform purely-azimuthal background travel azimuthally with the non-dispersive oscillation frequency, $\omega = \pm V_\mathrm{A} k$, they travel like solitons, maintaining their shape, energy, and angular momentum, unless acted on by drag/diffusion.

Next we include rotation. We shall refer to rotationally modified magneto-gravity waves as being in the "fast" or "magneto-gravity branch" and rotationally modified Alfvén waves as being in the "slow" or "Alfvén branch" of solutions (as in Schecter *et al.*, 2001).

3.2.2 f-plane solutions

Here we consider plane wave solutions in the absence of a latitudinal planetary vorticity gradient, $\beta = 0$. This is often referred to as the *f-plane* (e.g., Vallis, 2006). These are the modes which dominate at the poles as $f \sim f_0$ and $\beta \sim 0$. In this limit, Equation (3.7) reduces to

$$\omega^4 - \omega^2(K^2c_g^2 + 2k^2V_\mathrm{A}^2 + f_0^2) + k^2V_\mathrm{A}^2(K^2c_g^2 + k^2V_\mathrm{A}^2) = 0, \tag{3.10}$$

and has solutions satisfying

$$\omega^2 = \frac{K^2c_g^2}{2} + k^2V_\mathrm{A}^2 + \frac{f_0^2}{2} \pm \frac{1}{2}\sqrt{K^2c_g^2(K^2c_g^2 + 2f_0^2) + f_0^2(f_0^2 + 4k^2V_\mathrm{A}^2)}, \tag{3.11}$$

which is equivalent to the solutions found by in Heng & Spitkovsky (2009) but with an azimuthal, rather than vertical, magnetic field geometry. The two high frequency solutions with a positive plus/minus sign in Equation (3.11) belong to the magneto-gravity branch and travel in opposite directions in order to restore pressure gradients and magnetic tension, but with a Coriolis modification. Heng & Spitkovsky (2009) link these to magneto-Poincaré waves (as they reduce to the hydrodynamic Poincaré wave for $V_\mathrm{A} = 0$); while other authors (e.g., Márquez-Artavia *et al.*, 2017; Zaqarashvili, 2018) refer to them as magneto-inertial gravity waves (and inertial gravity waves). We choose the inertial gravity/magneto-inertial gravity nomenclature and, hereafter, we use the MIG abbreviation used by Márquez-Artavia *et al.* (2017). The two lower frequency solutions with a negative plus/minus sign in Equation (3.11) belong to the Alfvén branch, and drive a restoring force that balances magnetic tension and the Coriolis force. Heng & Spitkovsky (2009) termed these magnetostrophic waves and find them to be restricted to the poles of their model.

3.2.3 Alfvén-Rossby wave coupling (general beta-plane)

Next we consider the full dispersion relation given in Equation (3.7), which includes the effects of the latitudinal planetary vorticity gradient. The inclusion of the third term in this dispersion equation means that Equation (3.7) cannot be directly solved (easily). For the fast branch MIG waves the quartic and quadratic terms dominate the polynomial and solutions resemble the f-plane solutions (Hide, 1966; Acheson & Hide, 1973; Zaqarashvili *et al.*, 2007; Heng & Spitkovsky, 2009). However, in the slow branch, this planetary vorticity gradient term generally has an important effect. Some intuition can be gained by using a slow wave ($|\omega|/|2\Omega| \ll 1$) limit, and evaluating the general beta-plane approximation at the equator ($f_0 = 0$ and $\beta = 2\Omega/R$). This yields

$$\omega^2((c_m^2 + V_{\mathrm{A}}^2)k^2 + c_g^2 l^2) + \omega\beta k c_g^2 - k^2 V_{\mathrm{A}}^2(c_m^2 k^2 + c_g^2 l^2) = 0, \tag{3.12}$$

which has solutions that satisfy

$$\omega = \frac{-\beta k c_g^2 \mp \sqrt{(\beta k c_g^2)^2 + 4k^2 V_{\mathrm{A}}^2 (c_m^2 k^2 + c_g^2 l^2)((c_m^2 + V_{\mathrm{A}}^2)k^2 + c_g^2 l^2)}}{2((c_m^2 + V_{\mathrm{A}}^2)k^2 + c_g^2 l^2)}, \tag{3.13}$$

which, again, is equivalent to the solutions found by in Heng & Spitkovsky (2009) but with an azimuthal, rather than vertical, magnetic field geometry. These modes now represent rotationally modified waves in the slower Alfvén branch, with the inclusion of the effects caused by the introduction of the latitudinal planetary vorticity gradient. Indeed, in the limit where these solutions are dominated by the Alfvén speed, these become like Alfvén waves in nature (see by taking V_{A} dominatingly large). Further understanding of these Alfvén branch solutions can be gained by considering their reduction in the hydrodynamic limit ($V_{\mathrm{A}} = 0$):

$$\omega = \begin{cases} -\beta k/K^2, & (3.14\text{a}) \\ 0. & (3.14\text{b}) \end{cases}$$

Hence, in the hydrodynamic limit one of the two Alfvén branch solutions vanishes but the other persists. The remaining solution given by Equation (3.14a) can be recognised as the dispersion relation for hydrodynamic Rossby waves (see Equation (1.29) in Chapter 1).

This Alfvén-Rossby wave coupling is a well-documented feature of MHD in systems with a latitudinally dependent planetary vorticity (Hide, 1966, 1969*b*; Acheson & Hide, 1973; Diamond *et al.*, 2007; Zaqarashvili *et al.*, 2007, 2009; Heng & Spitkovsky, 2009; Márquez-Artavia *et al.*, 2017; Zaqarashvili, 2018) and raises some important questions. Firstly, when magnetic fields are introduced to the system, an extra eastward wave is recovered compared to the hydrodynamic case. What is the nature of this extra solution?

Table 3.1: Parameters for the shallow-water model of HAT-P-7b. c_g is the gravity wave speed, Ω is the planetary rotation frequency, R is the planetary radius, and H is the active layer thickness. These parameter choices are discussed in Chapter 2.

$c_g\,(\mathrm{m\,s^{-1}})$	$\beta\,(\mathrm{m^{-1}\,s^{-1}})$	$R\,(\mathrm{m})$	$H\,(\mathrm{m})$
3.0×10^3	6.6×10^{-13}	1×10^8	4.3×10^5

Secondly, the westward wave is some kind of Alfvén-Rossby hybrid. However, Alfvén waves are non-dispersive and travel in a direction aligned with the dominant azimuthal magnetic field geometry; whereas the Rossby waves are highly dispersive, behave geostrophically, and transfer energy and angular momentum to the surrounding system (in a manner that is important for hydrodynamic planetary circulation; see Chapter 1). Which characteristics does this hybrid wave possess and how does this affect the planetary dynamics of hot Jupiters (if at all)? The answers to these questions are subtle and will be answered through much of our discussions in the remainder of this chapter and through the work of Chapter 5.

First and foremost, some initial hints to these answers can be gleaned from considering the nature of the westward solution of Equation (3.13) and the dispersion relationships of the westward Alfvén wave and the Rossby wave. As highlighted by Hide (1966), Hide (1969*b*), and Acheson & Hide (1973), comparing the oscillation frequency of Rossby (ω_R) and Alfvén (ω_A) waves gives

$$|\omega_\mathrm{R}/\omega_\mathrm{A}| = \beta/V_\mathrm{A}(k^2 + l^2), \tag{3.15}$$

suggesting that, for given choices of β and $V_{\mathrm{A},0}$, Rossby wave characteristics dominate at large scales (i.e., smallest wavenumbers); whereas the westward Alfvén characteristics dominate at small scales (i.e., largest wavenumbers). Hence, for a given choice of V_A, there should be some scale at which this westward hybrid wave changes nature from one to the other.

We examine this in Figure 3.1, where we plot the oscillation frequencies corresponding to the solutions of unsimplified plane wave dispersion relation of Equation (3.7). In Figure 3.1, Equation (3.7) is solved directly for $-5/R < k < 5/R$, where positive/negative k

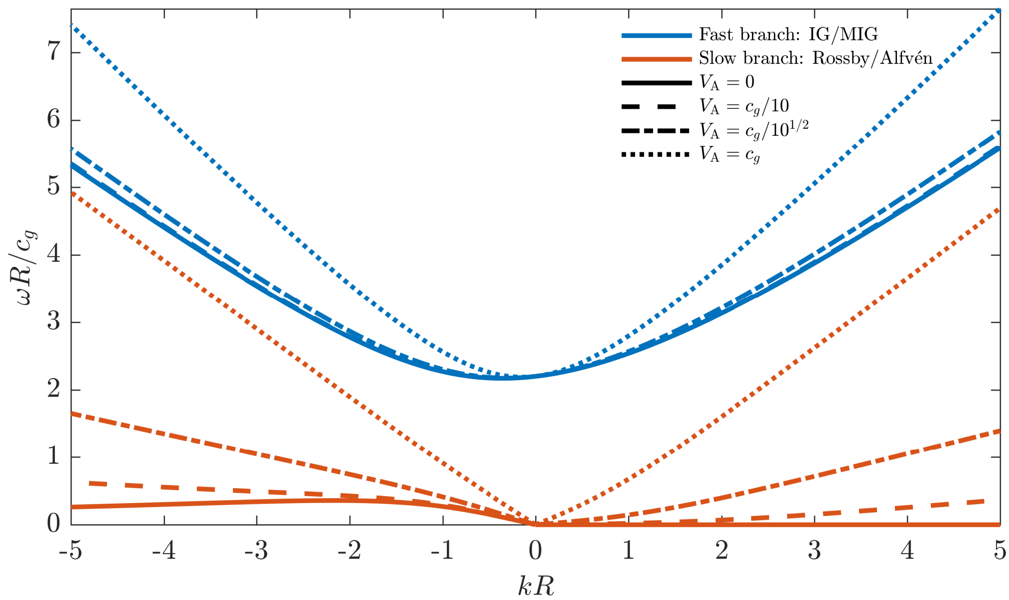

Figure 3.1: The fast (blue) and slow (red) branch solutions of Equation (3.7), which results from the local plane wave and general beta-plane approximations, are plotted for $5/R < k < 5/R$ with the constant azimuthal background Alfvén speeds $V_A = 0$ (hydrodynamic, solid lines), $V_A = c_g/10$ (dashed lines), $V_A = c_g/10^{1/2}$ (dot-dashed), and $V_A = c_g$ (dotted lines). The general beta-plane approximation is evaluated at $\theta_0 = \pi/4$ (mid-latitudes) and we set $l = L_D^{-1} = (c_g/f_0)^{-1}$. The parameters of HAT-P-7b that were discussed in Chapter 2 were used (see Table 3.1).

corresponds to an eastward/westward propagating phase, using MATLAB's in-built polynomial root finding methods. For this, we use the parameters of HAT-P-7b discussed in Chapter 2 (see Table 3.1), taking $\theta_0 = \pi/4$, $l = L_D^{-1} = (c_g/f_0)^{-1}$, and using the uniform azimuthal background magnetic field stengths $V_\mathrm{A} = 0$ (solid lines), $V_\mathrm{A} = c_g/10$ (dashed lines), $V_\mathrm{A} = c_g/10^{1/2}$ (dot-dashed lines), and $V_\mathrm{A} = c_g$ (dotted lines). The fast branch waves (i.e., the inertial gravity/MIG waves) are plotted in blue; whereas the slow branch waves are plotted in red. For hot Jupiters, the choices $V_\mathrm{A} = c_g/10$ and $V_\mathrm{A} = c_g/10^{1/2}$ are fairly weak/moderate; whereas the choice $V_\mathrm{A} = c_g$ is relatively extreme. That said, in their simulations Rogers & Komacek (2014) found that the toroidal field can reach energy equipartition, so $V_\mathrm{A} = c_g$ is not unreasonable in the hottest hot Jupiters.

The fast branch MIG waves are relatively unaffected by magnetism until $V_\mathrm{A} \sim c_g$, at which point it behaves like a magneto-gravity wave and rotation plays only a minor role. For the westward Alfvén-Rossby hybrid wave, solutions undergo a transition in nature at azimuthal length scales depending on (non-zero) V_A. At small azimuthal scales these solutions have an azimuthal group velocity that is approximately independent of k and the solution is Alfvénic in nature; whereas at some intermediate scale, which depends on V_A, the solution transitions in nature and the azimuthal group velocity becomes dispersive, like a Rossby wave. At large azimuthal length scales the eastward slow branch wave oscillates slower than the westward slow branch wave and its nature is not obvious. However, at small azimuthal length scales its dispersion relation converges to that of an Alfvén wave. To understand these solutions more completely, we need to move away from the approximate plane wave treatment of Equations (3.5a) to (3.5e), in the latitudinal direction, and consider the system exactly.

3.3 Equatorial shallow-water waves

We now study Equations (3.2a) to (3.2f), using the equatorial beta-plane approximation[1], $f = \beta y$, and various choices of $\mathbf{B}_0 = B_0\hat{\mathbf{x}}$, including the hydrodynamic case ($B_0 = 0$),

[1]Hereafter, we shall always use the equatorial beta-plane approximation (as opposed to the general beta-plane approximation), so "equatorial" may be dropped, though we shall attempt to avoid this.

with the plane wave ansatz:

$$\{u_1, v_1, h_1, A_1, B_{x,1}, B_{y,1}\} = \{\hat{u}(y), \hat{v}(y), \hat{h}(y), \hat{A}(y), \hat{B}_x(y), \hat{B}_y(y)\}\mathrm{e}^{i(kx-\omega t)}, \tag{3.16}$$

on time and the azimuthal direction, but not the latitudinal direction. This yields

$$-i\omega\hat{u} = \beta y\hat{v} - ikg\hat{h} + ikB_0\hat{B}_x + \frac{\mathrm{d}B_0}{\mathrm{d}y}\hat{B}_y, \tag{3.17a}$$

$$-i\omega\hat{v} = -\beta y\hat{u} - g\frac{\mathrm{d}\hat{h}}{\mathrm{d}y} + ikB_0\hat{B}_y, \tag{3.17b}$$

$$-i\omega\hat{h} = -H\left(ik\hat{u} + \frac{\mathrm{d}\hat{v}}{\mathrm{d}y}\right), \tag{3.17c}$$

$$-i\omega\hat{A} = -HB_0\hat{v}, \tag{3.17d}$$

where $\hat{B}_x = (\mathrm{d}\hat{A}/\mathrm{d}y - B_0\hat{h})/H$ and $\hat{B}_y = -ik\hat{A}/H$.

3.3.1 Hydrodynamic equatorial shallow-water waves

The hydrodynamic solutions to this system are termed equatorial shallow-water waves and were first studied by Matsuno (1966). On rotating spheres equatorial wave trapping, due to latitudinal variations in the Coriolis parameter, can amplify the signals of linear waves and increase their importance to system dynamics. Equatorial trapping of this kind arises as meridionally propagating planetary scale waves experience the latitudinal variations in f and, to adjust to these changes, their latitudinal wavenumber, l, decreases as they travel poleward. If the planetary rotation rate is large enough ($Ro \lesssim 1$), l vanishes at some critical latitude, over which waves may not propagate meridionally. Consequently, the energy associated with these waves is reflected back into the equatorial region, causing the linear superposition of equatorial shallow-water waves (i.e., eastward or westward propagating organised structures of velocity and geopotential), to have unusually strong signals at the equator (e.g., Pedlosky, 2013). Matsuno (1966) studied these (hydrodynamic) equatorially-trapped waves using the hydrodynamic versions of Equations (3.17a) to (3.17d):

$$-i\omega\hat{u} = \beta y\hat{v} - ikg\hat{h}, \tag{3.18a}$$

$$-i\omega\hat{v} = -\beta y\hat{u} - g\frac{\mathrm{d}\hat{h}}{\mathrm{d}y}, \tag{3.18b}$$

$$-i\omega\hat{h} = -H\left(ik\hat{u} + \frac{\mathrm{d}\hat{v}}{\mathrm{d}y}\right), \tag{3.18c}$$

where $\hat{A}$, $\hat{B}_x$, and $\hat{B}_y$ are identically zero everywhere. Together, Equations (3.18a) and (3.18c) yield

$$\hat{u} = \frac{i}{\omega^2 - c_g^2 k^2}\left(\omega\beta y\hat{v} - c_g^2 k\frac{\mathrm{d}\hat{v}}{\mathrm{d}y}\right). \tag{3.19}$$

Hence, for non-trivial solutions (i.e., $\hat{v}$ not identically zero everywhere), this can be substituted back into Equations (3.18b) and (3.18c) to provide

$$\frac{\mathrm{d}^2\hat{v}}{\mathrm{d}y^2} + \left(\frac{\omega^2 - c_g^2k^2}{c_g^2} - \frac{k\beta}{\omega} - \frac{\beta^2}{c_g^2}y^2\right)\hat{v} = 0. \tag{3.20}$$

Taking $\tilde{y} = y/L_{\mathrm{eq}}$ for $L_{\mathrm{eq}} \equiv (c_g/\beta)^{1/2}$, has the non-dimensional form (Matsuno, 1966):

$$\frac{\mathrm{d}^2\hat{v}}{\mathrm{d}\tilde{y}^2} + \left(\frac{\omega^2 - c_g^2k^2}{c_g\beta} - \frac{kc_g}{\omega} - \tilde{y}^2\right)\hat{v} = 0. \tag{3.21}$$

This is equation is known as the parabolic cylinder equation and, for infinite-bounded boundary conditions, $\hat{v} \to 0$ as $|y| \to \infty$, the meridional structure of its eigenfunctions can be written in terms of the parabolic cylinder functions of the first kind[2] (Abramowitz & Stegun, 1965; Matsuno, 1966):

$$\psi_n(y) \equiv C_n H_n(y/L_{\mathrm{eq}})\exp(-y^2/2L_{\mathrm{eq}}^2), \tag{3.22}$$

with $\hat{v} \propto \psi_n$, for $n = 0, 1, 2, \ldots$. In this equation H_n are Hermite polynomials of degree n (i.e., $H_0 = 1$, $H_1 = 2\tilde{y}$, $H_2 = 4\tilde{y}^2 - 2$, $H_3 = 8\tilde{y}^3 - 12\tilde{y}$, etc.) and the coefficient C_n is an arbitrary constant of integration. To illustrate their form, we plot the first few parabolic

[2]Only parabolic cylinder functions of the first kind satisfy the infinite-bounded boundary conditions, $\hat{v} \to 0$ as $|y| \to \infty$ (Abramowitz & Stegun, 1965).

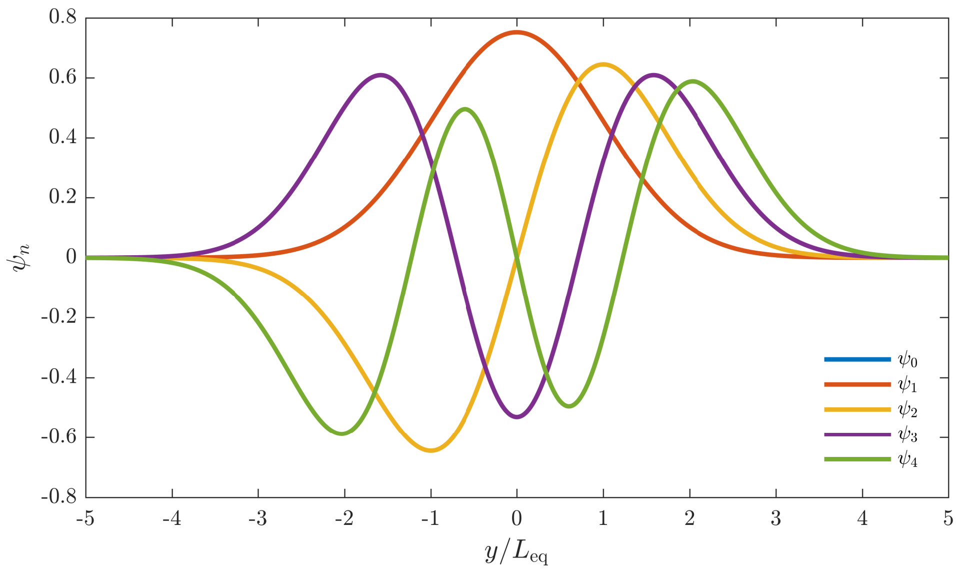

Figure 3.2: The parabolic cylinder functions of the first kind, ψ_n, as described in Equation (3.22), for $n = 0, 1, 2, 3, 4$. For the arbitrary constant, $C_n = (2^n n! \pi^{1/2})^{-1/2}$ is chosen so that ψ_n are orthonormal (Abramowitz & Stegun, 1965).

cylinder functions (of the first kind) in Figure 3.2, noting that their meridional profiles are oscillatory close to the equator ($y = 0$) and decay exponentially at higher latitudes. Using the recurrence relationship associated with the parabolic cylinder function, one can show that these eigenfunctions satisfy Equation (3.21) if the constant coefficients of $\hat{v}$ in Equation (3.21) equal $2n + 1$. This yields the equatorial shallow-water wave dispersion relation (Matsuno, 1966):

$$\frac{\omega^2}{\beta c_g} - \frac{k^2 c_g}{\beta} - \frac{k c_g}{\omega} = 2n + 1. \tag{3.23}$$

Equation (3.23) is cubic in ω, so generally (for $n \geq 1$) there are three different solutions for each n: two inertial gravity waves (one east and one west) and one Rossby wave. Matsuno (1966) also noticed that, for $n = 0$, Equation (3.23) can be factorised to give

$$(\omega + c_g k)(\omega^2 - c_g k\omega - c_g \beta) = 0, \tag{3.24}$$

yielding the $n = 0$ solutions:

$$\omega = \begin{cases} -c_g k, & (3.25a) \\ c_g k/2 + (c_g^2 k^2/4 + c_g \beta)^{1/2}, & (3.25b) \\ c_g k/2 - (c_g^2 k^2/4 + c_g \beta)^{1/2}. & (3.25c) \end{cases}$$

The solutions of Equations (3.25b) and (3.25c) have properties of inertial gravity waves and Rossby waves and are often called the mixed Rossby-gravity solutions (one eastward and one westward). However, Equation (3.19) shows that, for $\omega = \pm c_g k$, velocities are only finite for the trivial solutions with $\hat{v} = 0$ everywhere. Therefore, the $n = 0$ solution of Equation (3.25a), which has $\hat{v} = \psi_0(y)$, is spurious and should be rejected. For the trivial case, taking $\hat{v} = 0$ everywhere in Equations (3.18a) and (3.18c) yields

$$\omega = \pm c_g k, \qquad \hat{u} = \frac{k c_g^2}{\omega H} \hat{h}, \tag{3.26}$$

which can be used in Equation (3.18b) to give

$$\omega = \pm c_g k, \quad \hat{h} = h_0 \exp(\mp y^2 / 2L_{\mathrm{eq}}^2), \quad \hat{u} = \pm c_g \frac{h_0}{H} \exp(\mp y^2 / 2L_{\mathrm{eq}}^2). \tag{3.27}$$

The eastward solution of Equation (3.27), $\omega = c_g k$, $\{\hat{h}, \hat{u}\} \propto \exp(-y^2/2L_{\mathrm{eq}}^2)$, satisfies the infinite-bounded boundary conditions and is known as the equatorial Kelvin wave; whereas the westward solution, $\omega = -c_g k$, $\{\hat{h}, \hat{u}\} \propto \exp(y^2/2L_{\mathrm{eq}}^2)$, violates the infinite-bounded boundary conditions and is rejected. The equatorial Kelvin wave is named after the analogous boundary Kelvin wave. This is because the latitudinal variation of the Coriolis parameter causes the equatorial Kelvin wave to travel along the equator, just as rotation causes boundary Kelvin waves to travel parallel to the boundaries they are adjacent to (e.g., Pedlosky, 2013). Matsuno (1966) also founded the convention of labelling the equatorial Kelvin wave as the $n = -1$ solution. This stems from the fact that $\omega = c_g k$ is a solution to Equation (3.23) for $n = -1$. Moreover, this is consistent with setting $\psi_{-1} = \psi_{-2} = 0$ everywhere, in which case the latitudinal profile of the meridional velocity is $\hat{v} \propto \psi_n$, and $\hat{u}$ and $\hat{h}$ can be expressed as linear combinations of ψ_{n+1} and ψ_{n-1}, for any $n = -1, 0, 1, 2, \ldots$. Matsuno (1966) also showed that, when the system's eigenfunctions

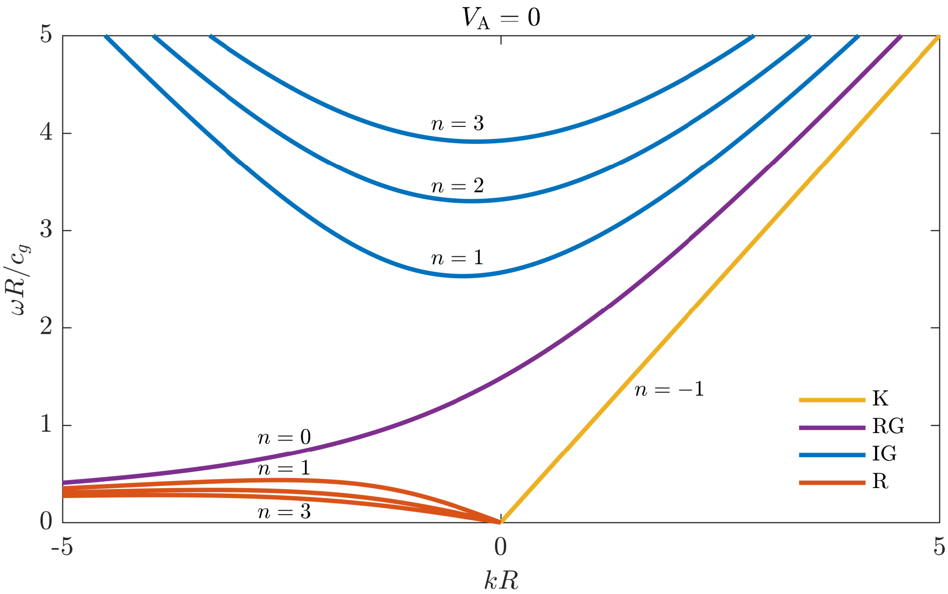

Figure 3.3: Azimuthal dispersion relations for the hydrodynamic equatorial shallow-water wave solutions up to $n = 3$ over the azimuthal wavenumber range, $-5/R < k < 5/R$, for the parameters of HAT-P-7b discussed in Chapter 2 (see Table 3.1). The azimuthal wavenumbers are scaled to by the planetary scale azimuthal wavenumber ($1/R$) and the oscillation frequencies are scaled by the frequency of a shallow-water gravity wave with a planetary scale azimuthal wavenumber (c_g/R).

are defined in this way, they form complete orthonormal set of basis functions.

In Figure 3.3, we plot the azimuthal dispersion relations of the $n = -1, 0, 1, 2, 3$ (hydrodynamic) equatorial shallow-water waves over the azimuthal wavenumber range, $-5/R < k < 5/R$. The equatorial Kelvin wave is plotted in yellow, the $n = 0$ mixed Rossby-gravity solutions are plotted in purple, the equatorial inertial gravity waves are plotted in blue, and the equatorial Rossby waves are plotted in red. Labels of n are annotated adjacent to lines where possible, with the exception of the $n = 2$ equatorial Rossby wave. Alongside this, in Figure 3.4 we plot the geopotential/velocity structures of the largest scale (hydrodynamic) equatorial equatorial shallow-water waves for the planetary scale azimuthal wavenumber $k = 1/R$, using parameters based on HAT-P-7b.

As stated above, there are three solutions for each $n \geq 1$: one eastward inertial gravity wave solution, one westward inertial gravity wave solution, and one Rossby wave solution. The equatorial inertial gravity waves are found in both eastward and westward travelling varieties and propagate zonally at high frequencies ($|\omega| > c_g k$), with their oscillation fre-

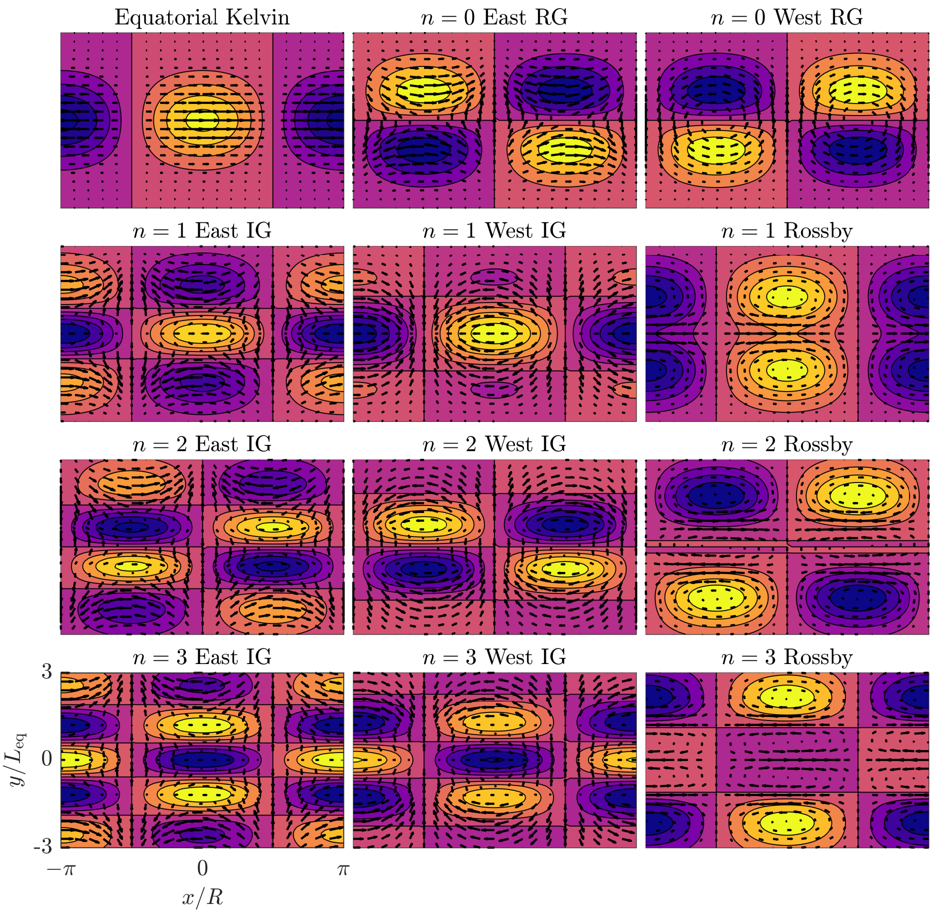

Figure 3.4: The structural forms (geopotential contours with overlaid velocity vectors) of the largest scale hydrodynamic equatorial shallow-water waves, with azimuthal wavenumber $k = 1/R$, are plotted and with the parameters of HAT-P-7b discussed in Chapter 2 (see Table 3.1). These include the $n = -1$ (first column, first row), $n = 0$ (columns two and three, first row), $n = 1$ (second row), $n = 2$ (third row), and $n = 3$ (fourth row) solutions, which are labelled to denote their types. In this labelling RG denotes the $n = 0$ mixed Rossby-gravity waves and IG denotes the inertial gravity waves.

quencies successively increasing for larger n solutions (see Figure 3.3). They are driven by pressure gradients and their associated velocity profiles experience relatively small deflections from planetary rotation as they propagate (see Figure 3.4). The Rossby waves oscillate at the low frequencies ($|\omega| < c_g k$), with their oscillation frequencies successively decreasing for larger n solutions. Rossby solutions only come in westward travelling varieties, with their velocity/geopotential profiles propagating westward while maintaining geostrophic balance. As n increases, the most extreme geopotential highs/lows of the $n \geq 1$ solutions become more poleward, with Rossby high/lows generally being more poleward than those of the inertial gravity wave for a given n. As n increases and the waves' predominant velocity/geopotential structures become located at higher latitudes, their equatorial pressure gradients lessen.

The three special solutions (i.e., the $n = -1$ and $n = 0$ solutions) display fairly unique k dependence in the dispersion diagram (see Figure 3.3). The equatorial Kelvin solution is non-dispersive and it travels eastward along the equator (where the Coriolis force vanishes) in order to restore pressure gradients, with its phase and group speeds always equal to the gravity wave speed. The latitudinal variation of the Coriolis parameter causes it to be tightly confined to the equatorial region, with the latitudinal length scale L_{eq}. The equatorial Kelvin solution's velocity/geopotential structures are most recognisable for their purely-zonal (east-west) velocity profiles. It propagates eastward with its geopotential structures and velocities aligned so that is has eastward velocities aligned along geopotential highs and westward velocities aligned along geopotential lows (see Figure 3.4). The other two special solutions are the eastward and westward $n = 0$ solutions. The eastward $n = 0$ solution has characteristics most like an inertial gravity wave and oscillates at high frequencies, particularly at large wave numbers; whereas the westward $n = 0$ solution tends to oscillate at low frequencies and behaves more similarly to the equatorial Rossby waves (see Figure 3.4). Due to this mixed behaviour the $n = 0$ solutions are often termed mixed Rossby-gravity waves (Matsuno, 1966; Pedlosky, 2013).

Figure 3.4 highlights that the solutions with n odd are are antisymmetric about the equator in v and symmetric about the equator in $\{u, h\}$; whereas the solutions with n

even are equatorially-symmetric in v and are equatorially-antisymmetric in $\{u, h\}$. In the context of hot Jupiters, this symmetry is useful as, to first order, the radiative heating in the atmospheres of tidally locked hot Jupiters is equatorially-symmetric and is expected to cause equatorially-symmetric temperature profiles (Showman & Polvani, 2011), for which h is a shallow-water proxy (as discussed in Chapter 2, see Table 3.1). This means that planetary scale dynamics will only tend to rely on the n odd solutions. As shown above (and in Figure 3.4), the typical latitudinal length scale of the equatorial shallow-water waves is L_{eq}, which for hot Jupiters is similar to the scale of the planetary radius (see Figure 1.10) so large n solutions are not expected to be important to planetary dynamics. In fact (as briefly discussed in Chapter 1) Showman & Polvani (2011) showed that, since $L_{\text{eq}} \sim R$ on hot Jupiters, the equatorial dynamics on hot Jupiters can be well described by the $n = -1$ and $n = 1$ solutions alone. Now that we have developed this underpinning hydrodynamical theory, we can look at how magnetism modifies the largest scale, n odd, equatorial shallow-water waves.

3.3.2 Equatorial SWMHD waves in a uniform azimuthal field

First we will consider equatorial SWMHD waves in a uniform azimuthal field, which is mathematically similar to the hydrodynamic system. If $\mathbf{B}_0 = V_{\text{A}}\widehat{\mathbf{x}}$, for the constant azimuthal background Alfvén speed, V_{A}, Equations (3.17a) to (3.17d) become

$$-i\omega\hat{u} = \beta y\hat{v} - ikg\hat{h} + ikV_{\text{A}}\hat{B}_x, \tag{3.28a}$$

$$-i\omega\hat{v} = -\beta y\hat{u} - g\frac{\mathrm{d}\hat{h}}{\mathrm{d}y} + ikV_{\text{A}}\hat{B}_y, \tag{3.28b}$$

$$-i\omega\hat{h} = -H\left(ik\hat{u} + \frac{\mathrm{d}\hat{v}}{\mathrm{d}y}\right), \tag{3.28c}$$

$$-i\omega\hat{A} = -HV_{\text{A}}\hat{v}, \tag{3.28d}$$

where $\hat{B}_x = (\mathrm{d}\hat{A}/\mathrm{d}y - V_{\mathrm{A}}\hat{h})/H$ and $\hat{B}_y = -ik\hat{A}/H$. From this we eliminate $\hat{u}$, $\hat{h}$, $\hat{A}$, $\hat{B}_x$, and $\hat{B}_y$ to obtain the single ordinary differential equation (ODE):

$$\mathcal{L}\{\hat{v}\} \equiv \left(\omega^2 - V_{\mathrm{A}}^2 k^2\right) \frac{\mathrm{d}^2\hat{v}}{\mathrm{d}y^2} + \frac{1}{c_g^2}\left[(\omega^2 - c_m^2 k^2)(\omega^2 - V_{\mathrm{A}}^2 k^2) - \omega^2\beta^2 y^2 - \omega k \beta c_g^2\right]\hat{v} = 0, \quad (3.29)$$

for $\hat{v}$ not identically zero. In this ODE $\mathcal{L}$ denotes the differential operator and $c_m \equiv (gH + V_{\mathrm{A}}^2)^{1/2}$ denotes the constant (rotationless) magneto-gravity wave speed. We comment that, for a given V_{A} and ω, $\mathcal{L}$ takes the same form as the hydrodynamic ODE (Equation (3.21)), albeit with a different scaling on y. This system has been solved before by Zaqarashvili (2018), who used the scaling $\tilde{y} = \mu^{1/2}y$ with

$$\mu = \frac{|\omega|\beta}{c_g\sqrt{\omega^2 - V_{\mathrm{A}}^2 k^2}}, \quad (3.30)$$

to write $\hat{v} \propto \psi_n$ with

$$\psi_n(y) \equiv C_n H_n(y/L_m)\exp(-y^2/2L_m^2), \quad (3.31)$$

for $n = 0, 1, 2, \ldots$ and $\psi_{-1} = 0$ everywhere, where we have defined $L_m \equiv \mu^{-1/2}$ as a magnetically-adjusted equatorial Rossby deformation radius, as it is the length scale over which stratification, rotation, and magnetic tension balance. However, the key difference between L_{eq} and L_m is that, while $L_{\mathrm{eq}} \equiv (c_g/\beta)^{1/2}$ is identical for any hydrodynamic wave, L_m varies depending on the relative magnitude of $|\omega|$ and its deviation from the Alfvén frequency, $V_{\mathrm{A}}k$. In a similar fashion to the hydrodynamic case, the dispersion relation becomes (Zaqarashvili, 2018)

$$(\omega^2 - V_{\mathrm{A}}^2 k^2)(\omega^2 - c_m^2 k^2) - k\beta c_g^2 \omega = \beta c_g |\omega|(2n+1)\sqrt{\omega^2 - V_{\mathrm{A}}^2 k^2}, \quad (3.32)$$

for $n = -1, 0, 1, 2, 3, \ldots$. Equation (3.32) is quartic in ω and its square root term means that one must seek solutions of its square: an octic. An analytic solution is therefore not guaranteed and numerical root finding techniques should be employed for further progress. Zaqarashvili (2018) solved this system for parameters based on the solar tachocline. We

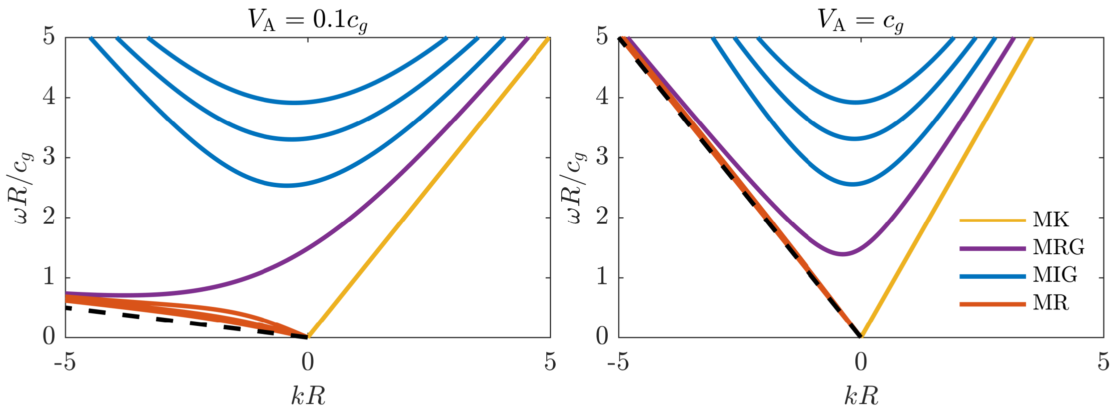

Figure 3.5: Azimuthal dispersion relations for the equatorial SWMHD wave solutions, with the constant azimuthal background magnetic fields $V_A = 0.1c_g$ (lefthand panel) and $V_A = c_g$ (righthand panel), up to $n = 3$ over the azimuthal wavenumber range, $-5/R < k < 5/R$, for the parameters of HAT-P-7b discussed in Chapter 2 (see Table 3.1). The azimuthal wavenumbers are scaled by the planetary scale azimuthal wavenumber ($1/R$) and the oscillation frequencies are scaled by the frequency of a shallow-water gravity wave with a planetary scale azimuthal wavenumber (c_g/R). The yellow line corresponds to the ($n = -1$) equatorial magneto-Kelvin solution, the purple lines correspond to the $n = 0$ (one eastward, one westward) mixed equatorial magneto-Rossby-gravity waves, the blue lines correspond to the equatorial magneto-inertial gravity waves, and the red lines correspond to the equatorial magneto-Rossby waves. Alongside these, on the westward half of the dispersion diagrams the Alfvén frequency ($V_A k$; dashed line) is included for reference.

find similar results for the hot Jupiter parameters that are based on HAT-P-7b, which we introduced in Chapter 2 (see Table 3.1). Using these parameters, we plot dispersion relation diagrams for the background magnetic field strengths $V_A = 0.1c_g$ (lefthand panel) and $V_A = c_g$ (righthand panel) in Figure 3.5. In these, the line colours and ranges are identical to Figure 3.5, but now the shorthands are prefixed with a "M" to denote the waves are magnetic (e.g., MK is the equatorial magneto-Kelvin wave).

Magnetic modifications

On the whole, the system behaves similarly to its hydrodynamic counterpart: there is one $n = -1$ equatorial magneto-Kelvin solution, there are two $n = 0$ mixed equatorial magneto-Rossby-gravity waves, and, for each $n \geq 1$, there are two equatorial magneto-inertial gravity waves and one equatorial magneto-Rossby wave. In the weakly-magnetic limit, the system's dispersion diagram is relatively unchanged. However, as one increases V_A, the Alfvén frequency ($V_A k$; dashed line) sets a minimum on $|\omega|$, which affects the magneto-Rossby waves the westward mixed equatorial magneto-Rossby-gravity solution. In the strong field limit, this Alfvén cut-off cause the magneto-Rossby waves to become approximately non-dispersive in the azimuthal direction, particularly at smaller scales. We comment that there is no eastward Alfvén branch wave in this model. We checked this up to $V_{\mathrm{A}} = 16c_g$, at which point the background Alfvén speed is so large that the rotational and gravitational properties of the system are meaningless and all waves are indistinguishable from Alfvén waves in the dispersion diagram.

We note that, as in the hydrodynamic case, the equatorial magneto-Kelvin solution can be obtained by setting $n = -1$ in Equation (3.32). This yields $\omega = c_m$, which one can see by substituting it back into Equation (3.32). Like the hydrodynamic case, this corresponds to a trivial case, where $\hat{v} = 0$ everywhere. Using this in Equation (3.28d), yields $\hat{A} = 0$, which can be used in Equations (3.28a) and (3.28c) to give

$$\omega = \pm c_m k, \qquad \hat{u} = \frac{kc_m^2}{\omega H}\hat{h}, \tag{3.33}$$

which can be used in Equation (3.17b) to give one bounded eastward solution (i.e., the $n = -1$ solution) and one spurious unbounded westward solution:

$$\omega = \pm c_m k, \quad \hat{h} = h_0 \exp(\mp y^2/2L_m^2), \quad \hat{u} = \pm c_m \frac{h_0}{H} \exp(\mp y^2/2L_m^2), \tag{3.34}$$

where $L_m = (c_g/c_m)^{1/2} L_{\mathrm{eq}}$, which is expected from Equation (3.30) and $\omega = \pm c_m k$.

In Figures 3.6 and 3.7 we plot the velocity/geopotential structure of the planetary scale $n = -1$, $n = 1$, and $n = 3$ solutions, with HAT-P-7b parameters, for $V_{\mathrm{A}} = 0.1c_g$ and $V_{\mathrm{A}} = c_g$ respectively. For $V_{\mathrm{A}} = 0.1c_g$, all of the plotted solutions are largely similar to their hydrodynamic counterparts. For $V_{\mathrm{A}} = c_g$ the MIG waves experience a small amount of equatorial confinement (especially the $n = 3$ solutions) but, again, remain largely similar. However, for $V_{\mathrm{A}} = c_g$, the restorative Lorentz force due to magnetic tension causes the equatorial magneto-Rossby waves and the magneto-Kelvin wave to experience significant equatorial trapping and become tightly confined to the lowest latitudes. The degree of this

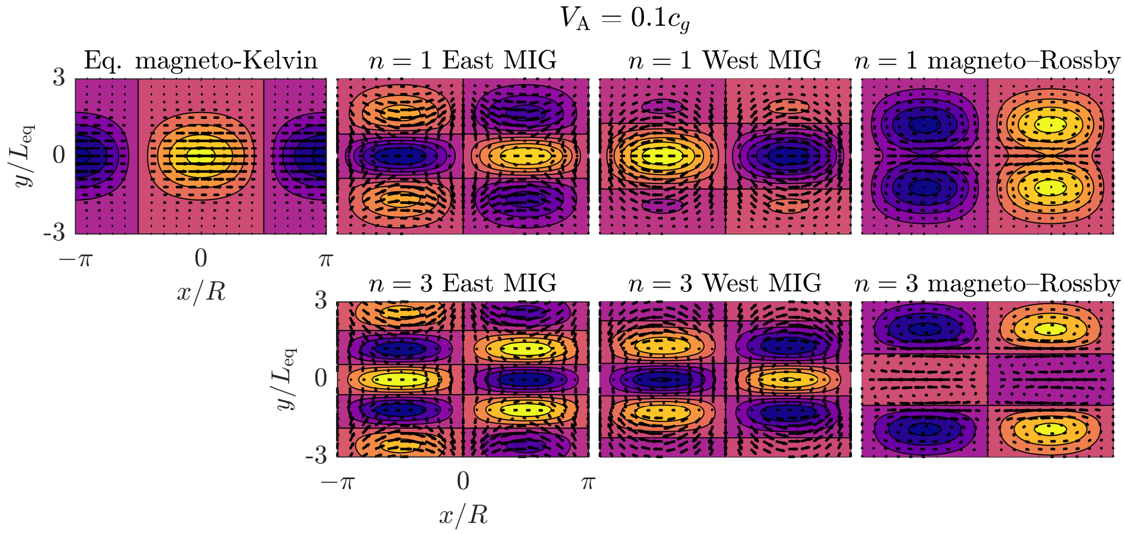

Figure 3.6: The structural forms (geopotential contours with overlaid velocity vectors) of the largest scale odd n equatorial SWMHD waves, with the constant azimuthal background magnetic fields $V_A = 0.1c_g$ and the azimuthal wavenumber $k = 1/R$, are plotted and with the parameters of HAT-P-7b discussed in Chapter 2 (see Table 3.1).

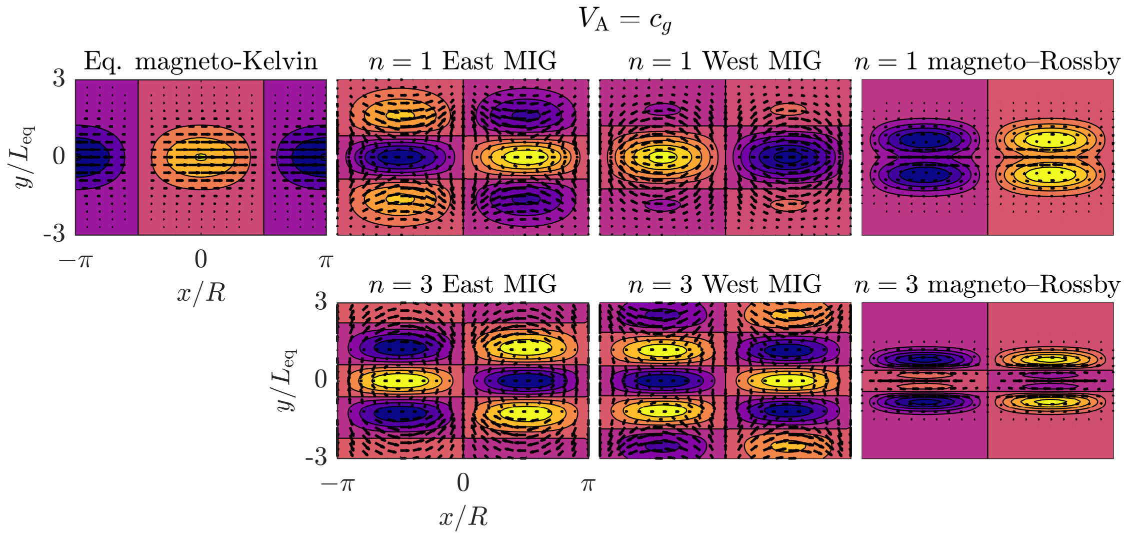

Figure 3.7: As in as Figure 3.7, but for $V_A = c_g$.

trapping is determined by $L_m = (c_g(\omega^2 - V_{\mathrm{A}}^2 k^2)^{1/2}/|\omega|\beta)^{1/2}$, which one can see becomes shortest for waves closest in frequency to the background Alfvén frequency. Other than this latitudinal rescaling, the velocity/geopotential structures remain qualitatively similar. For instance, the equatorial magneto-Rossby waves adjust to a magneto-geostrophic balance.

3.3.3 Equatorial SWMHD waves in a linear azimuthal field

While the uniform magnetic field case is illustrative, the toroidal magnetic field on hot Jupiters is thought to be antisymmetric about the equator (see Section 1.4.1). Alongside this, using numerical simulations of the kind we present in Chapter 4, we found that simulations with uniform background magnetic fields were unable to reproduce wind reversals for reasonable magnetic field strengths. Therefore, in this subsection, we look at some initial results using a linear azimuthal field:

$$\mathbf{B}_0 = B_0\widehat{\mathbf{x}} = \gamma y\widehat{\mathbf{x}}, \tag{3.35}$$

for constant γ. This is the simplest equatorially-antisymmetric azimuthal field profile and can be considered as the first order Taylor expansion of a more realistic equatorially-antisymmetric azimuthal field profile, in which $\gamma = \mathrm{d}B_0/\mathrm{d}y|_{y=0}$ can be considered the latitudinal variation of the toroidal field at the equator. With this choice of B_0, Equations (3.17a) to (3.17d) become

$$-i\omega\hat{u} = \beta y\hat{v} - ikg\hat{h} + ik\gamma y\hat{B}_x + \gamma\hat{B}_y, \tag{3.36a}$$

$$-i\omega\hat{v} = -\beta y\hat{u} - g\frac{\mathrm{d}\hat{h}}{\mathrm{d}y} + ik\gamma y\hat{B}_y, \tag{3.36b}$$

$$-i\omega\hat{h} = -H\left(ik\hat{u} + \frac{\mathrm{d}\hat{v}}{\mathrm{d}y}\right), \tag{3.36c}$$

$$-i\omega\hat{A} = -H\gamma y\hat{v}, \tag{3.36d}$$

where $\hat{B}_x = (\mathrm{d}\hat{A}/\mathrm{d}y - \gamma y \hat{h})/H$ and $\hat{B}_y = -ik\hat{A}/H$. From this we eliminate $\hat{u}$, $\hat{h}$, $\hat{A}$, $\hat{B}_x$, and $\hat{B}_y$ to obtain the single ODE:

$$\mathcal{L}\{\hat{v}\} \equiv F_1 \frac{\mathrm{d}^2\hat{v}}{\mathrm{d}y^2} + F_2 \frac{\mathrm{d}\hat{v}}{\mathrm{d}y} + F_3\hat{v} = 0 \tag{3.37a}$$

with the coefficient functions:

$$F_1 = \left(\omega^2 - \gamma^2 k^2 y^2\right)\left(\omega^2 - c_g^2 k^2 - \gamma^2 k^2 y^2\right), \tag{3.37b}$$

$$F_2 = 2\gamma^2 c_g^2 k^4 y, \tag{3.37c}$$

$$F_3 = \frac{(\omega^2 - c_g^2 k^2 - \gamma^2 k^2 y^2)}{c_g^2}[F_1 - \omega^2\beta^2 y^2 - \omega k \beta c_g^2] - 2\omega\beta\gamma^2 k^3 y^2. \tag{3.37d}$$

When the differential operator $\mathcal{L}$ takes this form there are three singular points in the positive half plane[3]: two regular singular points at $y_s = |\omega|/\gamma k$ and $y_s = (\omega^2 - c_g^2 k^2)^{1/2}/\gamma k$, and one irregular singular point as $y_s \to \infty$. We shall discuss the regular singular points more closely in Chapter 5.

To avoid these singularities, Zaqarashvili (2018) studied this system near the equator (i.e., $|\hat{v}| \to 0$ as $y \to \infty$) in the weakly-magnetic limit, taking

$$\epsilon_1 \equiv \left|\frac{\gamma^2 k^2 y^2}{\omega^2}\right| \ll 1, \tag{3.38a}$$

and

$$\epsilon_2 \equiv \left|\frac{\gamma^2 k^2 y^2}{\omega^2 - c_g^2 k^2}\right| \ll 1, \tag{3.38b}$$

which allows one to divide through by F_1 and carry out a binomial expansion on any singular terms. Doing so and keeping only the terms up to $O(y^2)$, yields an ODE that can be re-expressed in terms of the parabolic cylinder equation. Hence, using this approximation, Zaqarashvili (2018) found that, for $|\hat{v}| \to 0$ as $|y| \to \infty$, bounded solutions approximately take the form:

$$\hat{v}_n(y) = H_n(\sqrt{\mu}y)\mathrm{e}^{-(\mu+d)y^2/2}, \tag{3.39a}$$

[3]The system is symmetric about $y = 0$, so we can limit the problem to the positive half plane.

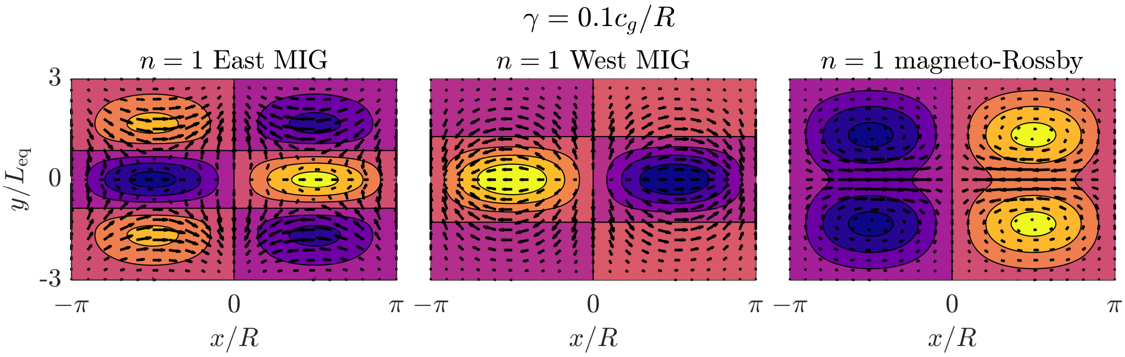

Figure 3.8: The structural forms (geopotential contours with overlaid velocity vectors) of the $n = 1$ equatorial SWMHD waves, with the azimuthal background magnetic field $B_0 = \gamma y$, for $\gamma = 0.1c_g/R$, and the azimuthal wavenumber $k = 1/R$, are plotted and with the parameters of HAT-P-7b discussed in Chapter 2 (see Table 3.1). The waves are qualitatively similar to their hydrodynamic counterparts (see Figure 3.4, second row).

where $d + \mu > 0$, for $n = 0, 1, 2, 3, \ldots$, and

$$\mu = \left(\frac{\gamma^2 k^2}{c_g^2} + \frac{\beta^2}{c_g^2} + \frac{2k^3\beta\gamma^2}{\omega(\omega^2 - c_g^2 k^2)} + \frac{k^3\beta\gamma^2}{\omega^3} + d^2\right)^{1/2}, \tag{3.39b}$$

$$d = \frac{c_g^2\gamma^2 k^4}{\omega^2(\omega^2 - c_g^2 k^2)}. \tag{3.39c}$$

In Equations (3.39a)–(3.39c) the azimuthal wavenumber, k, and oscillation frequency, ω, are linked by the dispersion relation:

$$\frac{\omega^2}{c_g^2} - k^2 - \frac{k\beta}{\omega} - \frac{c_g^2\gamma^2 k^4}{\omega^2(\omega^2 - c_g^2 k^2)} = (2n + 1)\mu, \tag{3.40}$$

for $n = 0, 1, 2, 3, \ldots$.

Magnetic modifications of $n = 1$ solutions (weak-field assumptions)

We solve Equation (3.40) using numerical root finding techniques and to seek the magnetically-modified $n = 1$ solutions. As in hydrodynamic theory, there are generally three bounded $n \geq 1$ solutions in the weak field limit: two MIG solutions and one magneto-Rossby solution. We plot the geopotential/velocity structures of the the planetary scale $n = 1$ solutions in Figures 3.8 to 3.10 for $\gamma = 0.1c_g/R$, $\gamma = 0.3c_g/R$, and $\gamma = 0.58c_g/R$ respectively. Generally, we find that the MIG solutions are qualitatively similar to their hydrodynamic

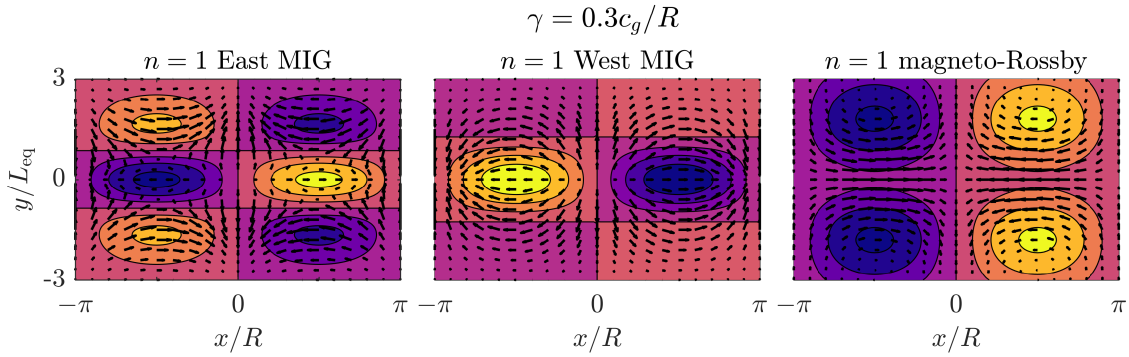

Figure 3.9: As in Figure 3.8, but with $\gamma = 0.3c_g/R$. The waves MIG waves are largely unchanged by the magnetic field, but the $n = 1$ equatorial magneto-Rossby wave becomes less tightly bound to the equator. Note that, for the HAT-P-7b parameter choices, the poles lie at $y/L_{\mathrm{eq}} \approx \pm 2.3$, so here the pressure structures are in the highest latitudes.

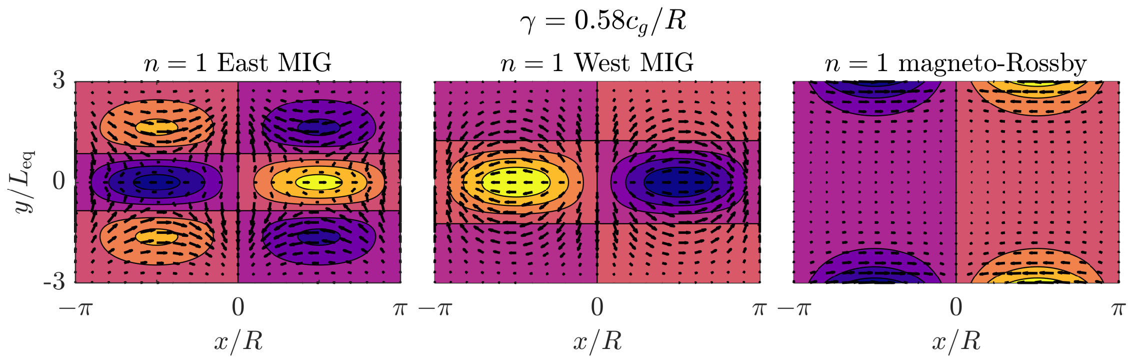

Figure 3.10: As in Figures 3.8 and 3.9, but with $\gamma = 0.58c_g/R$, which is the magnetic field strength where the $n = 1$ equatorial magneto-Rossby wave becomes unbounded. Beyond this point the $n = 1$ equatorial magneto-Rossby waves no longer satisfy the system's infinite-bounded boundary conditions and are removed from the system. For $\gamma = 0.58c_g/R$, the weak-field assumptions on the $n = 1$ equatorial magneto-Rossby solution have the validity criteria ~ 0.85, so are not suitable.

counterparts (see Figure 3.4, second row, and accompanying discussion) and the magnetic field acts to slightly increase their oscillation frequencies. For the eastward MIG wave, $\omega = 2.89c_g/R$ for $\gamma = 0.1c_g/R$ and $\omega = 2.94c_g/R$ for $\gamma = 0.58c_g/R$; while, for the westward MIG wave, $\omega = -2.60c_g/R$ for $\gamma = 0.1c_g/R$ and $\omega = -2.67c_g/R$ for $\gamma = 0.58c_g/R$. For all of the presented magnetic field strengths the assumptions of Equations (3.38a) and (3.38b) remain valid with $\epsilon_1 \sim \epsilon_2 \lesssim 10^{-2}$. However, upon examining Figures 3.8 to 3.10, one can see that the $n = 1$ magneto-Rossby solutions do experience a significant magnetic modification. The structure of the $n = 1$ equatorial magneto-Rossby solution for $\gamma = 0.1c_g/R$ is similar to its hydrodynamic counterpart and it travels westward, while satisfying a magneto-geostrophic balance at mid-to-high latitudes. However, as γ is increased the nature of the $n = 1$ equatorial magneto-Rossby solution changes, with its geootential contours becoming pushed poleward by the magnetic field and its velocities aligning to the azimuthal magnetic field. For $\gamma = 0.3c_g/R$, the most extreme geootential structures of the $n = 1$ equatorial magneto-Rossby solution are centred about $y/L_{\text{eq}} \sim 2$. For our parameters choices and geometry the poles are located $y_{\text{poles}} \approx \pm\pi R/2 \sim 2.3L_{\text{eq}}$, so these structures are siting at the poles. This poleward trapping corresponds to the point where the approximate equatorial model starts to become invalid, with $\epsilon_1 \approx \epsilon_2 \sim 10^{-2}$ for $\gamma = 0.1c_g/R$ and $\epsilon_1 \approx \epsilon_2 \approx 0.26$ for $\gamma = 0.3c_g/R$. If one pushes the model further to $\gamma = 0.58c_g/R$, $\mu + d < 0$ in Equation (3.39a), so the $n = 1$ equatorial magneto-Rossby solutions become unbounded from the equator, which can be seen in Figure 3.10. However, note that for $\gamma = 0.58c_g/R$, $\epsilon_1 \approx \epsilon_2 \approx 0.85$, so the model's assumptions are no longer valid. We comment that the higher n equatorial magneto-Rossby solutions undergo similar changes at smaller γ as their oscillation frequencies are successively smaller in magnitude. To understand the equatorial dynamics of the $n = 1$ equatorial magneto-Rossby solution when the assumptions of Equations (3.38a) and (3.38b) breakdown (i.e., at the point of this migration), one needs to solve the system exactly — a problem which we consider in Chapter 5.

We comment that Zaqarashvili (2018) finds a fourth solution for each $n \geq 1$, which is a slow (westward) magneto-Rossby solution. We find that, for our parameter choices, this solution is always unbounded in the equatorial system (i.e., $\mu + d < 0$) so should not be discussed in terms of the shallow-water dynamics. This solution may be spurious (as $\epsilon_1, \epsilon_2 \gg 1$), or could feasibly be connected to the slow magneto-Rossby solutions found by Márquez-Artavia *et al.* (2017), which are trapped at the poles.

Magnetic modifications of the solution (zero meridional velocity assumption)

Similarly to the hydrodynamic system, there are two valid $n = 0$ solutions and completeness is obtained by replacing the missing/third $n = 0$ solution with an equatorial magneto-Kelvin solution. Using $n = -1$ in the Equation (3.40) for $k = 1/R$ results in a solution with $\omega \sim c_g/R$. However, as the assumptions of Zaqarashvili (2018) require $|\omega/c_g k|$ to be either much greater or much less than one, this solution is not valid within the framework of the model's assumptions. Instead Zaqarashvili (2018) suggest, assuming $v_1 = 0$ everywhere, as in the hydrodynamic case.

With this assumption, Equations (3.2a) to (3.2f) become

$$\frac{\partial u_1}{\partial t} = -g\frac{\partial h_1}{\partial x} + B_0\frac{\partial B_{x,1}}{\partial x} + \frac{\mathrm{d}B_0}{\mathrm{d}y}B_{y,1}, \tag{3.41a}$$

$$0 = -fu_1 - g\frac{\partial h_1}{\partial y} + B_0\frac{\partial B_{y,1}}{\partial x}, \tag{3.41b}$$

$$\frac{\partial h_1}{\partial t} = -H\frac{\partial u_1}{\partial x}, \tag{3.41c}$$

$$\frac{\partial A_1}{\partial t} = 0, \tag{3.41d}$$

$$B_{x,1} = \frac{1}{H}\left(\frac{\partial A_1}{\partial y} - B_0 h_1\right), \tag{3.41e}$$

$$B_{y,1} = -\frac{1}{H}\frac{\partial A_1}{\partial x}. \tag{3.41f}$$

Hence, seeking oscillatory solutions ($\omega \neq 0$) of the form

$$\{\mathbf{u}_1, h_1, A_1, \mathbf{B}_1\} = \{\hat{\mathbf{u}}(y), \hat{h}(y), \hat{A}(y), \hat{\mathbf{B}}(y)\}\mathrm{e}^{i(kx-\omega(y)t)}, \tag{3.42}$$

Equations (3.41d) and (3.41f) yield $A_1 = B_{y,1} = 0$ everywhere, reducing the set of equations to

$$-i\omega u_1 = -ikgh_1 + ikB_0 B_{x,1}, \tag{3.43a}$$

$$fu_1 = -g\frac{\partial h_1}{\partial y}, \tag{3.43b}$$

$$-i\omega h_1 = -ikHu_1, \tag{3.43c}$$

$$B_{x,1} = -\frac{B_0}{H}h_1. \tag{3.43d}$$

Note that we have kept this set of equations in terms of the perturbation variables to allow for a latitudinally-dependent oscillation frequency, $\omega(y)$. This is because Equations (3.43a), (3.43c) and (3.43d) combine to give $(\omega^2 - c_m^2 k^2)u_1 = 0$, or the two oscillatory solutions:

$$\omega_\pm(y) = \pm c_m k \equiv \pm(c_g^2 + B_0^2)^{1/2}k, \tag{3.44}$$

where $c_m(y)$ is the latitudinally dependent magneto-gravity wave speed.

Since the wave-like solutions take the form $\{\mathbf{u}_1, h_1, \mathbf{B}_1\} = \{\hat{\mathbf{u}}(y), \hat{h}(y), \hat{\mathbf{B}}(y)\}\mathrm{e}^{i(kx-\omega(y)t)}$, this would appear to suggest that the structure of the Kelvin waves latitudinally-shear as they travel azimuthally. To attempt to glean some understanding of this, we combine Equations (3.43b), (3.43c) and (3.44), for $f = \beta y$ and $B_0 = \gamma y$, to yield

$$\frac{\partial h_1}{\partial y} = \mp\left(\frac{\beta y\omega(y)}{kc_g^2}\right)h_1, \tag{3.45}$$

or equivalently

$$\frac{\mathrm{d}\hat{h}}{\mathrm{d}y} - \left(i\frac{\mathrm{d}\omega}{\mathrm{d}y}t\right)\hat{h} = \mp\left(\frac{\beta y(c_g^2 + \gamma^2 y^2)^{1/2}}{c_g^2}\right)\hat{h}. \tag{3.46}$$

Zaqarashvili (2018) noted that this can be solved in the weakly-magnetic limit, where $(\gamma y/c_g)^2 \ll 1$. In this case, $\mathrm{d}\omega/\mathrm{d}y \approx 0$ and Equation (3.46) reduces to the separable first order ODE, $\hat{h}^{-1}\mathrm{d}\hat{h}/\mathrm{d}y = \mp(y/L_{\mathrm{eq}}^2)(1 + \gamma^2 y^2/c_g^2)^{1/2}$, which can be integrated directly to yield

$$\hat{h}_\pm = h_{0,\pm}\exp\left\{\mp\frac{1}{3}\left(\frac{c_g}{\gamma L_{\mathrm{eq}}}\right)^2\left(\frac{c_m^3}{c_g^3} - 1\right)\right\}, \tag{3.47a}$$

where $h_{0,\pm}$ are the normalisation constants for each of these respective profiles. From this Equations (3.36a) and (3.36c) give

$$\hat{u}_{\pm} = \pm \frac{h_{0,\pm}(c_g^2 + \gamma^2 y^2)^{1/2}}{H} \exp\left\{ \mp\frac{1}{3}\left(\frac{c_g}{\gamma L_{\rm eq}}\right)^2 \left(\frac{c_m^3}{c_g^3} - 1\right) \right\}, \tag{3.47b}$$

$$\hat{B}_{x,\pm} = \mp \frac{h_{0,\pm}\gamma y}{H} \exp\left\{ \mp\frac{1}{3}\left(\frac{c_g}{\gamma L_{\rm eq}}\right)^2 \left(\frac{c_m^3}{c_g^3} - 1\right) \right\}. \tag{3.47c}$$

giving one bounded (eastward) equatorial wave ($\{\omega_+, \hat{h}_+, \hat{u}_+, \hat{B}_{x,+}\}$). For $(\gamma y/c_g)^2 \ll 1$, Equation (3.47b) may be written as

$$\hat{u}_{\pm} = \pm \frac{c_g h_{0,\pm}}{H}\left(1 + \left(\frac{\gamma y}{c_g}\right)^2\right) \exp\left\{ \mp\frac{y^2}{2L_{\rm eq}^2} + O\left(\left(\frac{\gamma}{c_g L_{\rm eq}}\right)^2 y^4\right) \right\}, \tag{3.48}$$

which, to first order, can be approximately re-expressed in the following form (as presented by Zaqarashvili, 2018):

$$\hat{u}_{\pm} \approx \pm \frac{c_g h_{0,\pm}}{H} \exp\left\{ \left(\frac{\gamma y}{c_g}\right)^2 \mp \frac{y^2}{2L_{\rm eq}^2} \right\}, \tag{3.49}$$

Equation (3.49) was also used for the $\hat{u}_+$ solution in Hindle *et al.* (2019). We comment that Equation (3.49) contains a correction to Equation (48) in Zaqarashvili (2018) for the $\hat{u}_-$ solution (using the substitution $v_{\rm A0} = \gamma R$), which contains a typographic sign error in front of the magnetic part of the exponent.

In Hindle *et al.* (2019) we used numerical SWMHD simulations to highlight that hotspot reversals can be captured with shallow-water models and compared the findings to these equatorial free-wave solutions. We attempted use these weakly-magnetic solutions to estimate the degree of structural shear expected under these conditions by calculating the form of the freely travelling magneto-Kelvin wave at $\tau_{\rm trans} \equiv R^2\gamma^2\tau_{\rm adv}/c_g^2$, the timescale for the wave to transfer a local thickness perturbation, h_1, to surrounding regions for $\gamma = 0.25(c_g/R)$ (i.e., $(\gamma y/c_g)^2 = (y/4R)^2 \ll 1$ in equatorial regions)[4]. A geopotential

[4]This was estimated by considering approximate scalings of terms in the shallow-water continuity equation ($h_1/\tau_{\rm trans} \sim H\mathcal{U}/L$) and the shallow-water momentum equation for a rotationless non-diffusive SWMHD model. For hydrodynamic models and moderately magnetic SWMHD models, $\mathcal{U}/\tau_{\rm trans} \sim gh_1/L$, hence $\tau_{\rm trans} = L_{\rm eq}/c_g^2$ (Perez-Becker & Showman, 2013). We find numerically that for strong magnetic

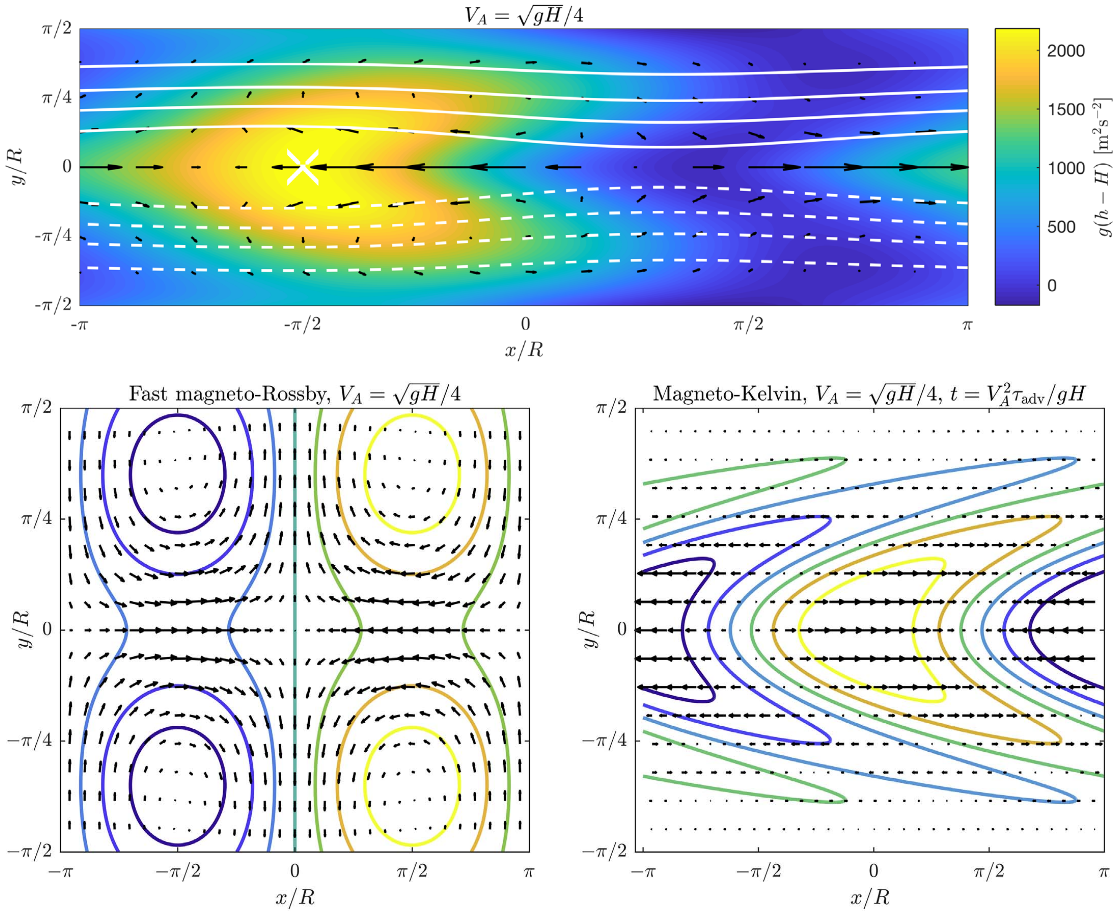

Figure 3.11: Taken from Hindle *et al.* (2019). Top panel: Contours of geopotential are plotted for quasi-steady non-linear solutions, with a forcing amplitude of $\Delta h_{\rm eq}/H = 0.001$ (weakly-forced regime), and the radiative/drag timescales $\tau_{\rm rad} = \tau_{\rm drag} = 1$ Earth days. This has slightly different forcing and initial magnetic field profiles to the solutions of Chapter 4, with $h_{\rm eq} = H + \cos(x/R)\cos(y/R)$ on the dayside and $h_{\rm eq} = H$ on the nightside (like Langton & Laughlin, 2007; Perez-Becker & Showman, 2013) and $\mathbf{B}_0 = V_{\rm A}\,(y/L)\exp\left(1/2 - y^2/2L^2\right)\hat{\mathbf{x}}$, with $L = L_{\rm eq}/2$. Wind velocity vectors are overplotted as black arrows, lines of constant horizontal magnetic flux (A) are overplotted as white lines (with solid/dashed lines representing positive/negative magnetic field values), and hotspots (maxima of h on the equatorial line) are marked by white crosses. The system origin lies at the substellar point and velocity vectors are independently normalised for each subplot. Bottom panels: Contours of geopotential perturbations, with overlaid velocity perturbations vectors, for two different wave types at $k = 1/R$. The $n = 1$ equatorial magneto-Rossby wave is plotted (lower left panel) for $V_A = \sqrt{gH}/4$, where $V_A = \gamma R$ in the discussion of the main body. Note that "fast" here is used to distinguish it from the slow equatorial magneto-Rossby wave discussed in Zaqarashvili (2018), which is unbounded at these parameter choices. The magneto-Kelvin mode is plotted (lower right panel) for $V_A = \sqrt{gH}/4$ at $t = \tau_{\rm trans} \equiv V_A^2\tau_{\rm adv}/gH$. Plots are made for the parameters based on the hot Jupiter HD 189733b.

contour plot of this is shown (lower right panel), alongside a non-linear quasi-steady[5] numerical solution of Equations (2.108a) to (2.108d) (upper panel) and the $n = 1$ magneto-Rossby wave contour (lower left panel), in Figure 3.11, which is taken from Hindle *et al.* (2019). The numerical solution in Figure 3.11, which we give the details of in its caption, displays a reversed westward hotspot, is characterised by a westward-pointing chevron-shaped geopotential distribution, and displays no distinguishable magneto-Rossby characteristics. In this numerical solution, the planetary-scale equatorial Rossby-Kelvin wave superposition, which Showman & Polvani (2011) found drives equatorial superrotation via eddy momentum pumping down the flanks of a eastward-pointing chevron-shaped velocity/geopotential structure, no longer emerges. Since this geopotential distribution looks remarkably similar to that of the latitudinally-sheared equatorial magneto-Kelvin wave, in Hindle *et al.* (2019) we conjectured that, in the absence of the equatorial $n = 1$ Rossby wave's equatorial influence, the latitudinal shearing of the equatorial magneto-Kelvin wave plays a significant role in the magnetically-driven wind/hotspot reversal process on hot Jupiters, though we highlighted that a quantification of each wave's degree of influence was needed to confirm this (which requires us to move away from the weakly-magnetic assumptions of Zaqarashvili, 2018). However, in Chapter 5, we consider exact numerical solutions to the linear wave problem (Equations (3.17a) to (3.17d)). We show that, in these exact solutions, the equatorial magneto-Kelvin wave has a constant (latitudinally-independent) oscillation frequency, which prevents this latitudinal structural shearing from occurring of this kind occurring by allowing ω to remain constant everywhere. Instead the magneto-Kelvin solution acquires small meridional velocity component. The consequences of this with respect to magnetically-driven wind/hotspot reversals are discussed in Chapter 5.

fields the pressure gradient and Lorentz force approximately balance, yielding $gh_1/L \sim \mathcal{B}^2/L$, hence $\tau_{\rm trans} = R^2\gamma^2\tau_{\rm adv}/c_g^2$, where $\tau_{\rm adv} \equiv L_{\rm eq}/\mathcal{U}$ is the hydrodynamic advection timescale defined in Perez-Becker & Showman (2013).

[5]By quasi-steady, we mean that the solution was steady until magnetic diffusion became significant and that changes due to magnetic diffusion occurred over comparatively large timescales compared to the dynamical timescales of the hotspot reversal.

3.3.4 Summary and discussion

In this chapter we have considered the linear waves of the SWMHD model. We began by discussing simple plane wave solutions that are valid in local regions of the atmosphere. We then discussed equatorial waves, which are eastward/westward travelling structures of velocity and geopotential that arise due to the planetary scale variations of the Coriolis parameter. These are known to be important to the large scale equatorial dynamics of hot Jupiters in the hydrodynamic limit. Here we summarise some common themes and questions that have arisen throughout the chapter.

Fast and slow branches

First, using the plane wave solutions we considered the behaviour of waves in a non-rotating electrically conducting fluid, with a locally uniform (azimuthal) background magnetic field. In this system there are two wave types: magneto-gravity waves and Alfvén waves, which are respectively categorised in the fast and slow branches of the system's wave-like solutions, and are both found in eastward and westward varieties. If f-plane rotation (which is valid in local polar regions) is included, the fast branch magneto-gravity solutions become magneto-inertial gravity (MIG) waves and the slow branch Alfvén solutions become magnetostrophic solutions (like the kind found in polar regions by Heng & Spitkovsky, 2009). Again, both of these wave types of are found in eastward and westward varieties.

Alfvén-Rossby wave coupling

If one considers the latitudinal dependence of planetary vorticity with a general beta-plane approximation, the westward slow branch solutions of the plane wave dispersion relation behave like either Alfvén waves or Rossby waves, depending on their azimuthal length scale, with Alfvén-Rossby hybrids behaving like Alfvén waves at small length scales and like Rossby at large length scales.

Eastward slow branch wave

The eastward slow branch solutions also behave like Alfvén waves at small azimuthal length scales but their behaviour is not obvious at large azimuthal length scales and they have no hydrodynamic counterpart.

Hydrodynamic equatorial shallow-water waves

These are structures of velocity and geopotential that arise due to the planetary scale variations of the Coriolis parameter and propagate parallel to the equator. They have associated latitudinal mode numbers, n, which generally denote the number of latitudes at which their meridional velocity profiles are zero. Symmetries about the equator mean that the dynamics of hot Jupiters generally depends on the n odd solutions, particularly $n = 1$ and $n = -1$. For each $n \geq 1$, there are two equatorial inertial gravity waves and one equatorial Rossby wave, which behaves geostrophically. The $n = -1$ solution is a special case: the equatorial Kelvin solution, which travels eastwards at the shallow-water gravity wave speed and its structure has no meridional velocity component.

Equatorial SWMHD waves

First we considered the uniform azimuthal background magnetic field case. In this case equatorial MIG waves are generally similar to their hydrodynamic counterparts, while strong magnetic fields can cause significant equatorial trapping of the equatorial magneto-Rossby waves and the planetary scale equatorial magneto-Kelvin wave. The equatorial Kelvin solution now travels eastwards at the magneto-gravity wave speed and, as before, its structure has no meridional velocity component.

Next we considered an azimuthal background magnetic field with a linear profile in the weak field approximation of Zaqarashvili (2018). Equatorial MIG waves remain largely similar to their hydrodynamic counterparts but the equatorial magneto-Rossby solutions experienced latitudinal elongation and became unbounded from the equator at large enough background magnetic field strengths, at which point the weak field approximations became invalid. The equatorial magneto-Kelvin wave could not be obtained from the weak field approximation and its structure was calculated directly under the assumption of no meridional velocity component. This lead to a latitudinally dependent propagation speed, which would suggest structural shearing as it travels. No eastward slow branch solution was recovered in either equatorial models, suggesting that it is likely to be a polar phenomenon,

Open questions

While giving an indication of some of the wave dynamics likely to be present in the atmospheres of the hottest hot Jupiters, linear theory alone can not easily answer questions concerning magnetically-driven wind/hotspot reversals. Hence, to study the phenomenon, we need to answer the following questions:

1. Can non-linear shallow-water models capture wind/hotspot reversals?
2. How do the large scale flows change in the presence of different magnetic field profiles? Is an azimuthal background magnetic field with a linear profile useful for modelling reversals?
3. Do the non-linear shallow-water flows resemble any of the behaviours of linear dynamics? Can a link be established between waves and simulations?

Once these answers have been established, we shall return to linear theory, dropping the weak field assumptions of Zaqarashvili (2018). This will allow us to tie together concepts such as equatorial trapping, polar trapping, and Alfvén-Rossby wave coupling in conditions specific to hot Jupiter atmospheres.

Chapter 4

Numerical Simulations of the SWMHD Model

In this chapter we present the results of numerical simulations of the SWMHD model we outlined in Chapter 2. First we consider an azimuthal magnetic field geometry with a simple monotonic latitudinal dependence that is most easily applicable to linear theory, then we consider a more realistic azimuthal field geometry that peaks in the mid-latitudes. We cover a range of parameter space for the forcing magnitudes ($\Delta h_{\mathrm{eq}}/H$) radiative timescales (τ_{rad}) and drag timescales (τ_{drag}), showing that hotspot reversals emerge in strongly magnetic models in all cases. We then study the mechanism that drives the hotspots westwards by considering numerical solutions alongside relevant force balances in various solution phases, highlighting some of its important features.

4.1 Numerical method

Using Cartesian horizontal spatial coordinates, the dynamical behaviour of the active layer of the reduced gravity SWMHD model discussed in Chapter 2 is governed by the equations:

$$\frac{\mathrm{D}\mathbf{u}}{\mathrm{D}t} + f(\widehat{\mathbf{z}} \times \mathbf{u}) = -g\nabla h + (\mathbf{B}\cdot\nabla)\mathbf{B} - \frac{\mathbf{u}}{\tau_{\mathrm{drag}}} + \mathbf{R} + \mathbf{D}_{\nu}, \tag{4.1}$$

$$\frac{\partial h}{\partial t} + \nabla\cdot(h\mathbf{u}) = \frac{h_{\mathrm{eq}} - h}{\tau_{\mathrm{rad}}} \equiv Q, \tag{4.2}$$

$$\frac{\mathrm{D}A}{\mathrm{D}t} = D_{\eta}, \tag{4.3}$$

$$h\mathbf{B} = \nabla \times A\widehat{\mathbf{z}}, \tag{4.4}$$

where $\mathbf{u}(x, y, t) \equiv (u, v)$, is the horizontal active layer fluid velocity, $h(x, y, t)$ is the active layer thickness which is used as the model's temperature proxy (see below), $\mathbf{B}(x, y, t) \equiv (B_x, B_y)$ is the horizontal active layer magnetic field (in velocity units), and $A(x, y, t)$ is the magnetic flux function of the active layer. Before continuing, we note that for small active layer thickness deviations (i.e., $(h - H)/H \ll 1$) lines of constant A approximately correspond to the field lines of the horizontal magnetic field (rather than the field lines of the total columnar horizontal magnetic field, which is a more abstract concept). This, combined with the fact that A is approximately materially conserved on short timescales (as τ_η, the magnetic diffusion timescale, is comparitively large), enables us to get a good intuitive sense of magnetic effects.

Geometrically, we fix a local Cartesian coordinate system about the equator, with $-R\pi \leq x < R\pi$ and $-R\pi/2 < y < R\pi/2$. We centre the system about the planet's substellar point so x/R approximately corresponds to the azimuthal coordinate and y/R approximately corresponds to the latitudinal coordinate. Rotational effects are included using the equatorial beta-plane approximation of Rossby (1939) (see Chapter 2). Recall that the only effects of sphericity that the equatorial beta-plane approximation captures are the dynamical effects caused by latitudinal variations in the planetary rotation vector's vertical component. Moreover, the approximation uses the fact that in equatorial regions the Coriolis parameter, f, is approximately linear to set $f = \beta y$, where the constant

$\beta = 2\Omega/R$ is the local latitudinal variation of the Coriolis parameter at the equator.

The system is driven by a Newtonian cooling treatment, Q, in the continuity equation (Equation (4.2)), which relaxes the system towards the prescribed radiative equilibrium thickness profile, h_{eq}, over a radiative timescale, τ_{rad}. The Newtonian cooling is implemented with

$$h_{\mathrm{eq}} = H + \Delta h_{\mathrm{eq}} \cos\left(\frac{x}{R}\right) \cos\left(\frac{y}{R}\right), \tag{4.5}$$

where H is the system's reference active layer thickness at radiative equilibrium and Δh_{eq} is the difference in h_{eq} between this reference thickness and the radiative equilibrium layer thickness at the substellar point. This profile is similar to the spherical forcing prescriptions used in comparable hydrodynamic models (e.g., Shell & Held, 2004; Langton & Laughlin, 2007; Showman & Polvani, 2010, 2011; Showman *et al.*, 2012; Perez-Becker & Showman, 2013).

In hydrodynamic shallow-water models (e.g., Shell & Held, 2004; Langton & Laughlin, 2007; Showman & Polvani, 2010, 2011; Showman *et al.*, 2012; Perez-Becker & Showman, 2013), the forcing profile is usually set so that $\Delta h_{\mathrm{eq}}/H \sim (T_{\mathrm{day}} - T_{\mathrm{eq}})/T_{\mathrm{eq}}$, where T_{eq} is the average reference temperature (for a given atmospheric depth) and T_{day} is the maximal dayside reference temperature (at that atmospheric depth). For comparison, applying the reference temperatures used for HAT-P-7b in Rogers (2017), this equates to $\Delta h_{\mathrm{eq}}/H \sim 0.22$, 0.19, and 0.14 at $P = 10^{-3}\,$bar, $10^{-2}\,$bar, and $10^{-1}\,$bar respectively. We consider models with $\Delta h_{\mathrm{eq}}/H = \{0.01, 0.05, 0.1, 0.2, 0.3, 0.4, 0.5, 0.6\}$ to cover forcing parameter regimes within and either side of the expected planetary parameter range.

Numerical solutions are obtained by evolving Equations (4.1) to (4.4) from an initial uniformly-flat rest state (i.e., $h(\mathbf{x}, 0) = H$, $\mathbf{u}(\mathbf{x}, 0) = \mathbf{0}$), in the presence of a purely azimuthal magnetic field ($A(\mathbf{x}, 0) = A_0(y)$). For hydrodynamic solutions we evolve until steady-state is achieved and for MHD solutions we run for a magnetic diffusion timescale. The system is solved on a 256×511 x-y grid, using an adaptive third-order Adam-Bashforth time-stepping scheme (Cattaneo *et al.*, 2003), with spatial derivatives taken pseudo-spectrally in x and using a fourth-order finite difference scheme in y. We use periodic boundary conditions on $\mathbf{u}$, h, and A in the x direction. On the y boundaries we impose $v = 0$ (impermeability), $\partial u/\partial y = 0$ (stress-free), and A fixed (no normal magnetic flux). These conditions do not fix values of h on the y boundaries, which are updated to ensure consistency in Equations (4.1) to (4.4) on the y boundaries. As discussed in Chapter 2, these boundary conditions forbid magnetic monopoles (i.e., $\iiint_{\mathcal{V}} \nabla_3 \cdot \mathbf{B}_3 \mathrm{d}x\mathrm{d}y\mathrm{d}z = \iint \nabla \cdot h\mathbf{B}\mathrm{d}x\mathrm{d}y = 0$), conserve total horizontal magnetic flux in the active layer (i.e., $\iint h\mathbf{B}\mathrm{d}x\mathrm{d}y$ is constant), conserve total active layer mass (i.e., $\iint h\mathrm{d}x\mathrm{d}y$ is constant) in the absence of prescribed mass exchanges, and do not allow energy to enter the system from any sources other than the imposed forcing.

4.2 Near-linear azimuthal magnetic field profile

4.2.1 Magnetic flux function

First, we choose to enforce the simple equatorially-antisymmetric, purely azimuthal, initial magnetic field:

$$\mathbf{B}_0 = B_0\widehat{\mathbf{x}} = V_{\mathrm{A}}\mathrm{e}^{1/2}\tanh(y/L_{\mathrm{eq}})\widehat{\mathbf{x}}, \tag{4.6}$$

where V_{A} is the constant parameter that sets the magnitude of the azimuthal magnetic field. This profile may appear an unintuitive choice at first, but London (2017) noted that it has the useful properties for wave dynamics, which we shall exploit in Chapter 5. It is monotonic, behaves linearly in the equatorial region, and is bounded as $y/L_{\mathrm{eq}} \to \infty$. The approximately linear latitudinal dependence of B_0 in the equatorial region means one can choose V_{A} in accordance with the first order Taylor expansion of non-monotonic equatorially-antisymmetric profiles. Upon comparing to other field profiles, we generally find that doing so reproduces similar equatorial dynamics. To illustrate this, in Section 4.2.3 we compare some basic results to the profile $B_0 = V_{\mathrm{A}}(y/L_{\mathrm{eq}})\exp(1/2-y^2/2L_{\mathrm{eq}}^2)$, which is the equatorially-antisymmetric profile used in Hindle *et al.* (2019). This has the same first order Taylor expansion as Equation (4.6), has the maximum $B_0 = V_{\mathrm{A}}$ at $y = L_{\mathrm{eq}}$ (i.e., V_{A} is the maximal initial Alfvén speed), and can be motivated from the simulations of Rogers & Komacek (2014). We implement the initial magnetic field profile of Equation (4.6) across an initially flat layer ($h(x, y, 0) = H$, everywhere), using the initial magnetic flux function $A_0(y) = HV_\mathrm{A}L_\mathrm{eq}\mathrm{e}^{1/2}\ln(\cosh(y/L_\mathrm{eq}))$. However, to ensure that $J|_{y=\pm L_y} \equiv (\partial B_y/\partial x - \partial B_x/\partial y)|_{y=\pm L_y} = 0$ initially, which is needed to consistently hold $\partial A/\partial t|_{y=\pm L_y}$, we take B_0 constant close to the y boundaries:

$$B_0 = \begin{cases} -V_\mathrm{A}\mathrm{e}^{1/2}\tanh(L_{y,\delta}/L_\mathrm{eq}) & \text{for } -L_y < y < -L_{y,\delta}, \\ V_\mathrm{A}\mathrm{e}^{1/2}\tanh(y/L_\mathrm{eq}) & \text{for } |y| \leq L_{y,\delta}, \\ V_\mathrm{A}\mathrm{e}^{1/2}\tanh(L_{y,\delta}/L_\mathrm{eq}) & \text{for } L_{y,\delta} < y < L_y, \end{cases} \tag{4.7}$$

where $L_{y,\delta} = (L_y - \delta)$ and $\delta = 5\Delta y$ is the width over which B_0 is constant, with Δy denoting grid spacings in the y direction. This corresponds to

$$A(x, y, 0) = A_0(y, 0) = \begin{cases} HV_\mathrm{A}L_\mathrm{eq}\mathrm{e}^{1/2}\ln(\cosh(y/L_\mathrm{eq})) & \text{for } |y| \leq L_{y,\delta}, \\ HV_\mathrm{A}\mathrm{e}^{1/2}\tanh(L_{y,\delta}/L_\mathrm{eq})|y| & \text{for } L_{y,\delta} < |y| < L_y, \end{cases} \tag{4.8}$$

Note that for this choice A_0 and $\mathrm{d}A_0/\mathrm{d}y$ are continuous and $\mathrm{d}^2A_0/\mathrm{d}y^2$ is piecewise continuous, though, once initiated, the system evolves so that the derivatives of A become continuous everywhere.

4.2.2 Free parameters

As discussed in Chapter 2, we fix the simulation parameters c_g, Ω, H, η, and ν based on the hot Jupiter HAT-P-7b (see Table 4.1 for values)[1]. The timescales τ_rad and τ_drag respectively determine the frequency over which Newtonian cooling and magnetic drag from the deep-seated (but not atmospheric) magnetic field are allowed to occur. Studies of hydrodynamic shallow-water analytics (Showman & Polvani, 2011) and simulations (Perez-Becker & Showman, 2013) show that varying τ_rad controls the efficiency of (geopotential) energy redistribution occurs; whereas varying τ_drag adjusts the distance over which at-

[1]Though, as discussed in Chapter 2, ν is enhanced to allow for numerically-calculable moderate Reynolds number flows.

Table 4.1: Fixed simulation parameters for the shallow-water model of HAT-P-7b (same as Table 2.2 in Chapter 2). c_g is the gravity wave speed, Ω is the planetary rotation frequency, H is the active layer thickness, η is the magnetic diffusivity, and ν is the kinematic viscosity.

$c_g\,(\mathrm{m\,s^{-1}})$	$\beta\,(\mathrm{m^{-1}\,s^{-1}})$	$H\,(\mathrm{m})$	$\eta\,(\mathrm{m^2\,s^{-1}})$	$\nu\,(\mathrm{m^2\,s^{-1}})$
3.0×10^3	6.6×10^{-13}	4.3×10^5	4×10^8	4×10^8

mospheric re-circulation patterns can flow before becoming significantly damped. Hence, since τ_{rad} and τ_{drag} adjust qualitatively similar (albeit non-identical) fundamental flow features, it can be beneficial to reduce the modelling problem by fixing $\tau_{\mathrm{drag}}=\tau_{\mathrm{rad}}$. We do so in three cases: (a) short τ_{rad} and strong drag, $\tau_{\mathrm{rad}}=\tau_{\mathrm{drag}}=\tau_{\mathrm{wave}}$; ($b$) moderate τ_{rad} and moderate drag, $\tau_{\mathrm{rad}}=\tau_{\mathrm{drag}}=5\tau_{\mathrm{wave}}$; and ($c$) long τ_{rad} radiative and weak drag, $\tau_{\mathrm{rad}}=\tau_{\mathrm{drag}}=25\tau_{\mathrm{wave}}$. However, as τ_{rad} and τ_{drag} are not necessarily equivalent in hot Jupiter atmospheres, we also consider the additional two cases: (d) short τ_{rad} and weak drag, $\tau_{\mathrm{rad}}=\tau_{\mathrm{wave}},\tau_{\mathrm{drag}}=25\tau_{\mathrm{wave}}$; and ($e$) long τ_{rad} and strong drag, $\tau_{\mathrm{rad}}=25\tau_{\mathrm{wave}},\tau_{\mathrm{drag}}=\tau_{\mathrm{wave}}$. Rogers & Komacek (2014) found magnetically-driven reversals to occur in the upper atmospheres of ultra-hot Jupiters, where $\tau_{\mathrm{rad}}\sim\tau_{\mathrm{wave}}$ and $\tau_{\mathrm{drag}}\sim\tau_{\mathrm{wave}}$, the conditions are most akin to case (a), though τ_{rad} and τ_{drag} are not generally exactly equal.

The remaining free parameter in our system is V_{A}, which determines the magnitude of the system's magnetic field. Our general approach is to increase V_{A}, from $V_{\mathrm{A}}=0$, until we find a change in the nature of the SWMHD system (i.e., hotspot reversals). Here we highlight that, for large enough V_{A}, we always find hotspot reversals in the SWMHD model, regardless of our choices of $\Delta h_{\mathrm{eq}}/H$, τ_{rad}, and τ_{drag}.

4.2.3 Numerical solutions

First we summarise the hydrodynamic solutions, then we highlight the predominant effects of magnetism. Finally, we discuss the detailed force balances of the numerical solutions. We visualise the basic form of our numerical solutions by plotting their (non-dimensionalised) geopotential distributions in Figure 4.1. As discussed in Chapter 2, we use geopotential energy, gh, as a shallow-water proxy of thermal energy so the geopo-

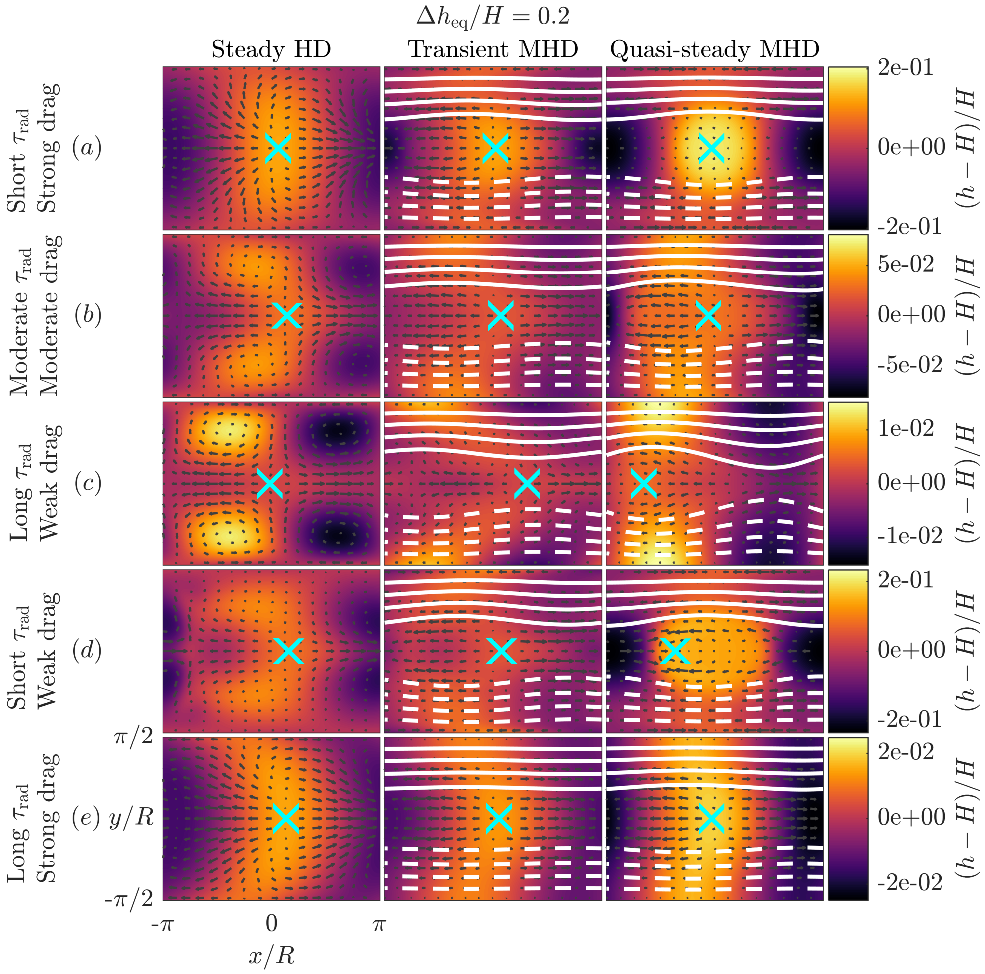

Figure 4.1: The effect of azimuthal magnetic fields on energy redistribution. Contours of the relative layer thickness deviations (rescaled geopotential energy deviations) are plotted on colour axes that are shared along rows, with (individually-normalised) velocity vectors, hotspots (cyan crosses), and lines of constant A (solid/dashed for B_x positive/negative) over-plotted. In each column, reading from left to right, we present hydrodynamic steady state solutions ($V_{\rm A} = 0$), supercritical MHD solutions moments before reversal, and supercritical MHD solutions in the reversed quasi-steady phase. We present solutions in the following parameter regimes: (a) $\tau_{\rm rad} = \tau_{\rm drag} = \tau_{\rm wave}$, with $V_{\rm A} = 0$ or $V_{\rm A} = 1.6c_g$ in the top row; (b) $\tau_{\rm rad} = \tau_{\rm drag} = 5\tau_{\rm wave}$, with $V_{\rm A} = 0$ or $V_{\rm A} = 0.7c_g$ in the second row; (c) $\tau_{\rm rad} = \tau_{\rm drag} = 25\tau_{\rm wave}$, with $V_{\rm A} = 0$ or $V_{\rm A} = 0.2c_g$ in the third row; (d) $\tau_{\rm rad} = \tau_{\rm wave}, \tau_{\rm drag} = 25\tau_{\rm wave}$, with $V_{\rm A} = 0$ or $V_{\rm A} = 1.4c_g$ in the fourth row; (e) $\tau_{\rm rad} = 25\tau_{\rm wave}, \tau_{\rm drag} = \tau_{\rm wave}$, with $V_{\rm A} = 0$ or $V_{\rm A} = 0.5c_g$ in the bottom row.

tential distributions are analogous to those of temperature perturbations. In the hydrodynamic version of our shallow-water model, solutions are known to converge upon a steady state (e.g., Langton & Laughlin, 2007; Showman & Polvani, 2010; Showman *et al.*, 2013; Perez-Becker & Showman, 2013) and we replicate such hydrodynamic steady state solutions in the lefthand column of Figure 4.1 for comparison with our MHD simulations, which we plot in the middle and righthand columns for two difference solution phases. In each row of Figure 4.1 (from top to bottom) we display the solutions for (*a*) short $\tau_{\rm rad}$ and strong drag, $\tau_{\rm rad} = \tau_{\rm drag} = \tau_{\rm wave}$; (*b*) moderate $\tau_{\rm rad}$ and moderate drag, $\tau_{\rm rad} = \tau_{\rm drag} = 5\tau_{\rm wave}$; (*c*) long $\tau_{\rm rad}$ and weak drag, $\tau_{\rm rad} = \tau_{\rm drag} = 25\tau_{\rm wave}$; (*d*) short $\tau_{\rm rad}$ and weak drag $\tau_{\rm rad} = \tau_{\rm wave}, \tau_{\rm drag} = 25\tau_{\rm wave}$; and (*e*) long $\tau_{\rm rad}$ and strong drag $\tau_{\rm rad} = 25\tau_{\rm wave}, \tau_{\rm drag} = \tau_{\rm wave}$. In this subsection, we will restrict ourselves to $h_{\rm eq}/H = 0.2$, before discussing dependencies on forcing magnitude in Section 4.4.

Basic hydrodynamic solutions

Generally, in the hydrodynamic steady state solutions (Figure 4.1, lefthand column) there are two dominant flow features. Drag-adjusted geostrophic circulations dominate at mid-to-high latitudes; while zonal jets dominate at the equator. The drag-adjusted geostrophic circulations satisfy a three-way force balance between horizontal pressure gradients, the Coriolis force, and Rayleigh drag (see the force balances below). In the northern hemisphere, this balance is characterised by flows that circulate clockwise about the geopotential maximum and anticlockwise about the geopotential minimum; while the converse is true in the southern hemisphere. The dominant acceleration components in the equatorial regions are horizontal pressure gradients, which are largest in the zonal direction; the Rayleigh drag, which is simply a damping force that reduces wind speeds; and an advection correction, which is of lower order importance if drags are not weak (again, see the force balances below). Hotspots are, by definition, located at the equatorial pressure maxima so the pressure driven zonally-directed equatorial jets diverge from them.

Newtonian cooling drives a solution's geopotential distribution towards the equilibrium geopotential (see that $gh \to gh_{\rm eq}$ as $\tau_{\rm rad} \to 0$). Therefore $\tau_{\rm rad}$ determines two things: how far planetary flows can redistribute geopotential energy before cooling occurs; and the magnitude of pressure gradients in the system, which in-turn determine planetary flows magnitudes (see Figure 4.1, lefthand column and axis scales). The Rayleigh drag reduces wind speeds everywhere. At equatorial latitudes, a strong Rayleigh drag decreases the distance that the zonal jets can redistribute geopotential energy along the equator, increasing the relative severity of zonal geopotential gradients. At mid-to-high latitudes the Coriolis force becomes significant and solutions satisfy the aforementioned drag-adjusted geostrophic balance. In a "true" geostrophic balance, without suppression from drags and forcing, pressure gradients are exactly balanced by the Coriolis force, which acts perpendicularly to the velocity causing flows to rotate (to their right in the northern hemisphere and to their left in the southern hemisphere). This yields large-scale mid-to-high latitude vortices that are aligned with isobars, similar to those seen in the short $\tau_{\rm rad}$, weak drag, hydrodynamic solution (Figure 4.1 (c), lefthand column). However, the slowing of winds from the Rayleigh drag reduces the magnitude of Coriolis deflection. Therefore in the strong drag limit large-scale vortices cannot fully develop. Similarly, when $\tau_{\rm rad}$ is short, heating/cooling occurs before large-scale vortices fully develop. Comparing the mid-to-high latitude flows of the hydrodynamic solutions, one finds a transition between the long-$\tau_{\rm rad}$/weak-drag solutions, with fully-formed geostrophic vortices, to the short-$\tau_{\rm rad}$/strong-drag solutions, in which the drag-adjusted geostrophic circulations are approximately aligned with the isobars of the equilibrium geopotential (see Figure 4.1, lefthand column). Aside from an unphysical special case discussed in Showman & Polvani (2011) and Perez-Becker & Showman (2013), for all finite physically-relevant choices of $\tau_{\rm rad}$ and $\tau_{\rm drag}$, the meridional mass transport into the equator, caused by the drag-adjusted geostrophic circulations, is maximised east of the substellar point.

These solutions always exhibit eastward hotspots. This is because the equatorward (rescaled) geopotential energy transport from the mid-to-high latitude circulations, $-\partial(hv)/\partial y$, always has its equatorial maximum located eastward of the substellar point. At the equator, the pressure gradient drives winds that diverge from hotspots, causing equatorial geopotential energy transport away from the hotspot regions (i.e., $-\partial(hu)/\partial x < 0$

in hotspot regions). Hence, by Equation (4.2) (geopotential energy conservation), the hotspots locate themselves at the equatorial point of maximal incoming geopotential energy flux, which is located between the equatorial maxima of $-\partial(hv)/\partial y$ and Q. The Newtonian cooling (Q) attempts to return a solution to its forcing equilibrium (i.e., with its hotspot at the substellar point); whereas, as stated above, the equatorial maximum of $-\partial(hv)/\partial y$ is always eastward. The degree of the hotspot's eastward offset is therefore determined by the location of the equatorial maximum of $-\partial(hv)/\partial y$ and its relative magnitude compared to Q. In short, the size of the (eastward) hotspot offset is determined by the efficiency over which the drag-adjusted geostrophic circulations can redistribute thermal[2] energy from the western equatorial dayside to the eastern equatorial dayside, by circulating it to-and-from the higher latitudes.

Showman & Polvani (2011) showed that the flow patterns of hydrodynamic steady state solutions of this kind have a linear wave analogy, with the solutions linked to the forcing responses of specific standing, planetary-scale, equatorial shallow-water waves. These arise because the freely-travelling planetary-scale equatorial shallow-water waves that we discussed in Chapter 3 redistribute geopotential perturbations as they travel (now in the presence of drags). The mid-to-high latitude circulations are associated with standing equatorial Rossby waves, which are characterised by the (drag-adjusted) geostrophic balance. The equatorial jets are associated with the forcing response caused by the planetary scale equatorial Kelvin wave, which is characterised by purely zonal flows. The zonal (east-west) direction in which the waves redistribute geopotential energy is tied to their azimuthal phase velocities. Equatorial Rossby waves have a westward azimuthal phase velocity, so the standing planetary scale equatorial Rossby wave redistributes energy westward at mid-to-high latitudes (i.e., mid-to-high latitude circulations are centred to the west of the forcing extrema). The planetary scale equatorial Kelvin wave has an eastward azimuthal phase velocity, so redistributes energy eastward. In the hydrodynamic system, the drag timescales determine the efficiency of geopotential redistribution by these waves (Showman & Polvani, 2011; Perez-Becker & Showman, 2013). When $\tau_{\rm rad} \gg \tau_{\rm wave}$ and

[2]Recall that the geopotential potential energy is a proxy for thermal energy in this model.

$\tau_{\rm drag} \gg \tau_{\rm wave}$, the standing equatorial waves redistribute energy efficiently, causing flat geopotential profiles along the equator and fully-formed geostrophic vortices with large westward shifts at mid-to-high latitudes. Conversely, when $\tau_{\rm rad} \lesssim \tau_{\rm wave}$ and $\tau_{\rm drag} \lesssim \tau_{\rm wave}$, energy redistribution by waves is highly damped, causing geopotential profiles to resemble forcing profiles and suppressing the formation of mid-to-high latitude vortices.

Basic magnetohydrodynamic solutions

In the weakly-magnetic limit, shallow-water magnetohydrodynamic solutions behave much like their hydrodynamic counterparts (i.e., solutions reach a steady state that is characterised by eastward hotspots, zonal equatorial winds, and drag-adjusted geostrophic circulations at mid-to-high latitudes). However, when the azimuthal magnetic field exceeds a critical magnitude the nature of the solution changes. *Supercritical* magnetic solutions have three phases: an *initial phase*, in which winds and geopotentials resemble their hydrodynamic counterparts but their circulations induce magnetic field evolution; a *transient phase*, in which mid-to-high latitude winds align with the azimuthal magnetic field and dayside equatorial winds experience a net westward acceleration, driving an east-to-west hotspot transition; and a reversed *quasi-steady phase*, in which westward zonally-dominated dayside winds maintain westward hotspots (until, after a comparably long period of time, the magnetic field decays via magnetic diffusion).[3]

We present geopotential distributions of supercritical magnetic solutions in the transient and quasi-steady phases in the two righthand columns of Figure 4.1 (middle and right respectively). The supercritical magnetic solutions are plotted for the same drag choices as the hydrodynamic solutions that they share a row with. However, now lines of constant A, which approximately correspond to field lines of the horizontal magnetic field, are also over-plotted for visualisation of the magnetic field.

After a magnetic solution's initial phase, in which it behaves similarly to its hydrodynamic counterpart, in mid-to-high latitude regions there is a competition between the

[3] Typically, for these parameters, $\tau_{\rm dyn}/\tau_\eta \sim$ 0.01-0.1, where $\tau_{\rm dyn}$ is the dynamical timescale of the hotspot transition and $\tau_\eta = L_{\rm eq}^2/\eta$ is the magnetic diffusion timescale.

drag-adjusted geostrophic balance and the magnetic tension (i.e., $\mathbf{B} \cdot \nabla \mathbf{B}$, the restorative force that acts to straighten bent horizontal magnetic field lines) that the circulating flows generate. Initially, the magnetic field is purely azimuthal, with only latitudinal gradients in its profile, so magnetic tension is zero everywhere. To understand the magnetic field's evolution we highlight that, as the magnetic diffusion timescale is large in comparison to the dynamical timescales of the system, A is approximately materially conserved. This means that lines of constant A are advected by the mid-to-high latitude circulations, bending them and causing a growth of magnetic tension. For subcritical magnetic field strengths, a drag-adjusted magneto-geostrophic balance can be supported, with winds and geopotential profiles making small adjustments to balance the magnetic contribution (before magnetic diffusion eventually returns the system to a hydrodynamic steady state). In contrast, for supercritical magnetic field strengths, magnetic tension becomes strong enough to obstruct the drag-adjusted geostrophic circulations and solutions enter into a transient phase, which ultimately results in hotspot reversals. Below, we shall see that the reversal is driven by a westward Lorentz force acceleration in the region surrounding the hotspot, which is itself generated by this obstruction of geostrophic balance. The westward Lorentz force acceleration causes the point of zonal wind divergence on the equator to shift eastwards, so that in hotspot regions geopotential energy flux is westward (i.e., $ghu < 0$) rather than zero. This shifts the hotspot westward until the system rebalances into a state with a westward hotspot (again, see below).

We find that this reversal mechanism (i.e., westward equatorial-dayside Lorentz force accelerations driven by the obstruction of geostrophic balance) always leads to hotspot reversals in the SWMHD model, regardless of our choice of $\Delta h_{\mathrm{eq}}/H$, τ_{rad}, and τ_{drag}. However, since these parameters control pressure gradient magnitudes and recirculation efficiency, they determine the critical magnetic field strength sufficient for reversal. We present bounds on the magnetic field strength's critical magnitude, $V_{\mathrm{A,crit}}$, for various parameter choices in Figure 4.9. Generally, $\Delta h_{\mathrm{eq}}/H$ and τ_{rad} set the magnitude of a solution's pressure gradients, and therefore the magnitude of the circulations to be overcome, so shorter τ_{rad} and larger $\Delta h_{\mathrm{eq}}/H$ correspond to larger $V_{\mathrm{A,crit}}$ magnitudes. Initially in long

$\tau_{\rm drag}$ solutions the fully formed large scale geostrophic vortices advect the lines of constant A efficiently until they are resisted by magnetic tension; whereas, for short $\tau_{\rm drag}$ solutions, the slowing of winds from drags decreases the distance over which winds initially advect the lines of constant A. Therefore weak drag solutions generally experience a larger degree of field line bending and hence more magnetic tension (relative to the other accelerations in their solutions for a given $V_{\rm A}$) than strong drag solutions. Put simply, strong drag solutions require larger $V_{\rm A,crit}$ magnitude to reverse. We quantify dependences of $V_{\rm A,crit}$ on $\Delta h_{\rm eq}/H$, $\tau_{\rm rad}$, and $\tau_{\rm drag}$ in later discussions.

In the quasi-steady phase of supercritical SWMHD solutions, the magnitudes of $\tau_{\rm rad}$ and $\tau_{\rm drag}$ determine the efficiency of the westward energy redistribution. For large $\tau_{\rm rad}$ and $\tau_{\rm drag}$ timescales, the (westward) hotspot offsets are large as the equatorial pressure-Lorentz balance is free to redistribute energy towards the point where the zonal winds converge, almost entirely without restriction; Conversely, for short $\tau_{\rm rad}$ and $\tau_{\rm drag}$ timescales, this equatorial energy redistribution is less efficient and hotspot offsets are smaller. Comparing between rows in Figure 4.1 (righthand column), suggests $\tau_{\rm drag}$ is the most influential timescale in determining westward hotspot offsets in the SWMHD system.

Force balances

With the basic characteristics of solutions established, we compare the force balances of Equation (4.1) for hydrodynamic and supercritical MHD solutions with the parameters of regime (b) in Figure 4.1 (i.e., for $\Delta h_{\rm eq}/H = 0.2$, $\tau_{\rm rad} = \tau_{\rm drag} = 5\tau_{\rm wave}$, with either $V_{\rm A} = 0$ or $V_{\rm A} = 0.7c_g$). We highlight how the presence of a strong equatorially-antisymmetric azimuthal magnetic field modifies the force balances of different planetary regions, and link these modifications to the more general discussions above.

In Figures 4.2 and 4.3 we respectively plot the dominant meridional and zonal acceleration components of Equation (4.1), for solutions in regime (b). In the lefthand column of Figures 4.2 and 4.3, we present the acceleration components for the hydrodynamic steady state solution; whereas in the middle and righthand columns of Figures 4.2 and 4.3, we present the acceleration components of the transient and quasi-steady phases of its su-

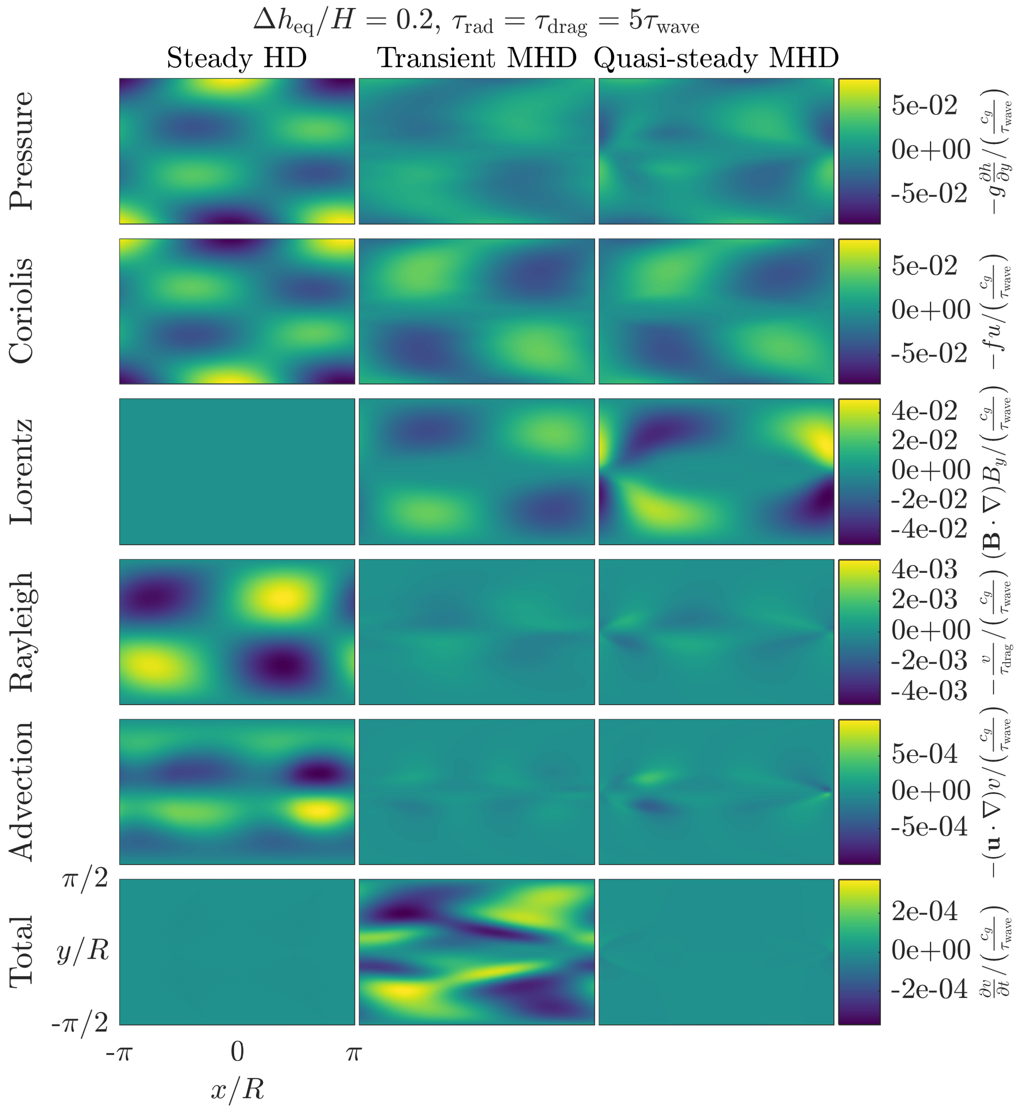

Figure 4.2: Meridional force balances. In each column, reading from left to right, we plot meridional accelerations corresponding to hydrodynamic steady state solutions, transient phase supercritical MHD solutions, and quasi-steady supercritical MHD solutions. In rows one to four, we respectively plot meridional accelerations due to horizontal pressure gradients, the Coriolis effect, the Lorentz force, and Rayleigh drag; the summed meridional accelerations are plotted in row five. The solutions are presented for $\Delta h_{\rm eq}/H = 0.2$, $\tau_{\rm rad} = \tau_{\rm drag} = 5\tau_{\rm wave}$, with $V_{\rm A} = 0$ (HD) or $V_{\rm A} = 0.7c_g$ (MHD) (i.e., parameter regime (b) in Figure 4.1).

percritical MHD counterpart. Along each row of Figures 4.2 (meridional components) and 4.3 (zonal components), we plot (from top downwards) the acceleration contributions due to horizontal pressure gradients ($-g\nabla h$), the Coriolis effect ($-f\,\widehat{\mathbf{z}} \times \mathbf{u}$), the Lorentz force ($\mathbf{B} \cdot \nabla \mathbf{B}$), Rayleigh drag ($-\mathbf{u}/\tau_{\mathrm{drag}}$), and advection ($-\mathbf{u} \cdot \nabla \mathbf{u}$). Additionally, in the bottom row of Figure 4.2 we plot the total meridional acceleration ($\partial v/\partial t$) and, likewise, in the bottom row of Figure 4.3 we plot the total zonal acceleration ($\partial u/\partial t$). For the presented parameter choices the acceleration contributions due vertical mass transport ($\mathbf{R}$) and viscous diffusion ($\mathbf{D}_\nu$) are much weaker so are not included in the plots.

At mid-to-high latitudes, the force balances of hydrodynamic solutions in steady state are well described by the three-way drag-adjusted geostrophic balance discussed above. In particular, Figures 4.2 and 4.3 (lefthand column) highlight this for regime (b), showing that in both horizontal directions the mid-to-high latitude accelerations due to horizontal pressure gradients and the Coriolis force almost exactly cancel, albeit with small Rayleigh drag adjustment and a yet smaller advection contribution. The meridional components of these accelerations remain balanced in equatorial regions, with all of them vanishing at the equator. However, in the zonal direction, the Coriolis force vanishes in equatorial regions but zonally-directed pressure gradients do not, so zonal pressure gradients are balanced by the Rayleigh drag, with an advection adjustment. Since hotspots in hydrodynamic solutions are always located where zonal equatorial jets diverge, these three acceleration components are equally zero at hotspots (see cyan markers in Figure 4.3). As discussed previously, hotspots are driven eastward by the net west-to-east equatorial energy transfer that results from the mid-to-high latitude drag-adjusted geostrophic circulations.

Recall that magnetic tension ($\mathbf{B} \cdot \nabla \mathbf{B}$) is initially zero everywhere so MHD solutions initially resemble their hydrodynamic counterparts. However, lines of constant A (which closely follow magnetic field lines) are advected by the mid-to-high latitude circulations that are archetypal of hydrodynamic solutions. This causes them to bend equatorward between the western and eastern dayside (where the initial circulations are poleward and equatorward respectively; see Figure 4.1, row (b), middle column). Consequently, a restorative Lorentz force that resists meridional winds is produced (see Figure 4.2, third

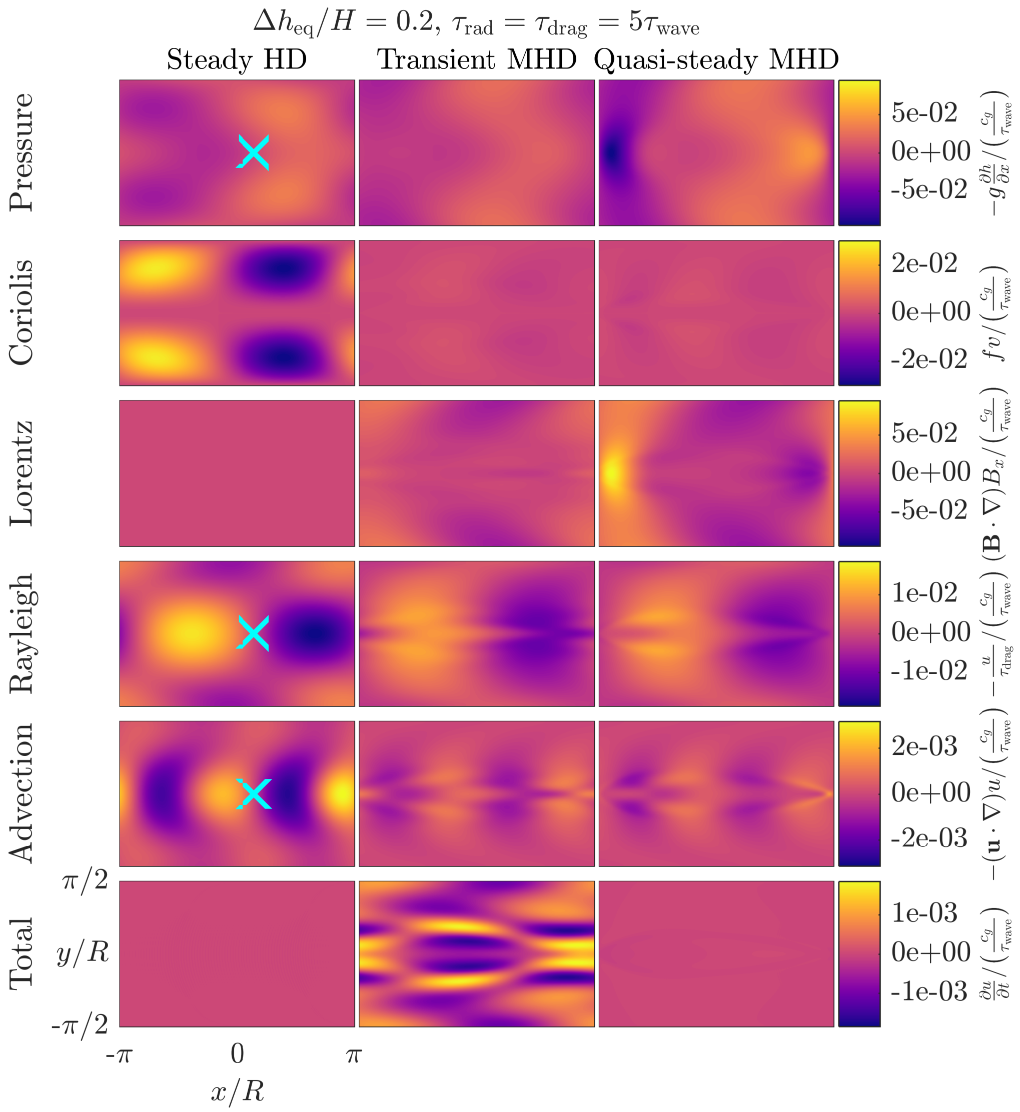

Figure 4.3: The zonal force balances corresponding to the meridional force balances of Figure 4.2 (see Figure 4.2 caption). As in Figure 4.2, we present solutions for the parameter choices $\Delta h_{\rm eq}/H = 0.2$, $\tau_{\rm rad} = \tau_{\rm drag} = 5\tau_{\rm wave}$, with $V_{\rm A} = 0$ (HD) or $V_{\rm A} = 0.7c_g$ (MHD) (i.e., parameter regime (*b*) in Figure 4.1). To aid discussion in the text, hotspot locations have been marked with cyan crosses in hydrodynamic solution panels that correspond to zonal acceleration components with a non-zero equatorial contribution.

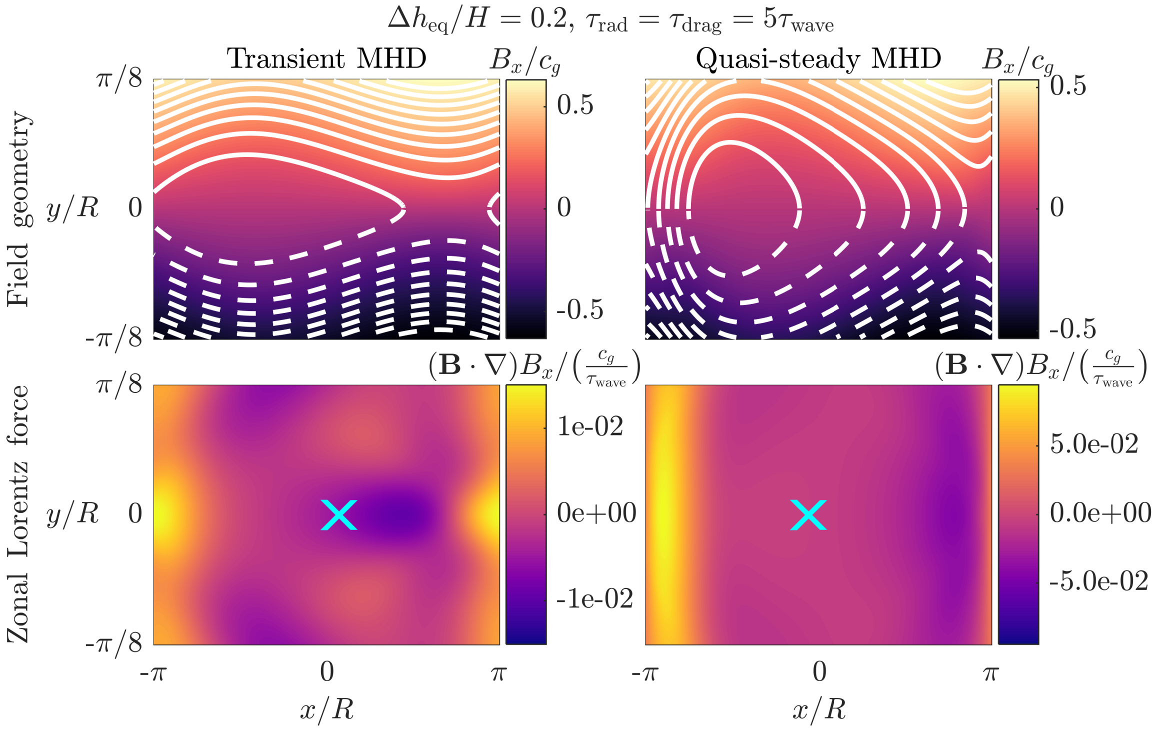

Figure 4.4: The Lorentz force drives westward accelerations in hotspot (cyan crosses) regions. The azimuthal component of the magnetic field is plotted in the top row, with contours of constant A overlaid (white solid/dashed contours for B_x positive/negative). The corresponding zonal Lorentz force component is plotted in the bottom row. As in the two righthand columns of Figures 4.2 and 4.3, we present the transient (lefthand column) and quasi-steady (righthand column) phases of the supercritical MHD solution with $\Delta h_{\rm eq}/H = 0.2$, $\tau_{\rm rad} = \tau_{\rm drag} = 5\tau_{\rm wave}$, and $V_{\rm A} = 0.7c_g$ (i.e., parameter regime (*b*) in Figure 4.1), though we restrict this plot to the equatorial region, $-\pi/8 < y/R < \pi/8$. The zonal Lorentz force acceleration is the directional derivative of B_x along horizontal magnetic field lines (approximately lines of constant A).

row, middle column). For subcritical MHD solutions (not plotted) this Lorentz force resists but does not fully obstruct the mid-to-high latitude circulations, which adjust into a (drag-adjusted) magneto-geostrophic balance. However, in supercritical MHD solutions, the Lorentz force resists meridional winds strongly enough to zonally-align the mid-to-high latitude winds. Hence, supercritical MHD solutions enter into the transient phase discussed above.

When the magnetic field geometry is azimuthally dominated, understanding Lorentz force accelerations is less intuitive in the zonal direction than in the meridional direction (in which they simply oppose meridional flows). The zonal Lorentz accelerations, $\mathbf{B}\cdot\nabla B_x$, are most easily understood geometrically when considered as the directional derivative of

B_x along horizontal magnetic field lines, which are approximately equivalent to lines of constant A.[4] When the magnetic field lines bend equatorward they generally move into regions of smaller $|B_x|$, hence the zonal Lorentz force component generally accelerates flows westward (as $\mathbf{B}\cdot\nabla B_x < 0$); conversely, when they bend poleward they generally move into regions of larger B_x, hence the zonal Lorentz force component generally accelerates flows eastward (as $\mathbf{B}\cdot\nabla B_x > 0$). One can see this by comparing lines of constant A in mid-to-high latitudes of Figure 4.1 (row (b), middle column) with the corresponding mid-to-high latitude zonal Lorentz force accelerations in Figure 4.3 (third row, middle column). Since magnetic field lines bend equatorward between the western and eastern dayside at mid-to-high latitudes, the Lorentz force accelerates mid-to-high latitude dayside flows westward (and eastward on the nightside).

Similar westward dayside Lorentz force accelerations are generated along the equator by magnetic field lines bending into equatorial regions. To visualise this, in Figure 4.4 we plot the horizontal magnetic field geometry (top row) and the zonal component of the Lorentz force (bottom row) in the equatorial region, $-\pi/8 < y/R < \pi/8$, for the transient (left) and quasi-steady (right) phases of the supercritical MHD solution (again, for parameter regime (b)). In the initial phase the Lorentz force primarily acts to resist drag-adjusted geostrophic circulations (see above). Therefore, in the early transient phase the magnetic field lines bend equatorward between the western and eastern dayside (where the initial circulations are poleward and equatorward respectively). For the lowest equatorial regions ($|y/R| \lessapprox \pi/32$ in Figure 4.4) such equatorward magnetic field line bending causes the lines to move into regions smaller $|B_x|$. Consequently, zonal Lorentz force accelerations are westward in regions surrounding the hotspot (see Figure 4.4, left-hand column). In fact, zonal Lorentz force accelerations are always westward in hotspot regions, regardless of radiative/drag/forcing parameter choices, because in hydrodynamic (and weak/early-phase MHD) solutions hotspots are located between the substellar point and the (eastward) maximum of equatorward flow (where lines of constant A are bent most

[4] Note that the directional derivative is taken from left to right for B_x positive (northern hemisphere) and vice versa for B_x negative (southern hemisphere). We also highlight that in this system $\mathbf{B}\cdot\nabla B_x$ is symmetric about the equator.

equatorward). The resulting westward accelerations cause an equatorial imbalance in the zonal momentum equation (see Figure 4.3, bottom row, middle column), which drives the point of zonal equatorial wind divergence eastwards of the hotspot and, consequently, shifts the hotspot westward (as hotspot lie in regions of westward geopotential flux). Finally, as these westward accelerations cause dayside equatorial winds to become more westward, lines of constant A are swept from east to west along the equator, bending them further and thus enhancing equatorial Lorentz force accelerations across all equatorial latitudes (see Figure 4.4, righthand column)[5].

Across radiative/drag/forcing parameter choices, when the hotspots have transitioned westwards the system rebalances into a quasi-steady state, which is characterised by westward hotspots, zonally-aligned winds, and magnetic field lines that have an equatorward bend along the line $x = 0$ in equatorial regions. The predominant meridional balance is between pressure gradients, the Coriolis force, and the Lorentz force (see Figure 4.2, righthand column); whereas the predominant zonal balance is between pressure gradients, the Lorentz force, and the Rayleigh drag (see Figure 4.3, righthand column). In these balances the zonally-aligned winds cause the meridional Rayleigh drag and the zonal Coriolis force to be small. We comment that as the magnetic field eventually diffuses away, the balance adjusts to the decreasing Lorentz force contribution, eventually restoring the drag-adjusted geostrophic/magneto-geostrophic balances associated with hydrodynamic and weakly-magnetic solutions (and hence eastward hotspots).

4.3 Linear-Gaussian azimuthal magnetic field

4.3.1 Magnetic flux function

Using the near-linear hyperbolic tangent azimuthal magnetic field profile in Section 4.2 was advantageous for analytic comparison and for identifying the fundamental features of the magnetically-driven hotspot reversal. In reality, as discussed in Chapter 1, one would

[5] This is equivalent to saying that the more westwardly-oriented dayside winds cause B_y to become more significant in equatorial regions, which in-turn enhances the westward Lorentz force accelerations.

expect the toroidal field to have maximal magnitudes at mid-latitudes then decreases towards both poles, like the dominant field profile found by Rogers & Komacek (2014). To mimic this, we use the following equatorially-antisymmetric, azimuthal initial magnetic field:

$$\mathbf{B}(x, y, 0) = \mathbf{B}_0 = B_0\widehat{\mathbf{x}} = V_{\mathrm{A}} \left(\frac{y}{L_{\mathrm{eq}}}\right) \exp\left(\frac{1}{2} - \frac{y^2}{2L_{\mathrm{eq}}^2}\right) \widehat{\mathbf{x}}, \tag{4.9}$$

where the maximal initial Alfvén speed, V_{A}, determines the magnetic field strength of the system. This linear-Gaussian profile is equatorially-antisymmetric, has a maximal magnitude V_{A} at $y = \pm L_{\mathrm{eq}}$ (recall $L_{\mathrm{eq}}/R \approx 0.67$ for our parameter choices), and decays exponentially towards the poles with the same decay width as the zonal flows that are expected to induce it (Showman & Polvani, 2011). For an initially uniform layer thickness, $h(x, y, 0) = H$, the magnetic flux function corresponding to this chose of B_0 is

$$A(x, y, 0) = A_0(y) = -HV_{\mathrm{A}}L_{\mathrm{eq}} \exp\left(\frac{1}{2} - \frac{y^2}{2L_{\mathrm{eq}}^2}\right). \tag{4.10}$$

4.3.2 Free parameters

As in Section 4.2 we fix the simulation parameters c_g, $\mathit{\Omega}$, H, η, and ν based on the hot Jupiter HAT-P-7b (see Table 4.1 for values). As above, in this subsection we will restrict ourselves to $h_{\mathrm{eq}}/H = 0.2$, before discussing dependencies on forcing magnitude in Section 4.4. Likewise, we vary V_{A} for the five drag choices: (a) short τ_{rad} and strong drag, $\tau_{\mathrm{rad}} = \tau_{\mathrm{drag}} = \tau_{\mathrm{wave}}$; ($b$) moderate τ_{rad} and moderate drag, $\tau_{\mathrm{rad}} = \tau_{\mathrm{drag}} = 5\tau_{\mathrm{wave}}$; and ($c$) long τ_{rad} radiative and weak drag, $\tau_{\mathrm{rad}} = \tau_{\mathrm{drag}} = 25\tau_{\mathrm{wave}}$. However, as τ_{rad} and τ_{drag} are not necessarily equivalent in hot Jupiter atmospheres, we also consider the additional two cases: (d) short τ_{rad} and weak drag, $\tau_{\mathrm{rad}} = \tau_{\mathrm{wave}}, \tau_{\mathrm{drag}} = 25\tau_{\mathrm{wave}}$; and ($e$) long τ_{rad} and strong drag, $\tau_{\mathrm{rad}} = 25\tau_{\mathrm{wave}}, \tau_{\mathrm{drag}} = \tau_{\mathrm{wave}}$. As before, we increase V_{A}, which determines the magnitude of the system's magnetic field, from $V_{\mathrm{A}} = 0$ until we find a change in the nature of the SWMHD system (i.e., hotspot reversals).

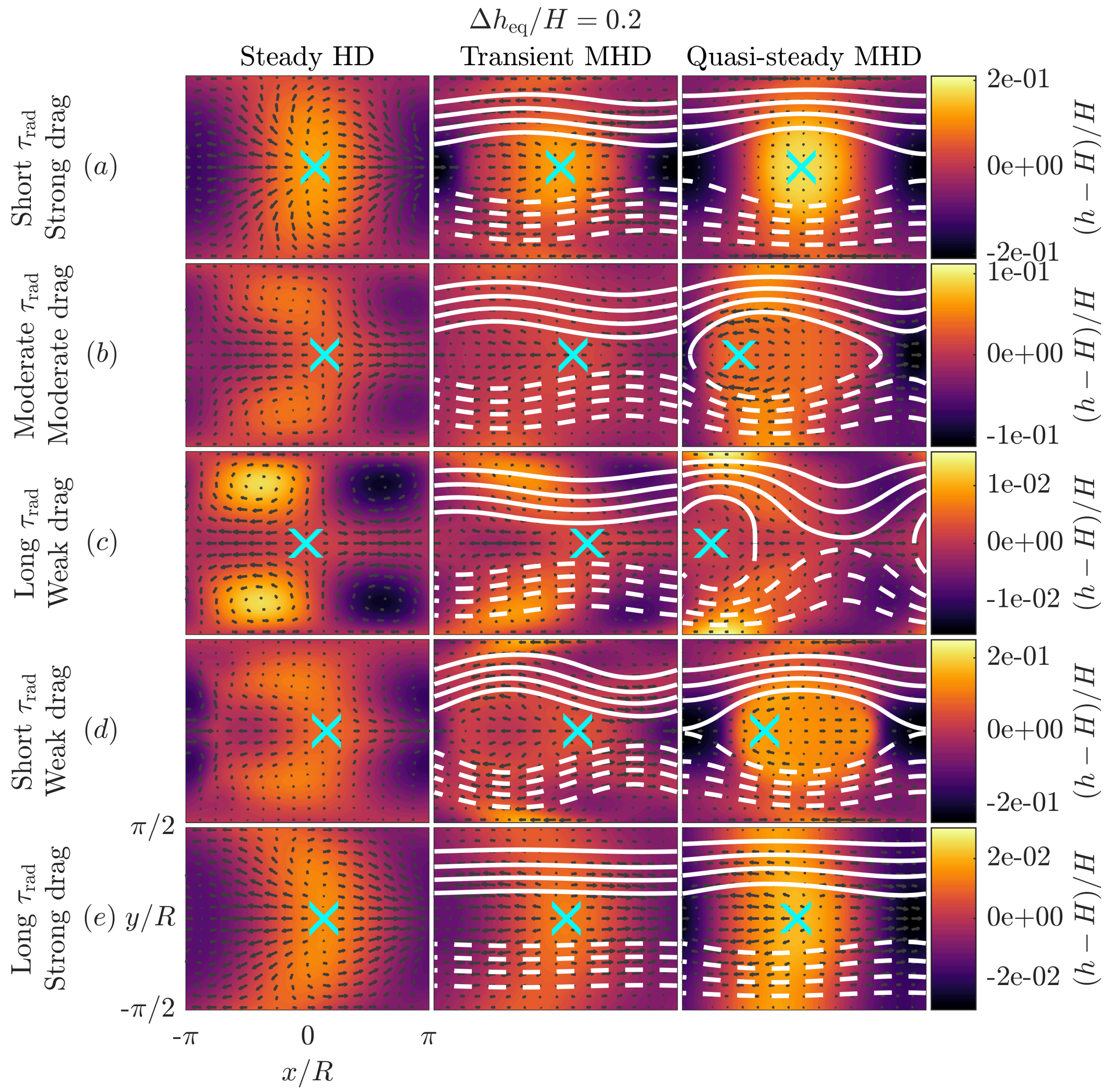

Figure 4.5: Similar to Figure 4.1, but for a linear-Gaussian azimuthal magnetic field profile. We present solutions in the following parameter regimes: (a) $\tau_{\rm rad} = \tau_{\rm drag} = \tau_{\rm wave}$, with $V_{\rm A} = 0$ or $V_{\rm A} = 1.7c_g$ in the top row; (b) $\tau_{\rm rad} = \tau_{\rm drag} = 5\tau_{\rm wave}$, with $V_{\rm A} = 0$ or $V_{\rm A} = 0.7c_g$ in the second row; (c) $\tau_{\rm rad} = \tau_{\rm drag} = 25\tau_{\rm wave}$, with $V_{\rm A} = 0$ or $V_{\rm A} = 0.2c_g$ in the third row; (d) $\tau_{\rm rad} = \tau_{\rm wave}, \tau_{\rm drag} = 25\tau_{\rm wave}$, with $V_{\rm A} = 0$ or $V_{\rm A} = 1.3c_g$ in the fourth row; (e) $\tau_{\rm rad} = 25\tau_{\rm wave}, \tau_{\rm drag} = \tau_{\rm wave}$, with $V_{\rm A} = 0$ or $V_{\rm A} = 0.7c_g$ in the bottom row. Note that the hydrodynamic versions of these solutions are the same as those plotted in the lefthand column of Figure 4.1.

4.3.3 Numerical solutions

As before, we visualise the basic form of our numerical solutions by plotting their (non-dimensionalised) geopotential distributions, with overlaid velocity vectors and lines of constant A. In Figure 4.5 we present the following solutions: (a) $\tau_{\mathrm{rad}} = \tau_{\mathrm{drag}} = \tau_{\mathrm{wave}}$, with $V_{\mathrm{A}} = 0$ or $V_{\mathrm{A}} = 1.7c_g$ in the top row; (b) $\tau_{\mathrm{rad}} = \tau_{\mathrm{drag}} = 5\tau_{\mathrm{wave}}$, with $V_{\mathrm{A}} = 0$ or $V_{\mathrm{A}} = 0.7c_g$ in the second row; (c) $\tau_{\mathrm{rad}} = \tau_{\mathrm{drag}} = 25\tau_{\mathrm{wave}}$, with $V_{\mathrm{A}} = 0$ or $V_{\mathrm{A}} = 0.2c_g$ in the third row; (d) $\tau_{\mathrm{rad}} = \tau_{\mathrm{wave}}, \tau_{\mathrm{drag}} = 25\tau_{\mathrm{wave}}$, with $V_{\mathrm{A}} = 0$ or $V_{\mathrm{A}} = 1.3c_g$ in the fourth row; (e) $\tau_{\mathrm{rad}} = 25\tau_{\mathrm{wave}}, \tau_{\mathrm{drag}} = \tau_{\mathrm{wave}}$, with $V_{\mathrm{A}} = 0$ or $V_{\mathrm{A}} = 0.7c_g$ in the bottom row.

We also plot meridional and zonal force balances (in Figures 4.6 and 4.7 respectively) for short τ_{rad} and strong drag supercritical solutions, (a), which have $\tau_{\mathrm{rad}} = \tau_{\mathrm{drag}} = \tau_{\mathrm{wave}}$ and $V_{\mathrm{A}} = 1.7c_g$. As in Section 4.2.3, the rows of Figures 4.6 and 4.7 correspond to each of the dominant acceleration contributions. As above, by plotting lines of constant A over the B_x distribution (top row) and the zonal Lorentz force component (bottom row), in Figure 4.8 we show how the bending of magnetic field lines in equatorial regions causes westward Lorentz force accelerations in hotspot regions, for the $\tau_{\mathrm{rad}} = \tau_{\mathrm{drag}} = \tau_{\mathrm{wave}}$ and $V_{\mathrm{A}} = 1.7c_g$ solution in the transient (lefthand column) and quasi-steady (righthand column) phases.

We find that the overall behaviour of these numerical solutions is both qualitatively and quantitively similar to the numerical solutions with a linear initial azimuthal magnetic field profile. Namely, subcritical solutions behave similarly to their hydrodynamic counterparts; whereas, for supercritical magnetic solutions, the obstruction of geostrophic circulations by the magnetic field causes zonal wind alignment, a westward Lorentz force acceleration, and therefore reversed hotspots. The only different qualitative flow features between the two field profiles arise at the poles, where $V_{\mathrm{A}}(y/L_{\mathrm{eq}})\exp(1/2 - y^2/2L_{\mathrm{eq}}^2)$ decays. However, our model and aims are not directed towards the polar regions, so this is of lower order importance to us. This is a useful observation as it means that in Chapter 5, where we consider linear theory corresponding to the simulations in this chapter, the near-linear hyperbolic tangent azimuthal magnetic field profile can reasonably describe the dynamics

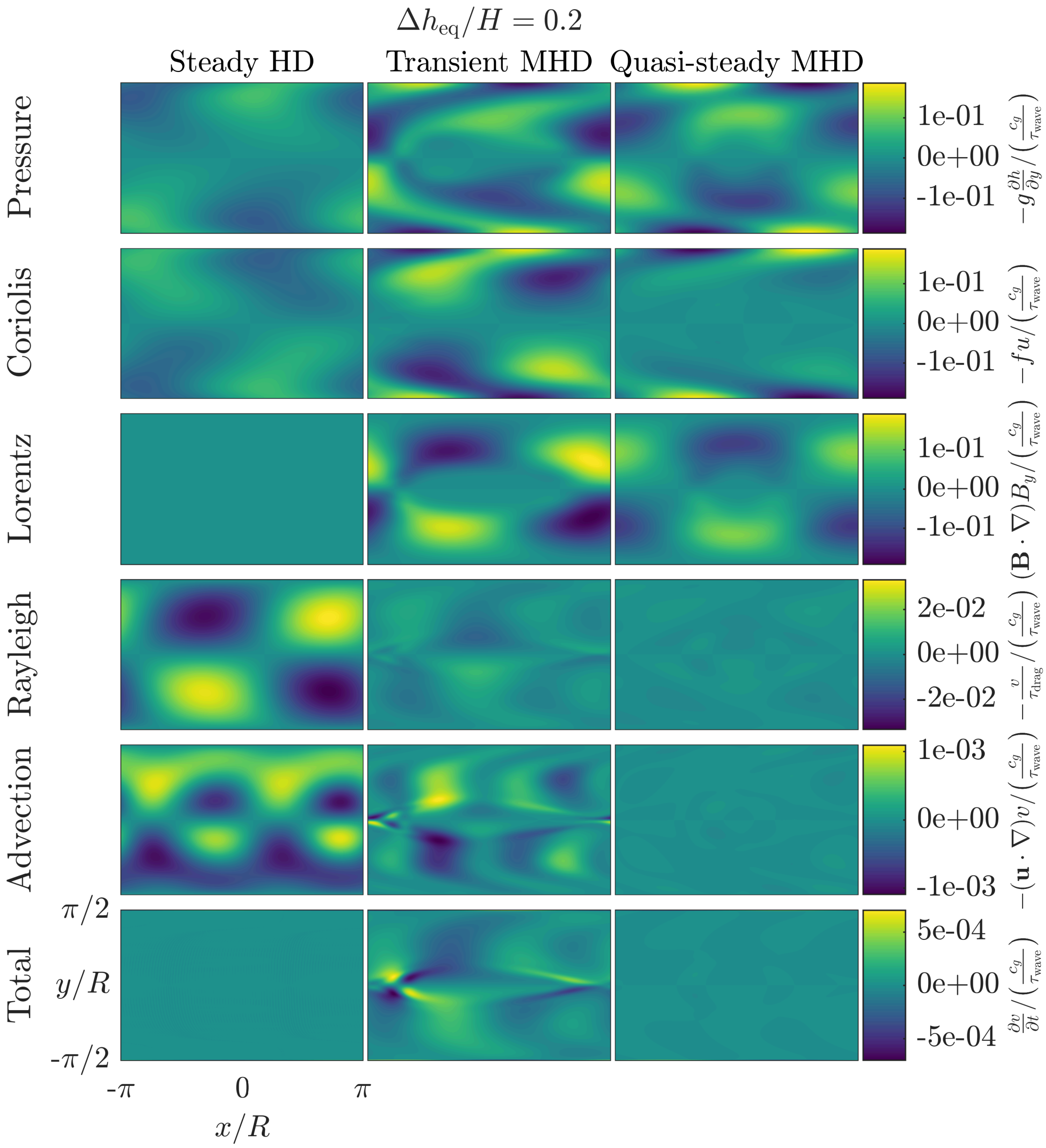

Figure 4.6: Meridional force balances. In each column, reading from left to right, we plot meridional accelerations corresponding to the initial, transient, and quasi-steady phase supercritical MHD solutions for $\tau_{\rm rad} = \tau_{\rm drag} = \tau_{\rm wave}$ and $V_{\rm A} = 1.7c_g$ (i.e., parameter regime (*b*) in Figure 4.5). In rows one to four, we respectively plot meridional accelerations due to horizontal pressure gradients, the Coriolis effect, the Lorentz force, and Rayleigh drag; the summed meridional accelerations are plotted in row five.

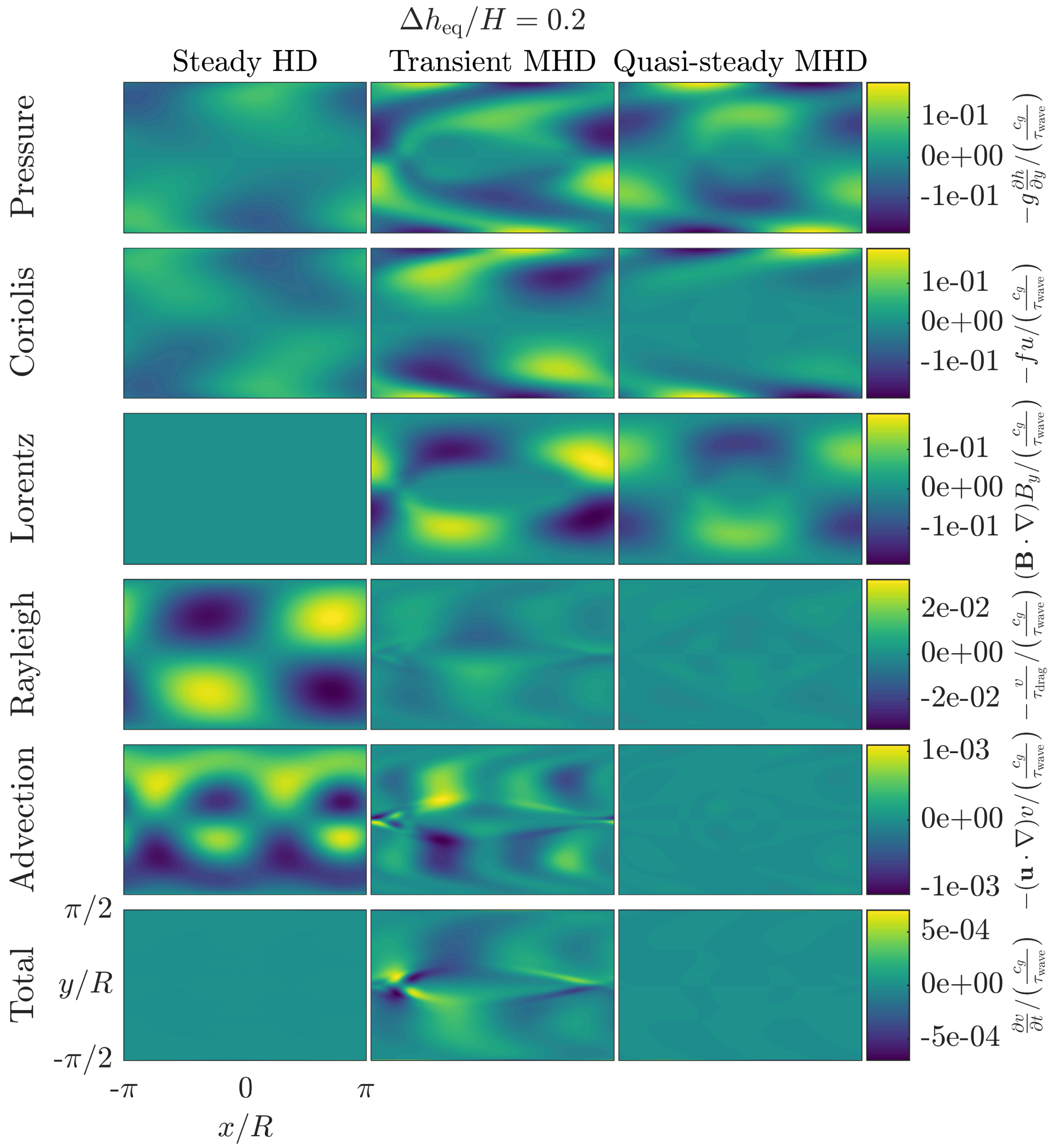

Figure 4.7: The zonal force balances corresponding to the meridional force balances of Figure 4.6 (see Figure 4.6 caption). As in Figure 4.6, we present solutions for the parameter choices $\tau_{\rm rad} = \tau_{\rm drag} = \tau_{\rm wave}$ and $V_{\rm A} = 1.7c_g$ (i.e., parameter regime (b) in Figure 4.5).

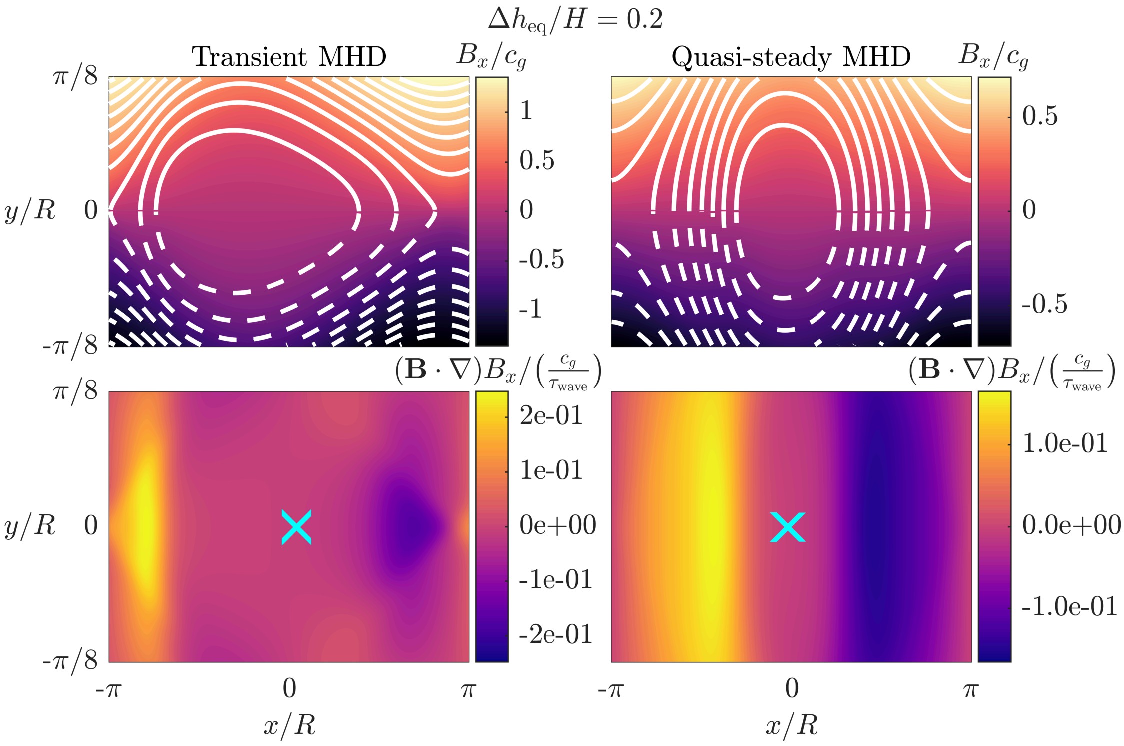

Figure 4.8: As in Figure 4.4, for $\tau_{\mathrm{rad}} = \tau_{\mathrm{drag}} = \tau_{\mathrm{wave}}$ and $V_{\mathrm{A}} = 1.7c_g$. The bending of magnetic field lines in equatorial regions (caused by drag-adjusted geostrophic circulations) causes the Lorentz force to drive westward accelerations in hotspot (cyan crosses) regions. Recall that the zonal Lorentz force accelerations (bottom row) are approximately equivalent to the directional derivative of B_x along the lines of constant A (top row).

of more realistic field profiles, but with much simpler analytic characteristics.

Generally, as before, we find that subcritical MHD solutions (not plotted) behave similarly to their hydrodynamic counterparts and reach a steady state that is characterised by eastward hotspots, zonal equatorial winds, and drag-adjusted geostrophic circulations at mid-to-high latitudes. Likewise, we also identify three solution phases in supercritical MHD solutions. Firstly, in the initial phase magnetic tension has little effect and solutions behave similarly to their hydrodynamic counterparts, but with mid-to-high latitude circulations bending magnetic field lines so that they bend equatorward in hotspot regions. Then in the transient phase, as the magnetic tension from this field line bending becomes significant, a significant Lorentz force acceleration is generated that opposes meridional flows at mid-to-high latitudes, causing them to align with the magnetic field (see middle columns of Figures 4.5 and 4.6) and causing the zonal Coriolis force to play a subdominant dynamical role (see middle column of Figure 4.7). As found in Section 4.2.3, the meridional flow component is diminished while the equatorward bending of magnetic field lines in hotspot regions causes a westward Lorentz force acceleration in hotspot regions (see middle column of Figure 4.7 and lefthand column of Figure 4.8). This causes the equatorial point of east-west wind divergence to shift eastward (see middle column of Figure 4.5), meaning that hotspots lie in regions of westward geopotential flux. Again, as before, the hotspots shift westward, which further enhances the westward Lorentz force acceleration at the equator and the system eventually rebalances in a quasi-steady state. In this quasi-steady solution phase winds are closely-aligned with magnetic field lines, zonal pressure gradients and Lorentz force accelerations balance with a Rayleigh drag adjustment, and there is a four way balance between meridional pressure gradient, Coriolis accelerations, Lorentz force accelerations, and linear drags that prevents meridional flows developing significantly at mid-to-high latitudes. Finally, the magnetic field diffuses away and the Lorentz force contribution slowly diminishes, returning solutions towards their hydrodynamic and weakly-magnetic counterparts.

4.4 Forcing dependence

We find that, when one compares marginally supercritical magnetic solutions with $\Delta h_{\mathrm{eq}}/H = \{0.01, 0.05,\ 0.1,\ 0.2,\ 0.3,\ 0.4,\ 0.5,\ 0.6\}$, the qualitative physical behaviours and balances discussed in Sections 4.2 and 4.3 remain highly similar (in fact, remarkably so). The only discernible changes we observe between marginally supercritical magnetic solutions, upon increasing $\Delta h_{\mathrm{eq}}/H$, are an approximately linear scaling of dependent variable magnitudes and a correction from advection, which generally only provides a lower order correction. This is to be expected from the theory we have developed so far, as the process that needs to be overcome in order to trigger hotspot reversals (i.e., the drag-adjusted geostrophic balance) is a linear one. Consequently, choices of $\Delta h_{\mathrm{eq}}/H$ do not change the mechanics of the hotspot reversals, though they do determine quantitive features of the system (such as magnitudes and $V_{\mathrm{A,crit}}$).

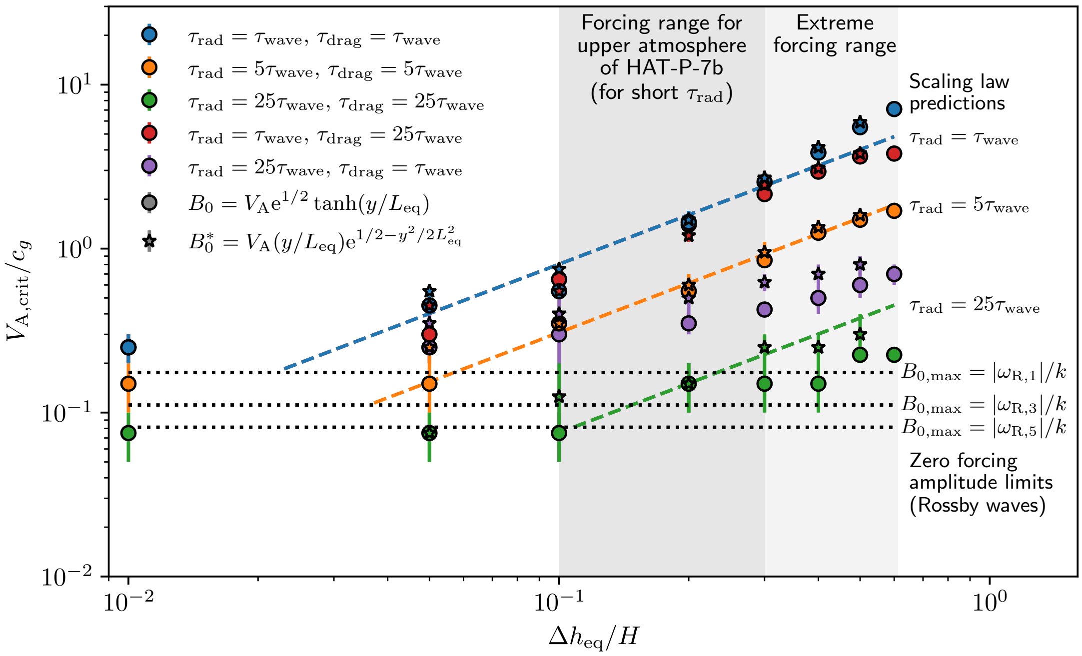

Figure 4.9: Quantitive dependencies of critical magnetic field amplitudes on the forcing magnitude parameter, $\Delta h_{\rm eq}/H$, for different choices of $\tau_{\rm rad}$ and $\tau_{\rm drag}$. Critical magnetic field amplitudes are illustrated with marker points. These are located mid-way between the upper/lower bounds of the identified critical amplitude range, for a particular parameter set, with error bars indicating these upper/lower bounds. Lines indicating scaling law predictions (dashed) and zero-amplitude limits based on the linear theory (dotted; see Chapter 5) are overlaid

The quantitative differences between solutions with the two initial field profiles also tends to be minor, with a second order change in $V_{\mathrm{A,crit}}$ as the two profiles cause a slightly different magnitude of Lorentz force to be generated for a given V_{A}. To make this comparison, we have marked $V_{\mathrm{A,crit}}$ for linear-Gaussian profiles on Figure 4.9 with starred markers. We conclude that the choice of a $B_0 \propto \tanh(y/L_{\mathrm{eq}})$ profile is a useful simplification when considering reversals. This can be advantageous due to properties of the hyperbolic tangent function, which is both monotonic and bounded as $y \to \infty$.

We can use our developed understanding of the reversal mechanism to predict magnitudes $V_{\mathrm{A,crit}}$, with simple scaling arguments based on the respective magnitudes of geostrophic circulations and the restorative Lorentz force. Let $\tau_{\mathrm{geo}}^{-1} = \mathcal{U}/L_{\mathrm{eq}}$ be the frequency over which geostrophic flows circulate and $\tau_{\mathrm{A}}^{-1} = \mathcal{V}/L_{\mathrm{A}}$ be the (Alfvén) frequency over which the azimuthal field attempts to zonally-align these circulations, where $\mathcal{U}$, $\mathcal{V}$, L_{eq} and L_{A} are the typical velocity and length scales associated with the two opposing processes. Reversals occur when $\tau_{\mathrm{A}}^{-1} \gtrsim \tau_{\mathrm{geo}}^{-1}$ or equivalently when $\mathcal{V} \gtrsim \mathcal{U}L_{\mathrm{A}}/L_{\mathrm{eq}}$ (i.e., when the azimuthal field is strong enough to restrict the geostrophic flows). Perez-Becker & Showman (2013) showed the velocities of geostrophic circulations in Coriolis dominated regions scale like

$$\frac{\mathcal{U}}{c_g} \sim \left(\frac{\Delta h_{\mathrm{eq}}}{H}\right)\left(\frac{\tau_{\mathrm{rad}}}{\tau_{\mathrm{wave}}}\right)^{-1}\left(\frac{2\Omega\tau_{\mathrm{wave}}^2}{\tau_{\mathrm{rad}}}+1\right)^{-1}, \tag{4.11}$$

highlighting that the reversal threshold is expected to have a linear dependence on $\Delta h_{\mathrm{eq}}/H$.

In Figure 4.9 we plot the dependence of $V_{\mathrm{A,crit}}$ on $\Delta h_{\mathrm{eq}}/H$ from our simulations. For comparison, we overplot the lines

$$\frac{V_{\mathrm{A,crit}}}{c_g} = \left(\frac{2\pi R(\Delta h_{\mathrm{eq}}/H)}{\kappa L_{\mathrm{eq}}(\tau_{\mathrm{rad}}/\tau_{\mathrm{wave}})}\right)\left(\frac{2\Omega\tau_{\mathrm{wave}}^2}{\tau_{\mathrm{rad}}}+1\right)^{-1}, \tag{4.12}$$

where, since the circulations bend field lines on the planetary azimuthal scale, we take $L_{\mathrm{A}} = 2\pi R$ and κ is a constant of order unity based on the profile of $B_0(y)$.[6]

We generally find reasonable agreement between this simple scaling prediction and

[6] κ is an estimate of the relative strength of B_0 (compared to V_{A}) at low latitudes, y_0, where westward Lorentz force accelerations first develop. In Figure 4.9, we take $\kappa = \mathrm{e}^{1/2}\tanh(y_0/L_{\mathrm{eq}}) \approx 0.47$ (using $y_0 \approx R\pi/16$ based on Figure 4.4).

numerical simulations, particularly in the realistic regimes of $\tau_{\rm rad}$ short and $\Delta h_{\rm eq}/H \sim$ 0.1-0.3, but note that $V_{\rm A,crit}$ approaches a minimum as $\Delta h_{\rm eq}/H \to 0$, which we shall consider in Chapter 5. This scaling law approximation deals less favourably in the (less physical) long $\tau_{\rm rad}$ cases, where $\tau_{\rm drag}$ dependencies become important. However, as we shall discuss in Chapter 6sect:discussion, the other uncertainties in atmospheric characteristics are likely to provide much larger uncertainties than those arising from this scaling law approximation.

4.5 Summary and discussion

In this chapter, we have used numerical simulations to demonstrate that magnetically-driven hotspot reversals are a shallow phenomenon. We also identified the mechanism responsible for driving hotspot reversals in our SWMHD model. The reversals are caused by the westward Lorentz force acceleration that is generated when strong equatorially-antisymmetric azimuthal magnetic fields obstruct the geostrophic circulation patterns responsible for energy redistribution in the hydrodynamic system. The understanding we have developed explains why such hotspot reversals always emerge in the SWMHD model, regardless of our choices for the free forcing/drag parameters $\Delta h_{\rm eq}/H$, $\tau_{\rm rad}$, and $\tau_{\rm drag}$. Moreover, this developed understanding has allowed us to use simple scaling arguments to predict the reversal threshold, $V_{\rm A,crit}$, in terms of planetary parameters, finding reasonable agreement between predictions and numerical simulations in realistic forcing regimes for our fiducial planet HAT-P-7b. However, our simulations also show that $V_{\rm A,crit}$ approaches a minimal threshold in the zero amplitude limit. In Chapter 5 we shall probe linear theory to explain this finding. For this, we shall use our finding that, when compared, equatorially-antisymmetric azimuthal magnetic field profiles with similar latitudinal dependence at equatorial and mid-latitudes behave similarly to one another.

Chapter 5

Hotspot Reversals in Relation to Linear Wave Dynamics

In Chapter 4 we showed that magnetically-driven hotspot reversals are a shallow phenomenon and are driven by the obstruction of mid-to-high latitude drag-adjusted geostrophic circulations. We now use the results of the numerical simulations of Chapter 4 to guide a semi-analytic analysis of equatorial SWMHD waves in an attempt to understand the reversal process further. In Chapter 3 we used the results linear theory, including the work of Zaqarashvili (2018), to derive simple results of linear wave theory in the hot Jupiter parameter regime. In this chapter move away from the weakly-magnetic assumptions taken when Zaqarashvili (2018) considered the equatorially-antisymmetric azimuthal background magnetic field, which become less valid for the typical magnetic field strengths that are sufficient to reverse hotspots, and solve the linearised SWMHD system numerically over a finite domain.

5.1 Linearised steady state solutions

First we seek to establish the features of the reversals that linear theory can capture, and its limitations. We do so by linearising the non-diffusive versions of Equations (4.1) to (4.4) about the background state $\{u_0, v_0, h_0, A_0\} = \{u_0(y), 0, H, A_0(y)\}$, where H is the (constant) background layer thickness, A_0 is defined such that $\mathrm{d}A_0/\mathrm{d}y = HB_0$ for the latitudinally-dependent azimuthal background magnetic field, $\mathbf{B}_0 = B_0(y)\widehat{\mathbf{x}}$, and $u_0(y)$ is to be fixed in a manner that balances the zeroth order zonal momentum equation of the hydrodynamic version of the system which we wish to investigate. To probe the system at the reversal threshold, we assume steady state perturbations exist about this background state and apply the plane wave ansatz, $\{u_1, v_1, h_1, A_1\} = \{\hat{u}(y), \hat{v}(y), \hat{h}(y), \hat{A}(y)\}\mathrm{e}^{ikx}$, where k denotes the azimuthal wavenumber and subscripts of unity denote perturbations from the background state. Such perturbations satisfy

$$(iku_0 + \tau_{\mathrm{drag}}^{-1})\hat{u} = \left(f - \frac{\mathrm{d}u_0}{\mathrm{d}y}\right)\hat{v} - ikg\hat{h} + ikB_0\hat{B}_x + \frac{\mathrm{d}B_0}{\mathrm{d}y}\hat{B}_y, \tag{5.1}$$

$$(iku_0 + \tau_{\mathrm{drag}}^{-1})\hat{v} = -f\hat{u} - g\frac{\mathrm{d}\hat{h}}{\mathrm{d}y} + ikB_0\hat{B}_y, \tag{5.2}$$

$$(iku_0 + \tau_{\mathrm{rad}}^{-1})\hat{h} = -H\left(ik\hat{u} + \frac{\mathrm{d}\hat{v}}{\mathrm{d}y}\right) + HS(y), \tag{5.3}$$

$$iku_0\hat{A} = -HB_0\hat{v}, \tag{5.4}$$

where $\hat{B}_x = (\mathrm{d}\hat{A}/\mathrm{d}y - B_0\hat{h})/H$, $\hat{B}_y = -ik\hat{A}/H$, $S(y) = (\mathit{\Delta} h_{\mathrm{eq}}/H)\,\tau_{\mathrm{rad}}^{-1}\exp(-y^2/2L_{\mathrm{eq}}^2)$ is the first order forcing contribution in the system based on the equilibrium thickness profile, $h_{\mathrm{eq}} = H + \mathit{\Delta} h_{\mathrm{eq}}\cos(kx)\exp(-y^2/2L_{\mathrm{eq}}^2)$, and based on our numerical findings we have assumed that $\mathbf{R}$ does not make a first order contribution to Equations (5.1) and (5.2). Before solving, we note that hydrodynamic solutions are never singular, but that Equation (5.4) causes the magnetic version of the system to be singular if $u_0 = 0$. To compare to the simulations of Chapter 4, we solve the system for $f = \beta y$ and $B_0 = V_{\mathrm{A}}\mathrm{e}^{1/2}\tanh(y/L_{\mathrm{eq}})$.

For a given $u_0(y)$, we seek solutions of Equations (5.1) to (5.4) on $-L_y < y < L_y$, with impermeable boundaries at $y = \pm L_y$, using the shooting method outlined in Appendix D.1. We take $L_y = 5L_{\mathrm{eq}}$ (see Equation (2.113)), which is large enough to ensure that the outer boundary condition has a negligible influence on solutions. We solve the system for $u_0(y) = U_0\exp(-y^2/2L_{\mathrm{eq}}^2)$, where U_0 is chosen so that in the hydrodynamic limit the zonally-averaged zonal-acceleration in Equation (22) of Showman & Polvani (2011)

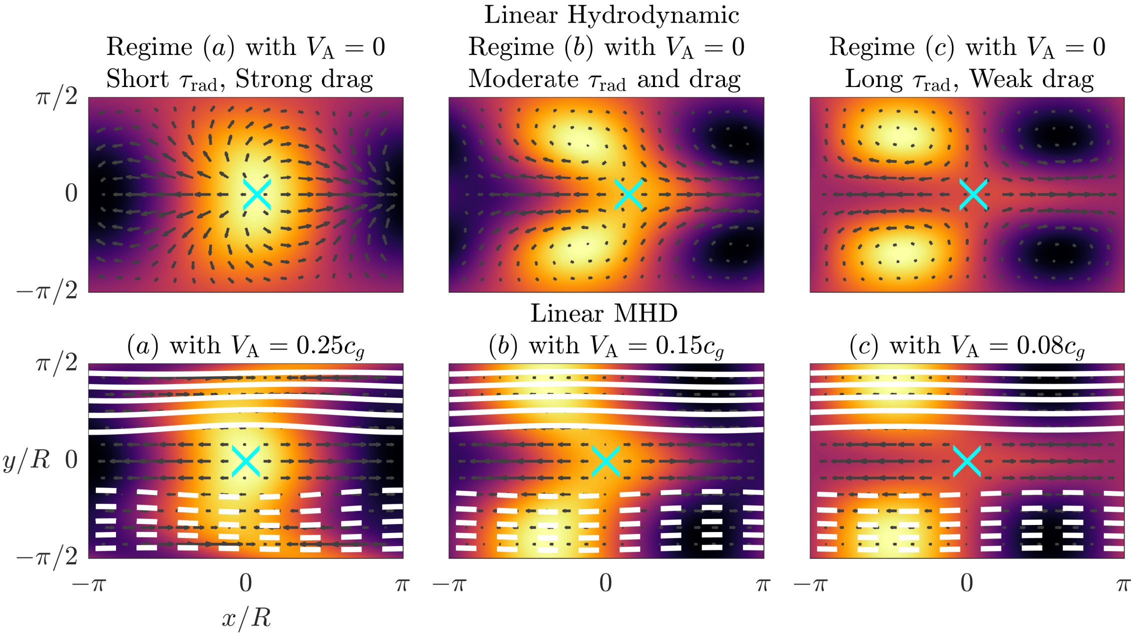

Figure 5.1: Linear solutions (for $\Delta h_{eq}/H = 0.01$ and $k = 1/R$). Contours of the relative layer thickness deviations (rescaled geopotential energy deviations) are plotted on (individually-normalised) colour axes, with (individually-normalised) velocity vectors ($\mathbf{u} = \mathbf{u}_0 + \mathbf{u}_1$), hotspots (cyan crosses) and, where relevant, lines of constant $A = A_0 + A_1$ (solid/dashed for B_x positive/negative) overplotted. Hydrodynamic solutions (top row) are compared to marginally critical MHD solutions (bottom row; compare V_A values to Figure 4.9). Solutions are plotted for (a) $\tau_{rad} = \tau_{drag} = \tau_{wave}$ (left); (b) $\tau_{rad} = \tau_{drag} = 5\tau_{wave}$ (middle); and (c) $\tau_{rad} = \tau_{drag} = 25\tau_{wave}$ (right). Solutions are calculated for $-5L_{eq} < y < 5L_{eq}$, but are cut off for $-R\pi/2 < y < R\pi/2$ (recall, $L_{eq}/R \approx 0.67$). The strong magnetic field aligns flows preventing geopotential recirculation between latitudes, but in the linearised model the (non-linear) equatorial Lorentz force is zero. Consequently, in the linearised model hotspot offsets of marginally critical MHD solutions tend to zero, but do not reverse like full SWMHD simulations.

vanishes at the equator. We plot linear solutions for $\Delta h_{\mathrm{eq}}/H = 0.01$ in Figure 5.1, on the reduced domain $-\pi/2 < y/R < \pi/2$, for three τ_{rad} and τ_{drag} choices, comparing hydrodynamic solutions with MHD solutions at the threshold of criticality, as found by simulations.

Hydrodynamic solutions generally resemble those discussed in Showman & Polvani (2011), albeit with an adjustment due to u_0 (as discussed by Tsai *et al.*, 2014, for u_0 constant). They are characterised by geostrophic circulations at mid-to-high latitudes and zonal pressure driven jets at equatorial latitudes. Such solutions closely resemble the non-linear hydrodynamic steady state solutions we discussed in Chapter 4. The characteristic flow patterns of hydrodynamic steady state solutions can also be directly linked to the forcing responses of specific standing, planetary scale, equatorial shallow-water waves (Matsuno, 1966; Showman & Polvani, 2011; Tsai *et al.*, 2014). The geostrophic circulations are linked to the planetary scale equatorial Rossby waves, which are geostrophic in nature at mid-to-high latitudes; while the equatorial jets are linked the superposition of the planetary scale equatorial Rossby waves and the equatorial Kelvin wave, which travels eastward about the equator in response to pressure perturbations. The presented linear hydrodynamic solutions all have eastward hotspots (located at points of zonal wind divergence), as the linearised meridional convergence of geopotential flux into the equator, $-gH\partial v_1/\partial y|_{y=0}$, is maximised eastward of the substellar point (due to the form of the geostrophic circulations; further discussion in Chapter 4).

The marginally critical MHD solutions share some common characteristics with their non-linear simulated counterparts. Specifically, in these solutions the aligning influence of the meridional Lorentz force is strong enough obstruct geostrophic circulations, which are replaced by zonally-aligned winds. However, unlike their simulated non-linear counterparts, the magnetohydrodynamic solutions do not have westward hotspots. The arises because in this simple linear model one can show that the Lorentz force components, which drive hotspots reversals in non-linear simulations (see Chapter 4), vanish at the equator.[1]

[1]For $S(y)$ equatorially-symmetric and B_0 equatorially-antisymmetric, $\hat{v}$ is antisymmetric and $\{\hat{u}, \hat{v}, \hat{A}\}$ are symmetric about the equator (see Appendix D.1). Hence, $\hat{B}_x = (\mathrm{d}\hat{A}/\mathrm{d}y - B_0\hat{h})/H$ is antisymmetric; while, by Equation (5.4), $\hat{A}(0) = 0$, so $\hat{B}_y(0) = -ik\hat{A}(0)/H = 0$. Consequently, $ikB_0\hat{B}_x + \mathrm{d}B_0/\mathrm{d}y\hat{B}_y$ and

Instead, marginally critical MHD solutions approach a limit of zero hotspot offset, as the obstruction of geostrophic circulations causes $-gH\partial v_1/\partial y|_{y=0} \to 0$. This highlights that in simple linear models, with similar linearisations of the Lorentz force and the induction equation (i.e., without more sophisticated treatments of magnetic diffusion and non-linear effects), one can identify the obstruction of geostrophic circulations that cause hotspot reversals in non-linear simulations, but not westward hotspot offsets explicitly. This observation is useful in the remainder of this chapter, where we aim to link the magnetic obstruction of geostrophic circulation patterns to wave dynamics.

5.2 Free wave solutions

5.2.1 Equatorial magnetohydrodynamic wave equations

To study the linear equatorial magnetohydrodynamic waves of the system, we linearise the non-diffusive, unforced, drag-free versions of Equations (4.1) to (4.4) about the background state, $\{u_0, v_0, h_0, A_0\} = \{0, 0, H, A_0(y)\}$, where H is the constant and $\mathrm{d}A_0/\mathrm{d}y = HB_0$ (for $\mathbf{B}_0 = B_0(y)\widehat{\mathbf{x}}$ in velocity units). Applying the plane wave ansatz, $\{u_1, v_1, h_1, A_1\} = \{\hat{u}(y), \hat{v}(y), \hat{h}(y), \hat{A}(y)\}\mathrm{e}^{i(kx-\omega t)}$, the evolution of the perturbations is determined by the following linearised SWMHD system:

$$- i\omega\hat{u} = f\hat{v} - ikg\hat{h} + ikB_0\hat{B}_x + \frac{\mathrm{d}B_0}{\mathrm{d}y}\hat{B}_y, \tag{5.5}$$

$$- i\omega\hat{v} = -f\hat{u} - g\frac{\mathrm{d}\hat{h}}{\mathrm{d}y} + ikB_0\hat{B}_y, \tag{5.6}$$

$$- i\omega\hat{h} = -H\left(ik\hat{u} + \frac{\mathrm{d}\hat{v}}{\mathrm{d}y}\right), \tag{5.7}$$

$$- i\omega\hat{A} = -HB_0\hat{v}, \tag{5.8}$$

$ikB_0\hat{B}_y$ both vanish at the equator.

where $\hat{B}_x = (\mathrm{d}\hat{A}/\mathrm{d}y - B_0\hat{h})/H$ and $\hat{B}_y = -ik\hat{A}/H$. From this we eliminate $\hat{u}$, $\hat{h}$, $\hat{A}$, $\hat{B}_x$, and $\hat{B}_y$ to obtain the single ordinary differential equation:

$$\mathcal{L}\{\hat{v}\} \equiv F_1\frac{\mathrm{d}^2\hat{v}}{\mathrm{d}y^2} + F_2\frac{\mathrm{d}\hat{v}}{\mathrm{d}y} + F_3\hat{v} = 0, \tag{5.9}$$

for the latitudinal solving domain, $-L_y < y < L_y$, with

$$F_1 = \left(\omega^2 - B_0^2k^2\right)\left(\omega^2 - c_m^2k^2\right), \tag{5.10}$$

$$F_2 = 2B_0\frac{\mathrm{d}B_0}{\mathrm{d}y}c_g^2k^4, \tag{5.11}$$

$$\begin{aligned} F_3 =& \frac{(\omega^2 - c_m^2k^2)}{c_g^2}\left[(\omega^2 - c_m^2k^2)(\omega^2 - B_0^2k^2) \quad - \omega^2 f^2 - \omega k\frac{\mathrm{d}f}{\mathrm{d}y}c_g^2\right] \\ & - 2\omega f B_0\frac{\mathrm{d}B_0}{\mathrm{d}y}k^3, \end{aligned} \tag{5.12}$$

where $c_m(y) \equiv (c_g^2 + B_0^2)^{1/2}$ denotes the (rotationless) magneto-gravity wave speed. This system can the contain singular points at $y = y_s$, if $\omega = \pm B_0(y_s)k$ (Alfvén singularity) or $\omega = \pm c_m(y_s)k$ (magneto-gravity singularity), which we label based on the ω-regions each singularity is associated with.

If one attempts to write $\mathcal{L}$ in Sturm-Liouville form[2], through use of an integrating factor, it is found that the highest order functional coefficient of the Sturm-Liouville operator, $p = (\omega^2 - B_0^2k^2)/(\omega^2 - c_m^2k^2)$, is not independent of the oscillation frequency. Therefore, the desirable properties of the Sturm-Liouville eigenvalue problem (e.g., real eigenvalues and orthogonality of eigenfunctions) are not generally guaranteed. Zaqarashvili (2018) studied this system in the weakly-magnetic limit where singular points do not influence the planetary scale waves.[3] In this approximation $\mathcal{L}$ can be re-expressed in terms of the parabolic cylinder Sturm-Liouville operator (the hydrodynamic version of $\mathcal{L}$, see Matsuno, 1966). Therefore, away from singular ω-regions, where the approximations of Zaqarashvili (2018) hold, one may expect solutions to conform to Sturm-Liouville properties (which we

[2]We use the Sturm-Liouville definition: $(p\hat{v}')' + q\hat{v} = \lambda w\hat{v}$, where $p(y), w(y) > 0$, and $p(y)$, $p'(y)$, $q(y)$, and $w(y)$ are continuous functions over the system's finite solving domain, $y \in [-L_y, L_y]$.

[3]Precisely, Zaqarashvili (2018) used $B_0 = \gamma y$ with constant γ, applying the weak-field assumptions $\omega^2 \gg \gamma^2k^2y^2$ and $|\omega^2 - c^2k^2| \gg \gamma^2k^2y^2$.

find in the following analysis).

5.2.2 Equatorial wave solving method

We now examine non-trivial eigenvalue-eigenfunction pairs, $\{\omega, \hat{v}(y)\}$, that satisfy $\mathcal{L}\{\hat{v}\} = 0$ everywhere in the latitudinal domain, $-L_y < y < L_y$, subject to impermeable boundary conditions (i.e., $\hat{v}(\pm L_y) = 0$). We use the planetary parameters discussed in Chapter 4, $f = \beta y$ and $B_0 = V_{\mathrm{A}} \mathrm{e}^{1/2} \tanh(y/L_{\mathrm{eq}})$. London (2017) found that this $B_0(y)$ choice is useful because it is bounded as $y \to \infty$, so there is no irregular singular point as $y \to \infty$ (as would be the case for $B_0 = \gamma y$). Moreover, since $B_0(y)$ is monotonic, there is at most one Alfvén singularity in each hemisphere. For this $B_0(y)$ choice, solutions with $c_g k \leq |\omega| \leq (c_g^2 + V_{\mathrm{A}}^2 \mathrm{e})^{1/2} k$ have magneto-gravity singularities; while solutions with $|\omega| \leq V_{\mathrm{A}} \mathrm{e}^{1/2} k$ have Alfvén singularities. We seek wave-like solutions with the planetary scale azimuthal wavenumber, $k = 1/R$. We find that solving this eigenvalue problem, without further approximation on $\mathcal{L}$, is an analytically intractable problem so we use a semi-analytic approach.

Since $\mathcal{L}$ is symmetric about the equator, homogeneous solutions will be either *symmetric* ($\hat{v}$ symmetric and $\hat{u}, \hat{h}, \hat{A}$ antisymmetric) or *antisymmetric* ($\hat{v}$ antisymmetric and $\hat{u}, \hat{h}, \hat{A}$ symmetric) about the equator.[4] Although the system we solve here is unforced, we wish to compare solutions to the numerical simulations of Chapter 4, which had equatorially-symmetric forcing on h. Therefore, we only consider antisymmetric homogeneous solutions and solve $\mathcal{L}\{\hat{v}\} = 0$ in the upper-half domain, $0 < y < L_y$, with the antisymmetric lower boundary condition $\hat{v}(0) = 0$, which replaces $\hat{v}(-L_y) = 0$. Eigenfunctions are defined up to a constant factor, so a third and final normalisation boundary condition must also be included. We set $\mathrm{d}\hat{v}/\mathrm{d}y|_{y=0} = \mathcal{N}$, where $\mathcal{N}$ is a normalisation constant chosen for numerical convenience, and take $L_y = 5L_{\mathrm{eq}}$ to ensure boundary influences are negligible.

We use a shooting method to seek eigensolutions. The shooting method calculates successive "shots" (or test solutions, $\hat{v}_T$) for given test frequencies, ω_T, where each shot satisfies $\mathcal{L}\{\hat{v}_T\} = 0$, subject to two of the three boundary conditions. The third boundary

[4] If $\hat{v}$ is equatorially-symmetric, Equations (5.5) to (5.8) yield $\hat{u}, \hat{h}, \hat{A}$ antisymmetric and vice versa.

condition is then satisfied by varying ω_T so that the deviation from the third boundary condition, $G[\omega_T]$, vanishes.

If the system has no singular points, shots are carried out by the inversion of the tridiagonal matrix that corresponds to Equation (5.9), with finite difference discretizations, such that the lower boundary conditions are satisfied. We find that magneto-gravity singularities are false singularities (i.e., $\mathcal{L}$ is singular but solutions are not; see Appendix D.2), so, for $V_\mathrm{A} > 0$, solutions in the magneto-gravity singularity ω-range can also be treated as regular everywhere. For solutions in the Alfvén singularity ω-range, we construct Frobenius power series solutions in the singular region (see Appendix D.2), fix constants of integration by shooting into, and matching with, the $y = 0$ boundary conditions, before finally shooting towards $y = L_y$ to obtain $G[\omega_T]$. Solutions are then checked via back-substitution.

As discussed above, Sturm-Liouville theory only guarantees real eigenvalues in the weakly-magnetic limit. Therefore, we examine convergence for complex test frequencies, which have $G = G_r + iG_i = 0$ for $G_r, G_i \in \mathbb{R}$. We find that G_rG_i is antisymmetric about $\omega_i = 0$, with contours $G_r = 0$ and $G_i = 0$ crossing exclusively on the real line, so $\omega \in \mathbb{R}$. We find the position of eigensolutions on the real line using the bracketed Newton-Raphson method discussed in Press *et al.* (1992).

5.2.3 Free wave eigensolutions

We label non-singular eigensolutions with a meridional mode number, n, based on the hydrodynamic convention. Generally, when the domain is finite and large enough, magnetic eigenfunctions for solutions without singularities are qualitatively similar to their hydrodynamic counterparts and n is the number of internal points where $\hat{v}(y) = 0$ in $-L_y < y < L_y$. However, hydrodynamic Kelvin solutions have the property $\hat{v} = 0$ everywhere so represent a special case. They are typically labelled with the meridional mode number $n = -1$, with $\psi_{-1} = 0$ (Matsuno, 1966). We find that solutions with $c_gk \leq |\omega| \leq (c_g^2 + V_\mathrm{A}^2\mathrm{e})^{1/2}k$ are the magnetic versions of Kelvin solutions, so we label them with $n = -1$ for consistency, although we find they have small non-zero $\hat{v}$ (see below).

Table 5.1: Oscillation frequencies, ω, for the $n = 1$, $n = 3$, and $n = -1$ equatorial wave solutions with the planetary scale azimuthal wavenumber, $k = 1/R$, are tabulated for three choices of V_{A}. In the *Solution type* column we use the following shorthands: R/MR denotes Rossby/magneto-Rossby solutions, WIG/WMIG denotes westward inertial gravity/magneto-inertial gravity solutions, EIG/EMIG denotes eastward inertial gravity/magneto-inertial gravity solutions, WA denotes (singular) westward Alfvén solutions, EA denotes (singular) eastward Alfvén solutions, K/MK denotes equatorial Kelvin/magneto-Kelvin solutions, and BK/BMK denotes boundary Kelvin/magneto-Kelvin solutions.

		$V_{\mathrm{A}} = 0$	$V_{\mathrm{A}} = 0.15c_g$	$V_{\mathrm{A}} = 0.2c_g$
n	Solution type	$\omega/(c_g/R)$	$\omega/(c_g/R)$	$\omega/(c_g/R)$
1	WIG/WMIG	-2.57	-2.61	-2.62
1	R/MR	-0.293	-0.326	*
1	EIG/EMIG	2.89	2.90	2.91
1	WA†	*	-0.117†	-0.142†
1	EA†	*	0.0329†	0.0556†
3	WIG/WMIG	-3.98	-3.99	-4.00
3	R/MR	-0.134	*	*
3	EIG/EMIG	4.11	4.12	4.13
3	WA†	*	-0.161†	-0.201†
3	EA†	*	0.0640†	0.102†
-1	K/MK	1	1.01	1.01
-1	BK/BMK	-1	-1.03	-1.05

* Empty entries indicate that no solution exists for this V_{A} value.
† Solutions with Alfvén singularities (see text).

For hydrodynamic and weakly-magnetic systems there are three solutions for each $n \geq 1$: one equatorial Rossby/magneto-Rossby solution, one westward equatorial IG/MIG solution, and one eastward equatorial IG/MIG solution. When magnetism is included another two sets of solutions (one east; one west), with $|\omega| \leq V_{\mathrm{A}}\mathrm{e}^{1/2}k$, emerge. These solutions, which have Alfvén singularities (where $\omega^2 = B_0(y_s)^2k^2$), differ significantly from regular equatorial wave solutions (see below). For convenience, we label these with a meridional mode number, n, determined by the scale of latitudinal variations in $\hat{v}$ (for $n = 1, 3, 5$, $\hat{v}$ is plotted in Figure 5.3). In Table 5.1 we present oscillation frequencies, ω, for the $n = 1$, $n = 3$, and $n = -1$ free wave eigensolutions, with each row representing a specific type of equatorial wave (see caption). We present the oscillation frequencies for $V_{\mathrm{A}} = 0$, $V_{\mathrm{A}} = 0.15c_g/R$ and $V_{\mathrm{A}} = 0.2c_g/R$ and, in cases where eigenfunctions are finite everywhere, we plot the corresponding free wave eigenfunctions for the equatorial $n = 1$ and $n = -1$ waves in Figure 5.2.

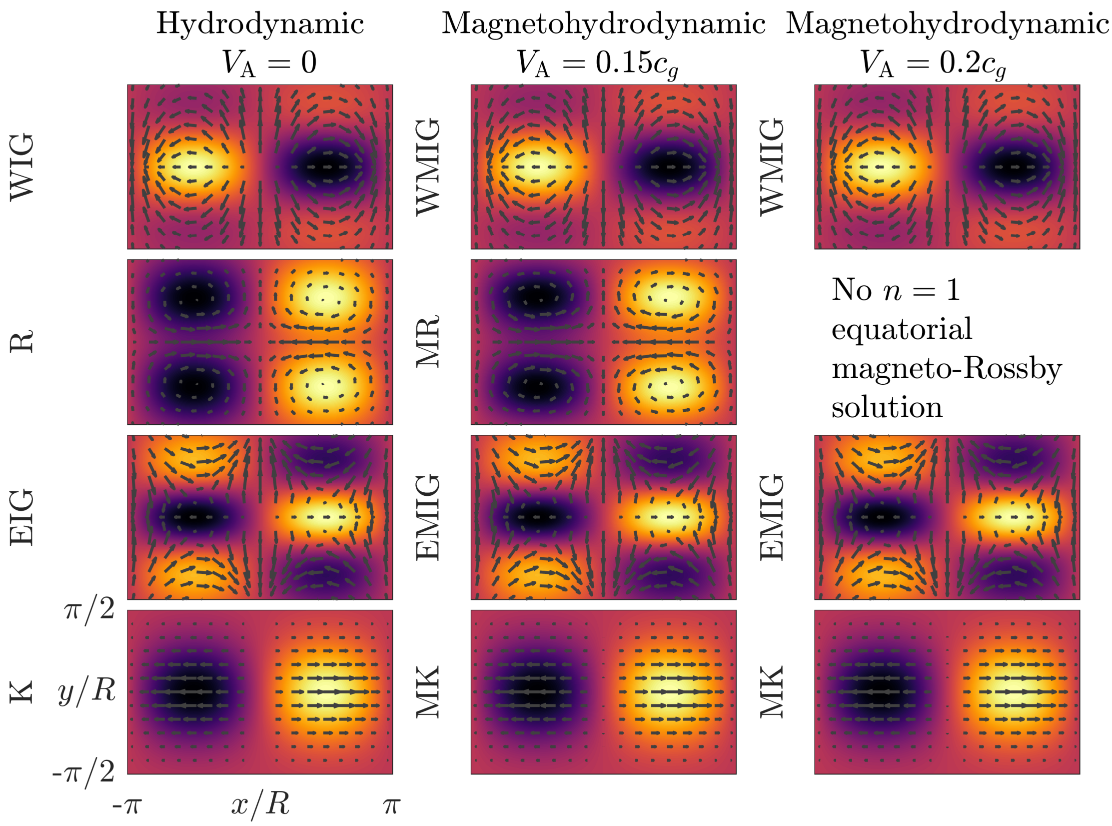

Figure 5.2: The regular equatorial $n = 1$ (rows one to three) and $n = -1$ (row four) free wave eigenfunctions (geopotential contours with overlaid velocity vectors) are plotted for $V_A = 0$, $V_A = 0.15c_g$, and $V_A = 0.2c_g$, taking $k = 1/R$. We label rows according to their wave types (see Table 5.1). Solutions are calculated for $-5L_{eq} < y < 5L_{eq}$, but are cut off for $-R\pi/2 < y < R\pi/2$ ($L_{eq}/R \approx 0.67$).

Eastward and westward equatorial IG/MIG solutions are the system's most rapidly oscillating waves (with $|\omega| > c_g k$). The azimuthal background magnetic field slightly increases the phase speed of the MIG modes (see Table 5.1). However, their energy redistribution patterns remain qualitatively similar to their hydrodynamic IG counterparts (see Figure 5.2, rows one and three).

Kelvin/magneto-Kelvin solutions are characterised by zonally-dominated winds. The are two hydrodynamic Kelvin solutions: an eastward equatorial Kelvin solution, with $\omega = c_g k$, $\hat{v} = 0$, $\{\hat{u}, \hat{h}\} \propto \exp(-y^2/2L_{\rm eq})$, and a westward boundary Kelvin solution, with $\omega = -c_g k$, $\hat{v} = 0$, $\{\hat{u}, \hat{h}\} \propto \exp(y^2/2L_{\rm eq})$.[5] These hydrodynamic solutions are special cases of magneto-Kelvin eigensolutions, which have $c_g k \leq |\omega| \leq (c_g^2 + V_{\rm A}^2 {\rm e})^{1/2} k$. While hydrodynamic Kelvin solutions have $\hat{v} = 0$ everywhere, we find that magneto-Kelvin solutions acquire a non-zero $\hat{v}$ in order to maintain latitudinally-independent oscillation frequencies. This can be understood by combining Equations (5.5), (5.7) and (5.8) to yield

$$(\omega^2 - c_m^2 k^2)\hat{u} = if\omega\hat{v} - ikc_g^2 \frac{{\rm d}\hat{v}}{{\rm d}y}. \tag{5.13}$$

For hydrodynamic Kelvin solutions, the lefthand and righthand sides of Equation (5.13) are identically zero throughout the domain; whereas magneto-Kelvin solutions have $c_g k \leq |\omega| \leq (c_g^2 + V_{\rm A}^2 {\rm e})^{1/2} k$, $\{\hat{u}, \hat{h}\}$ similar to their hydrodynamic counterparts, and a non-zero $\hat{v}$ that ensures Equation (5.13) remains balanced. Like in the hydrodynamic limit, we find two magneto-Kelvin solutions: an eastward equatorial magneto-Kelvin solution and a westward boundary magneto-Kelvin solution. Magnetism causes both varieties to have a small non-zero meridional velocity component ($|\hat{v}/\hat{u}| \ll 1$) and an increased $|\omega|$, but both are characteristically similar to their hydrodynamical counterparts. For the equatorial magneto-Kelvin solution, this is illustrated in Figure 5.2, which shows its energy redistribution pattern remains qualitatively similar as $V_{\rm A}$ is increased.

In the hydrodynamic version of the system, equatorial Rossby solutions propagate westward and oscillate slowly ($|\omega| < c_g k$), with their azimuthal phase speeds, $|\omega|/k$, suc-

[5]The westward boundary Kelvin solution is removed when the condition is $\{\hat{u}, \hat{v}, \hat{h}\} \to 0$ as $|y| \to 0$ is imposed (Matsuno, 1966).

cessively decreasing for larger n solutions. In the hydrodynamic limit, the structures of equatorial Rossby solutions are characterised by mid-to-high latitude geostrophic vortices (see Figure 5.2, row two, lefthand column). For weakly-magnetic equatorial magneto-Rossby solutions, we find that the presence of the azimuthal background magnetic field has little effect on the form of the waves' eigenfunctions, which are magnetogeostrophic in nature. Weakly-magnetic solutions adjust to the contribution of magnetic tension with small increases to their azimuthal phase speeds. However, when their oscillation frequencies are exceeded by the maximal background azimuthal Alfvén frequency (i.e., when $V_{\mathrm{A}} \geq \mathrm{e}^{-1/2}|\omega|/k$), equatorial magneto-Rossby solutions enter the ω-range of Alfvén singularities and are removed from the system. Higher n equatorial magneto-Rossby solutions are removed for the weakest V_{A} values, before successively lower n solutions are removed for larger V_{A} values (as Alfvénic properties become dynamically important at larger and larger scales). We attribute the removal of the planetary scale equatorial magneto-Rossby solutions to the breaking of potential vorticity conservation in regions of large Lorentz force

The shallow-water hydrodynamic definition of potential vorticity is, $q = h^{-1}(\partial v/\partial x - \partial u/\partial y + f)$ (e.g., Vallis, 2006). In the non-diffusive, unforced, drag-free version of the SWMHD model, the potential vorticity evolution satisfies

$$\frac{\mathrm{D}q}{\mathrm{D}t} = \frac{1}{h}[\nabla \times (\mathbf{J} \times \mathbf{B})] \cdot \widehat{\mathbf{z}}, \tag{5.14}$$

where $\mathbf{J} = (\partial B_y/\partial x - \partial B_x/\partial y)\widehat{\mathbf{z}}$. Equation (5.14) shows that the curl of the Lorentz force generated by the horizontal magnetic field component generally prevents potential vorticity conservation in the magnetic limit.[6] Since the material conservation of potential vorticity is essential to the propagation mechanism of Rossby waves (e.g., see Vallis, 2006), in regions of large Lorentz force their generation is inhibited.

In magnetic systems, two additional sets of solutions emerge. These solutions have $|\omega| \leq V_{\mathrm{A}}\mathrm{e}^{1/2}k$, so contain singularities, yet present some distinguishable properties of

[6]Further, Dellar (2002) showed that potential vorticity has no materially invariant counterpart in SWMHD.

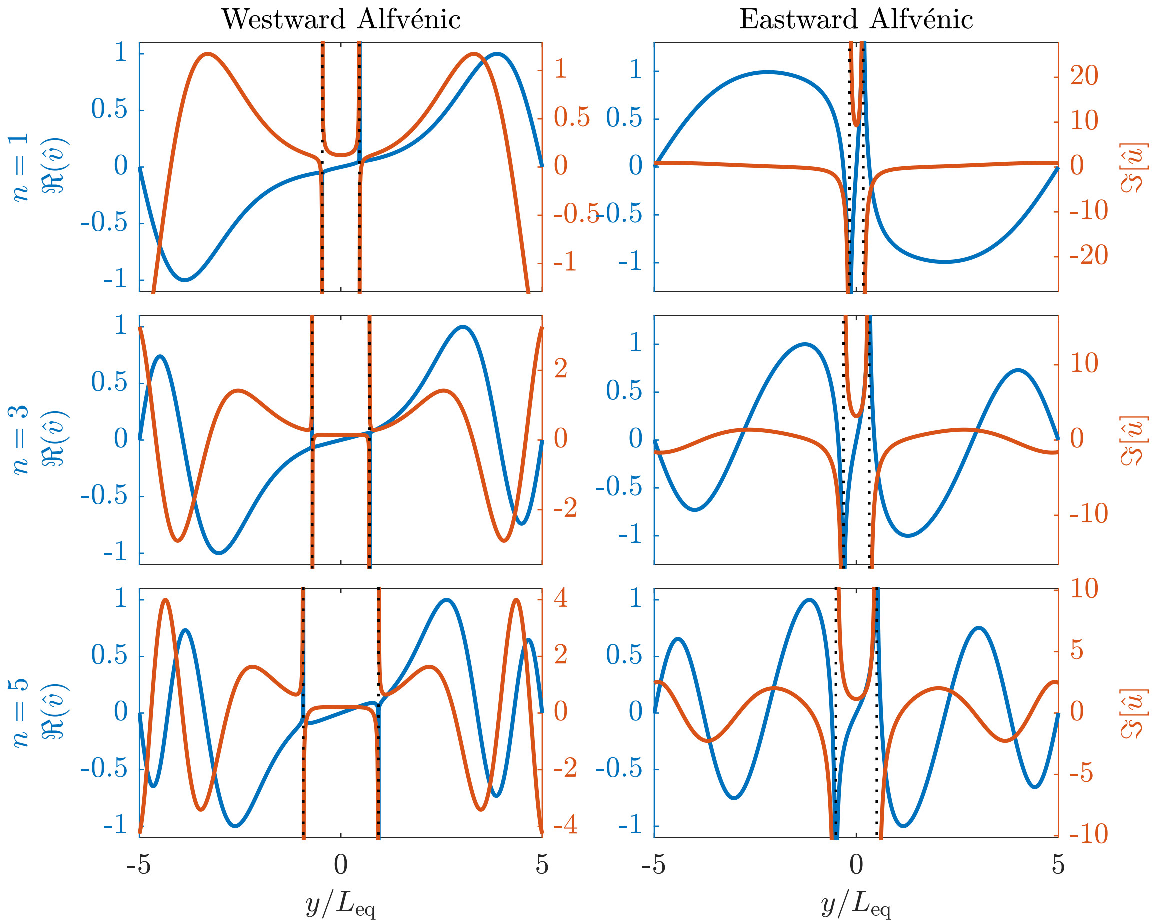

Figure 5.3: The velocity profiles of the first few singular free wave eigenfunctions are plotted for $V_{\rm A} = 0.2c_g/R$ and $k = 1/R$. Magnetic systems have two sets of singular solutions: one westward travelling and one eastward travelling, which have Alfvénic properties (see main text). $\hat{v}$ (blue) and $\hat{u}$ (red) are respectively purely real and purely imaginary for the normalisation we apply. We mark asymptotes at $y = \pm y_s$ with dotted black lines. The solutions are labelled with the latitudinal mode number, n, based on the latitudinal dependence of $\hat{v}$. The corresponding profiles for $V_{\rm A} = 0.15c_g/R$ are qualitatively identical.

Alfvén waves. Specifically, they arise in both eastward and westward travelling varieties, and $|\omega|$ increases with V_{A} and n. To assess their nature as $y \to y_s$ (for $\omega^2 = B_0(y_s)^2 k^2$), we use the Frobenius solutions discussed in Appendix D.2. In singular regions, $\hat{v} = O(\ln|(y - y_s)/L_{\mathrm{eq}}|)$, so by Equation (5.13) $\hat{u} = O([(y-y_s)/L_{\mathrm{eq}}]^{-1})$, meaning that $|\hat{u}/\hat{v}| \to \infty$ as $y \to y_s$. This highlights that Alfvén singularities cause a wave barrier to emerge at $y = y_s$, over-which wave-driven meridional energy/momentum transport mechanisms cannot cross. Since they are not finite everywhere, equatorial wave structures with Alfvén singularities cannot determine global energy redistribution in the same way that planetary-scale equatorial waves do in hydrodynamic hot Jupiter models. Hence, in the limit where magnetism becomes significant, dissipative and non-linear effects become essential for understanding equatorial dynamics. A non-singular analogue of these solutions could be present in systems that include these extra physical processes but, since we are focused on the breakdown of geostrophic balance, we do not investigate solutions of this kind further.[7]

Thus far, we have discussed magnetic free wave solutions about a flat rest state. However, Tsai *et al.* (2014) and Debras *et al.* (2020) find the redistributing properties of waves can be altered by the presence of a background zonal flow, though the fundamental characteristics of these waves remain unchanged. Compared to the system we have so far explored, taking $u_0 = U_0$ constant (as in Tsai *et al.*, 2014), simply manifests itself in the trivial phase translation $\omega \mapsto \omega^* - U_0 k$, where ω and ω^* are oscillation frequencies for a background at rest and a background with a zonal flow respectively. For this translation, Alfvén singularities emerge where $B_0(y_s)^2 k^2 = (\omega^* - U_0 k)^2 = \omega^2$, which is the same condition as the rest case. We have also considered solutions about the latitudinally dependent background state, $u_0 = u_0(y)$, finding that Alfvénic singularities, with similar Frobenius

[7]In the very strong field limit, London (2017) identified "outer band" solutions akin to these Alfvenic solutions that were trapped in polar regions in linear non-diffusive beta-plane systems, but concluded that they do not have a finite global (linear, non-diffusive) counterpart in London (2018). Spherical (linear, non-diffusive) SWMHD waves studies in other geometries have found additional slow magneto-Rossby (Márquez-Artavia *et al.*, 2017) and magnetostrophic (Heng & Spitkovsky, 2009) type waves at the poles of shallow-water systems, which may be useful in explaining the dynamics of the polar MHD flows. Márquez-Artavia *et al.* (2017) also found polar trapping of the "fast" magneto-Rossby solutions, which can plausibly be related to the removal of equatorial magneto-Rossby solutions (i.e., magneto-Rossby waves could become confined to regions of the atmosphere less influenced by magnetism).

solution dependencies, emerge at points where $B_0(y_s)^2k^2 = (\omega^* - u_0(y_s)k)^2$.

5.3 Comparisons with non-linear simulations

Our findings concerning Alfvén-Rossby wave coupling in an equatorial beta-plane model, with an equatorially-antisymmetric azimuthal background magnetic field, are consistent with our developed theory of hotspot reversals from the simulations of Chapter 4. In the hydrodynamic limit, planetary scale geostrophic circulations associated with equatorial Rossby waves are free to recirculate energy between the equatorial and mid-to-high latitudes in a manner described by Showman & Polvani (2011). In the weakly-magnetic limit, planetary scale circulations remain largely unchanged, with equatorial magneto-Rossby waves only altering slightly to account for the magnetic contribution to their magneto-geostrophic circulations. However, at a critical threshold magnetic tension becomes large enough to inhibit the magneto-geostrophic circulations associated with equatorial magneto-Rossby waves. This is the free wave manifestation of the obstruction of geostrophic circulations, which we identified as the trigger for hotspot reversals in Chapter 4. Here the analogy between global circulations and the standing wave description of linear steady-state solutions described by Showman & Polvani (2011) breaks down and the force balance description used in Chapter 4 is preferable. In Chapter 4, we saw that the meridional Lorentz force responsible for obstructing geostrophic circulations always has a corresponding westward component that, ultimately, results in hotspot reversals. Together, the developed theory of Chapter 4 and this chapter can be used to place a zero-amplitude limit on the reversal threshold, $V_{\mathrm{A,crit}}$. In linear theory, magnetic tension inhibits the propagation of equatorial Rossby waves, with the oscillation frequency

$$\omega_{\mathrm{R},n} = \frac{-\beta k}{k^2 + (2n+1)\beta/c_g}, \tag{5.15}$$

when $\omega_{\mathrm{A,max}} \geq |\omega_{\mathrm{R},n}|$, where $\omega_{\mathrm{A,max}} = B_{0,\mathrm{max}}k = V_{\mathrm{A}}\mathrm{e}^{1/2}k$ is the maximal Alfvén frequency. Our findings suggest that, when the slowest (largest n) equatorial Rossby wave that is important for supporting the planetary scale mid-to-high latitude geostrophic balance becomes inhibited by magnetic tension, geostrophic circulations are obstructed and hotspots are driven westward by the resulting zonal Lorentz force.

In Figure 4.9, we have overplotted the theoretical thresholds associated with the obstruction of the $n = 1, 3, 5$ equatorial Rossby solutions, for comparison with the zero-amplitude ($\mathit{\Delta} h_{\rm eq}/H \to 0$) limits of the simulated reversal thresholds, $V_{\rm A,crit}$. We generally find acceptable agreement between the simulations and these theoretical criteria, noting that in the most physically relatable case, where $\tau_{\rm rad}$ is short, reversals occur at the point where the $n = 1$ equatorial Rossby wave is overcome by magnetic tension. When $\tau_{\rm rad}$ and $\tau_{\rm drag}$ act over longer timescales, Figure 4.9 suggests that the obstruction of geostrophic circulations is associated with the loss of larger n equatorial Rossby solutions. This is somewhat consistent with the standing wave description of linear steady-state hydrodynamic solutions, as geostrophic circulations in solutions with longer $\tau_{\rm rad}$ and $\tau_{\rm drag}$ timescales are located at higher latitudes (e.g., see Figure 4.1), so require contributions to their energy recirculation patterns from larger n equatorial Rossby waves (e.g., Matsuno, 1966; Showman & Polvani, 2011; Tsai *et al.*, 2014). While a wave analysis with non-linear effects and diffusion may be able to more precisely define these weakly-forced limits, we note that this description provides a vast improvement on scaling predictions of typical toroidal field strengths on hot Jupiters, which have order of magnitude (or larger) uncertainties (discussion in Chapter 6).

Chapter 6

The Magnetic Reversal Mechanism

In Chapter 4, we used identified the mechanism that drives magnetic hotspot reversals in SWMHD simulations of hot Jupiters; whereas in Chapter 5 we linked the mechanism to wave dynamics. In the chapter we tie together all these ideas, discuss the relationship between hotspot reversals and wind reversals, and make comparisons with past three-dimensional (3D) MHD simulations of hot Jupiters. First, to recap the findings of Chapter 4, we provide a schematic and summarised explanation of the hotspot mechanism in Figure 6.1 and its caption. In short, when mid-to-high latitude planetary-scale drag-adjusted geostrophic circulations attempt to flow through a strong equatorially-antisymmetric toroidal field, they are resisted in the meridional direction and bend magnetic field lines in a manner that always induces westward Lorentz force accelerations in the hottest dayside regions. If the toroidal field exceeds critical magnitude, this results zonally-aligned winds and westward hotspot for all $\tau_{\rm rad}$, $\tau_{\rm drag}$, and $\Delta h_{\rm eq}/H$ choices.

This mechanism is also relevant for other, less idealised, magnetic field geometries. The reversal mechanism requires two features in the azimuthal field geometry: (1) large $|B_x|$ at mid-to-high latitudes to block/obstruct the circulation of the energy transporting geostrophic flows and (2) smaller or zero $|B_x|$ at equatorial latitudes, so that when

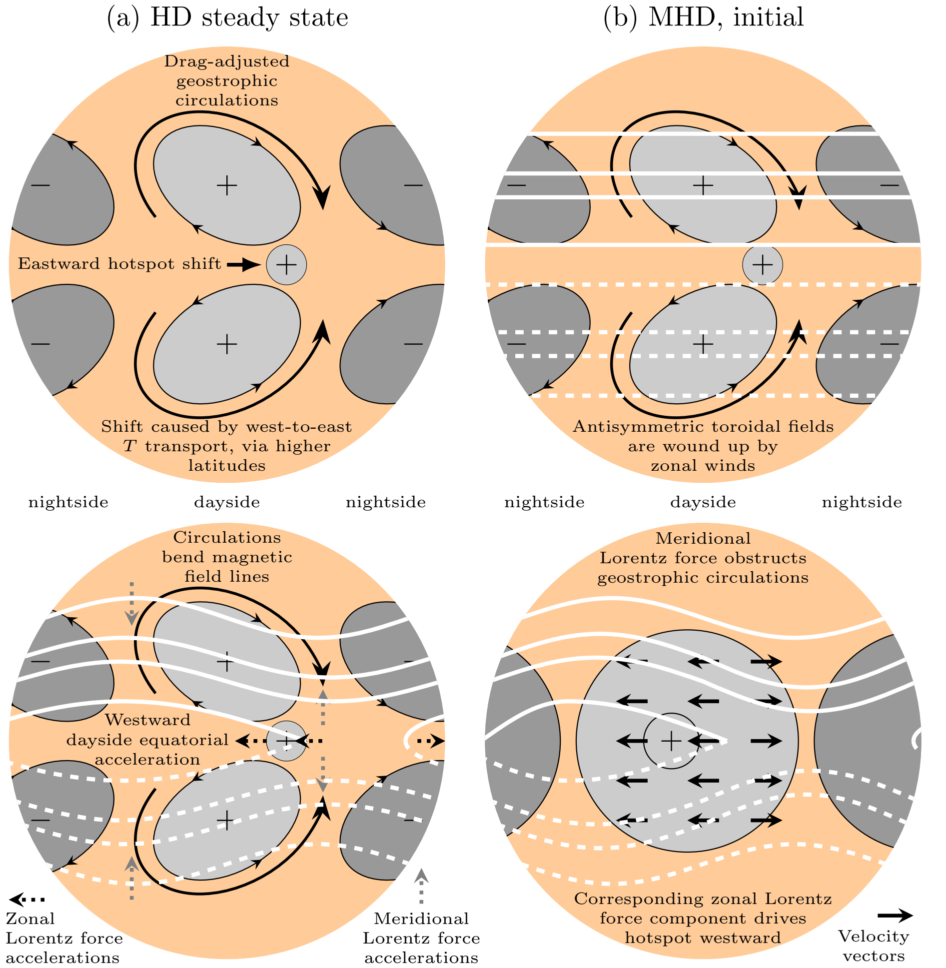

(c) MHD, magnetic tension build-up from circulations

(d) MHD, resultant Lorentz force aligns winds (confining T transport) and drives reversals

Figure 6.1: A schematic of the magnetic reversal mechanism, with grey temperature contours and white magnetic field lines (solid for $B_x > 0$; dashed for $B_x < 0$). (*a*) In hydrodynamic steady state solutions, drag-adjusted geostrophic circulations dominate at mid-to-high latitudes; whereas zonal pressure-driven jets dominate at the equator. Hotspots are shifted eastward as these circulations transport thermal energy from the western equatorial dayside to the eastern equatorial dayside, via higher latitudes. (*b*) In ultra-hot Jupiters, partially-ionised winds flow through the planet's deep-seated magnetic field, inducing a dominant equatorially-antisymmetric atmospheric toroidal magnetic field. When field lines are parallel to the equator, magnetic tension is zero, so flows behave hydrodynamically. (*c*) As the field and flow couple, the geostrophic circulations bend the magnetic field lines poleward on the western dayside and equatorward on the eastern dayside, generating a Lorentz force, $(\mathbf{B} \cdot \nabla)\mathbf{B}$. The meridional Lorentz force component acts to resist the geostrophic circulations; whereas, since $|B_x|$ is smallest in equatorial regions, the zonal Lorentz force component, $(\mathbf{B} \cdot \nabla)B_x$, is westward in hotspot regions, where field lines bend equatorward (and vice versa where field lines bend poleward). (*d*) Beyond a magnetic threshold, the system's nature changes. The meridional Lorentz force obstructs the circulating geostrophic winds, causing zonal wind alignment. This confines thermal structures and blocks the hydrodynamic transport mechanism. The zonal Lorentz force accelerates winds westward in the hottest dayside regions, causing a net westward dayside temperature flux. This drives the hottest thermal structures westward, until zonal pressure gradients can balance the zonal Lorentz force.

magnetic field lines are bent into the equatorial region (by the mid-to-high latitude circulations), they pass into regions of smaller $|B_x|$, generating a westward Lorentz force acceleration. This suggests that, as long as the profile is characterised by these two features, the developed theory does not depend on exact antisymmetry in the dominant magnetic field geometry. This observation is useful when comparing to the 3D MHD simulations of Rogers & Komacek (2014) and Rogers (2017), which are characterised by antisymmetrically-dominant, but not exactly antisymmetric, toroidal magnetic field geometries.

6.1 Hotspot reversal criterion

In Chapters 4 and 5, we identified two physically-motivated reversal criteria on the Alfvén speed. The azimuthal Alfvén speed is defined as $V_{\mathrm{A}} = B_\phi/\sqrt{\mu_0 \rho}$, where μ_0 and ρ are the permeability of free space and the density. Taking $c_g = \sqrt{\mathcal{R}T}$ (see Chapter 4) and applying the ideal gas law therefore yields $B_\phi \sim (V_{\mathrm{A}}/c_g)\sqrt{\mu_0 P}$, where T and P are the temperature and pressure at which the reversal occurs. From this, we have the following critical reversal criterion on the toroidal field magnitude:

$$B_{\phi,\mathrm{crit}} \approx \sqrt{\mu_0 P} \max\left[\frac{\beta/c_g}{k^2+3\beta/c_g}, \frac{2\pi R}{L_{\mathrm{eq}}}\left(\frac{\mathit{\Delta} h_{\mathrm{eq}}}{H}\right)\left(\frac{\tau_{\mathrm{rad}}}{\tau_{\mathrm{wave}}}\right)^{-1}\left(\frac{2\mathit{\Omega}\tau_{\mathrm{wave}}^2}{\tau_{\mathrm{rad}}}+1\right)^{-1}\right], \quad (6.1)$$

where $n = 1$ (largest scale Rossby wave) and $\kappa \approx 1$ (B_ϕ approaches maximal amplitudes close to the equator, as in Rogers & Komacek, 2014) have been taken. This criterion quantifies the toroidal field magnitude sufficient to obstruct geostrophic circulations, with the first term in the maximum relating to when the toroidal field inhibits the propagation of the largest scale equatorial Rossby wave (in the small $\mathit{\Delta} h_{\mathrm{eq}}/H$ limit).

Further, if the electric currents that generate the planet's assumed deep-seated dipolar field are located far below the atmosphere, Menou (2012*a*) argued that the toroidal and dipolar field magnitudes should be related by the scaling law: $B_\phi \sim R_m B_{\mathrm{dip}}$, where $R_m = \mathcal{U}_\phi H/\eta$ is the magnetic Reynolds number and $\mathcal{U}_\phi$ is the magnitude of zonal wind speeds. We use the toroidal field criterion, and apply $B_\phi \sim R_m B_{\mathrm{dip}}$, to quantitively compare the predictions of SWMHD theory to the 3D MHD simulations of Rogers & Komacek (2014) and Rogers (2017).

6.2 Comparisons between SWMHD and 3D MHD

6.2.1 Linking hotspot and wind reversals

Thus far, we have considered hotspot reversals, rather than the reversal of zonal-mean zonal winds, $\bar{u}$. Though time-correlated in 3D MHD models (Rogers, 2017), hotspot and wind reversals are not necessarily synonymous. While thermal/wind structures and geopotential/wind structures compare well between hydrodynamic shallow-water and 3D models (e.g., Perez-Becker & Showman, 2013; Komacek & Showman, 2016), Debras *et al.* (2020) found a consistent treatment of the vertical component of the eddy-momentum flux (i.e., the vertical Reynolds stress) is critical to the development of equatorial superrotation ($\bar{u} > 0$).[1]

In hydrodynamic models of hot Jupiters, equatorial superrotation emerges from the momentum transport mechanism of Showman & Polvani (2011). Showman & Polvani (2011) noted that the necessity for such a mechanism is a consequence of an angular momentum conservation theorem from Hide (due to Hide, 1969*a*), which implies that equatorial superrotation can only be maintained if driven by an up-gradient angular momentum pumping mechanism. Showman & Polvani (2011) showed that this up-gradient mechanism is provided by the same geostrophic circulations that result in eastward hotspots. Therefore, since we have shown that magnetically-driven hotspot reversals are caused by the obstruction these recirculation patterns, Hide's theorem provides an anti-theorem, which implies that the magnetically-driven hotspot reversals are accompanied by a disruption of superrotation.

The realisation of this anti-theorem can be identified in 3D MHD simulations. These found that mid-to-high latitude vortical structures zonally-align and, consequently, the

[1]Interestingly, while SWMHD does not include a consistent treatment of vertical eddy-momentum flux, we still find that $\bar{u}$ can reverse during the transition phase (only) of hotspot reversals in supercritical SWMHD simulations.

transport of eastward eddy-momentum (horizontal Reynolds stress) from mid-latitudes into equatorial regions is reduced at atmospheric depths were reversals occur (compare their Figures 2, 9, and 11 in Rogers & Komacek, 2014). Rogers & Komacek (2014) found that, when the up-gradient horizontal Reynolds stress component diminishes, westward equatorial zonal-mean zonal accelerations are driven by the remaining down-gradient momentum transport components (i.e., the vertical Reynolds stress and the Maxwell stresses). Thus, the above the application of Hide's theorem provides a meaningful connection between wind reversals and the magnetically-driven hotspot reversals mechanism we have presented.

6.2.2 Wave dynamics and turbulence

While we have not modelled turbulence in this work, actual planetary flows are expected to be highly turbulent. In hydrodynamic planetary systems, wave arguments have historically proved useful for developing understanding of geostrophic turbulence and how its conservational properties relate to eddies. Specifically, potential vorticity conservation is fundamental for both Rossby wave propegation and geostrophic turbulence, so Rossby wave properties can be used to understand the structures of planetary scale turbulence (e.g., Rhines, 1975; Vallis, 2006). Rogers & Komacek (2014) found that the relationship between zonal jets and magnetic fields in 3D MHD simulations shared intermittent features with MHD turbulence on a beta-plane that were identified by Tobias *et al.* (2007). Hydrodynamic geostrophic turbulence and MHD beta-plane turbulence have very different characteristics. Amongst them, the wave-wave/wave-zonal flow interactions associated with the inverse cascade of geostrophic turbulence are replaced with interactions that result in a forward MHD cascade, with MHD interactions occurring over scales on (and below) the planetary scale when the azimuthal Alfvén wave frequencies exceed the planetary scale Rossby wave frequency (Diamond *et al.*, 2007). This turbulence condition is remarkably similar to the hotspot reversal criterion we identified in the weakly forced regime, which was motivated by wave dynamics and the findings of non-turbulent SWMHD simulations. We attribute this kinship to the breaking of potential vorticity conservation in MHD models in regions of large horizontal Lorentz force, which inhibits geostrophic characteristics such as Rossby wave propagation (as discussed in Chapter 5). We also highlight that forcing and drags generate potential vorticity sources/sinks, so potential vorticity conservation is modified when drag and forcing treatments are strong, which is why reversal thresholds deviate from this simple criterion in the strongly forced limit.

6.2.3 Magnetic field evolution and structure

After the initial hotspot transition, long term temporal differences between SWMHD and 3D MHD models arise because SWMHD can only model the planetary dipolar field *or* the atmospheric toroidal field self-consistently (see Chapter 2), meaning that it cannot take into account toroidal field induction from reversed conducting zonal winds passing through the planetary dipolar field. If a strong toroidal field can be maintained indefinitely, the shallow-water theory predicts completely reversed winds, even in 3D models. However, at the onset of the wind reversals, the induction caused by the reversed winds flowing through the deep-seated magnetic field will result in a reduction of the atmospheric toroidal field's magnitude. Hence, while the quasi-steady magnetically-driven wind reversals of SWMHD are useful for modelling the reversal process, in reality one would expect to see oscillatory wind variations as toroidal fields successively strengthen and weaken in a wind-up-wind-down cycle of the toroidal magnetic field. Wind variations of this kind can be both observationally inferred from the oscillating peak brightness offsets of HAT-P-7b (Armstrong *et al.*, 2016) and directly measured in 3D MHD simulations of the HAT-P-7b parameter space (Rogers, 2017). This in itself has the interesting consequence that the reversal mechanism may provide a saturation process for the atmospheric toroidal magnetic field.

Due to the density dependence of the Alfvén speed, $B_{\phi,\mathrm{crit}}$ has a $\sim P^{1/2}$ pressure dependence (see Equation (6.1)). This explains why Rogers & Komacek (2014) and Rogers (2017) found that wind reversals first onset in the upper atmosphere, but move deeper for stronger field strengths. Furthermore, if the reversal mechanism is a toroidal field saturation process (as discussed above), B_ϕ should not greatly exceed $B_{\phi,\mathrm{crit}}$. Hence, B_ϕ should

Table 6.1: Estimates of reversal criteria compared to field strengths and reversal criteria from 3D MHD simulations (see Section 6.2.4 for definitions and an accompanying discussion).

Model	$P/$ mbar	$T_{\rm eq}/$ K	$\Delta T/T_{\rm eq}$	$B_{\phi,\rm crit}/$ G	3D comparison
M7b1[a]	20*	1850	0.1-0.2	175-350	$\lvert B_\phi\rvert = 220\,$G
M7b2[a]	200*	1950	0.05-0.1	430-545	$\lvert B_\phi\rvert = 510\,$G
M7b2[a]	10†	1750	0.15-0.2	185-247	$\lvert B_\phi\rvert = 190\,$G
HAT-P-7b[b]	1*	2200	0.22	92	$3\,$G $< B_{\rm dip,crit,base} < 10\,$G

* Critical wind reversal depth, $P \approx P_{\rm crit}$.
† Above critical wind reversal depth, $P < P_{\rm crit}$.
[a] Rogers & Komacek (2014); Parameters of HD209458b.
[b] Rogers (2017); Parameters of HAT-P-7b.

decrease above the deepest region where reversals occur (since $B_{\phi,\rm crit}$ decreases upwards), which is a feature of the toroidal field profiles found in Rogers & Komacek (2014), though other processes may also cause an upwards reduction in B_ϕ. Comparing the geometry of the toroidal fields in the quasi-steady reversed SWMHD solutions with those in oscillating 3D MHD solutions is difficult. However, when the toroidal field is approaching criticality in strength, we do find similarities between our toroidal field geometries and those of Rogers & Komacek (2014). In both models the equatorially-antisymmetric toroidal fields couple to mid-to-high latitude circulations in a manner that bends them towards the equator from west to east, which we showed is a geometry that results in westward Lorentz force accelerations (see Chapter 4).

6.2.4 Quantitive comparisons with 3D MHD

In Table 6.1, we compare predictions of the reversal criterion to magnetic field strengths of in three 3D MHD simulations: M7b1 and M7b2 of Rogers & Komacek (2014), and the HAT-P-7b model of Rogers (2017), all of which display wind reversals at some critical pressure depth, $P_{\rm crit}$. In these estimates, we take $T_{\rm eq} = \bar{T}$, $\Delta T = T_{\rm day} - \bar{T}$, $\tau_{\rm rad} = \tau_{\rm wave}$, and set $\Delta h_{\rm eq}/H = \Delta T/T_{\rm eq}$. For comparisons to the simulations of Rogers & Komacek (2014), we compare $B_{\phi,\rm crit}$ to $|B_\phi|$, the horizontally-averaged toroidal field component at the end of the run; whereas, for the HAT-P-7b simulation of Rogers (2017), we estimate the critical dipolar field strength at the atmospheric base, $B_{\rm dip,crit,base}$. This is calculated using the $B_\phi \sim R_m B_{\rm dip}$ scaling law of Menou (2012*a*). We take $\eta = 2 \times 10^6\,{\rm m^2\,s^{-1}}$ and $\mathcal{U}_\phi \sim 10^2\,{\rm m\,s^{-1}}$ from 3D simulations, to yield $B_{\rm dip,crit} \approx 4.3\,{\rm G}$ at $P = 1\,{\rm mbar}$, then noting that the atmospheric base is located at $r = 0.15R$ in the simulations yields $B_{\rm dip,crit,base} = 7$. We note that the reversal criterion compares reasonably to the magnitude of the horizontally-averaged toroidal component field in the simulations of Rogers & Komacek (2014), with uncertainties in $T_{\rm day}$ bracketing the true $|B_\phi|$ value. This occurs both at $P = P_{\rm crit}$ and above $P_{\rm crit}$, supporting the idea of reversals providing a toroidal field saturation process. The prediction of $B_{\rm dip,crit,base} = 7$ lies within the range $3\,{\rm G} < B_{\rm dip,crit,base} < 10\,{\rm G}$ identified by Rogers (2017). We note that, while $B_{\phi,\rm crit}$ has dependencies on $\mathit{\Delta} T/T_{\rm eq}$ and $\tau_{\rm rad}$, η can vary significantly between the day and night sides of ultra-hot Jupiters (by orders of magnitude). Therefore, current understanding of the connection between toroidal and poloidal fields on hot Jupiter is constrained by large uncertainties (in $B_\phi \sim R_m B_{\rm dip}$), which far outweigh uncertainties in the toroidal field criterion that we have developed.

Chapter 7

Observational Consequences

In this chapter we use results of Chapters 4 to 6 to place estimates on the minimum magnetic field strengths required to cause atmospheric wind variations (and therefore westward venturing hotspots) for a dataset of hot Jupiters.

Recall from Chapter 1 that, to date, westward hotspots/brightspots have been observationally inferred on five hot Jupiters: HAT-P-7b, CoRoT-2b, Kepler-76, WASP-12b, and WASP-33b. Continuous optical *Kepler* measurements have identified east-west brightspot oscillations on the ultra-hot Jupiters HAT-P-7b (Armstrong *et al.*, 2016) and Kepler-76b (Jackson *et al.*, 2019); optical phase curve measurements from *TESS* have found westward brightspot offsets on the ultra-hot Jupiter WASP-33b (von Essen *et al.*, 2020)[1]; while thermal phase curve measurements from *Spitzer* have found westward hotspots on the ultra-hot Jupiter WASP-12b (Bell *et al.*, 2019) and the cooler hot Jupiter CoRoT-2b (Dang *et al.*, 2018). Three explanations for these observations have been proposed: cloud asymmetries confounding optical measurements (Demory *et al.*, 2013; Lee *et al.*, 2016; Parmentier *et al.*, 2016; Roman & Rauscher, 2017); non-synchronous rotation (Rauscher & Kempton, 2014); and magnetism (Rogers, 2017). Ultra-hot Jupiters generally have near-zero eccentricities and are thought to be tidally-locked, so are expected to be synchronously rotating (again, see Chapter 1). They are also expected to have cloud-free

[1]Although von Essen *et al.* (2020) acknowledge that systematic effects in the data, due to host star variability, cannot be ruled out as a potential cause of their westward brightspot measurements.

daysides, where their atmospheres are too hot for condensates to form. Helling *et al.* (2019*b*) recently ruled out cloud asymmetries as the explanation for westward brightspots on HAT-P-7b. Using three-dimensional MHD simulations, Rogers (2017) showed that the westward venturing brightspot displacements on HAT-P-7b can be well explained by deep-seated dipolar magnetic field strengths exceeding $\sim 6\,\mathrm{G}$ at the atmospheric base.

HAT-P-7b, CoRoT-2b, Kepler-76, WASP-12b, and WASP-33b will be of particular interest but we shall also discuss estimates more generally for the whole exoplanet.eu dataset (introduced in Chapter 1). For HAT-P-7b our estimates agree with past results; for the cooler CoRoT-2b magnetism does not predict reversals and the observations are more plausibly explained by non-magnetic phenomena; for Kepler-76b we find that the critical dipolar magnetic field strength, over which the observed wind variations can be explained by magnetism, lies between $4\,\mathrm{G}$ and $19\,\mathrm{G}$; for WASP-12b and WASP-33b westward hotspots can be explained by $1\,\mathrm{G}$ and $2\,\mathrm{G}$ dipolar fields respectively. Additionally, to guide future observational missions, we identify 61 further hot Jupiters that are likely to exhibit magnetically-driven atmospheric wind variations.

7.1 Recap: Reversal condition from shallow-water MHD

The hottest hot Jupiters have weakly ionised atmospheres, strong zonal winds, and are expected to have planetary dynamos that generate deep-seated dipolar magnetic fields. If the atmosphere of a hot Jupiter is sufficiently ionised, the atmospheric flow becomes strongly coupled to the planet's deep-seated magnetic field, inducing a strong equatorially-antisymmetric toroidal field that dominates the atmosphere's magnetic field geometry (Menou, 2012*a*; Rogers & Komacek, 2014).

In hydrodynamic (and weakly-magnetic) systems, mid-to-high latitude geostrophic circulations cause a net west-to-east equatorial thermal energy transfer, yielding eastward hotspots, and a net west-to-east angular momentum transport into the equator from higher latitudes, driving superrotating equatorial jets (Showman & Polvani, 2011). We have shown that the presence of a strong equatorially-antisymmetric toroidal field obstructs these energy transporting circulations, which, by causing zonal wind alignment and westward Lorentz force accelerations, results in reversed flows with westward hotspots. The threshold for such reversals can be estimated using

$$\begin{aligned}\frac{V_{\mathrm{A,crit}}}{c_g} &\approx \max\left[\frac{\beta/c_g}{k^2+3\beta/c_g}, \frac{2\pi R}{L_{\mathrm{eq}}}\left(\frac{\Delta h_{\mathrm{eq}}}{H}\right)\left(\frac{\tau_{\mathrm{rad}}}{\tau_{\mathrm{wave}}}\right)^{-1}\left(\frac{2\Omega\tau_{\mathrm{wave}}^2}{\tau_{\mathrm{rad}}}+1\right)^{-1}\right], \\ &\approx \max\left[\frac{(R/L_{\mathrm{eq}})^2}{1+3(R/L_{\mathrm{eq}})^2}, \frac{2\pi R}{L_{\mathrm{eq}}}\left(\frac{\Delta h_{\mathrm{eq}}}{H}\right)\left(\frac{\tau_{\mathrm{rad}}}{\tau_{\mathrm{wave}}}\right)^{-1}\left(\frac{2\Omega\tau_{\mathrm{wave}}^2}{\tau_{\mathrm{rad}}}+1\right)^{-1}\right],\end{aligned} \tag{7.1}$$

The first term in the maximum corresponds to the point where the toroidal field can disrupt the geostrophic energy redistribution caused by planetary-scale equatorial Rossby waves in the zero-forcing-amplitude limit. The second term in the maximum corresponds to the point where the toroidal field can obstruct geostrophic circulations in the strongly (pseudo-thermally) forced limit. The parameters in Equation (7.1) have all been discussed previously but, to recap, R is the planetary radius, c_g is the shallow-water gravity wave speed, $\beta = 2\Omega/R$ is the latitudinal variation of the Coriolis parameter at the equator (for the planetary rotation frequency Ω), $k = 1/R$ is the planetary scale azimuthal wavenumber, $L_{\mathrm{eq}} \equiv (c_g/\beta)^{1/2}$, the equatorial Rossby deformation radius[2], $\alpha = 2\pi R/L_{\mathrm{eq}}$ is a longitude-latitude lengthscale ratio, $\tau_{\mathrm{wave}} \equiv L_{\mathrm{eq}}/c_g$ is the system's characteristic wave time scale (as in Showman & Polvani, 2011), and $\Delta h_{\mathrm{eq}}/H$ determines the magnitude of the shallow-water system's pseudo-thermal forcing profile, which the system is relaxed towards over a radiative timescale, τ_{rad}, using a Newtonian cooling treatment.

7.2 Method for Placing Magnetic Reversal Criteria on hot Jupiters

Equation (7.1) shows that the parameters R, c_g, Ω, τ_{rad}, and $\Delta h_{\mathrm{eq}}/H$ can be used to estimate the minimum magnetic field strengths required for reversals. In this section we apply this simple relation to a dataset of hot Jupiters taken from exoplanet.eu[3]. We

[2] The equatorial Rossby deformation radius is the fundamental latitudinal length scale of planetary-scale flows and waves at the equator.

[3] Accessed May 30, 2021. Hot Jupiters without data entries for R, M, t_{orbit}, a, e, R_*, or T_* are removed.

use planets with $0.1M_{\mathrm{J}} < M < 10M_{\mathrm{J}}$ and $a < 0.1\mathrm{AU}$, where M and M_{J} denote the planetary mass and Jupiter's mass respectively, and a is the semimajor axis. The criteria are calculated using T_{eq}, the equilibrium temperature, which we calculate using (Laughlin *et al.*, 2011)

$$T_{\mathrm{eq}} = \left(\frac{R_*}{2a}\right)^{1/2} \frac{T_*}{(1-e^2)^{1/8}}, \tag{7.2}$$

where R_* is the stellar radius, e is the orbital eccentricity, T_* is the stellar effective temperature, and zero albedos are assumed.

The validity of the shallow-water approximation can be assessed by comparing L_{eq} to the pressure scale height, $H \sim \mathcal{R}T_{\mathrm{eq}}R^2/GM$, where G is Newton's gravitational constant and $\mathcal{R}$ is the specific gas constant. Calculating $\mathcal{R}$ using the solar system abundances in Lodders (2010), for our sampled planets, $\mathrm{mean}(H/L_{\mathrm{eq}}) = 7.5 \times 10^{-3}$, so shallow-water theory is generally expected to capture their leading order atmospheric dynamics well. The shallow-water gravity wave speed is calculated by equating thermal and geopotential energies, yielding $c_g \equiv \sqrt{gH} \sim (\mathcal{R}T_{\mathrm{eq}})^{1/2}$. Doing implies $\Delta h/H \sim \Delta T/T_{\mathrm{eq}}$, where Δh are deviations in shallow-water layer thickness from the reference H and $\Delta T \equiv T_{\mathrm{day}} - T_{\mathrm{eq}}$ for the dayside temperature, T_{day}. Though not exactly equal, $\tau_{\mathrm{rad}} \sim \tau_{\mathrm{wave}}$ in the upper atmospheres of hot Jupiters (Fortney *et al.*, 2008; Rogers & Komacek, 2014; Rogers, 2017). Taking $\tau_{\mathrm{rad}} = \tau_{\mathrm{wave}}$ is also convenient for this analysis as, when $\tau_{\mathrm{rad}} \lesssim \tau_{\mathrm{wave}}$, $\Delta h \sim \Delta h_{\mathrm{eq}}$ (Perez-Becker & Showman, 2013, and see Chapter 4), so $\Delta h_{\mathrm{eq}}/H \sim \Delta T/T_{\mathrm{eq}}$.

An interesting feature of hot Jupiters is that the dynamical parameters c_g, Ω and R of a given hot Jupiter are all related to its proximity to its host star and the size/luminosity of its host star (i.e., they are all related to T_{eq}). The consequence of this interdependence is that, for the hottest hot Jupiters, L_{eq}/R and τ_{wave} approximately converge to the constant values $L_{\mathrm{eq}}/R \approx 0.7$ and $\tau_{\mathrm{wave}} \approx 2 \times 10^4\,\mathrm{s}$ as seen in Figure 7.1 (top left and top right panels).

In Figure 7.1 (bottom panel) we use Equation (7.1) to plot the ratio $V_{\mathrm{A,crit}}/c_g$ for $\Delta T/T_{\mathrm{eq}} = 0, 0.1, 0.2, 0.3$. Taking $\Delta T \approx (T_{\mathrm{day}} - T_{\mathrm{night}})/2$, $\Delta T/T_{\mathrm{eq}} = 0.1, 0.2, 0.3$ cover the expected range of relative dayside-nightside variations, with the cooler/hotter hot

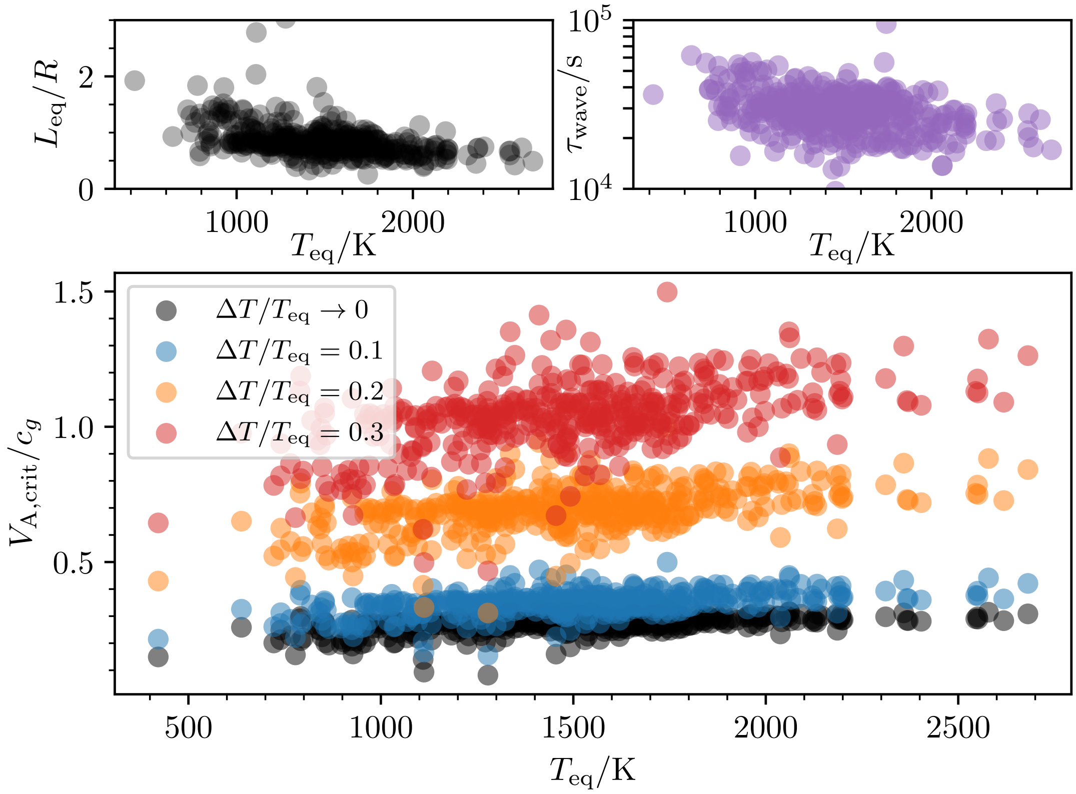

Figure 7.1: Important dynamical scales and ratios of hot Jupiters are plotted alongside critical Alfvén speed estimates, using the exoplanet.eu dataset. We plot $L_{\rm eq}/R$ (top left), $\tau_{\rm wave}$ (top right), and $V_{\rm A,crit}/c_g$ (bottom panel) as functions of $T_{\rm eq}$, where $V_{\rm A,crit}/c_g$ is calculated for $\Delta T/T_{\rm eq} = \{0, 0.1, 0.2, 0.3\}$.

Jupiters generally on the lower/upper end of this scale (e.g., Komacek *et al.*, 2017); whereas $\Delta T/T_{\rm eq} = 0$ shows the zero-amplitude limit. $V_{\rm A,crit}/c_g$ varies linearly with $\Delta T/T_{\rm eq}$ above $\Delta T/T_{\rm eq} = 0.1$, but approaches the zero-amplitude limit just below $\Delta T/T_{\rm eq} = 0.1$. A remarkable feature of the hot Jupiter dataset is that, due to the aforementioned interdependences, the ratio $V_{\rm A,crit}/c_g$ also converges in the large $T_{\rm eq}$ limit for a given $\Delta T/T_{\rm eq}$. This suggests that predictions of the ratio $V_{\rm A,crit}/c_g$ can be used somewhat universally when comparing reversal conditions between hot Jupiters for specific $\Delta T/T_{\rm eq}$ choices.

Equation (7.1) can be combined with the Alfvén speed definition and the ideal gas law to give

$$B_{\phi,\rm crit} = \left(\frac{\mu_0 P}{\mathcal{R}T}\right)^{1/2} V_{\rm A,crit} \sim \frac{V_{\rm A,crit}}{c_g}\sqrt{\mu_0 P}\ , \tag{7.3}$$

where $B_{\phi,\rm crit}$ is the critical reversal magnitude of B_ϕ, μ_0 is the permeability of free space, and T and P are the temperature and pressure at which the reversal occurs.

If the electric currents that generate the planet's assumed deep-seated dipolar field are located far below the atmosphere, Menou (2012*a*) showed that B_ϕ can be related to the strength of the dipolar field, $B_{\rm dip}$, by the scaling law

$$B_\phi \sim R_m B_{\rm dip}, \tag{7.4}$$

where $R_m = U_\phi H/\eta$ is the magnetic Reynolds number for a given magnetic diffusivity, η, zonal wind speed, U_ϕ, and pressure scale height, H. The magnetic Reynolds number estimates the relative importance of the atmospheric toroidal field's induction and diffusion. We note that U_ϕ/c_g scales linearly with $\Delta h/H \sim \Delta T/T_{\rm eq}$ in geostrophically or drag dominated flows (Perez-Becker & Showman, 2013). Taking a geostrophically dominated flow yields $fU_\phi \sim (\Delta T/T_{\rm eq})c_g^2/L_{\rm eq}$, so $U_\phi/c_g \sim (\Delta T/T_{\rm eq})L_D/L_{\rm eq}$, with $L_D = c_g/f$. We fix the constant of proportionality in this scaling by setting $U_\phi \sim 1.5\times 10^2\,{\rm m\,s^{-1}}$ for the conditions corresponding to the simulations of Rogers (2017). To calculate η we follow the method used by Rauscher & Menou (2013) and Rogers & Komacek (2014), taking

$$\eta = 230\times 10^{-4}\,\frac{\sqrt{T}}{\chi_e}\,{\rm m^2\,s^{-1}}, \tag{7.5}$$

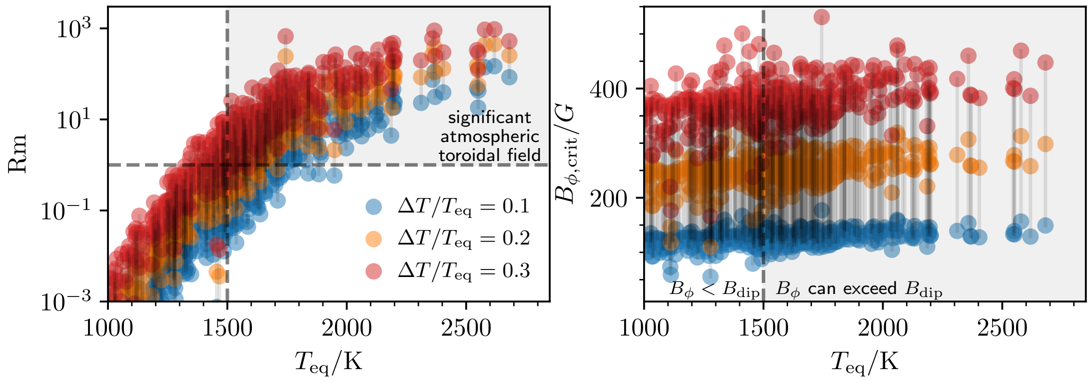

Figure 7.2: R_m (left) and $B_{\phi,\text{crit}}$ (right) are plotted as functions of T_{eq}, for the exoplanet.eu dataset. The estimates are calculated at $P = 10\,\text{mbar}$ with $T = T_{\text{eq}} + \varDelta T$, where $\varDelta T/T_{\text{eq}} = 0.1, 0.2, 0.3$ (blue, orange, red), using $\tau_{\text{drag}} = \tau_{\text{wave}}$. For each hot Jupiter, the three $\varDelta T/T_{\text{eq}}$ choices are connected by a translucent line. For reference, the dashed lines $T_{\text{eq}} = 1500\,\text{K}$ and $R_m = 1$ (lefthand panel only) are also overplotted.

where χ_e is the ionisation fraction. The ionisation fraction is calculated using a form of the Saha equation that takes into account all elements from hydrogen to nickel. It is given by

$$\chi_e = \sum_{i=1}^{28} \left(\frac{n_i}{n}\right) \chi_{e,i}\,. \tag{7.6}$$

In this sum the number density for each element, n_i, and the ionisation fraction of each element, $\chi_{e,i}$, are calculated using

$$n_i = n\left(\frac{a_i}{a_H}\right) = \frac{\rho}{\mu_m}\left(\frac{a_i}{a_H}\right), \tag{7.7}$$

$$\frac{\chi_{e,i}^2}{1-\chi_{e,i}^2} = n_i^{-1}\left(\frac{2\pi m_e}{h^2}\right)^{3/2} (kT)^{3/2} \exp\left(-\frac{\epsilon_i}{kT}\right), \tag{7.8}$$

where ρ is the atmospheric density, n is the total number density, μ_m is the molecular mass, a_i/a_H is the abundance of each element normalised to the hydrogen abundance, m_e is the electron mass, h is Plank's constant, k is the Boltzmann constant, and ϵ_i is the ionisation potential of each element. To calculate η, we use the solar system abundances in Lodders (2010) and take $T = T_{\text{eq}} + \varDelta T/\sqrt{2}$, which is the root mean squared temperature if a sinusoidal longitudinal temperature profile is assumed.

7.3 Magnetic field constraints

7.3.1 Estimates of R_m and $B_{\phi,\mathrm{crit}}$

Estimates of R_m and $B_{\phi,\mathrm{crit}}$ are calculated at depths corresponding to $P = 10\,\mathrm{mbar}$, at which Rogers & Komacek (2014) found magnetically-driven wind variations. In Figure 7.2 we plot R_m (lefthand panel) and $B_{\phi,\mathrm{crit}}$ (righthand panel) as functions of T_{eq}, for hot Jupiters in the dataset (with $T_{\mathrm{eq}} > 1000\,\mathrm{K}$), taking $\varDelta T/T_{\mathrm{eq}} = 0.1, 0.2, 0.3$.

Induction of the atmospheric toroidal field is expected to become significant when R_m exceeds unity. At $P = 10\,\mathrm{mbar}$, R_m exceeds unity for $T \gtrsim 1500\,\mathrm{K}$, depending on $\varDelta T/T_{\mathrm{eq}}$. However, due to the highly temperature dependent nature of Equation (7.8), R_m varies significantly when one compares $\varDelta T/T_{\mathrm{eq}} = 0.1, 0.3$ for a given hot Jupiter.

As we see in Section 7.3.2, B_ϕ is only likely to exceed $B_{\phi,\mathrm{crit}}$ if the hot Jupiter in question is hot enough to maintain a significant atmospheric toroidal field ($R_m \gg 1$). We therefore concentrate our discussion on these hotter hot Jupiters; however, we place hypothetical estimates on $B_{\phi,\mathrm{crit}}$ for all planets in the dataset with $T_{\mathrm{eq}} > 1000\,\mathrm{K}$ (Figure 7.2, righthand panel). Since, for a given $\varDelta T/T_{\mathrm{eq}}$, $V_{\mathrm{A,crit}}/c_g$ is virtually independent of T_{eq} in the hottest hot Jupiters, so is $B_{\phi,\mathrm{crit}}$, with $100\,\mathrm{G} \lesssim B_{\phi,\mathrm{crit}} \lesssim 450\,\mathrm{G}$ for $0.2 < \varDelta T/T_{\mathrm{eq}} < 0.3$; whereas larger L_{eq}/R values can cause $B_{\phi,\mathrm{crit}}$ to decrease in the cooler hot Jupiters (compare with Figure 7.1). We comment that $B_{\phi,\mathrm{crit}}$ is generally least severe in the uppermost regions of the atmosphere, where the atmosphere is least dense, explaining why Rogers & Komacek (2014) found the east-west wind variations at these depths.

Magnetically-driven wind variations can be viewed as a saturation mechanism for the atmospheric toroidal field. If the toroidal field is sufficiently strong to reverse winds, the induction caused by the reversed winds flowing through the deep-seated magnetic field will result in a reduction of the atmospheric toroidal field's magnitude. Therefore, the reversal mechanism prevents the toroidal field strength from greatly exceeding $B_{\phi,\mathrm{crit}}$. This suggests that B_ϕ should peak in the deepest regions satisfying $B_\phi \sim B_{\phi,\mathrm{crit}}$, where $B_{\phi,\mathrm{crit}}$ can be large, then decrease towards the surface where $B_{\phi,\mathrm{crit}}$ is smaller. This is consistent with Rogers & Komacek (2014), who found B_ϕ peaks in the mid-atmosphere

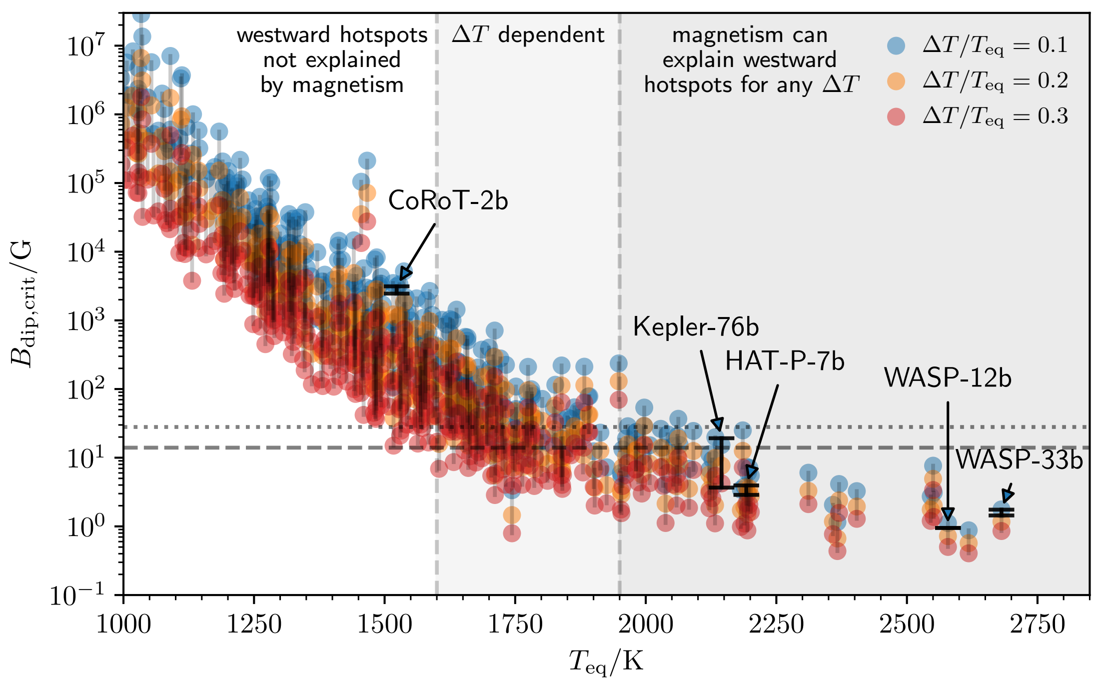

Figure 7.3: Critical dipole magnetic field strengths, $B_{\rm dip,crit}$, at $P = 10\,{\rm mbar}$. We plot $B_{\rm dip,crit}$ using $\tau_{\rm drag} = \tau_{\rm wave}$ and $T = T_{\rm eq} + \Delta T$, with $\Delta T/T_{\rm eq} = 0.1, 0.2, 0.3$ (blue, orange, red). For a given hot Jupiter, these are connected by translucent lines. We include error bars and labels for the planets discussed in this letter (see Table 7.1) along with reference lines at 14 G (dashed; Jupiter's polar surface magnetic field strength) and 28 G (dotted; twice this).

(and declined to $300\,{\rm G} \lesssim B_\phi \lesssim 450\,{\rm G}$ at $P = 10\,{\rm mbar}$ in their M7b simulations).

7.3.2 Dipolar magnetic field strengths

In Figure 7.3 we use Equation (7.4) to plot $T_{\rm eq}$ vs $B_{\rm dip,crit}$, the critical dipolar field (at $P = 10\,{\rm mbar}$) sufficient to drive magnetic wind variations for $\Delta T/T_{\rm eq} = 0.1, 0.2, 0.3$. Since there is a large amount of ambiguity regarding how planetary dynamo theory translates to the hot Jupiter parameter regime, we include a physically motivated reference line at $B_{\rm dip,crit} = 14\,{\rm G}$ (the magnitude of Jupiter's magnetic field at its polar surface) and a second reference line at 28 G (twice this). Due to the highly temperature dependent nature of R_m, these estimates of $B_{\rm dip,crit}$ carry a high degree of uncertainty (e.g., compare $B_{\rm dip,crit}$ of a given hot Jupiter for the different $\Delta T/T_{\rm eq}$ choices). Therefore, for useful

Table 7.1: Estimates of $B_{\phi,\mathrm{crit}}$ (2 significant figures) and $B_{\mathrm{dip,crit}}$ at $P = 10\,\mathrm{mbar}$, using the tabulated T_{day}, taken from phase curve measurements of the atmospheres of HAT-P-7b, CoRoT-2b, Kepler-76b, WASP-12b, and WASP-33b.

Planet	$T_{\mathrm{day}}/\,\mathrm{K}$	$B_{\phi,\mathrm{crit}}/\,\mathrm{G}$	$B_{\mathrm{dip,crit}}/\,\mathrm{G}$
HAT-P-7b	$(2610, 2724)$[1]	$(255, 324)$	$(3, 4)$
CoRoT-2b	$(1695, 1709)$[2]	$(145, 177)$	$(2500, 3100)$
Kepler-76b	$(2300, 2850)$[3]	$(107, 466)$	$(4, 19)$
WASP-12b	(2928)[4]	(212)	(0.9)
WASP-33b	$(2954, 3074)$[5]	$(152, 218)$	$(1.4, 1.8)$

[1]Wong *et al.* (2016); [2]Dang *et al.* (2018); [3]Jackson *et al.* (2019); [4]Cowan *et al.* (2012); [5]von Essen *et al.* (2020).

estimates of $B_{\mathrm{dip,crit}}$, accurate temperature estimates/measurements (at the depth being probed) are required.

Generally, T_{day} is not directly calculable from standard planetary/stellar parameters so measured values should be used where possible. For the five hot Jupiters with westward hotspot observations, we use dayside temperatures based on phase curve measurements to estimate $B_{\phi,\mathrm{crit}}$ and $B_{\mathrm{dip,crit}}$. We provide these numerical estimates in Table 7.1 and add labelled error bars to Figure 7.3. The ultra-hot Jupiters are found to have low-to-moderate $B_{\mathrm{dip,crit}}$ requirements. For HAT-P-7b we estimate $3\,\mathrm{G} < B_{\mathrm{dip,crit}} < 4\,\mathrm{G}$ at $P = 10\,\mathrm{mbar}$[4], recovering the previously-known result that westward hotspots on HAT-P-7b can be well explained by magnetism (Rogers, 2017). On the ultra-hot Jupiters WASP-12b and WASP-33b dipole fields respectively exceeding 1 G and 2 G at $P = 10\,\mathrm{mbar}$ would explain westward hotspots. Likewise, at $P = 10\,\mathrm{mbar}$, a dipole field exceeding $B_{\mathrm{dip,crit}}$ for $4\,\mathrm{G} < B_{\mathrm{dip,crit}} < 19\,\mathrm{G}$ is required to explain westward hotspot observations on Kepler-76b. Given that Cauley *et al.* (2019) predicted that surface magnetic fields on hot Jupiters could be range from 20 G to 120 G, these estimates support the idea that wind reversals on these ultra-hot Jupiters have a magnetic origin. If non-magnetic explanations can be ruled out, such estimates of $B_{\mathrm{dip,crit}}$ can be used as lower bounds for B_{dip} on ultra-hot Jupiters. In contrast, unless there is an unfeasibly large dipolar field that exceeds $\gtrsim 3\,\mathrm{kG}$, westward hotspots on the cooler CoRoT-2b are not explained by magnetism. To check our method's

[4]Since dipole field magnitude scales like r^{-3}, these estimates bracket the $B_{\mathrm{dip,crit,base}} \sim 6\,\mathrm{G}$ prediction of Rogers (2017), made for field magnitudes at the atmospheric base.

fidelity, we also compare predictions to the simulations in Rogers & Komacek (2014), where temperature differences are known, finding good agreement (for both $B_{\rm dip,crit}$ and $B_{\phi,\rm crit}$).

Using the range $\Delta T/T_{\rm eq} = (0.1, 0.3)$ to estimate $B_{\phi,\rm crit}$ generally has uncertainties between one-half and two orders of magnitude. However, Figure 7.3 shows that hot Jupiters divide into three clear categories: (i) those that are likely to have magnetically-driven atmospheric wind variations for any choice of $\Delta T/T_{\rm eq}$ ($T_{\rm eq} \gtrsim 1950\,{\rm K}$); (ii) those that are unlikely to have sufficiently strong toroidal field magnetic fields to explain atmospheric wind variations, for any choice of $\Delta T/T_{\rm eq}$ ($T_{\rm eq} \ll 1600\,{\rm K}$); and (iii) marginal cases that depend on the magnitude of horizontal temperature differences ($1600\,{\rm K} \lesssim T_{\rm eq} \lesssim 1950\,{\rm K}$).

Using the conservative criteria $B_{\rm dip,crit} < 28\,{\rm G}$, $P = 10\,{\rm mbar}$, and $\Delta T/T_{\rm eq} = 0.1$, we identify 61 further hot Jupiters that are likely to exhibit magnetically-driven wind variations. We present these in Table 7.2, which is ordered by ascending $B_{\rm dip,crit}$ (i.e., from most likely to least likely to exhibit reversals), to help guide future observational missions. We note that, of these 61 further reversal candidates, 37 reversal have weaker reversal requirements than Kepler-76b. Hence, using these fairly conservative criteria, we predict that magnetic wind variations could be present in ~ 60 and argue they are highly-likely to be present in ~ 40 of the hottest hot Jupiters. Using the more flexible, but still reasonable, criteria $B_{\rm dip,crit} < 28\,{\rm G}$ at $P = 10\,{\rm mbar}$, with $\Delta T/T_{\rm eq} = 0.2$, we find a total of 94 candidates (see Table E.1 in Appendix E for full list).

For hot Jupiters with intermediate temperatures ($1600\,{\rm K} \lesssim T_{\rm eq} \lesssim 1950\,{\rm K}$), the magnitude of $\Delta T/T_{\rm eq}$ (and our simplifying assumptions) plays a significant role in determining whether magnetic wind variations are plausible, specific dayside temperature measurements should be used for estimates. These intermediate temperatures hot Jupiters offer excellent opportunities to fine-tune magnetohydrodynamic theory, via cross-comparisons between observations and bespoke models.

7.4 Discussion

We have applied the theory developed in this thesis to a dataset of HJs to estimate the critical magnetic field strengths $B_{\rm dip,crit}$ and $B_{\phi,\rm crit}$ (at $P = 10\,\rm mbar$), beyond which strong toroidal fields cause westward hotspots. The new criterion differs both mathematically and in physical interpretation from the criterion of Rogers & Komacek (2014) and Rogers (2017), which identifies when Lorentz forces from the deep-seated dipolar field become strong enough to significantly reduce zonal winds, but doesn't theoretically explain wind variations. However, the estimates made in this work match well with typical magnetic fields in the three-dimensional simulations of Rogers & Komacek (2014) and Rogers (2017), which exhibit wind variations, and also match values resulting from their criterion in these regions of parameter space. This is because, while describing different magnetic effects, both criteria predict the critical magnetic field strengths at which magnetism becomes dynamically important in the atmospheres of HJs. Applying the new criterion to the HJ dataset, we found that brightness the variations on Kepler-76b can be explained by plausible planetary dipole strengths ($B_{\rm dip} \gtrsim 4\,\rm G$ using $T_{\rm day} = 2850$; $B_{\rm dip} \gtrsim 19\,\rm G$ using $T_{\rm day} = 2300$), and that westward hotspots can be explained for $B_{\rm dip} \gtrsim 1\,\rm G$ on WASP-12b and $B_{\rm dip} \gtrsim 2\,\rm G$ on WASP-33b. The estimates of $B_{\phi,\rm crit}$ and $B_{\rm dip,crit}$ for HAT-P-7b is consistent with the estimate of Rogers (2017). Unless there is an unfeasibly large dipolar field of the order of a few kilogauss, westward hotspots on the cooler CoRoT-2b are not explained by magnetism. While estimates of $B_{\rm dip,crit}$ are limited by the strong temperature dependence of R_m, we used an observationally motivated set of criteria ($B_{\rm dip,crit} < 28\,\rm G$, $\Delta T/T_{\rm eq} = 0.1$, and $P = 10\,\rm mbar$) to tabulate 65 HJs that are likely to exhibit magnetically-driven wind variations (see Table 7.2) and predict such effects are highly-likely in ~ 40 of the hottest HJs.

With exoplanet meteorology becoming increasingly developed, the results of this study suggests that further observations of hotspot variations in ultra-hot Jupiters should be expected. A combination of archival data and future dedicated observational missions (particularly those observing multiple transits) from Kepler, Spitzer, Hubble, TESS, CHEOPS, and JWST can be used to identify magnetically-driven wind variations and other interesting features at different atmospheric depths. This has the potential to drive new understanding of the atmospheric dynamics of the hottest HJs and provide important observational constraints for dynamo models of HJs. Parallel to this, future theoretical work can refine estimates of $B_{\mathrm{dip,crit}}$. In many cases combining observational measurements with bespoke three-dimensional MHD simulations offer the best prospect for providing accurate constraints on the magnetic field strengths of ultra-hot Jupiters, yet the simple concepts and results of this work can provide useful starting points for such studies. In this work, estimates of $B_{\mathrm{dip,crit}}$ are limited by R_m, which, for generality, we calculated using solar system abundances. The largest limiting factor in such estimates is the highly temperature dependent nature of R_m. Furthermore, the magnetic scaling law does not account for longitudinal asymmetries in the magnetic diffusivity or the dipolar field strength within the atmospheric region. In future work we shall investigate how these inhomogeneities effect the atmospheric dynamics more closely, using a three-dimensional model containing variable magnetic diffusivity, consistent poloidal-toroidal field coupling, stratification, and thermodynamics. To date, MHD models of HJs have strictly considered dipolar magnetic field geometries for the planetary magnetic field. Dynamo simulations would offer insight into the nature of magnetic fields in the deep interiors of HJs, which, at present, is not well-understood.

Table 7.2: Hot Jupiters in which $B_{\mathrm{dip,crit}} < 28\,\mathrm{G}$ at $P = 10\,\mathrm{mbar}$, with $\Delta T/T_{\mathrm{eq}} = 0.1$. Alongside T_{eq}, estimates of $B_{\mathrm{dip,crit}}$ and $B_{\mathrm{dip,crit}}$ (1 significant figure) using these choices are provided. If Hot Jupiters in this table are observed to magnetic wind variations, $B_{\mathrm{dip,crit},0.1}$ estimates the lower bound of B_{dip} and $B_{\phi,\mathrm{crit},0.1}$ estimates the magnitude of B_ϕ.

Rank	Candidate	$T_{\mathrm{eq}}/\,\mathrm{K}$	$B_{\phi,\mathrm{crit},0.1}/\,\mathrm{G}$	$B_{\mathrm{dip,crit},0.1}/\,\mathrm{G}$
1	WASP-189 b	2618	129	0.9
2†	† WASP-12 b	2578	156	1
3	WASP-178 b	2366	130	1
4†	† WASP-33 b	2681	149	2
5	WASP-121 b	2358	153	2

Continued on next page

Table 7.2 – *Continued from previous page*

Rank	Candidate	$T_{eq}/$ K	$B_{\phi,\mathrm{crit},0.1}/$ G	$B_{\mathrm{dip,crit},0.1}/$ G
6	MASCARA-1 b	2545	134	3
7	WASP-78 b	2194	139	3
8	HAT-P-70 b	2551	133	3
9	HD 85628 A b	2403	128	3
10	HATS-68 b	1743	177	3
11	WASP-76 b	2182	145	3
12	WASP-82 b	2188	132	4
13	HD 202772 A b	2132	125	4
14	Kepler-91 b	2037	105	4
15	TOI-1431 b/MASCARA-5 b	2370	129	4
16	HAT-P-65 b	1953	138	5
17	WASP-100 b	2201	131	6
18	WASP-187 b	1952	116	6
19	HATS-67 b	2195	146	6
20	WASP-87 A b	2311	139	6
21	HATS-56 b	1902	122	7
22	HATS-40 b	2121	126	7
23	KELT-18 b	2082	130	7
24	HAT-P-57 b	2198	130	7
25	HATS-26 b	1925	130	7
26†	† HAT-P-7 b	2192	134	7
27	WASP-48 b	2058	139	7
28	KOI-13 b	2550	139	8
29	HAT-P-49 b	2127	128	9
30	WASP-142 b	1992	139	11
31	WASP-111 b	2121	133	11

Continued on next page

Table 7.2 – *Continued from previous page*

Rank	Candidate	$T_{\mathrm{eq}}/\,\mathrm{K}$	$B_{\phi,\mathrm{crit},0.1}/\,\mathrm{G}$	$B_{\mathrm{dip},\mathrm{crit},0.1}/\,\mathrm{G}$
32	WASP-90 b	1840	124	12
33	HAT-P-66 b	1900	130	12
34	Qatar-10 b	1955	145	13
35	KELT-11 b	1711	113	13
36	HAT-P-33 b	1839	130	14
37	HATS-35 b	2033	140	14
38	HAT-P-60 b	1786	119	15
39	Qatar-7 b	2052	141	15
40	CoRoT-1 b	2007	146	15
$41^{\dagger}$	† Kepler-76 b	2145	142	15
42	K2-260 b	1985	132	15
43	WASP-71 b	2064	128	15
44	WASP-88 b	1763	119	16
45	WASP-172 b	1745	114	16
46	WASP-159 b	1811	120	17
47	Kepler-435 b	1731	109	18
48	HATS-31 b	1837	128	19
49	WASP-122 b	1962	147	19
50	HAT-P-32 b	1841	142	19
51	HAT-P-23 b	2133	148	20
52	WASP-92 b	1879	137	20
53	HATS-64 b	1800	119	21
54	WASP-19 b	2060	160	21
55	KELT-4 A b	1827	133	21
56	CoRoT-21 b	2041	126	22
57	HATS-9 b	1913	135	23

Continued on next page

Table 7.2 – *Continued from previous page*

Rank	Candidate	$T_{\mathrm{eq}}/\,\mathrm{K}$	$B_{\phi,\mathrm{crit},0.1}/\,\mathrm{G}$	$B_{\mathrm{dip},\mathrm{crit},0.1}/\,\mathrm{G}$
58	HAT-P-69 b	1980	118	23
59	OGLE-TR-132 b	1981	138	24
60	HATS-24 b	2091	148	25
61	Kepler-1658 b	2185	110	25
62	TOI-954 b	1704	109	26
63	WASP-114 b	2028	142	26
64	TOI-640 b	1749	120	27
65	WASP-153 b	1712	128	27

† More accurate estimates in Table 7.1.

Chapter 8

Conclusions and Further Work

8.1 Summary of approaches and findings

Aims and approach

The aim of this work was to study and attempt to clarify the role of the atmospheric toroidal field in the dynamics of hot Jupiter atmospheres. Specifically, we set out to understand how the toroidal field causes magnetically-driven hotspot reversals, which have previously been identified in three-dimensional MHD simulations (Rogers & Komacek, 2014; Rogers, 2017). This problem is likely to have observable astrophysical examples and recently westward hotspots/brightspots have been identified on four of the hottest hot Jupiters: HAT-P-7b (Armstrong *et al.*, 2016), Kepler-76b (Jackson *et al.*, 2019), WASP-12b (Bell *et al.*, 2019), and WASP-33b (von Essen *et al.*, 2020), as well as on the cooler CoRoT-2b (Dang *et al.*, 2018).

We focussed on this problem by constructing and studying a reduced-physics model based on the single-layer shallow-water MHD (SWMHD) model of Gilman (2000). For this we used a reduced-gravity geometry to allow for a pseudo-thermal forcing treatment, similar to the kind that has proved useful for modelling the atmospheres of hot Jupiters in the hydrodynamic limit (e.g., Shell & Held, 2004; Langton & Laughlin, 2007; Showman & Polvani, 2010, 2011; Perez-Becker & Showman, 2013). Since our interest is predominantly centred around the dynamics of the equatorial region, we used a Cartesian coordinate system in the equatorial beta-plane approximation. In Chapter 2, we outlined this model's features, assumptions, treatments, and properties in detail.

Linear wave dynamics

Before considering numerical simulations, in Chapter 3 we considered some of the linear wave dynamics expected to be present in hot Jupiter atmospheres. First, we used simple plane wave approximations to consider the waves that propagate in local regions of hot Jupiter atmospheres in the presence of magnetism and rotation. We initially discussed fast and slow branch waves in the hot Jupiter parameter space. This highlighted a result previously recovered in other magnetohydrodynamic settings (Hide, 1966, 1969*b*; Acheson & Hide, 1973; Diamond *et al.*, 2007; Zaqarashvili *et al.*, 2007, 2009; Heng & Spitkovsky, 2009; Márquez-Artavia *et al.*, 2017; Zaqarashvili, 2018) that, while the presence of magnetism does not fundamentally alter the dispersion relationships of the fast branch waves, the westward slow branch solutions of the plane wave dispersion relation behave like either (non-dispersive) Alfvén waves (at small length scales), which travel parallel to the magnetic field that they propagate in, or (dispersive) Rossby waves (at large length scales), which travel in a geostrophic manner. Since the geostrophic propagation of planetary-scale equatorial Rossby waves is known to be important to equatorial hydrodynamics on hot Jupiters (Showman & Polvani, 2011), we then looked for similar magnetic modifications to equatorial shallow-water waves in the equatorial beta-plane approximation. First we considered magnetic modifications to equatorial SWMHD waves in presence of a uniform azimuthal background magnetic field, in which case the fast branch equatorial MIG waves generally behave similarly to their hydrodynamic counterparts, but strong magnetic fields cause significant equatorial trapping of the planetary-scale equatorial magneto-Rossby and equatorial magneto-Kelvin waves. We then considered magnetic modifications to equatorial SWMHD waves in presence of an azimuthal background magnetic field with a linear latitudinal dependence, using the weak-field approximations considered for solar tachocline parameters by Zaqarashvili (2018). Like the uniform azimuthal magnetic field case, we found the fast branch equatorial MIG waves generally behave similarly to their hydrodynamic counterparts. However, in contrast, we found that towards the point where the weak-field approximations become less valid the equatorial magneto-Rossby solutions become less equatorially bounded and then, at some critical magnetic field strength, become unbounded from equatorial regions. The difference in the magnetic modification for these two field geometries highlights the need to consider physically motivated magnetic field and in the work beyond Chapter 3 we restricted ourselves to the azimuthal magnetic field that are antisymmetric about the equator, like those found in three-dimensional simulations with magnetically-driven wind variations (Rogers & Komacek, 2014; Rogers, 2017).

Numerical shallow-water MHD model

In Chapter 4 we used an adaptive third-order Adam-Bashforth time-stepping scheme, which calculates derivatives spectrally in x and with fourth-order finite difference schemes in y, to compute non-linear numerical solutions of the SWMHD equations. We calculated solutions across a range of damping timescales, radiative timescales, and psuedo-thermal forcing magnitudes, increasing the magnetic field strength until we found a change in the nature of the system. We found that, in the presence of an equatorially-antisymmetric azimuthal magnetic field, the simple SWMHD model we presented can capture the physics of magnetically-driven hotspot reversals, which have only previously been studied via full three-dimensional MHD simulations (Rogers & Komacek, 2014; Rogers, 2017). The implication of this is that the reversal process is a shallow phenomenon that can be studied with the accompanying mathematical simplicity of shallow-layered models. We identified that hotspots reverse when the azimuthal magnetic field is strong enough to prevent geostrophic flows from recirculating between the equatorial regions and higher latitudes. This prevents energy and angular momentum recirculation of the kind that Showman & Polvani (2011) showed drives equatorial superrotation and eastward hotspots on hot Jupiters in the hydrodynamic limit. In the supercritical MHD solutions the winds align with the magnetic field, whose field lines have an equatorward bend in hotspot regions. This configuration leads to westward Lorentz force accelerations in hotspot regions, as magnetic field lines pass into regions of less $|B_x|$, ultimately causing the hotspots to shift westward.

The fact that this westward Lorentz force acceleration relies on the magnitude of the azimuthal field to decrease/vanish in equatorial regions explains why we did not find similar reversals when we applied a uniform azimuthal magnetic field to our SWMHD model, though we omitted this case from this work as it is less physically interesting and relevant.

Using our developed understanding of the physical processes that drive reversals, we used a simple scaling law arguement, based on relative circulation/oscillation frequency of geostrophic circulations and the Alfvén frequency, to develop a physically-motivated reversal criterion. This criterion replicated with our numerical findings in the relevant forcing magnitude and radiative timescales ranges. That is, for moderately-to-strongly forced solutions with radiative timescales corresponding to the upper atmosphere.

We compared two different latitudinally-dependent azimuthal magnetic field profiles: a hyperbolic-tangent profile that varied linearly with latitude in equatorial regions and a profile with a more realistic linear-gaussian latitudinal dependence. We found that both of these azimuthal magnetic field profiles exhibited similar behaviours in equatorial regions, concluding that a hyperbolic-tangent dependence generally provides an adequate description of the dynamics of the wind reversals (for linear wave dynamics).

Consequences of linear theory

In Chapter 5 we explored the description of planetary flows with equatorial shallow-water waves that has been useful for explaining atmospheric dynamics on hot Jupiters in the hydrodynamic limit (Showman & Polvani, 2011). We did so by solving two version of the linearised SWMHD model in two cases: the non-diffusive steady-state forced linear system and the non-diffusive unforced oscillatory free-wave solution.

In the steady-state forced linear system, strongly-magnetic solutions could mimic the obstruction of geostrophic circulations that was found to trigger reversals in Chapter 4. However, due to the symmetries in the simplified linear system, east-west Lorentz force accelerations cannot form along the equator. Consequently, such solutions did not exhibit magnetically-reversed hotspots; instead hotspot displacements converged to zero in the strongly magnetic limit.

When we considered oscillatory solutions, we moved away from the weak-field assumptions of Chapter 3. The strongly-magnetic case involved considering the behaviour of equatorial magneto-Rossby around regular singular points and equatorial magneto-Kelvin waves around false singularities. We found that the equatorial magneto-Kelvin waves were qualitatively similar to their hydrodynamic counterparts, albeit with a small non-zero meridional velocity component. In contrast, if the azimuthal phase speeds of equatorial magneto-Rossby waves were exceeded by the background Alfvén speed, their solutions were removed from the linear system. We also found that in the magnetic limit, two sets of singular solutions with Alfvénic characteristics emerged, with azimuthal phase speeds bounded above by the maximal background Alfvén speed. We linked the loss of the equatorial magneto-Rossby wave in regions of the atmosphere with large background Alfvén speeds to the breakdown of material potential vorticity conservation, which is fundamental to their propagation. The removal of equatorial magneto-Rossby wave solutions is of particular interest for the following reasons: (1) in hydrodynamic systems, the recirculation patterns associated with the geostrophic propagation of equatorial Rossby waves are fundamental in maintaining eastward hotspots and equatorial superrotation (Showman & Polvani, 2011); (2) in Chapter 4 we identified that the obstruction of geostrophic circulations triggers hotspot reversals; and (3) the steady-state forced linear system can replicated this breakdown of geostrophy. Finally, we highlighted a quantitive agreement between the reversal threshold in the zero-forcing-amplitude limit and the loss of the planetary-scale equatorial Rossby solutions, providing a physically-motivated hotspot reversal condition in this limit.

Comparisons between SWMHD theory and three-dimensional MHD simulations

In Chapter 6 we identified a number of connections and consequences between our findings and the three-dimensional MHD simulations of Rogers & Komacek (2014) and (Rogers, 2017). First, we used the physically-motivated hotspot reversal criteria of Chapters 4 and 5 to place a single reversal criterion on the toroidal field. Second, we identified the connection between the magnetically-driven hotspot reversals and the (zonally-averaged zonal) wind reversals found in three-dimensional MHD models. We noted that an angular momentum conservation theorem (due to Hide, 1969*a*; presented in the hot Jupiter context by Showman & Polvani, 2011), implies that the hotspot reversal mechanism also causes wind reversals. The manifestation of this theorem in the atmosphere is that when the toroidal field obstructs mid-to-high latitude recirculating winds it inhibits horizontal momentum transport between the equatorial and mid-latitudes, leaving the remaining down-gradient momentum transport mechanisms to drive westward zonally-averaged zonal accelerations. This explains why Rogers (2017) found hotspot and wind reversals were time-correlated and explains the relative change in importance of the momentum transport components that Rogers & Komacek (2014) identified in regions of wind reversals. Third, we noted that our hotspot reversal criterion is consistent with a condition that determines a transition from geostrophic turbulence into MHD turbulence Diamond *et al.* (2007), citing that in both situations the breakdown of potential vorticity conservation (and therefore geostrophic characteristics) as the triggering factor. This strengthens the link Rogers & Komacek (2014) previously made between the intermittency of wind reversals in three-dimensional MHD simulations and MHD turbulence theory (Tobias *et al.*, 2007). Fourth, we discussed how the reversal of magnetic induction (due to wind reversals) can lead to a strengthening-weakening cycle in the atmospheric toroidal field's magnitude, which can drive the wind variations and hotspot oscillations observed in three-dimensional MHD models and observations. This cycle offers a possible a saturation process for the atmospheric toroidal magnetic field, which we found some evidence for when making quantitive comparisons. Finally, we identified common features between the magnetic field geometries of three-dimensional simulations and the those predicted by the developed SWMHD theory, including consistencies between predictions of reversal criticality.

Observational consequences

In Chapter 7 we used the developed physically-motivated hotspot reversal criterion to place estimates on minimal reversal conditions on hot Jupiters. For this we applied expected planetary parameters to estimate $B_{\phi,\mathrm{crit}}$, the critical toroidal field strength at which winds reverse. We found that at $P = 10\,\mathrm{mbar}$, hot Jupiters in the exoplanet.eu dataset generally have $100\,\mathrm{G} \lesssim B_{\phi,\mathrm{crit}} \lesssim 450\,\mathrm{G}$, which was consistent with typical B_ϕ magnitudes in the three-dimensional simulations that exhibited wind reversals in Rogers & Komacek (2014). We then used the relation $B_\phi \sim R_m B_{\mathrm{dip}}$ of Menou (2012a), which assumes a deep-seated dipolar field is located far below the atmospheric region of interest and was found to be consistent with the three-dimensional simulations of Rogers & Showman (2014), to estimate an equivalent critical dipole magnetic field strength, $B_{\mathrm{dip,crit}}$. Over the parameter range of hot Jupiters R_m, the magnetic Reynolds number, varies by orders of magnitude due to the temperature dependence of η, meaning that the hottest hot Jupiters are likely to have highly dominant atmospheric toroidal fields, with magnitudes exceeding $B_{\phi,\mathrm{crit}}$, but the cooler hot Jupiters are not. Since the hottest hot Jupiters had $B_{\mathrm{dip,crit}}$ comparable (or less) to the strength of Jupiter (14 G), we deemed it likely that their atmospheric toroidal field is large enough to drive hotspot reversals. Using this comparison we found that hot Jupiters with $T_{\mathrm{eq}} \gtrsim 1950\,\mathrm{K}$ are expected to have magnetically-driven atmospheric wind variations for any choice of relative day-night temperature difference; hot Jupiters with $T_{\mathrm{eq}} \ll 1600\,\mathrm{K}$ are unlikely to have magnetically-driven atmospheric wind variations; and the likelihood of magnetically-driven atmospheric wind variations on the marginal cases between these two temperature ranges generally depend on their relative day-night temperature differences (first order), as well as their other planetary parameters (second order). These marginal cases are particularly interesting as, with more observations of hotspot reversals on such hot Jupiters, highly accurate models of their planetary dynamics may be able to be combined with observations to identify typical magnetic field strengths on hot Jupiters. We also applied the hotspot reversal criterion to the five hot Jupiters with westward hotspot observations (to date), finding that, for HAT-P-7b, $3\,\mathrm{G} < B_{\mathrm{dip,crit}} < 4\,\mathrm{G}$

at $P = 10\,\mathrm{mbar}$, recovering the result that westward hotspots on HAT-P-7b can be well explained by magnetism (also found by Rogers, 2017, via three-dimensional simulations); on the ultrahot hot Jupiters WASP-12b and WASP-33b dipole fields exceeding $1\,\mathrm{G}$ at $P = 10\,\mathrm{mbar}$ would explain westward hotspots; on Kepler-76b westward hotspots can be explained by a dipole field exceeding $B_{\mathrm{dip,crit}}$ for $4\,\mathrm{G} < B_{\mathrm{dip,crit}} < 18\,\mathrm{G}$ (estimate limited by knowledge of the expected dayside temperature); and that westward hotspots on the cooler CoRoT-2b are not explained by magnetism, unless its assumed dipole magnetic field exceeds a few kilogauss in magnitude (which would appear unfeasible). Alongside these estimates, we identified 61 further hot Jupiters that are likely to exhibit magnetically-driven wind variations, which we tabulated to help guide future observational missions. If we relax the reasonably conservative criteria that the 61 tabulated hot Jupiters satisfy (i.e., $B_{\mathrm{dip,crit}} < 28\,\mathrm{G}$, $P = 10\,\mathrm{mbar}$, and $\Delta T/T_{\mathrm{eq}} = 0.1$ to the same but with $\Delta T/T_{\mathrm{eq}} = 0.2$), we estimated that one could expect magnetically-driven wind reversals in ~ 100 of the hottest hot Jupiters, suggesting that more multiple transit observations of the hottest hot Jupiters are likely to lead to further discoveries of westward hotspots.

8.2 Open questions, limitations, and future work

Cartesian approximation of spherical geometry

The advantage of using the Cartesian shallow-water geometry is first and foremost its simplicity. This makes it an excellent process model, however some of the complexities it excludes from its reduced physics should be considered in the future. Since our primary concern was with equatorial dynamics, in this work we used an equatorial beta-plane approximation in Cartesian geometry, including only the dynamical effects of sphericity that arise due to the latitudinal dependence of the planetary rotation vector's normal component (Rossby, 1939). While this approximation provides a valid description of rotation at equatorial latitudes, it does not include an accurate description of curvature or the Coriolis effect in polar regions. Another unphysical aspect of our imposed geometry is that it contains an impermeable boundary at the model's "poles". This wall has the potential to reflect flows back into the lower latitudes solving domain, though upon checking varying the latitudinal extent of our model has little qualitative effect on the solutions, particularly in equatorial regions of interest. Moreover, in the hydrodynamic limit, we reproduce results found in spherical models of hot Jupiters (e.g., Langton & Laughlin, 2007; Showman & Polvani, 2010, 2011; Perez-Becker & Showman, 2013) and, when magnetism is included, our results generally agree with the findings of spherical three-dimensional simulations (Rogers & Komacek, 2014; Rogers, 2017). We therefore expect the equatorial characteristics of our model will be reproduced in an equivalent spherical model. To properly model the polar flows and energy redistribution in the magnetic limit, a spherical SWMHD model would be beneficial. However, as there are not any observational constraints on such polar dynamics on hot Jupiters and three-dimensional MHD simulations find the equatorial-to-mid latitude regions to be of most dynamical importance (Rogers & Komacek, 2014), investigating such polar flows is of less immediate dynamical interest at present.

A spherical description of the wave dynamics (like that of Márquez-Artavia *et al.*, 2017, but with an equatorially-antisymmetric azimuthal magnetic field geometry) would be useful to determine the exact global nature of the planetary scale waves that are removed from the equatorial wave model in the highly magnetic limit. Polar trapping is one possibility, with Márquez-Artavia *et al.* (2017) finding that an equatorially-symmetric azimuthal magnetic field treatment confines magneto-Rossby waves to the polar regions in the strongly magnetic limit and Heng & Spitkovsky (2009) finding a slow branch magnetostrophic wave solution trapped in polar regions for a vertical magnetic field geometry. However, in a linear non-diffusive spherical system with an antisymmetric azimuthal magnetic field, London (2018) found no finite trapped solutions relating to Rossby-Alfvén coupling, so weakly non-linear assumptions and/or diffusion may need to be employed to fully-understand the nature of the system's waves once geostrophic balance has been overcome.

Three-dimensional modelling

Shallow-water models are good process models but do not account for vertical dependencies or stratification. In particular, three-dimensional models allow for more sophisticated thermodynamical treatments, which the SWMHD model can only mimic. Three-dimensional models can also further inform about connections between the atmospherical toroidal fields and the deep-seated poloidal planetary magnetic field, which cannot be studied with SWMHD as it only has one degree of freedom in the induction equation. Though Rogers & Showman (2014) found consistency between the $B_\phi \sim R_m B_{\mathrm{dip}}$ scaling relation of Menou (2012*a*), three-dimensional simulations also find longitudinal variations in the toroidal field strength between the dayside and the nightside (Rogers & Showman, 2014; Rogers & Komacek, 2014; Rogers, 2017). This is to be expected due to the temperature dependence of R_m, but applying longitudinal variations in the toroidal field strength to the SWMHD model adds additional complexity that we do not consider in our simple process model. This could be done in the future but the results of this study can also be further investigated in a more self-consistent manner in three-dimensional geometry.

Considering the vertical dependencies, stratification, and consistent thermodynamic treatments also allows one to gain a better understanding on some of the other interesting research questions concerning magnetism in hot Jupiters. In particular, investigating the role of an inhomogeneous temperature dependent magnetic diffusivity that is calculated explicitly from atmospheric conditions and whether it can sustain a variable-η-driven dynamo (Pétrélis *et al.*, 2016) as found using a spatially, but not temperature, dependent magnetic diffusivity by Rogers & McElwaine (2017). Such models could also produce enhanced Ohmic heating via the thermo-resistive instability proposed by (Menou, 2012*b*). Establishing whether such an instability can form in hot Jupiter atmospheres and, if so, how much heating the process would inject into the planetary interior/atmosphere is are questions that such a model could answer.

8.3 Concluding Remarks

The recent observational drive in exoplanet meteorology provides a timely backdrop around which theories regarding the mechanism of hotspot reversals on hot Jupiters can be tested and developed. Observational constraints on atmospheric properties continue to improve whilst a combination of archival data and dedicated observational missions from Kepler, Spitzer, Hubble, TESS, CHEOPS (and in the future JWST) are accelerating our understanding of the atmospheric theory of exoplanets. This initial sojourn into modelling hotspot reversals on hot Jupiters has yielded some interesting results but linking full three-dimensional modelling to the results of SWMHD is required and is likely to have subtle intricacies in places. That said, the power of the shallow-water models in describing hot Jupiters in the hydrodynamic limit gives cause for optimism. In particular, the properties that the hottest hot Jupiters have thin atmospheres, are expected to be synchronously rotating, and have equatorial Rossby deformation similar in magnitude to their planetary radius make quasi-geostrophic descriptions and thin layer models useful aids in the task of understanding their planetary dynamics. In the hydrodynamic limit planetary-scale quasi-geostrophic circulations are particularly important features that, due to their linear nature, have generally been probed with simple models to great success (e.g., Shell & Held, 2004; Langton & Laughlin, 2007; Showman & Polvani, 2010, 2011; Perez-Becker & Showman, 2013). Initial comparisons with three-dimensional MHD models indicate that simple SWHMD models can also provide similarly powerful tools in modelling magnetism in these planets, which until now has only been approached with complex three-dimensional spherical models of global magnetohydrodynamic circulation.

Since the prediction of magnetically-driven wind variations in hot Jupiters (Rogers & Komacek, 2014), westward hotspots/brightspots have been inferred on the hot Jupiters HAT-P-7b (Armstrong *et al.*, 2016), CoRoT-2b (Dang *et al.*, 2018), Kepler-76b (Jackson *et al.*, 2019), WASP-33b (von Essen *et al.*, 2020), and WASP-12b (Bell *et al.*, 2019). The predictions made in Chapter 7 of this work suggest that more observations of this kind should be expected. If this expectation is realised, the influx of data from such observations would provide useful comparisons for MHD modelling and dynamo theory on exoplanets, which are currently lacking.

Appendix A

Magnetic dissipation derivation

We present the derivation for $\mathbf{D}_\eta$ for the unforced version of our reduced gravity SWMHD model (see Equation (2.74) in Chapter 2). This was originally put forward by Andrew Gilbert (personal correspondence) for a single layer model, but we have made the adaptations (on interface boundary treatments) necessary for use in our reduced gravity model.

Full governing equations and boundary conditions

In constant density three-dimensional MHD systems, magnetic fields evolve subject to

$$\begin{aligned}\frac{\partial \mathbf{B}_3}{\partial t} &= \nabla_3 \times (\mathbf{u}_3 \times \mathbf{B}_3) - \nabla_3 \times (\eta \nabla_3 \times \mathbf{B}_3) \\ &= (\mathbf{B}_3 \cdot \nabla_3)\mathbf{u}_3 - (\mathbf{u}_3 \cdot \nabla_3)\mathbf{B}_3 + \mathbf{D}_{\eta,3},\end{aligned} \tag{A.1}$$

$$\nabla_3 \cdot \mathbf{B}_3 = 0. \tag{A.2}$$

where $\mathbf{D}_{\eta,3} = -\nabla_3 \times (\eta \nabla_3 \times \mathbf{B}_3)$. In our reduced gravity SWMHD model, we wish to approximate this evolution in a thin layer of electrically conducting fluid, $S_b < z < S_t$, with constant density (ρ) and magnetic permeability (μ_0), where the magnetic diffusivity, $\eta(x, y) = 1/\mu_0\sigma$, is allowed to vary horizontally but not vertically. The system is to be solved subject to zero normal magnetic field and tangential current boundary conditions:

$$\widehat{\mathbf{n}}_3 \cdot \mathbf{B}_3 = 0 \quad \text{and} \quad \widehat{\mathbf{n}}_3 \times (\nabla_3 \times \mathbf{B}_3) = \mathbf{0}, \tag{A.3}$$

on $z = S_t(x, y, t)$ and $z = S_b(x, y, t)$, where $\widehat{\mathbf{n}}_3 = \widehat{\mathbf{n}}_t \equiv \widehat{\mathbf{z}} - \nabla S_t$ and $\widehat{\mathbf{n}}_3 = \widehat{\mathbf{n}}_b \equiv \widehat{\mathbf{z}} - \nabla S_b$ are the unit normal vectors on the upper and lower surfaces respectively.

Rescaling the system

In the shallow-water approximation, both the ratios of the vertical and horizontal velocity field magnitudes and the ratios of the vertical and horizontal magnetic field magnitudes are assumed to scale with their spatial scales (i.e., $|w|/|u| \sim H/L$, $|w|/|v| \sim H/L$, $|B_z|/|B_x| \sim H/L$, and $|B_z|/|B_y| \sim H/L$). Hence, letting $\varepsilon = H/L$, one can write

$$\mathbf{u}_3 = \mathbf{u} + \varepsilon\tilde{w}\widehat{\mathbf{z}}, \quad \mathbf{B}_3 = \mathbf{B} + \varepsilon\tilde{B}_z\widehat{\mathbf{z}}, \quad \nabla_3 = \nabla + \varepsilon^{-1}\widehat{\mathbf{z}}\frac{\partial}{\partial\tilde{z}}, \tag{A.4}$$

where the rescalings $z = \varepsilon\tilde{z}$, $w = \varepsilon\tilde{w}$, and $B_z = \varepsilon\tilde{B}_z$ have been applied so $\tilde{z}$, $\tilde{w}$, and $\tilde{B}_z$ scale identically to their horizontal counterparts in the shallow-water limit (i.e., for $\varepsilon \ll 1$). Similarly, for $z = \varepsilon\tilde{z}$, unit normal vectors on the free surfaces become $\widehat{\mathbf{n}}_t = \widehat{\mathbf{z}} - \varepsilon\nabla\tilde{S}_t$ and $\widehat{\mathbf{n}}_b = \widehat{\mathbf{z}} - \varepsilon\nabla\tilde{S}_b$, where $S_t = \varepsilon\tilde{S}_t$ and $S_b = \varepsilon\tilde{S}_b$. With this rescaling, Equations (A.1) and (A.2) become

$$\frac{\partial\mathbf{B}_3}{\partial t} + \left(\mathbf{u}\cdot\nabla + \tilde{w}\frac{\partial}{\partial\tilde{z}}\right)\mathbf{B}_3 = \left(\mathbf{B}\cdot\nabla + \tilde{B}_z\frac{\partial}{\partial\tilde{z}}\right)\mathbf{u}_3 + \mathbf{D}_{\eta,3}, \tag{A.5}$$

$$\nabla\cdot\mathbf{B} + \frac{\partial\tilde{B}_z}{\partial\tilde{z}} = 0. \tag{A.6}$$

To write $\mathbf{D}_{\eta,3}$ in terms of this rescaling, first note that

$$\begin{aligned}\nabla_3\times\mathbf{B}_3 &= \nabla\times\mathbf{B} + \frac{\partial\tilde{B}_z}{\partial\tilde{z}}\cancelto{0}{(\widehat{\mathbf{z}}\times\widehat{\mathbf{z}})} + \varepsilon\left(\nabla\tilde{B}_z\times\widehat{\mathbf{z}}\right) + \varepsilon^{-1}\left(\widehat{\mathbf{z}}\times\frac{\partial\mathbf{B}}{\partial\tilde{z}}\right)\\ &= \varepsilon^{-1}\left(\widehat{\mathbf{z}}\times\frac{\partial\mathbf{B}}{\partial\tilde{z}}\right) + \nabla\times\mathbf{B} + \varepsilon\left(\nabla\tilde{B}_z\times\widehat{\mathbf{z}}\right),\end{aligned} \tag{A.7}$$

so

$$
\begin{aligned}
\mathbf{D}_{\eta,3} &= -\nabla_3 \times (\eta \nabla_3 \times \mathbf{B}_3) \\
&= -\left(\nabla + \varepsilon^{-1}\widehat{\mathbf{z}}\frac{\partial}{\partial \tilde{z}}\right) \times \left[\varepsilon^{-1}\left(\widehat{\mathbf{z}} \times \eta \frac{\partial \mathbf{B}}{\partial \tilde{z}}\right) + \eta \nabla \times \mathbf{B} + \varepsilon\left(\eta \nabla \tilde{B}_z \times \widehat{\mathbf{z}}\right)\right] \\
&= \varepsilon^{-2}\left[\widehat{\mathbf{z}} \times \left(\widehat{\mathbf{z}} \times \eta \frac{\partial^2 \mathbf{B}}{\partial \tilde{z}^2}\right)\right] + \varepsilon^{-1}\left[-\nabla \times \left(\widehat{\mathbf{z}} \times \eta \frac{\partial \mathbf{B}}{\partial \tilde{z}}\right) - \widehat{\mathbf{z}} \times \left(\eta \nabla \times \frac{\partial \mathbf{B}}{\partial \tilde{z}}\right)\right] \\
&\quad + \left[-\nabla \times (\eta \nabla \times \mathbf{B}) - \widehat{\mathbf{z}} \times \left(\eta \nabla \frac{\partial \tilde{B}_z}{\partial \tilde{z}} \times \widehat{\mathbf{z}}\right)\right] + \varepsilon\left[-\nabla \times (\eta \nabla \tilde{B}_z \times \widehat{\mathbf{z}})\right] \\
&= \varepsilon^{-2}\left[\eta \frac{\partial^2 \mathbf{B}}{\partial \tilde{z}^2}\right] + \varepsilon^{-1}\left[-\nabla \cdot \left(\eta \frac{\partial \mathbf{B}}{\partial \tilde{z}}\right)\widehat{\mathbf{z}}\right] + \left[-\nabla \times (\eta \nabla \times \mathbf{B}) - \eta \nabla\left(\frac{\partial \tilde{B}_z}{\partial \tilde{z}}\right)\right] \\
&\quad + \varepsilon\left[\nabla \cdot (\eta \nabla \tilde{B}_z)\widehat{\mathbf{z}}\right],
\end{aligned}
\tag{A.8}
$$

where $\partial \eta / \partial \tilde{z} = 0$ and $\mathbf{a} \times (\mathbf{b} \times \mathbf{c}) = \mathbf{b}(\mathbf{a} \cdot \mathbf{c}) - \mathbf{c}(\mathbf{a} \cdot \mathbf{b})$ have been applied (multiple times). We can also use Equation (A.7) to obtain

$$
\begin{aligned}
\widehat{\mathbf{n}}_t \times (\nabla_3 \times \mathbf{B}_3) &= (\widehat{\mathbf{z}} - \varepsilon \nabla \tilde{S}_t) \times \left[\varepsilon^{-1}\left(\widehat{\mathbf{z}} \times \eta \frac{\partial \mathbf{B}}{\partial \tilde{z}}\right) + \eta \nabla \times \mathbf{B} + \varepsilon\left(\eta \nabla \tilde{B}_z \times \widehat{\mathbf{z}}\right)\right] \\
&= \varepsilon^{-1}\left[\widehat{\mathbf{z}} \times \left(\widehat{\mathbf{z}} \times \frac{\partial \mathbf{B}}{\partial \tilde{z}}\right)\right] + \left[\cancelto{0}{\widehat{\mathbf{z}} \times (\nabla \times \mathbf{B})} - \nabla \tilde{S}_t \times \left(\widehat{\mathbf{z}} \times \frac{\partial \mathbf{B}}{\partial \tilde{z}}\right)\right] \\
&\quad + \varepsilon\left[\widehat{\mathbf{z}} \times (\nabla \tilde{B}_z \times \widehat{\mathbf{z}}) - \nabla \tilde{S}_t \times (\nabla \times \mathbf{B})\right] + \varepsilon^2\left[-\nabla \tilde{S}_t \times (\nabla \tilde{B}_z \times \widehat{\mathbf{z}})\right] \\
&= \varepsilon^{-1}\left[-\frac{\partial \mathbf{B}}{\partial \tilde{z}}\right] + \left[-\widehat{\mathbf{z}}\left(\nabla \tilde{S}_t \cdot \frac{\partial \mathbf{B}}{\partial \tilde{z}}\right)\right] + \varepsilon\left[\nabla \tilde{B}_z - \nabla \tilde{S}_t \times (\nabla \times \mathbf{B})\right] \\
&\quad + \varepsilon^2\left[\widehat{\mathbf{z}}\left(\nabla \tilde{S}_t \cdot \nabla \tilde{B}_z\right)\right],
\end{aligned}
\tag{A.9}
$$

where, again, the vector identity $\mathbf{a} \times (\mathbf{b} \times \mathbf{c}) = \mathbf{b}(\mathbf{a} \cdot \mathbf{c}) - \mathbf{c}(\mathbf{a} \cdot \mathbf{b})$ has been applied multiple times. With the rescaled variables, the zero normal magnetic field boundary conditions (i.e., $\widehat{\mathbf{n}}_3 \cdot \mathbf{B}_3 = 0$) become

$$
\varepsilon(\tilde{B}_z - \mathbf{B} \cdot \nabla \tilde{S}_t) = 0 \quad \text{on} \quad \tilde{z} = \tilde{S}_t(x, y, t), \tag{A.10a}
$$

$$
\varepsilon(\tilde{B}_z - \mathbf{B} \cdot \nabla \tilde{S}_b) = 0 \quad \text{on} \quad \tilde{z} = \tilde{S}_b(x, y, t), \tag{A.10b}
$$

which is mathematically identical to the standard $B_z|_{z=S_t} = \mathbf{B} \cdot \nabla S_t$ and $B_z|_{z=S_b} = \mathbf{B} \cdot \nabla S_b$ no magnetic flux boundary conditions applied in Chapter 2. However, with the inclusion of magnetic diffusion, tangential current boundary conditions are also required (i.e., $\widehat{\mathbf{n}}_3 \times \mathbf{J}_3 = 0$). For these, using Equation (A.7) in Equation (A.3) yields

$$\begin{aligned}\frac{\partial \mathbf{B}}{\partial \tilde{z}} = \varepsilon\left[-\widehat{\mathbf{z}}\left(\nabla \tilde{S}_t \cdot \frac{\partial \mathbf{B}}{\partial \tilde{z}}\right)\right] + \varepsilon^2\left[\nabla \tilde{B}_z - \nabla \tilde{S}_t \times (\nabla \times \mathbf{B})\right] \\ + \varepsilon^3\left[\widehat{\mathbf{z}}\left(\nabla \tilde{S}_t \cdot \nabla \tilde{B}_z\right)\right] \quad \text{on} \quad \tilde{z} = \tilde{S}_t(x, y, t),\end{aligned} \tag{A.10c}$$

$$\begin{aligned}\frac{\partial \mathbf{B}}{\partial \tilde{z}} = \varepsilon\left[-\widehat{\mathbf{z}}\left(\nabla \tilde{S}_b \cdot \frac{\partial \mathbf{B}}{\partial \tilde{z}}\right)\right] + \varepsilon^2\left[\nabla \tilde{B}_z - \nabla \tilde{S}_b \times (\nabla \times \mathbf{B})\right] \\ + \varepsilon^3\left[\widehat{\mathbf{z}}\left(\nabla \tilde{S}_b \cdot \nabla \tilde{B}_z\right)\right] \quad \text{on} \quad \tilde{z} = \tilde{S}_b(x, y, t),\end{aligned} \tag{A.10d}$$

Asymptotic expansion

Up to this point, we have not made any approximations, but have simply rescaled the governing equations. With these rescaled expression, we can now introduce the following asymptotic expansions for all variables in the $\varepsilon \ll 1$ limit:

$$\begin{aligned}&\mathbf{u} = \mathbf{u}_0 + \varepsilon^2 \mathbf{u}_1 + \dots, \quad \tilde{w} = \tilde{w}_0 + \varepsilon^2 \tilde{w}_1 + \dots, \\ &\mathbf{B} = \mathbf{B}_0 + \varepsilon^2 \mathbf{B}_1 + \dots, \quad \tilde{B}_z = \tilde{B}_{z,0} + \varepsilon^2 \tilde{B}_{z,1} + \dots, \\ &\tilde{S}_t = \tilde{S}_{t,0} + \varepsilon^2 \tilde{S}_{t,1} + \dots, \quad \tilde{S}_b = \tilde{S}_{b,0} + \varepsilon^2 \tilde{S}_{b,1} + \dots \\ &\tilde{h} = \tilde{h}_0 + \varepsilon^2 \tilde{h}_1 + \dots = (\tilde{S}_{t,0} - \tilde{S}_{b,0}) + \varepsilon^2 (\tilde{S}_{t,1} - \tilde{S}_{b,1}) + \dots.\end{aligned} \tag{A.11}$$

In hydrodynamic shallow-water systems, non-advective terms in the shallow-water momentum equation are independent of z (at $O(\varepsilon^0)$), so an initially vertically-independent flow will remain vertically-independent for all time (see Chapter 2). Hence,

$$\frac{\partial \mathbf{u}_0}{\partial \tilde{z}} = \mathbf{0}. \tag{A.12}$$

Moreover, as in Chapter 2, incompressibility (at $O(\varepsilon^0)$) implies

$$[\tilde{w}_0]_{\tilde{z}=\tilde{S}_{b,0}}^{\tilde{z}=\tilde{S}_{t,0}} = -\tilde{h}_0 \nabla \cdot \mathbf{u}_0, \tag{A.13}$$

and free material surface surface conditions imply $\tilde{w}_0|_{\tilde{z}=\tilde{S}_{t,0}} = \mathrm{D}S_{t,0}/\mathrm{D}t$ and $\tilde{w}_0|_{\tilde{z}=\tilde{S}_{b,0}} = \mathrm{D}S_{b,0}/\mathrm{D}t$ (see Section 2.2.1). Hence, as usual,

$$\frac{\partial \tilde{h}_0}{\partial t} + \nabla \cdot (\tilde{h}_0 \mathbf{u}_0) = 0. \tag{A.14}$$

For the induction equation, applying the expansions in Equation (A.11) to Equation (A.5), with Equation (A.8), gives $\eta \partial^2 \mathbf{B}_0 / \partial \tilde{z}^2 = \mathbf{0}$ at leading order, $O(\varepsilon^{-2})$. Therefore, for $\eta \neq 0$, $\partial^2 \mathbf{B}_0 / \partial \tilde{z}^2 = \mathbf{0}$. Further, Equations (A.10c) and (A.10d) give $\partial \mathbf{B}_0 / \partial \tilde{z} = \mathbf{0}$ on both $\tilde{z} = \tilde{S}_{t,0}$ and $\tilde{z} = \tilde{S}_{b,0}$ at $O(\varepsilon^0)$, which yield

$$\frac{\partial \mathbf{B}_0}{\partial \tilde{z}} = \mathbf{0} \quad \text{for all } \tilde{z}, \tag{A.15}$$

when combined with $\partial^2 \mathbf{B}_0 / \partial \tilde{z}^2 = 0$ (everywhere).

This recovers the standard SWMHD requirement of vertically-independent horizontal magnetic fields, which causes the $O(\varepsilon)$ contributions to Equations (A.10c) and (A.10d) and the $O(\varepsilon^{-1})$ term in the expansion of $\mathbf{D}_{\eta,3}$ to vanish. The latter leaves the highest order non-zero contributions to $\mathbf{D}_{\eta,3}$ at $O(\varepsilon^0)$. Before considering contributions to the induction equation at $O(\varepsilon^0)$, we note that together $\partial \mathbf{B}_0 / \partial \tilde{z} = \mathbf{0}$ and Gauss' law (i.e., Equation (A.6) at $O(\varepsilon^0)$) produce

$$[\tilde{B}_{z,0}]_{\tilde{z}=\tilde{S}_{b,0}}^{\tilde{z}=\tilde{S}_{t,0}} = -\tilde{h}_0 \nabla \cdot \mathbf{B}_0, \tag{A.16}$$

which can be combined with the no magnetic flux boundary conditions (i.e., Equations (A.10a) and (A.10b)) to yield

$$\nabla \cdot (\tilde{h}_0 \mathbf{B}_0) = 0. \tag{A.17}$$

as in Section 2.2.2. Now, at $O(\varepsilon^0)$, the horizontal components of Equations (A.5) and (A.8) give

$$\frac{\partial \mathbf{B}_0}{\partial t} + (\mathbf{u}_0 \cdot \nabla) \mathbf{B}_0 = (\mathbf{B}_0 \cdot \nabla) \mathbf{u}_0 + \eta \frac{\partial^2 \mathbf{B}_1}{\partial \tilde{z}^2} - \nabla \times (\eta \nabla \times \mathbf{B}_0) - \eta \nabla \left(\frac{\partial \tilde{B}_{z,0}}{\partial \tilde{z}} \right), \tag{A.18}$$

where $\partial \mathbf{u}_0/\partial \tilde{z} = \mathbf{0}$ and $\partial \mathbf{B}_0/\partial \tilde{z} = \mathbf{0}$ have been applied. This equation can be closed by integrating Equation (A.18) vertically over the extent of the fluid column:

$$h_0\left(\frac{\partial \mathbf{B}_0}{\partial t}+(\mathbf{u}_0\cdot\nabla)\mathbf{B}_0-(\mathbf{B}_0\cdot\nabla)\mathbf{u}+\nabla\times(\eta\nabla\times\mathbf{B}_0)\right)=\eta\left[\frac{\partial \mathbf{B}_1}{\partial \tilde{z}}-\nabla\tilde{B}_{z,0}\right]_{\tilde{z}=\tilde{S}_{b,0}}^{\tilde{z}=\tilde{S}_{t,0}}, \quad \text{(A.19)}$$

where we have noted that the terms inside the bracket on the lefthand side are vertically-independent. Terms on the righthand side can be evaluated using the $O(\varepsilon^2)$ contributions to Equations (A.10c) and (A.10d), which are

$$\frac{\partial \mathbf{B}_1}{\partial \tilde{z}}=\left[\nabla\tilde{B}_{z,0}-\nabla\tilde{S}_{t,0}\times(\nabla\times\mathbf{B}_0)\right] \quad \text{on} \quad \tilde{z}=\tilde{S}_{t,0}(x,y,t), \quad \text{(A.20)}$$
$$\frac{\partial \mathbf{B}_1}{\partial \tilde{z}}=\left[\nabla\tilde{B}_{z,0}-\nabla\tilde{S}_{b,0}\times(\nabla\times\mathbf{B}_0)\right] \quad \text{on} \quad \tilde{z}=\tilde{S}_{b,0}(x,y,t), \quad \text{(A.21)}$$

so $\eta[\partial \mathbf{B}_1/\partial \tilde{z}-\nabla\tilde{B}_{z,0}]_{\tilde{z}=\tilde{S}_{b,0}}^{\tilde{z}=\tilde{S}_{t,0}}=-\nabla h_0\times(\eta\nabla\times\mathbf{B}_0)$. Thus,

$$\begin{aligned}\frac{\partial \mathbf{B}_0}{\partial t}+(\mathbf{u}_0\cdot\nabla)\,\mathbf{B}_0-(\mathbf{B}_0\cdot\nabla)\,\mathbf{u}_0&=-\nabla\times(\eta\nabla\times\mathbf{B}_0)-h_0^{-1}\nabla h_0\times(\eta\nabla\times\mathbf{B}_0),\\&=-h_0^{-1}\nabla\times(\eta h_0\nabla\times\mathbf{B}_0),\end{aligned} \quad \text{(A.22)}$$

so, dropping the subscripts on our leading order dependent variables, we have

$$\mathbf{D}_\eta=-h^{-1}\nabla\times(\eta h\nabla\times\mathbf{B}), \quad \text{(A.23)}$$

as quoted in Chapter 2. Since $\mathbf{D}_\eta$ is vertically-independent, the implicit assumption that $\partial \mathbf{B}_0/\partial t$ is vertically-independent, which was used to obtain Equation (A.18), holds.

Appendix B

Potential vorticity evolution

Here we derive the evolution equation for the potential vorticity, $q \equiv (\zeta + f)/h$, where $\zeta \equiv \boldsymbol{\omega} \cdot \widehat{\mathbf{z}} \equiv (\nabla \times \mathbf{u}) \cdot \widehat{\mathbf{z}} \equiv \partial v/\partial x - \partial u/\partial y$ is the relative vorticity of flows in the horizontal plane and $f = \beta y$ is the Coriolis parameter in the equatorial beta-plane approximation. In the reduced-gravity SWMHD model of Chapter 2, the shallow-water momentum and continuity equations are respectively

$$\frac{\partial \mathbf{u}}{\partial t} + (\mathbf{u} \cdot \nabla)\mathbf{u} + f(\widehat{\mathbf{z}} \times \mathbf{u}) = -g\nabla h + (\mathbf{B} \cdot \nabla)\mathbf{B} + \mathbf{R} - \frac{\mathbf{u}}{\tau_{\mathrm{drag}}} + \mathbf{D}_\nu, \tag{B.1a}$$

$$\frac{\mathrm{D}h}{\mathrm{D}t} + h\nabla \cdot \mathbf{u} = Q, \tag{B.1b}$$

where, as defined in the main text, $\mathbf{u}(x, y, t) \equiv (u, v)$, $h(x, y, t)$ and $\mathbf{B}(x, y, t) \equiv (B_x, B_y)$ are independent variables g and τ_{drag} are constants, and $\mathbf{R}$, $\mathbf{D}_\nu$ and Q are prescriptions that depend on $\mathbf{u}$ and h.

Before we manipulate Equations (B.1a) and (B.1b) we highlight the following useful relations:

$$(\mathbf{u}\cdot\nabla)\mathbf{u} = \frac{1}{2}\nabla(\mathbf{u}\cdot\mathbf{u}) - \mathbf{u}\times\boldsymbol{\omega}, \tag{B.2a}$$

$$(\mathbf{B}\cdot\nabla)\mathbf{B} = \frac{1}{2}\nabla(\mathbf{B}\cdot\mathbf{B}) + \mathbf{J}\times\mathbf{B}, \tag{B.2b}$$

$$\nabla\times[f(\widehat{\mathbf{z}}\times\mathbf{u})] = \left[v\frac{\partial f}{\partial y} + f\nabla\cdot\mathbf{u}\right]\widehat{\mathbf{z}}, \tag{B.2c}$$

$$\frac{\mathrm{D}(hq)}{\mathrm{D}t} = h\frac{\mathrm{D}q}{\mathrm{D}t} + q\frac{\mathrm{D}h}{\mathrm{D}t} = \frac{\mathrm{D}(\zeta+f)}{\mathrm{D}t} = \frac{\mathrm{D}\zeta}{\mathrm{D}t} + v\frac{\partial f}{\partial y}. \tag{B.2d}$$

where $\mathbf{J} \equiv J\widehat{\mathbf{z}} \equiv (\nabla\times\mathbf{B})$ and $J = \partial B_y/\partial x - \partial B_x/\partial y$. Moreover, in two-dimensional geometry,

$$\nabla\times(\mathbf{u}\times\boldsymbol{\omega}) = -(\mathbf{u}\cdot\nabla)\zeta\widehat{\mathbf{z}} - \zeta(\nabla\cdot\mathbf{u})\widehat{\mathbf{z}}. \tag{B.2e}$$

Taking the curl of Equation (B.1a), while using Equations (B.2a) and (B.2b), yields

$$\frac{\partial\boldsymbol{\omega}}{\partial t} + \nabla\times(-\mathbf{u}\times\boldsymbol{\omega}) + \nabla\times[f(\widehat{\mathbf{z}}\times\mathbf{u})] = \nabla\times(\mathbf{J}\times\mathbf{B}) + \nabla\times\mathbf{F}, \tag{B.3}$$

where $\mathbf{F} = \mathbf{R} - \mathbf{u}/\tau_{\text{drag}} + \mathbf{D}_\nu$ and $\nabla\times\nabla\Phi = \mathbf{0}$ has been applied to note that $\nabla\times\nabla(\mathbf{u}\cdot\mathbf{u}/2) = \mathbf{0}$, $\nabla\times\nabla(gh) = \mathbf{0}$, and $\nabla\times\nabla(\mathbf{B}\cdot\mathbf{B}/2) = \mathbf{0}$. Taking the vertical component of Equation (B.3) and using Equations (B.2c) and (B.2e), gives

$$\frac{\partial\zeta}{\partial t} + (\mathbf{u}\cdot\nabla)\zeta + \zeta(\nabla\cdot\mathbf{u}) + v\frac{\partial f}{\partial y} + f\nabla\cdot\mathbf{u} = [\nabla\times(\mathbf{J}\times\mathbf{B})]\cdot\widehat{\mathbf{z}} + (\nabla\times\mathbf{F})\cdot\widehat{\mathbf{z}}. \tag{B.4}$$

Hence, from Equations (B.1b), (B.2d) and (B.4),

$$\begin{aligned}
h\frac{\mathrm{D}q}{\mathrm{D}t} &= \frac{\mathrm{D}\zeta}{\mathrm{D}t} + v\frac{\partial f}{\partial y} - q\frac{\mathrm{D}h}{\mathrm{D}t} \\
&= -\zeta(\nabla\cdot\mathbf{u}) - \cancel{v\frac{\partial f}{\partial y}} - f\nabla\cdot\mathbf{u} + [\nabla\times(\mathbf{J}\times\mathbf{B})]\cdot\widehat{\mathbf{z}} + (\nabla\times\mathbf{F})\cdot\widehat{\mathbf{z}} + \cancel{v\frac{\partial f}{\partial y}} \\
&\quad - q(-h\nabla\cdot\mathbf{u} + Q) \\
&= \cancelto{0}{(hq-\zeta-f)}(\nabla\cdot\mathbf{u}) + [\nabla\times(\mathbf{J}\times\mathbf{B})]\cdot\widehat{\mathbf{z}} + (\nabla\times\mathbf{F})\cdot\widehat{\mathbf{z}} - qQ \\
&= [\nabla\times(\mathbf{J}\times\mathbf{B})]\cdot\widehat{\mathbf{z}} - qQ + (\nabla\times\mathbf{F})\cdot\widehat{\mathbf{z}}.
\end{aligned} \tag{B.5}$$

Hence,

$$\frac{\mathrm{D}q}{\mathrm{D}t} = \frac{1}{h}[\nabla \times (\mathbf{J} \times \mathbf{B})] \cdot \widehat{\mathbf{z}} - q\frac{Q}{h} + \frac{1}{h}(\nabla \times \mathbf{R}) \cdot \widehat{\mathbf{z}} - \frac{\zeta}{h\tau_{\mathrm{drag}}} + (\nabla \times \mathbf{D}_\nu) \cdot \widehat{\mathbf{z}}, \tag{B.6}$$

as used in the main text.

Appendix C

Integral conservation laws

Total mass conservation

Using the shallow-water continuity condition (Equation (2.85b)),

$$\begin{aligned}\frac{\mathrm{d}}{\mathrm{d}t}\iint h\mathrm{d}x\mathrm{d}y &= -\iint \nabla\cdot(h\mathbf{u})\mathrm{d}x\mathrm{d}y + \iint Q\mathrm{d}x\mathrm{d}y \\ &= -\int_{-L_y}^{L_y} \cancel{[hu]_{-L_x}^{L_x}}\mathrm{d}y - \int_{-L_x}^{L_x} \cancel{[hv]_{-L_y}^{L_y}}\mathrm{d}x + \iint Q\mathrm{d}x\mathrm{d}y \\ &= \iint Q\mathrm{d}x\mathrm{d}y,\end{aligned} \tag{C.1}$$

where periodicity in x and impermeability in y have been applied. Hence, the rate of change of the active layer's total mass is equal to the total mass transported into the active layer. In the absence of mass exchanges ($Q = 0$), the total mass in the active layer is constant for all time.

Divergence-free condition

In Section 2.2.2, we showed that integrating Gauss' law of magnetism over the active layer with no normal magnetic flux boundary conditions at interfaces yields the shallow-water divergence-free condition. Applying our boundary conditions to the integral form of this gives

$$\int_{\mathcal{V}} \nabla_3 \cdot \mathbf{B}_3 = \iint \nabla \cdot (h\mathbf{B})\mathrm{d}x\mathrm{d}y = \int_{-L_y}^{L_y} \cancel{[hB_x]_{-L_x}^{L_x}}\mathrm{d}y + \int_{-L_x}^{L_x} \cancel{[hB_y]_{-L_y}^{L_y}}\mathrm{d}x = 0, \tag{C.2}$$

where the first term cancels due to our periodic boundary conditions in x and the second term cancels due to our no normal magnetic flux condition, $B_y|_{y=\pm L_y} = 0$.

Total horizontal magnetic flux conservation

From Equation (2.87c),

$$\begin{aligned}
\frac{\mathrm{d}}{\mathrm{d}t}\iint hB_x\mathrm{d}x\mathrm{d}y &= -\iint \nabla \cdot \left[h\mathbf{u}B_x - h\mathbf{B}u - \eta h\left(\nabla B_x - \frac{\partial \mathbf{B}}{\partial x}\right)\right]\mathrm{d}x\mathrm{d}y \\
&= -\int_{-L_y}^{L_y} \cancel{\left[huB_x - hB_xu - \eta h\left(\frac{\partial B_x}{\partial x} - \frac{\partial B_x}{\partial x}\right)\right]_{-L_x}^{L_x}}\mathrm{d}y \\
&\quad - \int_{-L_x}^{L_x} \left[hvB_x - hB_yu - \eta h\left(\frac{\partial B_x}{\partial y} - \frac{\partial B_y}{\partial x}\right)\right]_{-L_y}^{L_y}\mathrm{d}x \\
&= -\int_{-L_x}^{L_x} \left[\cancel{hvB_x} - \cancel{hB_yu} - \cancel{\eta hJ}\right]_{-L_y}^{L_y}\mathrm{d}x \\
&= 0,
\end{aligned} \tag{C.3a}$$

applying periodicity in x alongside $v|_{y=\pm L_y} = B_y|_{y=\pm L_y} = J|_{y=\pm L_y} = 0$, and

$$\begin{aligned}
\frac{\mathrm{d}}{\mathrm{d}t}\iint hB_y\mathrm{d}x\mathrm{d}y &= -\iint \nabla \cdot \left[h\mathbf{u}B_y - h\mathbf{B}v - \eta h\left(\nabla B_y - \frac{\partial \mathbf{B}}{\partial y}\right)\right]\mathrm{d}x\mathrm{d}y \\
&= -\int_{-L_y}^{L_y} \cancel{\left[huB_y - hB_xv - \eta h\left(\frac{\partial B_y}{\partial x} - \frac{\partial B_x}{\partial y}\right)\right]_{-L_x}^{L_x}}\mathrm{d}y \\
&\quad - \int_{-L_x}^{L_x} \left[\cancel{hvB_y} - \cancel{hB_yv} - \eta h\left(\cancel{\frac{\partial B_y}{\partial y} - \frac{\partial B_y}{\partial y}}\right)\right]_{-L_y}^{L_y}\mathrm{d}x \\
&= 0,
\end{aligned} \tag{C.3b}$$

using periodicity in x. Hence, the total horizontal magnetic flux of the active layer is conserved in both horizontal directions.

Total active layer columnar momentum

Using the x and y components of Equation (2.87a),

$$
\begin{aligned}
\frac{\mathrm{d}}{\mathrm{d}t}\iint hu\mathrm{d}x\mathrm{d}y &= -\iint \left(\nabla\cdot\left[h\mathbf{u}u - h\mathbf{B}B_x + \nu h(\widehat{\mathbf{x}}\cdot\boldsymbol{\tau})\right] + \frac{\partial}{\partial x}(\tfrac{1}{2}gh^2)\right)\mathrm{d}x\mathrm{d}y \\
&\quad + \iint\left(fhv + Qu + hR_x - \frac{hu}{\tau_{\mathrm{drag}}}\right)\mathrm{d}x\mathrm{d}y \\
&= -\int_{-L_y}^{L_y}\cancel{\left[hu^2 - hB_x^2 + \tfrac{1}{2}gh^2 + 2\nu h\frac{\partial u}{\partial x}\right]_{-L_x}^{L_x}}\mathrm{d}y \\
&\quad - \int_{-L_x}^{L_x}\left[\cancel{huv} - \cancel{hB_xB_y} + \nu h\left(\frac{\partial \cancel{u}}{\cancel{\partial y}} + \frac{\partial \cancel{v}}{\cancel{\partial x}}\right)\right]_{-L_y}^{L_y}\mathrm{d}x \\
&\quad + \iint\left(fhv + Qu + hR_x - \frac{hu}{\tau_{\mathrm{drag}}}\right)\mathrm{d}x\mathrm{d}y \\
&= \iint\left(fhv + Qu + hR_x - \frac{hu}{\tau_{\mathrm{drag}}}\right)\mathrm{d}x\mathrm{d}y,
\end{aligned}
\tag{C.4a}
$$

applying periodicity in x alongside $v|_{y=\pm L_y} = \partial u/\partial y|_{y=\pm L_y} = B_y|_{y=\pm L_y} = 0$, and

$$
\begin{aligned}
\frac{\mathrm{d}}{\mathrm{d}t}\iint hv\mathrm{d}x\mathrm{d}y &= -\iint \left(\nabla\cdot\left[h\mathbf{u}v - h\mathbf{B}B_y + \nu h(\widehat{\mathbf{y}}\cdot\boldsymbol{\tau})\right] + \frac{\partial}{\partial y}(\tfrac{1}{2}gh^2)\right)\mathrm{d}x\mathrm{d}y \\
&\quad + \iint\left(-fhu + Qv + hR_y - \frac{hv}{\tau_{\mathrm{drag}}}\right)\mathrm{d}x\mathrm{d}y \\
&= -\int_{-L_y}^{L_y}\cancel{\left[hub - hB_xB_y + \nu h\left(\frac{\partial v}{\partial x} + \frac{\partial u}{\partial y}\right)\right]_{-L_x}^{L_x}}\mathrm{d}y \\
&\quad - \int_{-L_x}^{L_x}\left[\cancel{hv^2} - \cancel{hB_y^2} + \tfrac{1}{2}gh^2 + 2\nu h\frac{\partial v}{\partial y}\right]_{-L_y}^{L_y}\mathrm{d}x \\
&\quad + \iint\left(-fhu + Qv + hR_y - \frac{hv}{\tau_{\mathrm{drag}}}\right)\mathrm{d}x\mathrm{d}y \\
&= -\int_{-L_x}^{L_x}\left[\tfrac{1}{2}gh^2 + 2\nu h\frac{\partial v}{\partial y}\right]_{-L_y}^{L_y}\mathrm{d}x \\
&\quad + \iint\left(-fhu + Qv + hR_y - \frac{hv}{\tau_{\mathrm{drag}}}\right)\mathrm{d}x\mathrm{d}y,
\end{aligned}
\tag{C.4b}
$$

applying periodicity in x alongside $v|_{y=\pm L_y} = B_y|_{y=\pm L_y} = 0$. Equation (C.4) shows that in the unforced ($Q = 0$ and $\mathbf{R} = \mathbf{0}$), drag-free ($\tau_{\mathrm{drag}}^{-1} \to 0$), non-rotating ($f = 0$) limit, total specific active layer columnar momentum is conserved in the x direction but is *not* generally conserved in the y direction. This asymmetry arises because our choice of boundary conditions break the translational invariance present in a fully periodic system, for instance. Moreover, when rotation is included, the asymmetries introduced by the Coriolis effect breaks the total specific columnar momentum conservation in the active layer in both directions (regardless of our choice of boundary conditions). However, the Coriolis effect acts to deflect of the flow and does not affect total columnar energy conservation (see below).

Total columnar energy conservation

From Equation (2.99), applying periodicity in x alongside $v|_{y=\pm L_y} = \partial u/\partial y|_{y=\pm L_y} = B_y|_{y=\pm L_y} = J|_{y=\pm L_y} = 0$ yields

$$
\begin{aligned}
\frac{\mathrm{d}}{\mathrm{d}t}\iint E\mathrm{d}x\mathrm{d}y &= -\iint \nabla\cdot\mathbf{F}\mathrm{d}x\mathrm{d}y + \iint(\mathcal{Q}_\nu+\mathcal{Q}_\eta+\mathcal{Q}_f)\mathrm{d}x\mathrm{d}y \\
&= -\int_{-L_y}^{L_y}\cancel{\left[\left(\tfrac{1}{2}h|\mathbf{u}|^2+gh^2\right)u+S_x-\nu h\widehat{\mathbf{x}}\cdot(\mathbf{u}\cdot\boldsymbol{\tau})\right]_{-L_x}^{L_x}}\mathrm{d}y \\
&\quad -\int_{-L_x}^{L_x}\left[\cancel{\left(\tfrac{1}{2}h|\mathbf{u}|^2+gh^2\right)v}+S_y-\nu h\widehat{\mathbf{y}}\cdot(\mathbf{u}\cdot\boldsymbol{\tau})\right]_{-L_y}^{L_y}\mathrm{d}x \\
&\quad +\iint(\mathcal{Q}_\nu+\mathcal{Q}_\eta+\mathcal{Q}_f)\mathrm{d}x\mathrm{d}y \\
&= -\int_{-L_x}^{L_x}\Bigg[\cancel{\tfrac{1}{2}h|\mathbf{B}|^2v}-\cancel{h(\mathbf{u}\cdot\mathbf{B})B_y}+\cancel{\eta hB_xJ} \\
&\qquad\qquad -\nu h\cdot\left(u\cancel{\frac{\partial v}{\partial x}}+v\cancel{\frac{\partial v}{\partial y}}+u\cancel{\frac{\partial u}{\partial y}}+v\cancel{\frac{\partial v}{\partial y}}\right)\Bigg]_{-L_y}^{L_y}\mathrm{d}x \\
&\quad +\iint(\mathcal{Q}_\nu+\mathcal{Q}_\eta+\mathcal{Q}_f)\mathrm{d}x\mathrm{d}y \\
&= \iint(\mathcal{Q}_\nu+\mathcal{Q}_\eta+\mathcal{Q}_f)\mathrm{d}x\mathrm{d}y,
\end{aligned}
\tag{C.5}
$$

where $\mathbf{S}\equiv(S_x,S_y)$. Hence, energy can only enter the system through $\mathcal{Q}_f$ (recall that $\mathcal{Q}_\nu$ and $\mathcal{Q}_\eta$ were shown to be negative semi-definite in Section 2.2.7).

Appendix D

Linear solving methods

D.1 Linearised steady state solutions

To solve the linearised, non-diffusive, steady state SWMHD system considered in Chapter 3 (i.e., Equations (5.1) to (5.4)), we reduce the system to a single inhomogenenous ordinary differential equation of the form

$$\mathcal{L}\{\hat{v}\} \equiv F_1(y)\frac{\mathrm{d}^2\hat{v}}{\mathrm{d}y^2} + F_2(y)\frac{\mathrm{d}\hat{v}}{\mathrm{d}y} + F_3(y)\hat{v} = \mathcal{Q}(y), \tag{D.1}$$

where $F_1(y)$, $F_2(y)$, and $F_3(y)$ are latitudinally dependent coefficient functions, $\mathcal{L}$ is the system's second order differential operator, and $\mathcal{Q}(y)$ is the system's source term We have omitted the exact dependencies of $F_1(y)$, $F_2(y)$, $F_3(y)$, $\mathcal{Q}(y)$ for steady forced solutions (due to their cumbersome forms). These can be provided upon reasonable request. If $S(y)$ and $u_0(y)$ are symmetric about the equator and $B_0(y)$ is antisymmetric about the equator, $\mathcal{L}$ and $\mathcal{Q}$ are respectively symmetric and antisymmetric about the equator.

Solutions of Equation (D.1) on $-L_y < y < L_y$ are obtained by noting that, since $\mathcal{L}$ and $\mathcal{Q}$ are respectively symmetric and antisymmetric about the equator, inhomogeneous solutions are antisymmetric (i.e., $\hat{v}$ antisymmetric and $\hat{u}, \hat{h}, \hat{A}$ symmetric). Consequently, we solve Equation (D.1) in the upper-half domain, $0 < y < L_y$, with $\hat{v}(L_y) = 0$ (impermeability) and $\hat{v}(0) = 0$ (antisymmetry), before reflecting solutions. This reduced boundary value problem is solved by inverting the tridiagonal matrix that corresponds to Equation (D.1) with finite difference discretizations. We fix the equatorial boundary condition $\hat{v}(0) = 0$ and vary $\mathrm{d}\hat{v}/\mathrm{d}y|_{y=0}$ in order to satisfy $\hat{v}(L_y) = 0$, converging upon $\mathrm{d}\hat{v}/\mathrm{d}y|_{y=0}$ with the complex equivalent of the bracketed Newton-Raphson method discussed in Press *et al.* (1992).

D.2 Singular test solutions in the linear equatorial wave solving method

For $V_\mathrm{A} > 0$, we examine the nature of the test solutions of Equation (5.9) in the upper-half domain, $0 < y < L_y$, about the singular points, $y = y_s$. For $|\omega| \leq B_{0,\mathrm{max}}k$, y_s is located where $B_0(y_s)k = |\omega|$ (Alfvén singularities); whereas for $c_g k \leq |\omega| \leq (c_g^2 + B_{0,\mathrm{max}}^2)^{1/2}k$, y_s is located where $B_0(y_s)k = (\omega^2 - c_g^2k^2)^{1/2}$ (magneto-gravity singularities). The method of Frobenius gives

$$\hat{v} = C_1\hat{v}_1 + C_2\hat{v}_2, \qquad \hat{v}_1 = \sum_{n=0}^{\infty} a_n\hat{y}^{n+\mu_1}, \qquad \hat{v}_2 = D\hat{v}_1 \ln|\hat{y}| + \sum_{n=0}^{\infty} b_n\hat{y}^{n+\mu_2}; \tag{D.2}$$

where $\hat{y} = (y - y_s)/L_\mathrm{eq}$, C_1 and C_2 are the constants of integration, $\hat{v}_1$ and $\hat{v}_2$ are the first and second fundamental solutions, a_n, b_n and D are constant coefficients to be set or determined, and $\mu_1 \in \mathbb{Z}$ and $\mu_2 \in \mathbb{Z}$ are the roots of the indicial equation given by Equation (5.9).

About magneto-gravity singular points, $\mu_1 = 2$ and $\mu_2 = 0$, so

$$\hat{v} = C_1 \sum_{n=0}^{\infty} a_n\hat{y}^{n+2} + C_2\left(\sum_{n=0}^{\infty} b_n\hat{y}^{n} + D\ln|\hat{y}| \sum_{n=0}^{\infty} a_n\hat{y}^{n+2}\right), \tag{D.3}$$

where one is free to set $a_0 = 1$, $b_0 = 1$, $b_2 = 0$ (in fact, or b_2 can be set to any constant), and use Equation (5.9) to determine D, a_n, and b_n. In this case neither of the fundamental solutions are singular at $y = y_s$, so we are free to search for regular solutions using our regular solving method. Upon doing so, we find regular solutions, hence magneto-gravity singularities are in fact so-called "false" singularities with finite solutions as $y \to y_s$.

About Alfvén singular points, $\mu_1 = 0$ and $\mu_2 = 0$, so

$$\hat{v} = C_1 \sum_{n=0}^{\infty} a_n \hat{y}^n + C_2 \left(\sum_{n=0}^{\infty} b_n \hat{y}^n + D \ln|\hat{y}| \sum_{n=0}^{\infty} a_n \hat{y}^n \right), \tag{D.4}$$

where one is free to set $a_0 = 1$, $b_1 = 1$, $b_0 = 0$ (again, or b_0 can be set to any constant), and use Equation (5.9) to determine D, a_n, and b_n. Solutions of this kind are dominated by the $\hat{v} = O(\ln|\hat{y}|)$ component as $y \to y_s$, so solutions with Alfvén singularities have infinite discontinuities for $D \neq 0$ (which we always find).

Appendix E

Candidate hot Jupiters for magnetically-driven wind variations: relaxed criteria

Table E.1: Hot Jupiters in which $B_{\mathrm{dip,crit}} < 28\,\mathrm{G}$ at $P = 10\,\mathrm{mbar}$, with $\Delta T/T_{\mathrm{eq}} = 0.2$. Alongside T_{eq}, estimates of $B_{\mathrm{dip,crit}}$ and $B_{\mathrm{dip,crit}}$ (1 significant figure) using these choices are provided. If Hot Jupiters in this table are observed to magnetic wind variations, $B_{\mathrm{dip,crit,0.2}}$ estimates the lower bound of B_{dip} and $B_{\phi,\mathrm{crit,0.2}}$ estimates the magnitude of B_{ϕ}.

Rank	Candidate	$T_{\mathrm{eq}}/\,\mathrm{K}$	$B_{\phi,\mathrm{crit},0.2}/\,\mathrm{G}$	$B_{\mathrm{dip,crit},0.2}/\,\mathrm{G}$
1	WASP-189 b	2618	258	0.6
2	WASP-178 b	2366	259	0.7
3†	† WASP-12 b	2578	313	0.7
4†	† WASP-33 b	2681	298	1
5	WASP-121 b	2358	307	1
6	HATS-68 b	1743	354	1
7	WASP-78 b	2194	277	2
8	WASP-76 b	2182	291	2
9	MASCARA-1 b	2545	267	2

Continued on next page

Table E.1 – *Continued from previous page*

Rank	Candidate	$T_{\mathrm{eq}}/\,\mathrm{K}$	$B_{\phi,\mathrm{crit},0.2}/\,\mathrm{G}$	$B_{\mathrm{dip},\mathrm{crit},0.2}/\,\mathrm{G}$
10	WASP-82 b	2188	265	2
11	HD 85628 A b	2403	255	2
12	HAT-P-70 b	2551	266	2
13	HD 202772 A b	2132	251	2
14	Kepler-91 b	2037	209	2
15	TOI-1431 b/MASCARA-5 b	2370	258	2
16	WASP-100 b	2201	262	3
17	HAT-P-65 b	1953	276	3
18	HATS-67 b	2195	292	3
19	WASP-187 b	1952	232	3
20	WASP-87 A b	2311	278	3
21	HATS-40 b	2121	252	3
22	KELT-18 b	2082	259	4
23	HAT-P-57 b	2198	261	4
24	HATS-56 b	1902	244	4
25†	† HAT-P-7 b	2192	267	4
26	WASP-48 b	2058	279	4
27	HATS-26 b	1925	260	4
28	HAT-P-49 b	2127	257	5
29	KOI-13 b	2550	278	5
30	KELT-11 b	1711	227	6
31	WASP-111 b	2121	266	6
32	WASP-142 b	1992	277	6
33	WASP-90 b	1840	248	6
34	HAT-P-66 b	1900	261	7
35	HAT-P-60 b	1786	238	7

Continued on next page

Table E.1 – *Continued from previous page*

Rank	Candidate	$T_{\mathrm{eq}}/\,\mathrm{K}$	$B_{\phi,\mathrm{crit},0.2}/\,\mathrm{G}$	$B_{\mathrm{dip},\mathrm{crit},0.2}/\,\mathrm{G}$
36	HAT-P-33 b	1839	261	7
37	WASP-172 b	1745	229	7
38	Qatar-10 b	1955	289	7
39	WASP-88 b	1763	238	7
40	HATS-35 b	2033	281	7
41	Kepler-435 b	1731	217	8
42†	† Kepler-76 b	2145	284	8
43	Qatar-7 b	2052	282	8
44	WASP-71 b	2064	257	8
45	WASP-159 b	1811	240	8
46	CoRoT-1 b	2007	291	8
47	K2-260 b	1985	265	8
48	HATS-31 b	1837	256	10
49	HAT-P-32 b	1841	285	10
50	HATS-64 b	1800	238	10
51	HAT-P-23 b	2133	297	10
52	WASP-122 b	1962	295	10
53	TOI-954 b	1704	217	11
54	KELT-4 A b	1827	265	11
55	WASP-19 b	2060	319	11
56	WASP-92 b	1879	273	11
57	WASP-153 b	1712	256	11
58	CoRoT-21 b	2041	253	12
59	TOI-640 b	1749	240	12
60	HATS-24 b	2091	296	13
61	Kepler-1658 b	2185	221	13

Continued on next page

Table E.1 – *Continued from previous page*

Rank	Candidate	$T_{\rm eq}/\,\rm K$	$B_{\phi,\rm crit,0.2}/\,\rm G$	$B_{\rm dip,crit,0.2}/\,\rm G$
62	HATS-9 b	1913	271	13
63	HAT-P-69 b	1980	236	13
64	WASP-118 b	1725	241	13
65	OGLE-TR-132 b	1981	276	13
66	TrES-4 b	1777	257	14
67	WASP-114 b	2028	284	14
68	HATS-11 b	1771	253	14
69	WASP-17 b	1660	264	15
70	WASP-79 b	1755	255	15
71	WASP-3 b	1996	280	16
72	TOI-849 b	1965	244	16
73	HAT-P-47 b	1604	229	16
74	HATS-27 b	1674	237	18
75	Kepler-41 b	1788	276	18
76	K2-237 b	1838	280	18
77	Kepler-7 b	1632	239	19
78	HATS-18 b	2062	314	19
79	HAT-P-50 b	1857	247	19
80	NGTS-2 b	1686	239	20
81	Kepler-412 b	1850	281	20
82	XO-7 b	1744	257	21
83	HATS-39 b	1663	240	22
84	WASP-176 b	1715	246	22
85	HD 149026 b	1751	221	22
86	WASP-1 b	1766	269	23
87	OGLE-TR-211 b	1729	239	23

Continued on next page

Table E.1 – *Continued from previous page*

Rank	Candidate	$T_{\mathrm{eq}}/\,\mathrm{K}$	$B_{\phi,\mathrm{crit},0.2}/\,\mathrm{G}$	$B_{\mathrm{dip},\mathrm{crit},0.2}/\,\mathrm{G}$
88	Kepler-8 b	1679	249	25
89	HAT-P-56 b	1881	262	25
90	WASP-4 b	1870	296	26
91	KELT-3 b	1823	257	26
92	HAT-P-8 b	1773	258	27
93	WASP-15 b	1652	246	27
94	KELT-8 b	1677	268	28

† More accurate estimates in Table 7.1.

Bibliography

Abramowitz, M. & Stegun, I. A. 1965 *Handbook of mathematical functions with formulas, graphs, and mathematical tables*. New York City: Dover.

Acheson, D. J. & Hide, R. 1973 Hydromagnetics of rotating fluids. *Reports on Progress in Physics* **36** (2), 159–221.

Agol, E., Steffen, J., Sari, R. & Clarkson, W. 2005 On detecting terrestrial planets with timing of giant planet transits. *Monthly Notices of the Royal Astronomical Society* **359** (2), 567–579.

Armstrong, D. J., de Mooij, E., Barstow, J., Osborn, H. P., Blake, J. & Saniee, N. F. 2016 Variability in the atmosphere of the hot giant planet HAT-P-7 b. *NatAs* **1**, 0004.

Ballard, S., Fabrycky, D., Fressin, F., Charbonneau, D., Desert, J.-M., Torres, G., Marcy, G., Burke, C. J., Isaacson, H., Henze, C., Steffen, J. H., Ciardi, D. R., Howell, S. B., Cochran, W. D., Endl, M., Bryson, S. T., Rowe, J. F., Holman, M. J., Lissauer, J. J., Jenkins, J. M., Still, M., Ford, E. B., Christiansen, J. L., Middour, C. K., Haas, M. R., Li, J., Hall, J. R., McCauliff, S., Batalha, N. M., Koch, D. G. & Borucki, W. J. 2011 The Kepler-19 System: A Transiting $2.2R_\oplus$ Planet and a Second Planet Detected via Transit Timing Variations. *The Astrophysical Journal* **743** (2), 200.

Baraffe, I., Chabrier, G., Barman, T. S., Allard, F. & Hauschildt, P. H. 2003 Evolutionary models for cool brown dwarfs and extrasolar giant planets. The case of HD 209458. *A&A* **402** (2), 701–712.

Batchelor, G. K. 1967 *An Introduction to Fluid Dynamics*. Cambridge University Press.

Batygin, K. & Stevenson, D. J. 2010 Inflating Hot Jupiters with Ohmic Dissipation. ApJ **714** (2), L238–L243.

Bell, T. J., Zhang, M., Cubillos, P. E., Dang, L., Fossati, L., Todorov, K. O., Cowan, N. B., Deming, D., Zellem, R. T., Stevenson, K. B., Crossfield, I. J. M., Dobbs-Dixon, I., Fortney, J. J., Knutson, H. A. & Line, M. R. 2019 Mass loss from the exoplanet WASP-12b inferred from Spitzer phase curves. MNRAS **489** (2), 1995–2013.

Bodenheimer, P., Laughlin, G. & Lin, D. N. C. 2003 On the radii of extrasolar giant planets. ApJ **592** (1), 555–563.

Bodenheimer, P., Lin, D. N. C. & Mardling, R. A. 2001 On the tidal inflation of short-period extrasolar planets. ApJ **548** (1), 466–472.

Boffetta, G. & Ecke, R. E. 2012 Two-Dimensional Turbulence. *Annual Review of Fluid Mechanics* **44** (1), 427–451.

Bond, I. A., Udalski, A., Jaroszyski, M., Rattenbury, N. J., Paczyski, B., Soszyski, I., Wyrzykowski, L., Szymaski, M. K., Kubiak, M., Szewczyk, O., ebru, K., Pietrzyski, G., Abe, F., Bennett, D. P., Eguchi, S., Furuta, Y., Hearnshaw, J. B., Kamiya, K., Kilmartin, P. M., Kurata, Y., Masuda, K., Matsubara, Y., Muraki, Y., Noda, S., Okajima, K., Sako, T., Sekiguchi, T., Sullivan, D. J., Sumi, T., Tristram, P. J., Yanagisawa, T. & and, P. C. M. Y. 2004 OGLE 2003-BLG-235/MOA 2003-BLG-53: A planetary microlensing event. *The Astrophysical Journal* **606** (2), L155–L158.

Burrows, A., Guillot, T., Hubbard, W. B., Marley, M. S., Saumon, D., Lunine, J. I. & Sudarsky, D. 2000 On the Radii of Close-in Giant Planets. ApJ **534** (1), L97–L100.

Burrows, A., Hubbard, W. B., Lunine, J. I. & Liebert, J. 2001 The theory of brown dwarfs and extrasolar giant planets. *Reviews of Modern Physics* **73** (3), 719–765.

Carroll, B. W. & Ostlie, D. A. 2006 *An introduction to modern astrophysics and cosmology*.

Cattaneo, F., Emonet, T. & Weiss, N. 2003 On the Interaction between Convection and Magnetic Fields. ApJ **588**, 1183–1198.

Cauley, P. W., Shkolnik, E. L., Llama, J. & Lanza, A. F. 2019 Magnetic field strengths of hot Jupiters from signals of star-planet interactions. *Nature Astronomy* **3**, 1128–1134.

Chabrier, G. & Baraffe, I. 2000 Theory of Low-Mass Stars and Substellar Objects. ARA&A **38**, 337–377.

Chabrier, G., Barman, T., Baraffe, I., Allard, F. & Hauschildt, P. H. 2004 The Evolution of Irradiated Planets: Application to Transits. ApJ **603** (1), L53–L56.

Charbonneau, D., Brown, T. M., Latham, D. W. & Mayor, M. 2000 Detection of planetary transits across a Sun-like star. ApJ **529** (1), L45–L48.

Charbonneau, D., Knutson, H. A., Barman, T., Allen, L. E., Mayor, M., Megeath, S. T., Queloz, D. & Udry, S. 2008 The Broadband Infrared Emission Spectrum of the Exoplanet HD 189733b. ApJ **686** (2), 1341–1348.

Charney, J. G. 1971 Geostrophic Turbulence. *Journal of Atmospheric Sciences* **28** (6), 1087–1094.

Chauvin, G., Lagrange, A. M., Dumas, C., Zuckerman, B., Mouillet, D., Song, I., Beuzit, J. L. & Lowrance, P. 2004 A giant planet candidate near a young brown dwarf. Direct VLT/NACO observations using IR wavefront sensing. A&A **425**, L29–L32.

COLOMBO, G. & SHAPIRO, I. I. 1966 The Rotation of the Planet Mercury. ApJ **145**, 296.

COOPER, C. S. & SHOWMAN, A. P. 2005 Dynamic Meteorology at the Photosphere of HD 209458b. ApJ **629**, L45–L48.

COOPER, C. S. & SHOWMAN, A. P. 2006 Dynamics and Disequilibrium Carbon Chemistry in Hot Jupiter Atmospheres, with Application to HD 209458b. ApJ **649** (2), 1048–1063.

COWAN, N. B., AGOL, E. & CHARBONNEAU, D. 2007 Hot nights on extrasolar planets: mid-infrared phase variations of hot Jupiters. MNRAS **379** (2), 641–646.

COWAN, N. B., MACHALEK, P., CROLL, B., SHEKHTMAN, L. M., BURROWS, A., DEMING, D., GREENE, T. & HORA, J. L. 2012 Thermal Phase Variations of WASP-12b: Defying Predictions. ApJ **747** (1), 82.

CROSSFIELD, I. J. M., HANSEN, B. M. S., HARRINGTON, J., CHO, J. Y. K., DEMING, D., MENOU, K. & SEAGER, S. 2010 A New 24 μm Phase Curve for υ Andromedae b. ApJ **723** (2), 1436–1446.

DANG, L., COWAN, N. B., SCHWARTZ, J. C., RAUSCHER, E., ZHANG, M., KNUTSON, H. A., LINE, M., DOBBS-DIXON, I., DEMING, D., SUNDARARAJAN, S., FORTNEY, J. J. & ZHAO, M. 2018 Detection of a westward hotspot offset in the atmosphere of hot gas giant CoRoT-2b. *NatAs* **2**, 220–227.

DAWSON, R. I. & JOHNSON, J. A. 2018 Origins of hot Jupiters. *Annual Review of Astronomy and Astrophysics* **56** (1), 175–221.

DEBRAS, F., MAYNE, N., BARAFFE, I., JAUPART, E., MOURIER, P., LAIBE, G., GOFFREY, T. & THUBURN, J. 2020 Acceleration of superrotation in simulated hot Jupiter atmospheres. A&A **633**, A2.

DELLAR, P. J. 2002 Hamiltonian and symmetric hyperbolic structures of shallow water magnetohydrodynamics. *Physics of Plasmas* **9**, 1130–1136.

Dellar, P. J. 2003 Common Hamiltonian structure of the shallow water equations with horizontal temperature gradients and magnetic fields. *Physics of Fluids* **15** (2), 292–297.

Demory, B.-O., de Wit, J., Lewis, N., Fortney, J., Zsom, A., Seager, S., Knutson, H., Heng, K., Madhusudhan, N., Gillon, M., Barclay, T., Desert, J.-M., Parmentier, V. & Cowan, N. B. 2013 Inference of Inhomogeneous Clouds in an Exoplanet Atmosphere. ApJ **776**, L25.

Diamond, P. H., Itoh, S.-I., Itoh, K. & Silvers, L. J. 2007 β-Plane MHD turbulence and dissipation in the solar tachocline. In *The Solar Tachocline* (ed. D. W. Hughes, R. Rosner & N. O. Weiss), p. 213.

Dobbs-Dixon, I., Cumming, A. & Lin, D. N. C. 2010 Radiative Hydrodynamic Simulations of HD209458b: Temporal Variability. ApJ **710** (2), 1395–1407.

Dobbs-Dixon, I. & Lin, D. N. C. 2008 Atmospheric Dynamics of Short-Period Extrasolar Gas Giant Planets. I. Dependence of Nightside Temperature on Opacity. ApJ **673**, 513–525.

Dowling, T. E. 1995 Dynamics of jovian atmospheres. *Annual Review of Fluid Mechanics* **27** (1), 293–334.

Fjørtoft, R. 1953 On the Changes in the Spectral Distribution of Kinetic Energy for Twodimensional, Nondivergent Flow. *Tellus* **5** (3), 225.

Fortney, J. J., Baraffe, I. & Militzer, B. 2010 *Giant Planet Interior Structure and Thermal Evolution*, pp. 397–418.

Fortney, J. J., Lodders, K., Marley, M. S. & Freedman, R. S. 2008 A Unified Theory for the Atmospheres of the Hot and Very Hot Jupiters: Two Classes of Irradiated Atmospheres. ApJ **678** (2), 1419–1435.

Gilbert, A. D., Riedinger, X. & Thuburn, J. 2014 On the form of the viscous term for two dimensional Navier-Stokes flows. *QJMAM* **67** (2), 205–228.

Gilman, P. A. 2000 Magnetohydrodynamic "Shallow Water" Equations for the Solar Tachocline. ApJ **544**, L79–L82.

Guillot, T. 2005 The Interiors of Giant Planets: Models and Outstanding Questions. *Annual Review of Earth and Planetary Sciences* **33**, 493–530.

Guillot, T., Burrows, A., Hubbard, W. B., Lunine, J. I. & Saumon, D. 1996 Giant Planets at Small Orbital Distances. ApJ **459**, L35.

Guillot, T. & Showman, A. P. 2002 Evolution of "51 Pegasus b-like" planets. A&A **385**, 156–165.

Harrington, J., Hansen, B. M., Luszcz, S. H., Seager, S., Deming, D., Menou, K., Cho, J. Y. K. & Richardson, L. J. 2006 The Phase-Dependent Infrared Brightness of the Extrasolar Planet υ Andromedae b. *Science* **314** (5799), 623–626.

Held, I. M. & Suarez, M. J. 1994 A Proposal for the Intercomparison of the Dynamical Cores of Atmospheric General Circulation Models. *Bulletin of the American Meteorological Society* **75**, 1825–1830.

Helling, C., Gourbin, P., Woitke, P. & Parmentier, V. 2019*a* Sparkling nights and very hot days on WASP-18b: the formation of clouds and the emergence of an ionosphere. A&A **626**, A133.

Helling, C., Iro, N., Corrales, L., Samra, D., Ohno, K., Alam, M. K., Steinrueck, M., Lew, B., Molaverdikhani, K., MacDonald, R. J., Herbort, O., Woitke, P. & Parmentier, V. 2019*b* Understanding the atmospheric properties and chemical composition of the ultra-hot Jupiter HAT-P-7b. I. Cloud and chemistry mapping. A&A **631**, A79.

Heng, K., Menou, K. & Phillipps, P. J. 2011 Atmospheric circulation of tidally locked exoplanets: a suite of benchmark tests for dynamical solvers. MNRAS **413** (4), 2380–2402.

HENG, K. & SPITKOVSKY, A. 2009 Magnetohydrodynamic Shallow Water Waves: Linear Analysis. ApJ **703**, 1819–1831.

HENRY, G. W., MARCY, G. W., BUTLER, R. P. & VOGT, S. S. 2000 A transiting "51 peg–like" planet. ApJ **529** (1), L41–L44.

HIDE, R. 1966 Free Hydromagnetic Oscillations of the Earth's Core and the Theory of the Geomagnetic Secular Variation. *Philosophical Transactions of the Royal Society of London Series A* **259** (1107), 615–647.

HIDE, R. 1969*a* Dynamics of the Atmospheres of the Major Planets with an Appendix on the Viscous Boundary Layer at the Rigid Bounding Surface of an Electrically-Conducting Rotating Fluid in the Presence of a Magnetic Field. *Journal of Atmospheric Sciences* **26**, 841–853.

HIDE, R. 1969*b* On hydromagnetic waves in a stratified rotating incompressible fluid. *Journal of Fluid Mechanics* **39**, 283–287.

HINDLE, A. W., BUSHBY, P. J. & ROGERS, T. M. 2019 Shallow-water Magnetohydrodynamics for Westward Hotspots on Hot Jupiters. ApJ **872**, L27.

HUANG, X. & CUMMING, A. 2012 Ohmic Dissipation in the Interiors of Hot Jupiters. ApJ **757** (1), 47.

HUNTER, S. 2015 Waves in shallow water magnetohydrodynamics. PhD thesis, University of Leeds.

JACKSON, B., ADAMS, E., SANDIDGE, W., KREYCHE, S. & BRIGGS, J. 2019 Variability in the atmosphere of the hot Jupiter Kepler-76b. *The Astronomical Journal* **157** (6), 239.

KNUTSON, H. A., CHARBONNEAU, D., ALLEN, L. E., FORTNEY, J. J., AGOL, E., COWAN, N. B., SHOWMAN, A. P., COOPER, C. S. & MEGEATH, S. T. 2007 A map of the day-night contrast of the extrasolar planet HD 189733b. Nature **447** (7141), 183–186.

KNUTSON, H. A., CHARBONNEAU, D., COWAN, N. B., FORTNEY, J. J., SHOWMAN, A. P., AGOL, E., HENRY, G. W., EVERETT, M. E. & ALLEN, L. E. 2009 Multiwavelength Constraints on the Day-Night Circulation Patterns of HD 189733b. ApJ **690**, 822–836.

KOLMOGOROV, A. 1941*a* The Local Structure of Turbulence in Incompressible Viscous Fluid for Very Large Reynolds' Numbers. *Akademiia Nauk SSSR Doklady* **30**, 301–305.

KOLMOGOROV, A. N. 1941*b* Dissipation of Energy in Locally Isotropic Turbulence. *Akademiia Nauk SSSR Doklady* **32**, 16.

KOMACEK, T. D. & SHOWMAN, A. P. 2016 Atmospheric Circulation of Hot Jupiters: Dayside-Nightside Temperature Differences. ApJ **821**, 16.

KOMACEK, T. D., SHOWMAN, A. P. & TAN, X. 2017 Atmospheric Circulation of Hot Jupiters: Dayside-Nightside Temperature Differences. II. Comparison with Observations. ApJ **835** (2), 198.

KRAICHNAN, R. H. 1971 Inertial-range transfer in two- and three-dimensional turbulence. *Journal of Fluid Mechanics* **47**, 525–535.

LANGTON, J. & LAUGHLIN, G. 2007 Observational Consequences of Hydrodynamic Flows on Hot Jupiters. ApJ **657**, L113–L116.

LAUGHLIN, G., CRISMANI, M. & ADAMS, F. C. 2011 ON THE ANOMALOUS RADII OF THE TRANSITING EXTRASOLAR PLANETS. ApJ **729** (1), L7.

LAUGHLIN, G., WOLF, A., VANMUNSTER, T., BODENHEIMER, P., FISCHER, D., MARCY, G., BUTLER, P. & VOGT, S. 2005 A comparison of observationally determined radii with theoretical radius predictions for short-period transiting extrasolar planets. ApJ **621** (2), 1072–1078.

LAURIE, J., BOFFETTA, G., FALKOVICH, G., KOLOKOLOV, I. & LEBEDEV, V. 2014 Universal profile of the vortex condensate in two-dimensional turbulence. *Physical review letters* **113** (25), 254503.

Lee, G., Dobbs-Dixon, I., Helling, C., Bognar, K. & Woitke, P. 2016 Dynamic mineral clouds on HD 189733b. I. 3D RHD with kinetic, non-equilibrium cloud formation. A&A **594**, A48.

Liu, B. & Showman, A. P. 2013 Atmospheric Circulation of Hot Jupiters: Insensitivity to Initial Conditions. ApJ **770**, 42.

Lodders, K. 2010 Solar system abundances of the elements. In *Principles and Perspectives in Cosmochemistry* (ed. A. Goswami & B. E. Reddy), pp. 379–417. Berlin, Heidelberg: Springer Berlin Heidelberg.

London, S. D. 2017 Solitary waves in shallow water magnetohydrodynamics. *Geophysical and Astrophysical Fluid Dynamics* **111** (2), 115–130.

London, S. D. 2018 Solitary waves in shallow water hydrodynamics and magnetohydrodynamics in rotating spherical coordinates. *Geophysical and Astrophysical Fluid Dynamics* **112** (1), 62–73.

Mak, J. 2013 Shear flow instabilities in shallow-water magnetohydrodynamics. PhD thesis, University of Leeds.

Márquez-Artavia, X., Jones, C. A. & Tobias, S. M. 2017 Rotating magnetic shallow water waves and instabilities in a sphere. *Geophysical and Astrophysical Fluid Dynamics* **111** (4), 282–322.

Matsuno, T. 1966 Quasi-Geostrophic Motions in the Equatorial Area. *Journal of the Meteorological Society of Japan. Ser. II* **44**, 25–43.

Mayor, M. & Queloz, D. 1995 A Jupiter-mass companion to a solar-type star. Nature **378** (6555), 355–359.

Menou, K. 2012*a* Magnetic Scaling Laws for the Atmospheres of Hot Giant Exoplanets. ApJ **745**, 138.

MENOU, K. 2012*b* Thermo-resistive Instability of Hot Planetary Atmospheres. ApJ **754** (1), L9.

MENOU, K. & RAUSCHER, E. 2009 Atmospheric Circulation of Hot Jupiters: A Shallow Three-Dimensional Model. ApJ **700** (1), 887–897.

MIRALDA-ESCUDE, J. 2002 Orbital perturbations of transiting planets: A possible method to measure stellar quadrupoles and to detect Earth-mass planets. *The Astrophysical Journal* **564** (2), 1019–1023.

OCHOA, J., SHEINBAUM, J. & JIMÉNEZ, A. 2011 Lateral friction in reduced-gravity models: parameterizations consistent with energy dissipation and conservation of angular momentum. *Journal of Physical Oceanography* **41** (10), 1894–1901.

OKUNO, A. & MASUDA, A. 2003 Effect of horizontal divergence on the geostrophic turbulence on a beta-plane: Suppression of the rhines effect. *Physics of Fluids* **15** (1), 56–65.

PARMENTIER, V., FORTNEY, J. J., SHOWMAN, A. P., MORLEY, C. & MARLEY, M. S. 2016 Transitions in the Cloud Composition of Hot Jupiters. ApJ **828**, 22.

PEDLOSKY, J. 2013 *Waves in the ocean and atmosphere: introduction to wave dynamics*. Springer Science & Business Media.

PEREZ-BECKER, D. & SHOWMAN, A. P. 2013 Atmospheric Heat Redistribution on Hot Jupiters. ApJ **776**, 134.

PERNA, R., MENOU, K. & RAUSCHER, E. 2010 Magnetic Drag on Hot Jupiter Atmospheric Winds. ApJ **719**, 1421–1426.

PERNA, R., MENOU, K. & RAUSCHER, E. 2010 Ohmic Dissipation in the Atmospheres of Hot Jupiters. *The Astrophysical Journal* **724** (1), 313–317.

PÉTRÉLIS, F., ALEXAKIS, A. & GISSINGER, C. 2016 Fluctuations of Electrical Conductivity: A New Source for Astrophysical Magnetic Fields. Phys. Rev. Lett. **116** (16), 161102.

Press, W. H., Teukolsky, S. A., Vetterling, W. T. & Flannery, B. P. 1992 *Numerical recipes in FORTRAN. The art of scientific computing.*. Cambridge: Cambridge Univ. Press.

Rauscher, E. & Kempton, E. M. R. 2014 The Atmospheric Circulation and Observable Properties of Non-synchronously Rotating Hot Jupiters. ApJ **790**, 79.

Rauscher, E. & Menou, K. 2010 Three-dimensional Modeling of Hot Jupiter Atmospheric Flows. ApJ **714** (2), 1334–1342.

Rauscher, E. & Menou, K. 2013 Three-dimensional Atmospheric Circulation Models of HD 189733b and HD 209458b with Consistent Magnetic Drag and Ohmic Dissipation. ApJ **764**, 103.

Rauscher, E. & Menou, K. 2013 Three-Dimensional Atmospheric Circulation Models of HD 189733b and HD 209458b with Consistent Magnetic Drag and Ohmic Dissipation. *The Astrophysical Journal* **764** (1), 103.

Read, P. L. & Lebonnois, S. 2018 Superrotation on venus, on titan, and elsewhere. *Annual Review of Earth and Planetary Sciences* **46** (1), 175–202.

Rhines, P. B. 1975 Waves and turbulence on a beta-plane. *Journal of Fluid Mechanics* **69** (3), 417?443.

Richardson, L. F. 1926 Atmospheric Diffusion Shown on a Distance-Neighbour Graph. *Proceedings of the Royal Society of London Series A* **110** (756), 709–737.

Rogers, T. M. 2017 Constraints on the magnetic field strength of HAT-P-7 b and other hot giant exoplanets. *NatAs* **1**, 0131.

Rogers, T. M. & Komacek, T. D. 2014 Magnetic Effects in Hot Jupiter Atmospheres. ApJ **794**, 132.

Rogers, T. M. & McElwaine, J. N. 2017 The Hottest Hot Jupiters May Host Atmospheric Dynamos. ApJ **841** (2), L26.

Rogers, T. M. & Showman, A. P. 2014 Magnetohydrodynamic Simulations of the Atmosphere of HD 209458b. ApJ **782** (1), L4.

Roman, M. & Rauscher, E. 2017 Modeling the Effects of Inhomogeneous Aerosols on the Hot Jupiter Kepler-7b's Atmospheric Circulation. ApJ **850**, 17.

Rossby, C. G. 1939 Relation between variations in the intensity of the zonal circulation of the atmosphere and the displacements of the semi-permanent centres of action. *J. Mar. Res.* **2**, 38–55.

Salby, M. L. 1996 *Fundamentals of atmospheric physics*. Elsevier.

Saumon, D., Hubbard, W. B., Burrows, A., Guillot, T., Lunine, J. I. & Chabrier, G. 1996 A Theory of Extrasolar Giant Planets. ApJ **460**, 993.

Schecter, D. A., Boyd, J. F. & Gilman, P. A. 2001 "Shallow-Water" Magnetohydrodynamic Waves in the Solar Tachocline. ApJ **551** (2), L185–L188.

Seager, S. & Deming, D. 2010 Exoplanet atmospheres. *Annual Review of Astronomy and Astrophysics* **48** (1), 631–672.

Shell, K. M. & Held, I. M. 2004 Abrupt Transition to Strong Superrotation in an Axisymmetric Model of the Upper Troposphere. *Journal of Atmospheric Sciences* **61**, 2928–2935.

Showman, A. P. 2007 Numerical simulations of forced shallow-water turbulence: Effects of moist convection on the large-scale circulation of jupiter and saturn. *Journal of the atmospheric sciences* **64** (9), 3132–3157.

Showman, A. P., Cho, J. Y. K. & Menou, K. 2010 *Atmospheric Circulation of Exoplanets*, pp. 471–516.

Showman, A. P., Fortney, J. J., Lewis, N. K. & Shabram, M. 2012 Doppler Signatures of the Atmospheric Circulation on Hot Jupiters. *The Astrophysical Journal* **762** (1), 24.

Showman, A. P., Fortney, J. J., Lewis, N. K. & Shabram, M. 2013 Doppler Signatures of the Atmospheric Circulation on Hot Jupiters. ApJ **762**, 24.

Showman, A. P. & Guillot, T. 2002 Atmospheric circulation and tides of "51 Pegasus b-like" planets. A&A **385**, 166–180.

Showman, A. P., Lewis, N. K. & Fortney, J. J. 2015 3D Atmospheric Circulation of Warm and Hot Jupiters. ApJ **801** (2), 95.

Showman, A. P. & Polvani, L. M. 2010 The Matsuno-Gill model and equatorial superrotation. Geophys. Res. Lett. **37**, L18811.

Showman, A. P. & Polvani, L. M. 2011 Equatorial Superrotation on Tidally Locked Exoplanets. ApJ **738**, 71.

Silvotti, R., Schuh, S., Janulis, R., Solheim, J. E., Bernabei, S., Østensen, R., Oswalt, T. D., Bruni, I., Gualandi, R., Bonanno, A., Vauclair, G., Reed, M., Chen, C. W., Leibowitz, E., Paparo, M., Baran, A., Charpinet, S., Dolez, N., Kawaler, S., Kurtz, D., Moskalik, P., Riddle, R. & Zola, S. 2007 A giant planet orbiting the 'extreme horizontal branch' star V391 Pegasi. Nature **449** (7159), 189–191.

Smith, K. S. 2004 A local model for planetary atmospheres forced by small-scale convection. *Journal of the atmospheric sciences* **61** (12), 1420–1433.

Stevenson, D. J. 1991 The search for brown dwarfs. ARA&A **29**, 163–193.

Swain, M. R., Vasisht, G., Tinetti, G., Bouwman, J., Chen, P., Yung, Y., Deming, D. & Deroo, P. 2009 Molecular Signatures in the Near-Infrared Dayside Spectrum of HD 189733b. ApJ **690** (2), L114–L117.

Tabeling, P. 2002 Two-dimensional turbulence: a physicist approach. Phys. Rep. **362** (1), 1–62.

Thorngren, D. P. & Fortney, J. J. 2018 Bayesian analysis of hot-jupiter radius anomalies: Evidence for ohmic dissipation? *The Astronomical Journal* **155** (5), 214.

Thorsett, S. E., Arzoumanian, Z. & Taylor, J. H. 1993 PSR B1620-26: A Binary Radio Pulsar with a Planetary Companion? ApJ **412**, L33.

Tobias, S. M., Diamond, P. H. & Hughes, D. W. 2007 β-Plane Magnetohydrodynamic Turbulence in the Solar Tachocline. ApJ **667** (1), L113–L116.

Traub, W. A. & Oppenheimer, B. R. 2010 *Direct Imaging of Exoplanets*, pp. 111–156.

Tsai, S.-M., Dobbs-Dixon, I. & Gu, P.-G. 2014 Three-dimensional Structures of Equatorial Waves and the Resulting Super-rotation in the Atmosphere of a Tidally Locked Hot Jupiter. ApJ **793** (2), 141.

Tsapras, Y. 2018 Microlensing Searches for Exoplanets. *Geosciences* **8** (10), 365.

Vallis, G. K. 2006 *Atmospheric and Oceanic Fluid Dynamics*. Cambridge: Cambridge Univ. Press.

Vallis, G. K. & Maltrud, M. E. 1993 Generation of Mean Flows and Jets on a Beta Plane and over Topography. *Journal of Physical Oceanography* **23** (7), 1346–1362.

von Essen, C., Mallonn, M., Borre, C. C., Antoci, V., Stassun, K. G., Khalafinejad, S. & Tautvaivsiene, G. 2020 TESS unveils the phase curve of WASP-33b. Characterization of the planetary atmosphere and the pulsations from the star. *arXiv e-prints* p. arXiv:2004.10767.

Wolszczan, A. & Frail, D. A. 1992 A planetary system around the millisecond pulsar PSR1257 + 12. Nature **355** (6356), 145–147.

Wong, I., Knutson, H. A., Kataria, T., Lewis, N. K., Burrows, A., Fortney, J. J., Schwartz, J., Shporer, A., Agol, E., Cowan, N. B., Deming, D., Désert, J.-M., Fulton, B. J., Howard, A. W., Langton, J., Laughlin, G., Showman,

A. P. & Todorov, K. 2016 3.6 and 4.5 μm Spitzer Phase Curves of the Highly Irradiated Hot Jupiters WASP-19b and HAT-P-7b. ApJ **823**, 122.

Wu, Y. & Lithwick, Y. 2013 Ohmic Heating Suspends, Not Reverses, the Cooling Contraction of Hot Jupiters. ApJ **763** (1), 13.

Youdin, A. N. & Mitchell, J. L. 2010 The Mechanical Greenhouse: Burial of Heat by Turbulence in Hot Jupiter Atmospheres. *The Astrophysical Journal* **721** (2), 1113–1126.

Zaqarashvili, T. 2018 Equatorial Magnetohydrodynamic Shallow Water Waves in the Solar Tachocline. ApJ **856**, 32.

Zaqarashvili, T. V., Oliver, R. & Ballester, J. L. 2009 Global Shallow Water Magnetohydrodynamic Waves in the Solar Tachocline. ApJ **691** (1), L41–L44.

Zaqarashvili, T. V., Oliver, R., Ballester, J. L. & Shergelashvili, B. M. 2007 Rossby waves in "shallow water" magnetohydrodynamics. A&A **470**, 815–820.